

SUPERIOR SURFACE INTEGRITY BY HYBRID DRY CUTTING-HYDROSTATIC
BURNISHING FOR CONTROLLED BIOFLUID CORROSION PERFORMANCE
OF NOVEL BIODEGRADABLE MAGNESIUM-CALCIUM IMPLANTS

by

MEISAM SALAHSHOOR PIRSOLTAN

YUEBIN GUO, COMMITTEE CHAIR

MARK E. BARKEY

BETH A. TODD

GARRY W. WARREN

MARK L. WEAVER

KEITH A. WOODBURY

A DISSERTATION

Submitted in partial fulfillment of the requirements
for the degree of Doctor of Philosophy
in the Department of Mechanical Engineering
in the Graduate School of
The University of Alabama

TUSCALOOSA, ALABAMA

2012

Copyright Meisam Salahshoor Pirsoltan 2012
ALL RIGHTS RESERVED

ABSTRACT

Compared to Young's moduli (3~30 GPa) of bones, the higher moduli (100~200 GPa) of traditional permanent metallic implants cause stress shielding and result in artificial osteoporosis. To avoid the progress of this undesirable side effect, annually many second surgeries with all their social and economical consequences must be performed to remove the permanent implants after one or two years. Magnesium-Calcium (Mg-Ca) alloys are a promising alternative to tackle the aforementioned issues since they have modulus of elasticity (40 GPa) close to those of bones and they are biodegradable. However, these alloys corrode very fast and produce a large amount of dissolved Mg cations, a large volume of hydrogen, and a remarkable increase in local pH value which will cause significant imbalance in physiological reactions.

To develop Mg-Ca alloys as a successful orthopedic material, corrosion rate of these alloys should be adjusted to match the healing rate of bone tissue and local absorption rate of corrosion by-products. In this context, hybrid cutting-burnishing process has been utilized to tailor surface integrity of the Mg-Ca implants in such a way which results in gaining control on the corrosion kinetics.

A synergistic numerical-experimental investigation was conducted to study process mechanics in hybrid dry cutting-hydrostatic burnishing and to characterize the induced surface integrity on processed implants. A series of short-term and long-term in-vitro corrosion tests were performed to evaluate the effects of the hybrid technique on degradation kinetics and to

find the likely correlations between process parameters, surface integrity characteristics, and bioperformance of the processed Mg-Ca0.8 implants.

Hybrid dry cutting-hydrostatic burnishing technique was able to reduce the in-vitro degradation kinetics. The amount of this reduction was also adjustable depending on the selected process parameters and the subsequent induced surface integrity characteristics on the implants. These results suggest that it is feasible to tailor degradation kinetics of the Mg-Ca0.8 implants at the manufacturing stage so that the degradation rate matches healing rate of the bone trauma and absorption rate of the corrosion products under various physiological conditions. Magnitude of the compressive residual stresses and the depth of the compressed layer were key parameters affecting the bioperformance.

DEDICATION

This work is dedicated to all treasured teachers, mentors, friends, and family members, particularly my parents, Mohammadali and Farideh, and my lovely siblings, Somayeh and Hossein, who encouraged, guided, and supported me throughout my academic endeavors.

ACKNOWLEDGMENTS

I am pleased to have this opportunity to thank my research advisor, fellow graduate students, Ph.D. committee members, friends, and faculty members who have helped me with this research project. I am mostly indebted to Dr. Yuebin Guo, the chairman of this dissertation, for giving me the opportunity to conduct this research, providing technical guidance and financial aid, and sharing his research expertise and wisdom with me. I would like to thank all of my committee members, Dr. Keith Woodbury, Dr. Beth Todd, Dr. Mark Barkey, Dr. Mark Weaver and Dr. Garry Warren for their invaluable inputs, inspiring questions, and support of both the dissertation and my academic progress. I would also like to thank Mr. Kenneth Dunn, machine shop chief, for his assistance in making burnishing fixture and sharing his experience in troubleshooting of machining problems. Thanks also go to undergraduate research assistants Joseph McCreless, David Mitchell, Chad Ethridge, Nathan Ivey, Ross Gray, and Samuel Gray who assisted me in performing machining tests and surface integrity characterization. Last, but not least, this research would have been much more difficult without the general support of my fellow graduate students Subhash Anurag, Rahul Waiker, Michael Sealy, Hardik Singh, and Wei Li and, of course, of my family who never stops encouraging me to persist.

CONTENTS

ABSTRACT.....	ii
DEDICATION.....	iv
ACKNOWLEDGMENTS.....	v
LIST OF TABLES.....	xiii
LIST OF FIGURES.....	xiv
1. INTRODUCTION.....	1
2. BIODEGRADABLE ORTHOPEDIC MAGNESIUM-CALCIUM (Mg-Ca) ALLOYS, PROCESSING, AND CORROSION PERFORMANCE.....	4
Abstract.....	4
2.1. Introduction.....	5
2.2. Orthopedic implants.....	6
2.3. Biodegradable Mg-Ca orthopedic biomaterials.....	8
2.4. Microstructure of Mg-Ca alloys.....	12
2.5. Mechanical properties of Mg-Ca alloys.....	14
2.6. Ca alloying and surface treatment processes.....	17
2.7. Corrosion property of Mg-Ca alloys.....	22
2.8. Concluding remarks.....	30
References.....	32

3. MACHINING CHARACTERISTICS OF HIGH SPEED DRY MILLING OF BIODEGRADABLE MAGNESIUM-CALCIUM ALLOY FOR ORTHOPEDIC IMPLANTS.....	39
Abstract	39
3.1. Introduction.....	39
3.2. Machining of biodegradable magnesium alloys	42
3.3. Experimental procedure of high speed face milling	46
3.3.1. Mg-Ca _{0.8} material preparation.....	46
3.3.2. Experimental set-up and test plan.....	47
3.4. Results and discussions.....	49
3.4.1. Tool geometry and chip morphology.....	49
3.4.2. Material adhesion and flank built-up	53
3.4.3. Abrasion and tool wear	58
3.5. Conclusions.....	61
References.....	63
4. SURFACE INTEGRITY OF BIODEGRADABLE ORTHOPEDIC MG-CA ALLOY BY HIGH SPEED DRY FACE MILLING.....	67
Abstract	67
4.1. Introduction.....	68
4.2. Fabrication and microstructure of Mg-Ca _{0.8} alloy.....	71
4.3. Experimental conditions of high speed dry milling.....	71
4.4. Results and discussion	71
4.4.1. Surface topography and roughness	71
4.4.2. Microstructure and microhardness profile	74
4.4.3. Residual stresses	80

4.5. Conclusions.....	82
References.....	83
5. CUTTING MECHANICS IN HIGH SPEED DRY MACHINING OF BIOMEDICAL MAGNESIUM-CALCIUM ALLOY USING INTERNAL STATE VARIABLE PLASTICITY MODEL.....	86
Abstract.....	86
5.1. Introduction.....	87
5.2. Material model.....	91
5.2.1. Split Hopkinson pressure bar (SHPB) test.....	91
5.2.2. Internal state variable (ISV) plasticity model.....	97
5.3. Simulation scheme of high speed dry cutting.....	100
5.4. Cutting experiments.....	102
5.4.1. Material.....	102
5.4.2. Experimental setup and test plan.....	102
5.5. Results and discussions.....	103
5.5.1. Cutting forces.....	103
5.5.2. Temperature distribution and chip morphology.....	105
5.5.3. Stress distribution.....	110
5.5.4. Strain distribution.....	113
5.6. Conclusions.....	115
References.....	116
6. COMPUTATIONAL MODELING AND EXPERIMENTAL STUDY OF RESIDUAL STRESSES IN HIGH SPEED MACHINING OF BIODEGRADABLE MAGNESIUM-CALCIUM ALLOY.....	120
Abstract.....	120

6.1. Introduction.....	121
6.2. Materials model	126
6.3. Residual stress prediction model	126
6.4. Cutting setup and residual stress measurements	131
6.5. Simulation results and discussions.....	132
6.5.1. Machining forces	132
6.5.2. Residual stress evolution.....	134
6.5.3. Cutting speed effect on residual stress profile	136
6.5.4. Plowing depth effect on residual stress profile	137
6.6. Experimental validation and discussion.....	138
6.7. Conclusions.....	140
References.....	141
7. PROCESS MECHANICS IN HYDROSTATIC BURNISHING OF BIOMEDICAL MAGNESIUM-CALCIUM ALLOY	144
Abstract.....	144
7.1. Introduction.....	145
7.2. Hydrostatic burnishing.....	147
7.3. Indentation using hydrostatic burnishing tool.....	150
7.3.1. Experimental plan and setup.....	150
7.3.2. Fabrication of novel Mg-Ca _{0.8} orthopedic biomaterial	153
7.4. Results and discussions.....	153
7.4.1. Dent geometry.....	153
7.4.2. Normal force vs. hydraulic pressure	154
7.4.3. Penetration depth vs. hydraulic pressure	156

7.4.4. Acoustic emission signals	156
7.5. Simulation procedure	157
7.5.1. Mesh.....	157
7.5.2. Material model	159
7.6. Simulation results and discussion	159
7.6.1. Dent geometry.....	159
7.6.2. Temperature	160
7.6.3. Strains	161
7.6.4. Stresses.....	163
7.7. Conclusions.....	165
References.....	167
8. SURFACE INTEGRITY OF BIODEGRADABLE MAGNESIUM-CALCIUM ORTHOPEDIC IMPLANT BY BURNISHING	170
Abstract.....	170
8.1. Introduction.....	171
8.2. Background on surface integrity by burnishing.....	174
8.3. Burnishing experiment.....	180
8.3.1. Mg-Ca material	180
8.3.2. Experiment setup and plan.....	180
8.4. Results and discussion	183
8.4.1. Surface topography	183
8.4.2. Surface roughness	190
8.4.3. Microstructure.....	194
8.4.4. Surface and subsurface microstructure	198

8.4.5. Residual stresses	202
8.4.6. Statistical significance analysis.....	204
8.4.7. Discussion on the effect of surface integrity on degradation.....	206
8.5. Conclusions.....	208
References.....	210
9. FINITE ELEMENT ANALYSIS OF HYDROSTATIC BURNISHING USING INTERNAL STATE VARIABLE PLASTICITY MODEL	215
Abstract.....	215
9.1. Introduction.....	216
9.2. FE analysis of burnishing: literature review	217
9.3. Internal state variable (ISV) plasticity model	224
9.4. Hydrostatic burnishing experiments	224
9.5. Residual stress measurement procedure	226
9.6. Simulation scheme	230
9.6.1. Pre-existing roughness left from face milling.....	230
9.6.2. Finite element model of burnishing	231
9.6.3. Load-penetration characteristic curve.....	234
9.6.4. Displacement vs. time control curves	237
9.7. Results and discussion	239
9.7.1. Steady state burnishing	239
9.7.2. Effect of pressure and feed on surface roughness.....	242
9.7.3. Effect of pressure and feed on residual stress profiles.....	243
9.8. Conclusions.....	259
References.....	261

10. SURFACE INTEGRITY AND CORROSION PERFORMANCE OF MAGNESIUM-CALCIUM IMPLANTS PROCESSED BY SYNERGISTIC DRY CUTTING-HYDROSTATIC BURNISHING	265
Abstract.....	265
10.1. Introduction.....	265
10.2. Synergistic dry cutting-hydrostatic burnishing of Mg-Ca0.8 alloy	267
10.3. Surface integrity by synergistic dry cutting-hydrostatic burnishing.....	268
10.4. Corrosion performance	275
10.5. Conclusions.....	282
References.....	283
11. ADJUSTING DEGRADATION KINETICS OF A NOVEL BIODEGRADABLE MAGNESIUM-CALCIUM BIOMATERIAL BY HYBRID CUTTING-FORMING TREATMENT – LONG TERM TESTS	285
Abstract.....	285
11.1. Introduction.....	285
11.2. Mg and its alloys as biomaterials.....	286
11.3. Immersion test.....	299
11.4. Hydrogen evolution vs. time.....	301
11.4.1. Effect of burnishing pressure on degradation kinetics.....	302
11.4.2. Effect of burnishing feed on degradation kinetics	304
11.5. Surface morphology and elemental composition.....	308
11.6. Subsurface micrographs.....	313
11.7. Conclusions.....	315
References.....	316
12. SUMMARY AND FUTURE WORK	320

LIST OF TABLES

3.1 Experimental plan of high speed face milling	50
5.1 ISV material constants of Mg-Ca0.8 alloy at compression test mode.....	99
5.2 Cutting parameters used in numerical/experimental study.....	103
6.1 Thermal properties of PCD tool and Mg-Ca0.8 alloy.....	130
6.2 Elastic properties of PCD tool and Mg-Ca0.8 alloy	130
6.3 Cutting speed and plowed depth in residual stress prediction cases.....	131
7.1 Hydraulic pressure and coordinates of each dent	152
8.1 Burnishing test plan	182
9.1 Burnishing parameters used in numerical/experimental study	226
9.2 Parameters of second-order displacement polynomials.....	238
10.1 Synergistic dry cutting-hydrostatic burnishing conditions	269
10.2 Composition of simulated body fluid (SBF).....	277

LIST OF FIGURES

2.1 Hospital discharge rates for fractures, by age and body region of injury: USA, 2004-2005	7
2.2 Stress shielding in locking compression plate fixing fractures in distal tibia....	9
2.3 A ring of bone (arrow) had covered the Mg-Ca0.8 implant surface after 12 month implantation	11
2.4. Optical micrographs of (a) pure Mg, (b) Mg-Ca0.5, (c) Mg-Ca1.25, (d) Mg-Ca2.5, (e) Mg-Ca5.0, (f) Mg-Ca10.0	13
2.5 Tensile strength, 0.2% elastic limit, elongation at rupture, and elongation at the tensile strength of several Mg-Ca alloys.....	16
2.6 The effect of grain size on degradation rate of Mg alloy AZ31	19
2.7 Potential-pH equilibrium diagram for magnesium-water system at 25 °C.....	23
2.8 Subcutaneous gas bubble observed on postoperative radiographs for 4 weeks during magnesium implant degradation.....	25
3.1 Phase diagram of Mg-Ca alloy and microstructure of Mg-Ca0.8.....	48
3.2 High speed machining setup with on-line optical inspection system	49
3.3 SEM image of a fresh PCD insert.....	51
3.4 Theoretical (a,b) and actual (c,d) geometry of chip in face milling of Mg-Ca0.8 alloy	51
3.5 Effect of cutting speed (A,B), feed (C,D), and depth-of-cut (E,F) on chip morphology (A,C,E free surface; B,D,F back surface).....	54
3.6 Primary Mg phase on the bulk of grains and secondary Mg phase plus Mg ₂ Ca on the grain boundary	55

3.7 Theoretical stages in FBU formation and rake face SEM images of fresh and used PCD inserts	56
3.8 Local melting marks on the back face of a chip (a) and local surface deterioration on the machined surface due to temporary FBU formation (b).....	57
3.9a Tool abrasion in high speed diamond face milling of Mg-Ca _{0.8} without coolant.....	59
3.9b Effect of cutting speed on flank face adhesion of PCD inserts.....	60
3.9c Effect of cutting feed on flank face adhesion of PCD inserts	60
3.9d Effect of cutting depth on flank face adhesion of PCD inserts.....	61
4.1 Effect of cutting speed (a,b,c,d,e), feed (f,g,h,i,j), and depth-of-cut (k,l,m,n,p) on surface topography.....	72
4.2 Effect of cutting parameters on surface roughness	73
4.3 Effects of cutting speed (a,b), feed (c,d), and depth-of-cut (e,f) on subsurface microstructure along with typical higher magnification images (g,h)	76
4.4 Effect of cutting parameters in microhardness profile and microdent pattern	77
4.5 Effect of cutting conditions on surface microhardness in parallel and normal to feed directions.....	79
4.6 2D frame and integrated diffraction profile	81
4.7 Effect of cutting parameters on normal residual stresses.....	82
5.1 Strain-time and stress-strain data in quasi-static compression testing.....	93
5.2 Strain-time and stress-strain data in SHPB testing at various loading rates	94
5.3 Stress-strain and stress-plastic strain	96
5.4 Effect of strain rate on flow stress	96
5.5 FE mesh of chip formation simulation in orthogonal cutting of Mg-Ca _{0.8} alloy.....	101
5.6 Effect of cutting speed on cutting force: (a) time history, (b) bar chart	104

5.7 Effect of cutting speed on thrust force: (a) time history, (b) bar chart	105
5.8 Effect of cutting speed on chip morphology and temperature distributions ..	107
5.9 (a) Influence of random material voids on chip back face; (b) Chip morphology; (c) Random surface deterioration due to chip adhesion; (d) slight chip adhesion on tool flank face	109
5.10 Effect of cutting speed on von Mises stress contour.....	112
5.11 Pie-shaped shear zone in cutting soft materials and equivalent shear plane (AB)	113
5.12 Effect of cutting speed on equivalent strain (PEEQ) contour.....	114
6.1 Schematic of plowed depth and material stagnation in a cutting process.....	127
6.2 FE mesh of residual stress prediction simulation using plowed depth concept	128
6.3 Time histories of plowing and thrust forces under various cutting speeds ($\delta=0.6\text{mm}$)	133
6.4 Effect of cutting speed on plowing and thrust forces ($\delta=0.6\text{mm}$)	134
6.5 Residual stress evolution in machined Mg-Ca0.8 surface ($V=1200\text{m/min}$; $\delta=0.6\mu\text{m}$).....	135
6.6 Effect of cutting speed on residual stress profiles of machined Mg-Ca0.8 ($\delta=0.6\mu\text{m}$)	137
6.7 Effect of plowing depth on residual stress profiles of machined Mg-Ca0.8 ($V=1200\text{m/min}$).....	138
6.8 Residual stress predictions and measurements ($V=1200\text{m/min}$; $\delta=0.6\mu\text{m}$) ...	139
7.1 Experimental setup of burnishing Mg-Ca alloy.....	151
7.2 Dent fabrication map.....	152
7.3 Optical images of dents at different hydraulic pressures	154
7.4 Experimental and simulated dent profiles.....	155
7.5 Experimental and theoretical normal force at different hydraulic pressure...	156

7.6 Time history of AE signal's RMS	157
7.7 Axisymmetrical FE simulation of indentation using hydrostatic burnishing tool	158
7.8 Simulated half dent profiles before and after recovery.....	160
7.9 Temperature distribution at different hydraulic pressures	161
7.10 Strain distributions at different hydraulic pressures	162
7.11 Residual stress distribution at different hydraulic pressures.....	164
8.1 Experimental setup of burnishing	181
8.2 Different burnish patterns; A-2 parallel pass, B-2 cross pass	182
8.3a Effect of burnishing pressures on surface topography ($f=0.1\text{mm}$, $V=890\text{mm/min}$).....	184
8.3b Effect of lateral feed on surface topography ($P_h=4\text{MPa}$, $V=890\text{mm/min}$) ..	185
8.3c Effect of burnishing speed on surface topography ($P_h=4\text{MPa}$, $f=0.1\text{mm}$)...	186
8.3d Effect of burnishing pattern on surface topography ($P_h=4\text{MPa}$, $f=0.1\text{mm}$, $V=890\text{mm/min}$).....	187
8.4 Interaction between the pre-existing surface roughness and burnishing tool	188
8.5 Cold welds formed under high pressure ($P_h=10\text{MPa}$, $f=0.1\text{mm}$, $V=890\text{mm/min}$).....	189
8.6 Typical surface profiles ($P_h=4\text{MPa}$, $f=0.1\text{mm}$, $V=890\text{mm/min}$)	191
8.7 Effects of burnishing pressure, feed, speed, and pattern on surface roughness	192
8.8 Typical microstructures ($P_h=4\text{MPa}$, $f=0.1\text{mm}$, $V=890\text{mm/min}$)	196
8.9 Effect of burnishing parameters on surface microhardness	199
8.10 Virtual hardening effect of cutting marks; a) machined surface, b) polished surface.....	199

8.11a Effect of burnishing pressure on subsurface microhardness ($f=0.1\text{mm}$, $V=890\text{mm/min}$).....	201
8.11b Effects of burnishing pass and pattern on subsurface microhardness ($P_h=4\text{MPa}$, $f=0.1\text{mm}$, $V=890\text{mm/min}$)	201
8.12a Effect of burnishing parameters on normal residual stresses.....	203
8.12b Effect of burnishing parameters on principal residual stresses.....	203
8.13 Calculated p -values in the F test for one-way ANOVA (R_a roughness; HK hardness; σ residual stress; \perp perpendicular to burnish track; \parallel parallel to burnish track.....	206
9.1 Experimental setup of burnishing.....	225
9.2 Diffraction spectrum of Mg-Ca0.8 alloy	227
9.3 Schematic diagram of the electro-polishing setup	228
9.4 Surface profile and morphology of the electro-polished area.....	229
9.5 Mathematical model of material removal dynamics in electro-polishing of Mg-Ca0.8	230
9.6 Surface profile and optical micrograph of the face turned sample	231
9.7 2D plane strain FE model to simulate hydrostatic burnishing of Mg-Ca0.8 biomaterial	233
9.8 2D axisymmetric FE model to obtain load-penetration characteristic curve.....	235
9.9 Load-penetration characteristic curve in hydrostatic burnishing of Mg-Ca0.8 biomaterial	236
9.10 Displacement vs. time control curves (burnishing speed $V_b=890\text{mm/min}$).....	238
9.11a Time history of contact stress at $X_1=2.4\text{mm}$ under different burnishing pressures ($f=0.1\text{mm}$; $V=890\text{mm/min}$).....	240
9.11b Time history of contact stress at $X_1=2.4\text{mm}$ under different feeds ($P=40\text{MPa}$; $V=890\text{mm/min}$)	241

9.12 Predicted and measured surface roughness under various combinations of burnishing pressure and feed	243
9.13 Effect of pre-existing roughness on transient stresses in burnishing Mg-Ca0.8 ($P=2\text{MPa}$; $f=100\mu\text{m}$; $V=890\text{mm/min}$; first indentation cycle).....	245
9.14 Effect of pre-existing roughness on residual stresses ($P=2\text{MPa}$; $f=100\mu\text{m}$; $V=890\text{mm/min}$).....	246
9.15a Effect of burnishing pressure on residual stresses	247
9.15b Effect of burnishing feed on residual stresses.....	248
9.16 Comparison between residual stresses in-feed and in-burnish directions ...	251
9.17a Comparison between predicted and measured residual stresses (pressure effect)	254
9.17b Comparison between predicted and measured residual stresses (feed effect).....	256
9.18a Time histories of normal forces under different burnishing pressures ($f=100\mu\text{m}$; $V=890\text{mm/min}$).....	257
9.18b Time histories of normal forces under different burnishing feeds ($P=4\text{MPa}$; $V=890\text{mm/min}$).....	258
9.19 Optical images of the subsurface microstructure before and after burnishing along with resulted diffraction rings	259
10.1 Synergistic dry cutting-hydrostatic burnishing set up (a: high speed dry face milling; b: hydrostatic/low plasticity burnishing; c: high pressure hydraulic unit).....	269
10.2 Effects of process parameters on surface roughness.....	271
10.3 Effects of process parameters on residual stresses	272
10.4 Effects of process parameters on microhardness	274
10.5 Subsurface microstructure	275
10.6 Potentiodynamic polarization curves	276
10.7 Effects of process parameters on E_{corr} , I_{corr} , and C.R.....	278

10.8 Energy dispersive spectrum of corroded and uncorroded surfaces	280
10.9 Scanning electron microscopy of corroded surfaces (a:2000m/min; b:2400m/min; c:2800m/min; d:400N; e:600N; f:800N).....	281
11.1 Immersion test on processed samples using hybrid cutting-forming technique	300
11.2 Effect of pressure in hybrid dry cutting (DC)/hydrostatic burnishing (HB) on cumulative hydrogen evolution in 50, 100, 200, and 300 hrs immersion in SBF	302
11.3 Time history of solution temperature and pH in pressure-effect test.....	305
11.4 Effect of feed in hybrid dry cutting (DC)/hydrostatic burnishing (HB) on cumulative hydrogen evolution in 50, 100, 200, and 300 hrs immersion in SBF	306
11.5 Time history of solution temperature and pH in feed-effect test	307
11.6 Surface morphology and EDS spectrum of Mg-Ca0.8 implants processed under different pressure and feed in hybrid dry cutting-hydrostatic burnishing	309
11.7 Quantitative EDS and elemental composition of the corroded Mg-Ca0.8 surfaces	312
11.8a Subsurface micrographs of the corroded Mg-Ca0.8 surfaces processed under different burnishing pressures.....	314
11.8b Subsurface micrographs of the corroded Mg-Ca0.8 surfaces processed under different burnishing feeds	315

CHAPTER 1

INTRODUCTION

Several million people suffer bone fractures caused by accidents or diseases per year in the US alone. In addition, the number of bone fractures caused by age-related diseases such as osteoporosis will rapidly escalate in the coming years due to the increase of life expectancy. Expenses exceeding \$1.0 billion have to be incurred in the national health care system annually. Many of those fractures are too complex for an external medical treatment and have to be surgically fixed by internal bone implants. Current permanent metallic implants, e.g. bone screws and plates, are made of titanium, stainless steel, and cobalt-chromium alloys. These permanent metallic implants suffer two grand challenges, i.e., “stress shielding” and “secondary surgical interventions”. First, the permanent metallic implant materials are too stiff (modulus 100 ~ 200 GPa) compared to the adjacent cancellous bones (modulus 10~30 GPa). Internal loads will be mainly supported by the implants that shield tissues such as the bone from carrying the normal mechanical stresses. This “stress shielding” results in a number of critical clinical issues such as early implant loosening, damage to healing process and adjacent anatomical structures, skeleton weakening, and chronic inflammation. Second, metallic implants should be removed 1 or 2 years after the first surgery to avoid further progress of the mentioned undesirable side effects. Therefore, another surgical intervention is necessary with all the personal, medical, social and economical consequences and costs. Biodegradable implants with comparable stiffness to bone

tissues will be an ideal solution to the grand challenges of “stress shielding” and “secondary surgical interventions.

Previous *in vivo* studies have shown that magnesium-calcium (Mg-Ca) alloys may be suitable as degradable biomaterial for use in medical implants. The close Young’s modulus between magnesium (40 GPa) and cancellous bones (modulus 10~30 GPa) has the potential to minimize stress shielding. Furthermore, magnesium, an essential element of the human organism, is biocompatible with the human body. However, *the Achilles heel of a Mg-Ca implant is that it corrodes too fast* in a saline media such as the human body environment.

Addressing this issue is critical for the development of the next generation of biodegradable implants. While a number of methods such as heat treatment and alloying element have been tried to mitigate the corrosion rate of Mg alloys, the effects are very limited. The fabrication of a biodegradable Mg-based implant and corrosion control of the Mg-Ca implant through adjustable surface integrity are still in the infancy. This research aims to control corrosion rate of Mg-Ca alloys through adjusting surface integrity by a novel hybrid dry cutting – hydrostatic burnishing technique.

This dissertation is compiled in twelve chapters. The second chapter contains the relevant literature survey. Chapter 3 contains machining aspects of Mg-Ca_{0.8} at high speed cutting regime. Surface integrity of the machined surfaces is characterized in chapter 4. Numerical models are also developed in parallel to experimental work to study process mechanics and predict surface integrity characteristics. These models will make the further development of Mg-Ca_{0.8} implants more time and cost effective by alleviating the need for further experiments and measurements. Chapter 5 provides a model to investigate chip formation mechanics in high speed dry cutting of Mg-Ca_{0.8} alloy. Cutting-induced residual stresses, as a key surface integrity

characteristic, are predicted using the plowing-based cutting model in Chapter 6. To improve the surface integrity further, hydrostatic burnishing is adopted to process the machined surfaces. Process mechanics of the hydrostatic burnishing is studied in Chapter 7. Surface integrity of the burnished implants is characterized in Chapter 8. A numerical model is developed in Chapter 9 to predict burnishing-induced surface roughness and residual stresses. Short-term, electrochemical corrosion tests are performed in Chapter 10 to study the likely correlations among surface integrity and corrosion resistance of the processed implants. Long term eudiometric tests are conducted in Chapter 11 to further investigate the effect of near surface layers on in-vitro degradation. Finally, Chapter 12 summarizes key findings of this research and addresses the remaining issues which need further investigation in future studies.

CHAPTER 2

BIODEGRADABLE ORTHOPEDIC MAGNESIUM-CALCIUM (Mg-Ca) ALLOYS, PROCESSING, AND CORROSION PERFORMANCE

Abstract

Magnesium-Calcium (Mg-Ca) alloy as an emerging biodegradable implant material has received considerable attentions in orthopedic fixation applications. The biodegradable Mg-Ca alloys avoid stress shielding and secondary surgery inherent with permanent metallic implant materials. They also provide sufficient mechanical strength in load carrying applications as opposed to biopolymers. However, the key issue facing a biodegradable Mg-Ca implant is the fast corrosion in the human body environment. The ability to adjust degradation rate of Mg-Ca alloys is critical in the successful development of biodegradable orthopedic implants. This paper focuses on the functions and requirements of bone implants and critical issues of current implant biomaterials. Microstructures and mechanical properties of Mg-Ca alloys, and the unique properties of novel magnesium-calcium implant materials have been reviewed. Various manufacturing techniques to process Mg-Ca based alloys have been analyzed regarding their impacts on implant performance. Corrosion performance of Mg-Ca alloys processed by different manufacturing techniques was compared. In addition, the societal and economical impacts of developing biodegradable orthopedic implants have been emphasized.

2.1. Introduction

Several million people suffer bone fractures caused by accidents or diseases per year in USA alone. In addition, the number of bone fractures caused by age-related diseases such as osteoporosis will rapidly escalate in the coming years due to the increase of life expectancy. Expenses exceeding \$1.0 billion annually [1] have to be incurred in the national health system in 2004-05. Many of those fractures are too complex for an external medical treatment but have to be surgically fixed by internal bone implants such as the orthopedic implant. Current commercial permanent metallic implants, e.g. bone screws and plates, are made of titanium, stainless steel, and cobalt-chromium alloys. Current permanent metallic implants suffer two grand challenges, i.e. “stress shielding” and “surgical interventions”. First, the permanent metallic implant materials are too stiff (Young’s modulus 100 ~ 200 GPa) compared to the adjacent cancellous bones (Young’s modulus 10 ~ 30 GPa). Internal loads will be mainly supported by the implants that shield tissues such as the bone from carrying the normal mechanical stresses. This “stress shielding” results in a number of critical clinical issues such as early implant loosening, damage to healing process and adjacent anatomical structures, skeleton thickening, and chronic inflammation. Second, metallic implants should be removed 1 or 2 years after the first surgery. Therefore, another surgical intervention is necessary with all the personal, medical, social, and economical consequences and costs. Biodegradable implants, which dissolve in the human organism, will be an ideal solution to the grand challenges of “stress shielding” and “surgical interventions”.

Previous *in-vivo* studies [2-7] have shown that magnesium-calcium (Mg-Ca) alloys may be suitable as degradable biomaterial for use in medical implant. The close Young’s modulus between magnesium (40 GPa) and cancellous bones (Young’s modulus 10 ~ 30 GPa) has the

potential to minimize stress shielding. Furthermore, magnesium, an essential element of the human organism, is biocompatible with the human body. However, the Achilles heel of a Mg-Ca implant is that it corrodes too fast in saline media such as in the environment of the human organism.

Answering these questions is critical for the development of the next generation of biodegradable implants, which has significant societal and economic impacts. While a number of methods such as heat treatment and alloying element have been tried to mitigate the corrosion rate of Mg alloys, the effects are very limited. The fabrication of a biodegradable Mg-based implant and corrosion control of the Mg-Ca implant through adjustable surface integrity are still in the infancy. This paper aims to review the works performed in last decade in processing Magnesium alloys especially Mg-Ca alloys and the achievements in controlling their corrosion performance.

2.2. Orthopedic implants

Fractures in skeleton system continue to be the leading cause of injury hospitalization in the United States, accounting for more than one-half of all injury hospitalizations in 2004-05 [1]. For the older population, 75 years of age and over, almost three-fourths of injury hospitalizations were for fractures. As indicated in figure 2.1, fractures in skeleton system can be categorized in four broad groups as fractures in head and neck, spine and back, torso, and extremities (upper and lower). It is noticeable that more than half of the fractures happen in extremities including shoulder, upper arm, forearm, elbow, wrist, hand, fingers, hip, upper leg, thigh, knees, lower leg, foot, ankle, and toes.

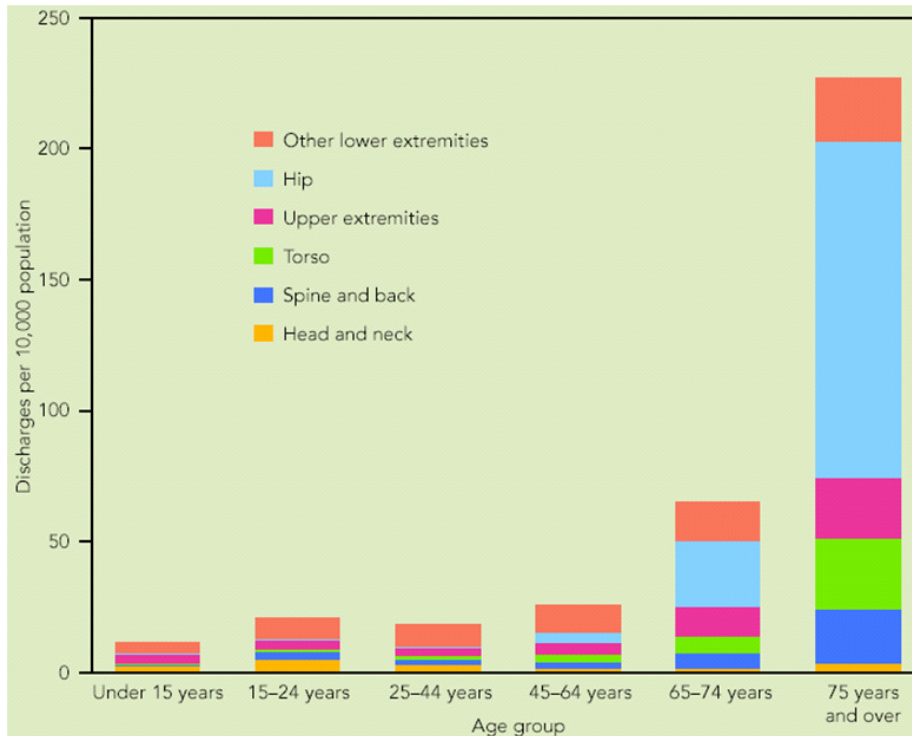


Fig. 2.1 Hospital discharge rates for fractures, by age and body region of injury: USA, 2004-2005 [1].

When a bone fractures, the fragments lose their alignment in the form of displacement or angulation. For the fractured bone to heal without any deformity the bony fragments must be re-aligned to their normal anatomical position. Orthopedic surgeons attempt to recreate the normal anatomy of the fractured bone by *reduction*.

In orthopedic surgery, implants may refer to devices that are placed over or within bones to hold a *fracture reduction* while prosthesis would be the more appropriate term for devices that replace a part or whole of a defunct joint. In this context, implants may be placed within or outside the body. Dental implants are one of the few medical devices which permanently cross the boundary between the inside and the outside of the body, since the base of the implant is

connected to the bone of the lower or upper jaw and the top of the implant is in the mouth, where it can be crowned with an artificial tooth.

2.3. Biodegradable Mg-Ca orthopedic biomaterials

Traditional methods of osteosynthesis or osteotomy use permanent metallic implants e.g. bone screws and bone plates made of stainless steel, titanium, cobalt alloys [9,10,12]. The conventional metallic implants are too stiff compared bones' moduli. The modulus mismatch between permanent implants and bones shields the healing bone from being exposed to mechanical loads. This "stress shielding" (figure 2.2) results in critical clinical issues such as early implant loosening, damage healing process and adjacent anatomical structures, skeleton thickening, and chronic inflammation. [15-23]. Another issue for permanent implants is that revision surgeries are necessary when the bone heals. So personal, medical (the risk of refractures and additional days of after-treatment), social and economical consequences and costs have to be performed, in which the implants are excised. Only in patients older than 60 years it is acceptable to leave metal in situ. Usually, metal implants should be removed 1 to 2 years after the first operation [11,12]. In this context, Mg-based alloys, especially Mg-Ca alloys, have received a lot of attention due to their close modulus between Mg-based alloys and bones.

The first-generation biomaterials [23] were selected based on only two criteria: (i) suitable combination of physical properties to match those of the replaced tissue and (ii) minimal toxic effect in human body [22]. The second generation of biomaterials encompasses two broad groups: (i) bioactive materials with the ability to interact with the biological environment in order to enhance the biological response as well as the tissue/surface bonding, and (ii)

biodegradable materials with the ability to undergo a progressive degradation while new tissue regenerates and heals. Currently, biodegradable implants are mainly made of polymers, such as poly-L-Lactic acid. However, these polymer based implants usually does not have enough mechanical strength and consequently low load-bearing capacity which have led researchers to seek for biodegradable metallic substitutes. Mg and especially Mg-Ca alloys are among the most interested options.

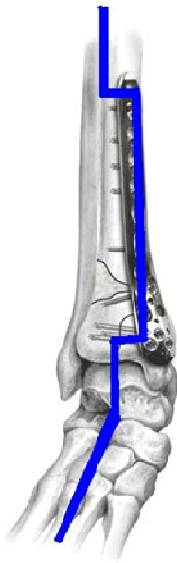


Fig. 2.2 Stress shielding in locking compression plate fixing fractures in distal tibia.

Magnesium is an essential element to metabolic activities of the human body and intake of 300 ~ 400 mg of magnesium is normally required daily [24]. According to the measured weight loss rate (19 ~ 44 mg/cm²/day), as long as the total surface area of a magnesium implant is less than 9 cm², the dissolved Mg²⁺ would be easily absorbed or consumed by the human body

[25]. However, the rapid generation of by-products such as hydrogen, hydroxide anion or OH⁻ could cause serious problems, even a fatal threat to a patient. Particularly, the severe side effect of rapid generation of hydrogen bubbles in the blood circulating system may finally exclude the possible application of magnesium stent in vascular system.

Alloying is one of the possible solutions to reduce the corrosion rate of Mg in the human body. A concern with alloying approach is biocompatibility of the alloying elements. Therefore unfavorable alloying elements largely limit the alloying approach and alloying elements should be carefully selected. Feser et al [2] studied the influence of degradable Mg-Ca alloys with 0.6, 0.8, 1.0, and 1.2 wt.% Ca on dendritic cell function. These cells are the major antigen representing the body cells. They concluded that Mg-Ca alloys have excellent biocompatibility and Mg²⁺ and Ca²⁺ cations produced as the result of in-vitro degradation do not significantly interfere with dendritic cell functions. Li et al [3] made binary Mg-Ca alloys with various Ca contents (1 to 3%) and different fabrication conditions for use as biodegradable materials within bone. The cytotoxicity evaluation using L-929 cells revealed that MgCa1.0 alloy did not induce toxicity to cells, and the viability of cells for MgCa1.0 alloy extraction medium was better than that for commercial pure c.p. Ti. They implanted MgCa1.0 alloy and c.p. Ti pins into the left and right rabbit femoral shafts and observed the degradation process for 1, 2, and 3 months. MgCa1.0 alloy pins had degraded gradually during the whole experiment period, which was evident by the reducing diameter of pins. At month 3, the MgCa1.0 alloy pin was totally absorbed and an irregular shaped hole was left in the implant position. Moreover, new bone was formed around the MgCa1.0 alloy pin while no remarkable radiographic signs indicating new bone formation was discovered around c.p. Ti pins during the experimental period. Gas shadows were observed around the MgCa1.0 alloy pins at month one, but they were vanished without any adverse effects

in second month after operation. X-ray diffraction showed that the mineral phases in the precipitated white layer on MgCa1.0 pin were $Mg(OH)_2$ and Hydroxy-Apatite (HA).

Beside an adequate primary stability and the ability to degrade without side effects, a good biocompatibility is required to use Mg alloys as materials for osteosynthesis. Thomann et al [4] conducted in-vivo experiments to study effects of alloying Mg with calcium (in MgCa0.8), lithium, aluminum, and rare earth (in LAE442) elements on corrosion process. Extruded implants of these resorbable Mg alloys were implanted for a period of 12 month into the marrow cavity of both tibiae of New Zealand White rabbits. Figure 2.3 clearly shows a ring of bone covering the MgCa0.8 implant surface. This indicates the osteogenic effect of this alloy. After 12 months the bone-implant contact was clearly stronger in MgCa0.8 case. However, it degraded more than LAE442 but slow enough to avoid any gas bubble generation. Stability of the implants is of major concern at beginning of the implantation.



Fig. 2.3 A ring of bone (arrow) has covered the MgCa0.8 implant surface after 12 month implantation [4].

Thomann et al reported a pitting corrosion of MgCa0.8 implants after three months into implantation which increased till 6 months. MgCa0.8 implants showed an average loss in the cross section of more than half of the initial area after 12 months. The decrease in volume of MgCa0.8 implants were 11%, 31%, and 51% after 3, 6, and 12 month implantation, respectively.

2.4. Microstructure of Mg-Ca alloys

Binary alloy system of Mg-Ca has attracted a considerable attention in recent years to be used as implant material [3,11,12,26-29]. On the magnesium rich side of this system, the maximum solubility of calcium in the magnesium lattice at room temperature amounts to 0.8wt%. At a calcium concentration of 16.2 wt% the alloy solidifies in eutectic composition. Low alloyed Mg-Ca systems consist of an α -phase solid solution (magnesium with interstitial calcium) and a eutectic structure (α phase + Mg₂Ca). Electrochemically, Mg₂Ca phase is more active than α -Mg and assumes the role of anode contradicting other intermetallics which are cathode in relation to Mg. Mg₂Ca has the identical crystal structure as Mg, however, twice the lattice parameter magnitudes [29]. This reveals that Ca is a unique alloying addition to Mg in the context of biodegradable implants. The addition of a small amount of calcium has two distinct effects on Mg-Ca alloys. First, it increases the corrosion resistance and second, it minimizes the grain growth and leads to smaller grains in casts. A possible disadvantage of this grain refinement is the increased sensitivity to hot crack creation during the deformation process [27]. Rad et al [30] studied the effect of calcium content on microstructure of Mg-Ca alloys containing 0.5, 1.25, 2.5, 5.0, and 10.0 wt.% Ca (figure 2.4). Their results revealed that the grain size and dendritic cell size decrease significantly with higher amounts of Ca while more Mg₂Ca

intermetallic phase appears in grain boundaries for higher Ca content. The mechanical behavior under dynamic and quasi-static conditions is influenced by the microstructure which in return is determined by the thermo-mechanical treatment history [31]. A fine grain structure possesses the lowest ductility and with increasing grain size ductility increases.

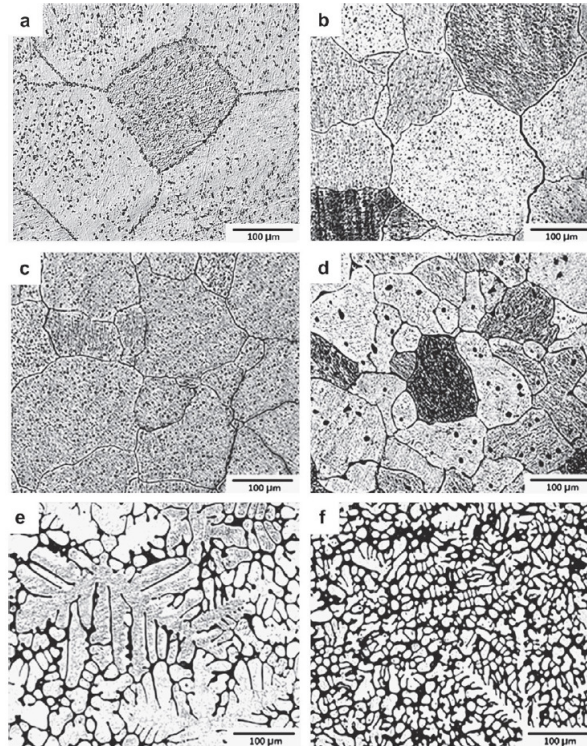


Fig. 2.4 Optical micrographs of (a) pure Mg, (b) Mg-Ca0.5, (c) Mg-Ca1.25, (d) Mg-Ca2.5, (e) Mg-Ca5.0, (f) Mg-Ca10.0 [30].

A high density of twins characterizes the micrograph in Mg alloys generally and in Mg-Ca alloys specifically. It seems that twinning governs the onset of plastic deformation in Mg alloys. They are responsible for the higher compressive strain to failure in the quasi static compression test. However, the quasi static compression stress is lower than the dynamic

compression stress. Knowing that twins' density is lower in dynamic compression, this translates into the fact that twinning increases the ductility of Mg alloys. The alloys in the as extruded condition have a very inhomogeneous distribution of grain size and after dynamic compression test the twin density in the coarse grains is higher. The competitive mechanisms of dislocation and twinning lead to transcrystalline fracture in coarse grains and to crack propagation in fine grains. In non-extruded condition the grain size distribution is more homogeneous.

2.5. Mechanical properties of Mg-Ca alloys

Hassel et al [27] and Drynda et al [32] studied the influence of Ca amount on mechanical properties of Mg-Ca binary alloys. To produce this special Mg alloy, they used pure magnesium (99.8%) and Mg-Ca30.0 pre alloy (30.0 wt.% Ca) and mixed them to produce Mg-Ca alloys with different calcium concentration. Alloying magnesium with low amounts of calcium, up to 4.0 wt.%, leads to an increase in tensile strength up to approximately 240 MPa while the tensile strength of pure magnesium in extruded condition is about 200 MPa. The 0.2% elastic limit also increases steadily with increasing concentration of calcium. For low alloyed compositions, the 0.2% elastic limit is about 80 MPa lower than the tensile strength. This is an indication of relatively high plasticity (figure 2.5). The difference between tensile strength and elastic limit decreases down to 40 MPa for higher concentrations of calcium. No significant increase in the tensile strength can be observed above 2.0 wt.% calcium.

Moreover, the workability decreases and extrusion force increases significantly for higher amounts of calcium in direct extrusion. The processing of alloys containing more than 4.0 wt.% calcium can only be done by indirect extrusion due to low workability and since the container

friction, as a limiting factor, can be ignored in this case [27]. For higher amounts of calcium an increased amount of eutectic with a melting temperature of 516.5 C° can be observed. This may lead to considerable hot cracking if the deformation temperature is same as the melting temperature of the eutectic phase.

Investigations regarding the influence of Ca amount on plasticity and ductility of Mg-Ca alloys have shown that calcium content dramatically affects the elongation at rupture (figure 2.5). For calcium concentrations below the solubility limit at room temperature, i.e. 0.8 wt.%, the elongation at rupture is about 13 to 15%. There is a continuous decrease in elongation above 1.5 wt.% Ca. The alloy with the highest Ca content, i.e. 4.0 wt.%, has the lowest elongation of 5%. The elongation at the tensile strength decreases continuously from 12% at 0.4 wt.% Ca to 4.5% at 4.0 wt.% calcium. Precipitation of brittle Mg₂Ca intermetallic phase on grain boundaries and inside the grains is responsible for poor ductility above 1.5 wt.% Ca concentration.

Forming and machining of brittle materials such as magnesium alloys with conventional methods are limited and intermediate treatments of the workpiece would be necessary. Under dynamic loading, metallic materials exhibit an increase in flow stress with increasing deformation rate. Materials of lower ductility can be formed up to large strains through implementing high strain rate deformation processes such as laser shock peening and high speed machining. Furthermore, constitutive material laws are necessary to describe the material behavior in simulation of high strain rate deformation processes [33-38]. The strain rate and temperature considerably influence the material flow behavior in deformation processes. Under quasi-static loading strain hardening causes an increase of force and acts as a stabilizing factor on deformation process. In case of dynamic loading, additional influences on the flow stress and the ductility of the material have to be taken into consideration. With increasing deformation

rate, the strain rate sensitivity increases leading to a higher value of flow stress and stabilizes the deformation. On the other hand, the adiabatic character of the deformation process reduces the flow stress and promotes instability. Furthermore, the deformation process is influenced by inertia and mechanical wave propagation effects [39-42].

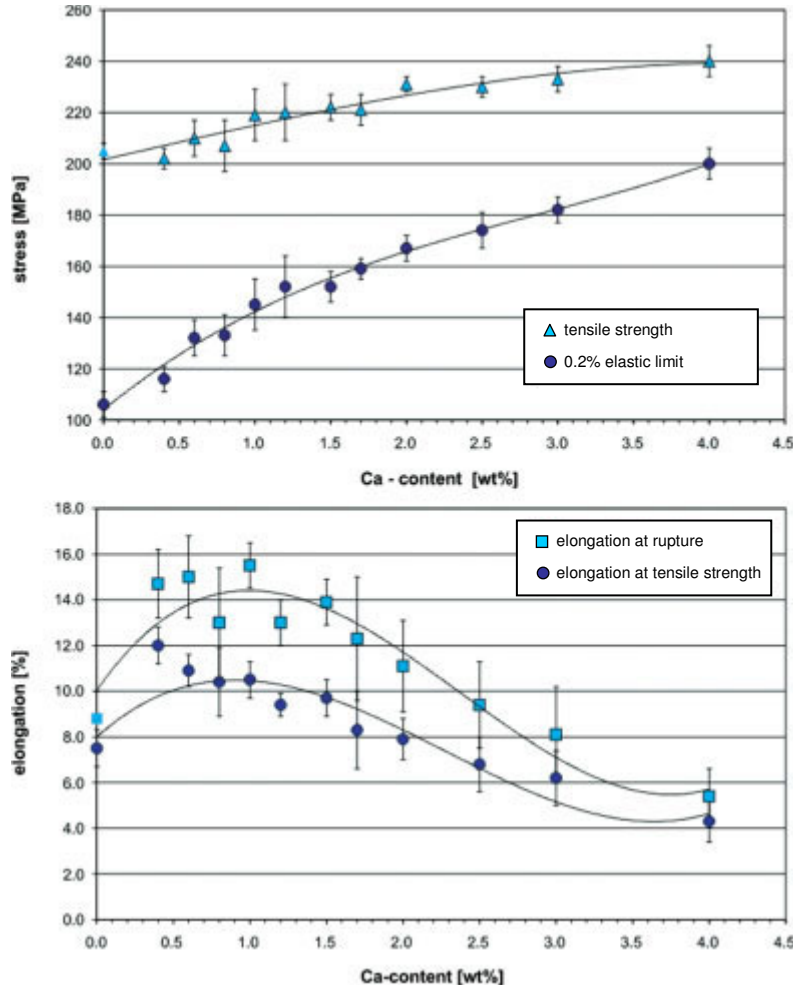


Fig. 2.5 Tensile strength, 0.2% elastic limit, elongation at rupture, and elongation at the tensile strength of several Mg-Ca alloys [27,32].

2.6. Ca alloying and surface treatment processes

Successful application of biodegradable Mg implants requires a controlled kinetics of degradation to avoid disruption of metabolic reactions during the healing process. As discussed in section 4, alloying is one way to achieve that control on degradation. Further adjustment of degradation rate is mainly achieved through two methods: (i) surface coatings and (ii) mechanical treatments. Drynda et al [32] developed binary fluoride-coated Mg-Ca alloys with improved degradation kinetics. The Ca content was 0.4, 0.6, 0.8, 1.2, and 2.0 wt% in their study. Electrochemical properties of uncoated and coated alloys were characterized in 0.5, 0.9 (physiological chloride concentration), 2.5, and 5.0% NaCl solutions at 37°C. Solutions were buffered with tris-solution to a constant pH value of 7.4 (physiological pH value). Degradation rates were investigated using hydrogen evolution technique. Calcium concentration of 0.8 wt% resulted in the minimum degradation rate compared to other Ca contents. MgF₂ coated Mg-Ca alloys showed slower rates (lower than 150 $\mu\text{A}/\text{cm}^2$), regardless of the Ca content of the substrate Mg-Ca alloy. Moreover, no H₂ gas formation was detected within the first 8 to 40 hours in fluorinated alloys. Thomann et al [5] examined if the corrosion resistance of previously in vivo tested Mg-Ca0.8 implants could be increased by applying a magnesium fluoride coating. The gravimetric analysis before implantation, and 3 and 6 months after implantation showed a slight decrease in volume as compared to uncoated implants. The mean loss in volume after 3 months was 8.54% ($\pm 2.32\%$). After 6 months, this loss had approximately tripled (25.33% \pm 12.66%). However, the mechanical properties of the coated implants exhibited a reduction in strength after 3 months. After 6 months, the strength of the coated implants was higher than that of uncoated cylinders.

Gu et al [43] studied the effect of alkaline heat treatment on biocorrosion rate of Mg-Ca1.4 alloy. In this process coupons were soaked in three alkaline solutions (Na_2HPO_4 , Na_2CO_3 , and NaHCO_3) for 24 hrs and then heat treated at 500 °C for 12 hrs. As the result, magnesium oxide layers with 13, 9, and 26 μm thick were formed on test surfaces, respectively, and in-vitro corrosion of Mg-Ca1.4 alloy decreased effectively in simulated body fluid. This improvement in biocorrosion was in direct relation to oxide film thickness. The thicker film resulted in slower corrosion rate. Beside, the cytotoxicity with L-292 cells revealed no toxic effect of the formed oxide layers. Zhang et al [44] coated Mg-Ca1.0 alloy with calcium phosphate using electrochemical deposition. The deposited calcium phosphate was mainly formed of flaky brushite crystallites. Electrochemical tests in Hank's solution showed an increase in open circuit potential and a decrease in corrosion current density for coated samples indicating an enhancement in corrosion resistance. Moreover, coated samples produced much lower hydrogen initially but hydrogen evolution rate increased rapidly once pits happened in coatings. Li et al [45] investigated the corrosion behavior of TiO_2 coated Mg-Ca1.0 alloy in SBF. Uncoated Mg-Ca1.0 corroded considerably after 48 hrs immersion in SBF, however, the coated alloy remained almost intact after 168 hrs immersion except than a few break down sites. Corrosion current density of coated alloy was three orders of magnitude smaller than unprotected alloy. Although TiO_2 is nontoxic and therefore biocompatible in that sense, however, in case of biodegradable Mg-Ca1.0 it is not clear if it could be absorbed or discharged by the body.

Another approach to enhance the bioperformance of Mg-Ca alloys is the mechanical treatment of the near surface or bulk material which will effectively reduce the corrosion rate. An advantage of using mechanical processing over surface coating is that it also enhances the material's strength and fatigue resistance which are also critical in implant applications. The

previous study [46] has shown that grain refinement may be a proper route to control the corrosion rate of Mg alloy AZ31 in Hank's solution, figure 2.6. The samples were processed by squeeze casting (SC), hot rolling (HR), and equal channel angular pressing (ECAP), respectively. The corrosion rates of the HR and ECAP processed samples with fine grains ($\sim 10 \mu\text{m}$) were only about 50% of the coarse grained ($\sim 400 \mu\text{m}$) SC sample. However, fine grains alone would not increase corrosion rate. However, the effect of grain refinement for Mg-Ca alloys on corrosion has been yet reported.

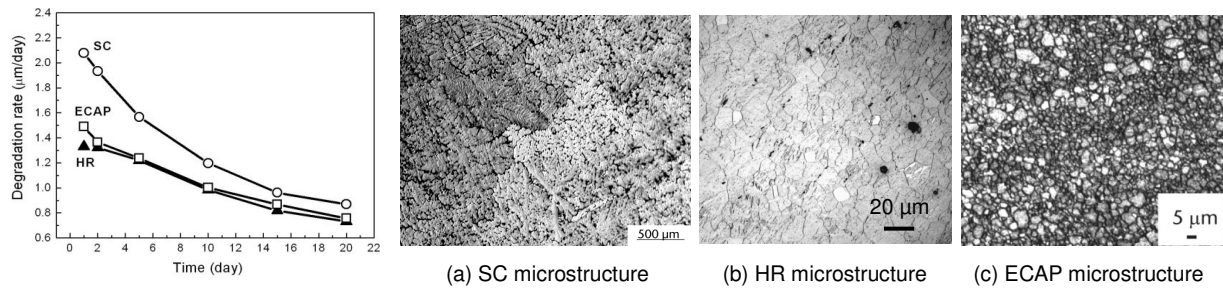


Fig. 2.6 The effect of grain size on degradation rate of Mg alloy AZ31 [46].

Mechanical treatments like cutting and micro-forming are more focused on the near surface zone of the implants. Bach et al [47] analyzed the influence of surface treatment, different alloy compositions and varying heat treatments on corrosion kinetics of work piece surfaces in salt spray corrosion tests according to DIN 50021 SS. Lower feed rates for a constant cutting speed resulted in harder layers close to surface caused by longer exposure to thermo-mechanical loads and therefore higher chances for microstructural changes. Higher cutting speeds for a constant feed rate gave rise to a smoother surface due to thermally induced reduction

of the material strength on the shear plane and the increased easiness of cut. They ended up with more surface roughness using polycrystalline diamond (PCD) inserts than cemented carbides. The corrosion rate of the samples machined with PCD inserts was significantly higher than the corrosion rate of the samples machined with uncoated cemented carbide inserts. The more corrosion resistance was related to lower surface roughness produced by cemented carbide tools. It was also observed that increasing cutting speed intensifies the corrosion rate. However, the corrosion test with 5.0 wt.% salt solution is too aggressive and only indicates the tendency.

Denkena et al [12] sought to adjust the degradation kinetics of Mg-Ca3.0 alloy through modifying surface (i.e. topography) and subsurface (i.e. residual stresses) characteristics by applying turning process. They explored different combinations of cutting process parameters to create a specific degradation profile appropriate for certain medical application. They noticed that for same amount of depth of cut and feed, lower cutting speed shows lower corrosion rate and they related that to higher cutting forces and consequently higher and deeper compressive residual stresses. However, the better surface finish at lower feed rates did not show a significant influence on corrosion resistance.

Von Der Hoh et al [6] examined the degradation behavior of Mg-Ca0.8 implants with different surface conditions for 3 to 6 months in-vivo. The employed Mg-Ca0.8 implants received turning, sand-blasting, and threading treatments. Roughness depths were 3.65 μm for turned implants and 32.7 μm for sand-blasted implants. New bone formation and hydrogen gas evolution were used as metrics to study the degradation behavior. Their study could confirm the generally good clinical compatibility and osteoinductive potency of Mg-Ca0.8 alloy. Increase in *surface roughness* led to a faster degradation rate. However, a univaribale analysis of variance with significance level of 0.05 showed that the influence of the surface roughness was statically

not significant ($p = 0.257$). The faster decomposition of Mg implants leads to more H_2 gas release. The sand-blasted cylinders decomposed the fastest. Furthermore, 53% of the radiographically detectable gas generation appeared in sand-blasted implants. The turned cylinders which exhibited the least structural loss showed hardly any gas formation. The formed gas was resorbed in all cases except one without any clinical problems. Moreover, they found that Mg-Ca0.8 shows obvious pitting corrosion for threaded cylinders but not for turned and sand-blasted implants. In addition, turned implants showed the best integration into the bone compared to sand-blasted and threaded cylinders. Therefore, it seems a smooth surface is particularly suitable when using resorbable implants made of Mg alloys as bone implants in osteosynthesis. This is against conventional implants which will make better and stronger bone-implant bonding if the implant surface is rougher.

Literature survey on mechanical surface treatments reveals another process named deep rolling or shortly DR. This process, which is developed by Ecoroll, is very similar to the low plasticity burnishing (LPB) process developed by Lambda Technologies in terms of working principle [48], even though it is claimed that DR produces more cold work than LPB [49]. Using LPB/DR in medical device manufacturing applications is new and there are only a few published research works for that [50-52]. Denkena et al [12] tried to control the corrosion of the Mg-Ca3.0 implant by mechanical treating the implant surface using DR technique and ultimately to achieve adaptable degradation profile for various medical applications. As compared to shot peening, LPB/DR avoids the contamination of the processed surfaces and consequently prevents the third body wear [53]. Besides, LPB/DR produces higher and deeper compressive residual stresses with less amount of cold work [49,54]. High levels of cold work leave a severely deformed surface layer with a high dislocation density that adversely affects the thermal and mechanical stability

of compressive layer. However, Gill et al [55] reported lower levels of cold work as a promising potential of DR where they compared this process with shot peening (SP) in terms of compressive residual stress and amount of cold work.

There is a general consensus [55-61] that more stable compressive residual stresses will be achieved by minimizing the amount of cold work necessary to generate them. Severe plastic deformation in shot peening makes compressive residual stresses less stable. LPB/DR could be an effective means of mitigating corrosion initiated failures without altering either material or design of the implants [62]. The depth of compression from LPB/DR can greatly exceed the maximum corrosion pit depth in orthopedic implants and therefore prevent failure from pitting or cracking and ensure safe-life operation of the implant [63]. LPB/DR is a novel process and it needs an extensive study of the effect(s) of various process parameters, e.g. lateral feed, speed, force, ball diameter, tool path, lubricant, etc., on surface integrity and product performance to develop the required database for different materials [64-66].

2.7. Corrosion property of Mg-Ca alloys

The basic electrochemical character of the magnesium with standard potential of -2.375 volts leads to a low corrosion resistance. Magnesium implants' surface passivates and builds up a thin grey layer of magnesium oxide, when exposed to air, which prevents further chemical reactions. However, magnesium is attacked significantly in saline media such as human body environment. These characteristics primarily enable Mg alloys particularly Mg-Ca alloys to be used as absorbable implant materials [11]. Magnesium can be entirely absorbed in human body like absorbable polymers when it is considered to be used in biomedical applications.

Meanwhile, it offers the great advantage of higher mechanical strength as opposed to biopolymers. Dissolution of magnesium in chloride containing media like human body happens through the following reaction [27]:



Magnesium reacts with water which is plentiful in body fluid and produces hydroxide and hydrogen. In high pH (>11.5) environments, magnesium hydroxide will play as a stable protective layer on the surface of magnesium implants, but lower pH (<11.5) will facilitate corrosion of magnesium alloys in aqueous solution (figure 2.7).

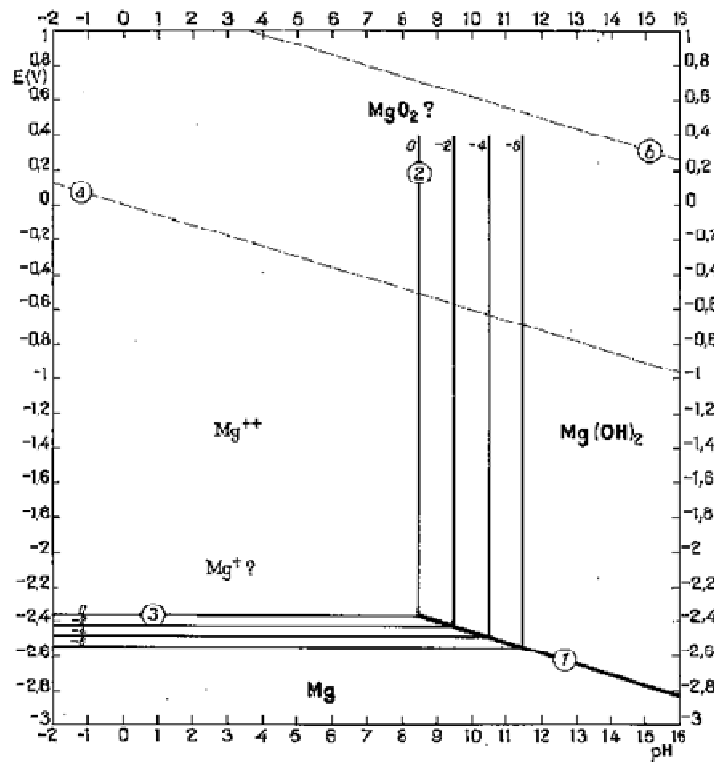


Fig. 2.7 Potential-pH equilibrium diagram for magnesium-water system at 25 °C [67].

Since the local pH at implant-bone interface is about 7.4 or even lower due to secondary acidosis resulting from metabolic and resorptive processes after surgery [68], the magnesium hydroxide layer cannot cover the implant surface. Therefore, the constant exposure to high chloride containing electrolyte of the physiological system causes an accelerated corrosion on the Mg implant surface in vivo.

During magnesium dissolution, hydrogen gas is produced and actually hydrogen evolution rate equals to magnesium implant dissolution/corrosion rate. As such, eudiometry of hydrogen has been used as a tool to study long term degradation behavior of Mg-Ca implants in vivo. Corrosion of one gram magnesium results in production of 1.081 liter hydrogen gas [27,68]. The accelerated corrosion will lead to early loss of mechanical integrity and to generate hydrogen at rates too fast for human body to deal with which will result in the formation of subcutaneous gas bubbles [68,69]. Figure 2.8 shows a typical gas bubble containing hydrogen. As mentioned before, several possibilities exist to adjust the corrosion rate and two of them are using alloying elements and protective coatings. In alloying approach, critical issues are using minimized alloying elements, non-toxic elements, and biological compatibility. Magnesium alloys exhibit different degradation rates depending on the alloying element they contain. Most alloying elements such as aluminum and zinc are suggested to increase the rate of oxidation, while alloying magnesium with rare earth elements is suggested to decrease the oxidation rate of magnesium alloys [68].

Hassel et al [27] studied the influence of Ca amount and chloride concentration in corroding media on corrosion behavior of Mg-Ca alloys. A negative shift of about -0.1 volts in open circuit potential (OCP) was observed by increasing chloride concentration in the electrolyte for all the investigated alloys. Polarization curves showed that with increasing amount of Ca in

the alloy, mixed corrosion potential (E_{corr}) becomes more noble or positive. The magnitude of the corrosion current density (i_{corr}) also changed with Ca content and the higher the Ca content was, the larger the current density became. NaCl concentration showed similar effect and increased amount of chloride led to higher corrosion current density and corrosion rates.

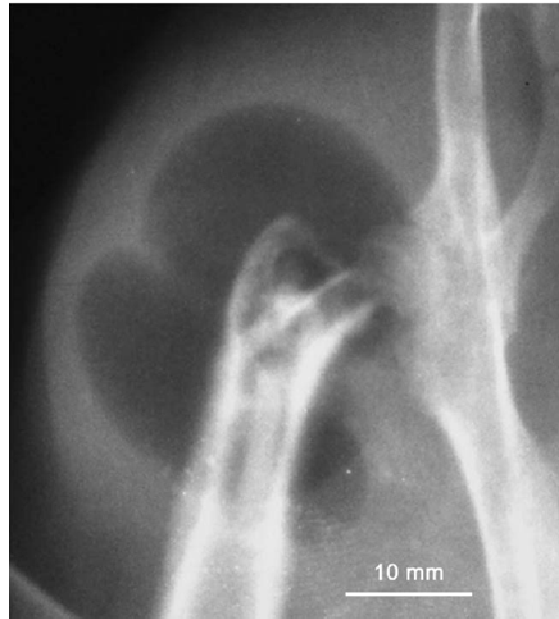


Fig. 2.8 Subcutaneous gas bubble observed on postoperative radiographs for 4 weeks during magnesium implant degradation [68].

The eudiometric investigations revealed that all tested Mg-Ca alloys corrode slower than pure magnesium and hydrogen evolution rate or corrosion rate depends strongly on electrolyte concentration. In Mg-Ca2.0 alloy case, increase in NaCl concentration up to 0.9% led to increase in hydrogen formation. Between 0.9% to 2.5% chloride concentrations, the gas formation stayed almost constant and decreased by further increasing the chloride content up to 5%. The same

trend was observed for other Ca amounts in Mg-Ca binary system. Decrease in the gas formation under high chloride contents was related to a layer of precipitated corrosion products which were rich in chloride. This layer covers the implant's surface and weakens the chemical attack of the electrolyte. However, thick and white corrosion products precipitated on the specimen surface were not characterized.

Rad et al [30] studied the effect of Ca content on in-vitro corrosion behavior of Mg-Ca alloys with varying Ca content ranging from 0.5 to 10.0 wt.%. Corrosion rate of Mg-Ca alloys increased significantly with higher amounts of Ca. This decrease in corrosion resistance was related to more Mg₂Ca intermetallic phase formed in grain boundaries under high Ca contents. Higher corrosion rates led to higher pH value during the tests. Corrosion was more moderate and uniform in low Ca content alloys. Kirkland et al [29] also investigated the influence of increasing calcium (Ca) content in binary Mg-Ca alloys along with the composition of the bio-fluid on in-vitro degradation rate. Different Ca contents of 0.4, 0.8, 1.34, 5.0, 10.0, 16.2, and 28.0 wt.% were considered. Three different bio-fluids were used starting with regular SBF and progressing to more human serum-like fluids by adding amino acids and vitamins (the second bio-fluid) and finally proteins (the third bio-fluid) to SBF. All three bio-fluids were buffered and the pH and temperature values were kept constant at 7.15 ± 0.05 and $37 \text{ }^{\circ}\text{C} \pm 1 \text{ }^{\circ}\text{C}$, respectively. The bio-fluid volume to exposed area ratio was 300 mL:1 cm². It was observed that above solid solubility limit of ~ 1.34 wt.% Ca, the corrosion rate increased with increasing Ca content and the corrosion potential became more negative. However, below the solubility limit, the corrosion rate stayed the same or even slightly decreased with increasing Ca additions. As the bio-fluid mimicked the human serum more closely, corrosion rate decreased between 10 to 290% and corrosion potential became more positive. This emphasizes that using more physiologically

relevant test environments are necessary to effectively study the in-vitro biodegradation behavior of Mg-Ca alloys.

Krause et al [7] investigated the initial mechanical strength and in-vivo degradation behavior of Mg-Ca0.8, LAE442, and WE42 alloys along with the change in their mechanical properties due to degradation. Mg-Ca0.8 showed an insufficient initial strength and a fast degradation. However, its ductility was constant during degradation and the degradation products were naturally occurring components in the human organism. LAE442 degraded slower and its initial strength seemed sufficient for load-bearing applications. However, rare earth alloying elements present in LAE442 resulted in products which their biocompatibility has to be studied yet. They did not recommend WE43 as an orthopedic material for fracture repair due to its heterogeneous and unpredictable degradation behavior.

Kannan and Raman [28] examined the degradation behavior and mechanical integrity of calcium-containing Mg alloys using electrochemical techniques and slow strain rate test (SSRT) method, respectively, in modified-SBF. AZ91Ca (1.0 wt.% Ca), AZ61Ca (0.4 wt.% Ca), and AZ91 (without Ca) were used. Potentiodynamic polarization tests were performed at 36.5 ± 0.5 °C in m-SBF buffered at 7.4. The general and pitting corrosion resistance of calcium-containing Mg alloys in m-SBF was significantly improved as compared to the base alloy. The corrosion current was significantly lower in AZ91Ca alloy than that in AZ91 alloy. Furthermore, AZ91Ca alloy exhibited a five-fold increase in the surface film resistance than AZ91 alloy. The mechanical properties of the Ca-containing Mg alloys decreased only by ~ 15% (for ultimate strength) and 20 % (for elongation at fracture) in m-SBF as compared to these properties in air.

Rapid corrosion is almost an intrinsic response of magnesium to a chloride containing solution, like the human body fluid or plasma. Corrosion in bone plates mostly occurs at the

plate-screw interface [70]. Previous experimental investigations have shown a correlation between cutting and non-cutting processes and the corrosion behavior of different magnesium alloys [47,71]. Theoretically, a bio degradable material should have a controllable dissolution rate or a delayed corrosion process. An implant made of such a material should be able to fully function before surgical region recovers or heals. After that, the implant should be gradually dissolved, consumed or absorbed. Obviously, a suitable corrosion rate is critical to a biodegradable Mg-Ca implant. To make this possible understanding the corrosion behavior of Mg-Ca alloys in body fluids is an essential step.

Bach et al [47] used correlated noise measuring technique (CorrELNoise) in addition to gravimetric method to characterize the corrosion behavior of different surface conditions which were generated in milling under various process parameters. The aim was to find the correlation between different machining parameters and corrosion rate. The CorrELNoise has adequate sensitivity to analyze the initial corrosion events on the influenced test surfaces [72]. The sample which was machined with higher cutting speed (2400 m/min) showed a stronger corrosion attack at the surface.

Denkena and Lucas [12] studied the possibility of adjusting degradation kinetics of biocompatible Mg-Ca3.0 implants through adjusting surface and subsurface properties by machining processes. They focused on differences in subsurface properties while similar surface properties were achieved. Turning and deep rolling processes were used to change subsurface properties especially residual stresses. The process parameters were selected in a way to achieve comparable surface properties especially surface roughness. The deep rolled surfaces were smoother than the turned surfaces. However, the turned surfaces were still located in a comparable range of finish quality. Significant differences occurred in subsurface residual

stresses. Larger and deeper compressive residual stresses were achieved by deep rolling. Changes in microstructure (compression of grains) especially at maximum residual stress area were visible. However a significant modification in microhardness was not detected. The degradation behavior was determined through mass loss in 0.9 wt.% NaCl solution (representing the salt content of body fluid). To determine the mass loss due to degradation, the hydrogen gas evolved as the result of Mg oxidation/dissolution was collected and the corresponding mass of degraded Mg was calculated using stoichiometry in the chemical reaction, i.e. $\text{Mg} + \text{H}_2\text{O} \rightarrow \text{Mg}(\text{OH})_2 + \text{H}_2$. The pH value of the solution was kept constant by a compensating reservoir and a periodic change of solution. The corrosion rates of the turned surfaces were *approximately 100 times* faster than the corrosion rates of the deep rolled surfaces. Within the range of surface qualities applied in their study, the better surface finish at low feed rate had no significant influence on the corrosion resistance. A homogeneous corrosion attack with moderate corrosion rates was observed in deep rolled surfaces. The corrosion resistance was improved until the modified layer of subsurface was dissolved and the unmodified bulk region was uncovered.

The corrosion mechanism is important, particularly with regard to the biomechanical properties of medical implant devices. Mg-alloys, in general, tend to pitting corrosion, especially close to chloride ions. In contrast, carbonate ions are able to suppress pitting corrosion totally. Calcium addition to Mg-based alloys enhances their general and pitting corrosion resistance significantly. Up to 0.8 wt.% Ca, Mg-Ca alloys show a homogenous texture and a uniformly distributed corrosion. Higher percentages of calcium lead to irregular and more widespread corrosion [6].

The corrosion process depends not only on the element composition of the biomaterial and its processing, but also on the *corrosive environment* to which magnesium alloys are

subjected. In vivo environment has two basic and important characteristics: it contains chloride anions (saline media includes NaCl) and its pH is 7.4. According to Pourbaix diagram (figure 2.7), the passivating magnesium hydroxide ($\text{Mg}(\text{OH})_2$) cannot be stable and it will dissolve in body fluid producing Mg cations and hydroxide anions if pH stays at 7.4. Therefore, it seems an appropriate way to control Mg corrosion is to increase the surrounding pH in order to stabilize the products in the corrosion layer. Calcium has been known for years to reduce the susceptibility of magnesium to corrode when added in amounts of a few tenths of weight percents [73]. Gu et al [74] studied the influence of artificial biological fluid composition on the biocorrosion of potential orthopedic Mg-Ca, AZ31, and AZ91 alloys. Their results showed that chloride ion reduces the corrosion resistance and the hydrocarbonate ions induce rapid surface passivation. Surface adsorption of amino acids increases polarization resistance and reduces current densities. Mg-Ca alloy showed higher corrosion rate in presence of proteins. Liu et al [75] investigated the effect of albumin on in-vitro degradation behavior of Mg-Ca1.5 alloy. Adsorption of albumin molecule on the surface led to decreased corrosion and hydrogen evolution rates. Filiform corrosion caused by chloride ions was also significantly inhibited due to surface adsorption of albumin. This inhibitive effect became stronger with higher concentrations of albumin in the solution.

2.8. Concluding remarks

Magnesium-calcium (Mg-Ca) alloys have shown very promising in development of biodegradable, biocompatible, metallic orthopedic implants. Microstructure, mechanical properties, electrochemical behavior, and degradation kinetics of Mg-Ca implants are all affected

by the amount of alloying element, i.e. Ca. Beside alloying, surface coating and thermo-mechanical processing of the implants have been explored by researchers as potential ways to tackle high degradation kinetics of Mg-Ca implants in physiological environment and to postpone or to slower the degradation process. In this context, adjusting the kinetics of degradation through thermo-mechanical processing seems more advantageous. Surface mechanical treatment can tailor surface integrity of the orthopedic implant in such a way that not only their degradation rate matches the healing rate but also the mechanical properties and fatigue life of the implants improve. Although, there have been studies on Mg-Ca orthopedic products very recently, however, there is a lot left to be done in order to successfully realize Mg-Ca alloys as degradable orthopedic material in medical device manufacturing. Exact simulation of the physiology, surrounding a bone trauma in human body, should be a major concern in future studies. There is still a considerable need to explore how surface integrity relates to bioperformance of Mg-Ca alloys. In this respect, isolating surface integrity characteristics (surface roughness, microhardness, residual stresses, and microstructure) and studying their effects on degradation kinetics of Mg-Ca implants remains as a major challenge for future studies.

References

1. G. Bergen, L.H. Chen, M. Warner, L. A. Fingerhut, Injury in the United States: 2007 Chart book, National Center for Health statistics, Hyattsville, MD (2008).
2. K. Feser, M. Kietzmann, W. Bäumer, C. Krause, F.W. Bach, Effects of degradable Mg-Ca alloys on dendritic cell function, *J. Biomater. Appl.* 25(2011) 685 – 697.
3. Z. Li, X. Gu, S. Lou, Y. Zheng, The development of binary Mg-Ca alloys for use as biodegradable materials within bone, *Biomaterials* 29 (2008) 1329 – 1344.
4. M. Thomann, C. Krause, D. Bormann, N. von der Hoh, H. Windhagen, A. Meyer-Lindenberg, Comparison of the resorbable magnesium alloys LAE442 und MgCa0.8 concerning their mechanical properties, their progress of degradation and the bone-implant contact after 12 months implantation duration in a rabbit model, *Materialwiss. Werkst.* 40 (2009) 82 – 87.
5. M. Thomann, C. Krause, N. Angrisani, D. Bormann, T. Hassel, H. Windhagen, A. Meyer-Lindenberg, Influence of a magnesium-fluoride coating of magnesium-based implants (MgCa0.8) on degradation in a rabbit model, *J. Biomed. Mater. Res. A* 93 (2010) 1609 – 1619.
6. N. von Der Hoh, D. Bormann, A. Lucas, B. Denkena, C. Hackenbroich, A. Meyer-Lindenberg, Influence of different machining treatments of magnesium-based resorbable implants on the degradation behavior in rabbits, *Adv. Eng. Mater.* 11 (2009) B47 – B54.
7. A. Krause, N. von Der Hoh, D. Bormann, C. Krause, F.W. Bach, H. Windhagen, A. Meyer-Lindenberg, Degradation behavior and mechanical properties of magnesium implants in rabbit tibiae, *J. Mater. Sci.* 45 (2010) 624 – 632.
8. H. Amelfarзад, M.T. Peivandi, S.M.R. Yusofsani, In body corrosion fatigue failure of a stainless steel orthopaedic implant with a rare collection of different damage mechanisms, *Eng. Fail. Anal.* 14 (2007) 1205 – 1217.
9. G.K. Triantafyllidis, A.V. Kazantzis, K.T. Karageorgiou, Premature fracture of a stainless steel 316L orthopedic plate implant by alternative episodes of fatigue and cleavage decoherence, *Eng. Fail. Anal.* 14 (2007) 1346 – 1350.
10. C. Kanchanomai, V. Phiphobmongkol, P. Muanjan, Fatigue failure of an orthopedic implant – a locking compression plate, *Eng. Fail. Anal.* 15 (2008) 521 – 530.
11. B. Denkena, F. Witte, C. Podolsky, A. Lucas, Degradable implants made of magnesium alloys, *Proc. of 5th Euspen Int. Conf.*, Montpellier, France (2005).

12. B. Denkena, A. Lucas, Biocompatible magnesium alloys as absorbable implant materials – adjusted surface and subsurface properties by machining processes, *Ann. CIRP* 56 (2007) 113 – 116.
13. S. Benli, S. Aksoy, H. Havitcioglu, M. Kucuk, Evaluation of bone plate with low stiffness material in terms of stress distribution, *J. Biomech.* 41 (2008) 3229 – 3235.
14. A. Completo, F. Fonseca, J.A. Simoes, Strain shielding in proximal tibia of stemmed knee prosthesis: experimental study, *J. Biomech.* 41 (2008) 560 – 566.
15. A. Completo, F. Fonseca, J.A. Simoes, Experimental evaluation of strain shielding in distal femur in revision TKA, *Exp. Mech.* 48 (2008) 817 – 824.
16. A.G. Au, V.J. Raso, A.B. Liggins, A. Amirfazli, Contribution of loading conditions and material properties to stress shielding near the tibial component of total knee replacements, *J. Biomech.* 40 (2007) 1410 – 1416.
17. J.F. Shi, C.J. Wang, T. Laoui, W. Hart, R. Hall, A dynamic model of simulating stress distribution in the distal femur after total knee replacement, *Proc. I. MECH E. Part H: J. Eng. Med.* 221 (2007) 903 – 912.
18. H. Isaksson, A.L. Lerner, Mathematical modeling of stress shielding with bioresorbable materials for internal fracture fixation, *Bioengineering Conf.* (2003) 1041 – 1042.
19. J. Nagels, M. Stokdijk, P.M. Rozing, Stress shielding and bone resorption in shoulder arthroplasty, *J. Shoulder Elb. Surg.* 12 (2003) 35 – 39.
20. J. Wolff, *The Law of Bone Remodeling*, Heidelberg: Springer-Verlag (1986).
21. A. Gefen, Computational simulations of stress shielding and bone resorption around existing and computer-designed orthopaedic screws, *Med. Biol. Eng. Comput.* 40 (2002) 311 – 322.
22. M. Navarro, A. Michiardi, O. Castano, J.A. Planell, Biomaterials in orthopaedic., *J. Roy. Soc. Interface* 5 (2008) 1137 – 1158.
23. L. Hench, J. Polak, Third generation biomedical materials, *Science* 295 (2002) 1014 – 1017.
24. H.G. Seiler, *Handbook on toxicity of inorganic compounds*, 1st ed., CRC Press (1987).
25. G. Song, Control of biodegradation of biocompatible magnesium alloys, *Corros. Sci.* 49 (2007) 1696 – 1701.
26. T. Hassel, F.W. Bach, Production and properties of small tubes made from MgCa0.8 for application as stent in biomedical science, In: *Proc. 7th Int. Conf. Magnesium Alloys and Their Applications*, K.U. Kainer, Ed., Wiley-VCH Verlag GmbH & Co. (2007) 432 – 437.

27. T. Hassel, F.W. Bach, C. Krause, Influence of alloy composition on the mechanical and electrochemical properties of binary Mg-Ca alloys and its corrosion behavior in solutions at different chloride concentrations, In: Proc. 7th Int. Conf. Magnesium Alloys and Their Applications, K.U. Kainer, Ed., Wiley-VCH Verlag GmbH & Co. (2007) 789 – 795.
28. M.B. Kannan, R.K.S. Raman, In vitro degradation and mechanical integrity of calcium containing magnesium alloys in modified simulated body fluid, *Biomaterials* 29 (2008) 2306 – 2314.
29. N.T. Kirkland, N. Birbilis, J. Walker, T. Woodfield, G.J. Dias, M.P. Staiger, In-vitro dissolution of magnesium-calcium binary alloys: clarifying the unique role of calcium additions in bioresorbable magnesium implant alloys, *J. Biomed. Mater. Res. B* 95 (2010) 91 – 100.
30. H.R.B. Rad, M.H. Idris, M.R.A. Kadir, S. Farahany, Microstructure analysis and corrosion behavior of biodegradable Mg-Ca implant alloys, *Mater. Design* 33 (2012) 88 – 97.
31. K.U. Kainer, E. Lach, Deformation behavior of AZ alloys at high strain rates, In: *Magnesium Alloys and Their Applications*, B.L. Mordike, K.U. Kainer, Eds., Werkstoff-Informationsgesellschaft (1998) 369 – 374.
32. A. Drynda, T. Hassel, R. Hoehn, A. Perz, F.W. Bach, M. Peuster, Development and biocompatibility of a novel corrodible fluoride-coated magnesium-calcium alloy with improved degradation kinetics and adequate mechanical properties for cardiovascular applications, *J. Biomed. Mater. Res. A* 93 (2010) 763 – 775.
33. E. El-Magd, M. Abouridouane, Compression test on magnesium alloy MgAl8Zn at high strain rates and temperatures, In: *Magnesium Alloys and Their Applications*, K.U. Kainer, Ed., Wiley-VCH Verlag GmbH & Co. (2000) 324 – 329.
34. E. El-Magd, M. Abouridouane, Influence of strain rate and temperature on deformation and fracture behavior of magnesium alloy MgAl8Zn: tests and numerical simulations, In: Proc. 6th Int. Conf. Magnesium Alloys and Their Applications, K.U. Kainer, Ed., Wiley-VCH Verlag GmbH & Co. (2004) 402 – 408.
35. E. El-Magd, M. Abouridouane, Characterization, modeling and simulation of deformation and fracture behavior of the light-weight wrought alloys under high strain rate loading, *Int. J. Impact Eng.* 32 (2006) 741 – 758.
36. M.P. Sealy, Y.B. Guo, Surface integrity and process mechanics of laser shock peening of novel biodegradable magnesium-calcium (Mg-Ca) alloy, *J. Mech. Behav. Biomed.* 3 (2010) 488 – 496.
37. Y.B. Guo, M. Salahshoor, Process mechanics and surface integrity by high-speed dry milling of biodegradable magnesium-calcium implant alloys, *CIRP Ann-Manuf. Tech.* 59 (2010) 151 – 154.

38. M. Salahshoor, Y.B. Guo, Cutting mechanics in high speed dry machining of biomedical magnesium-calcium alloy using internal state variable plasticity model, *Int. J. Mach. Tool Manu.* 51 (2011) 579 – 590.
39. E. El-Magd, M. Abouridouane, Influence of strain rate and temperature on the compressive ductility of Al, Mg, Ti alloys, *J. Phys-Paris* 110 (2003) 15 – 20.
40. E. El-Magd, H. Scholles, H. Weisshaupt, Adiabatic flow curves of metallic materials at high strain rates, *Mat.-Wiss. U. Werkstofftech* 27 (1996) 408 – 413.
41. S. Ataya, E. El-Magd, Quasi-static behavior of Mg alloys with and without short fiber reinforcement, *Theor. Appl. Fract. Mec.* 47 (2007) 102 – 112.
42. Y.E. Essa, J.L. Perez-Castellanos, Effects of the strain rate and temperature on the mechanical behavior of a Mg-5%Zn alloy reinforced with SiC particles, *J. Mater. Process. Tech.* 143/144 (2003) 856 – 859.
43. X.N. Gu, W. Zheng, Y. Cheng, Y.F. Zheng, A study on alkaline heat treated Mg-Ca alloy for the control of the biocorrosion rate, *Acta Biomater* 5 (2009) 2790 – 2799.
44. C.Y. Zhang, R.C. Zeng, C.L. Liu, J.C. Gao, Comparison of calcium phosphate coatings on Mg-Al and Mg-Ca alloys and their corrosion behavior in Hank's solution, *Surf. Coat. Tech.* 204 (2010) 3636 – 3640.
45. M. Li, Q. Chen, W. Zhang, W. Hu, Y. Su, Corrosion behavior in SBF for Titania coatings on Mg-Ca alloy, *J. Mater. Sci.* 46 (2011) 2365 – 2369.
46. H. Wang, Y. Estrin, Z. Zuberova, Bio corrosion of a magnesium alloy with different processing histories, *Mater. Lett.* 62/16 (2007) 2476 – 2479.
47. F.W. Bach, B. Denkena, K. Weinert, P. Alpers, M. Bosse, N. Hammer, Influence of cutting and non-cutting processes on the corrosion behavior and the mechanical properties of magnesium alloys, *Proc. 7th Int. Conf. Magnesium Alloys and Their Applications* (2007) 1076 – 1084.
48. A.T. Bozdana, N.N.Z. Gindy, Comparative experimental study on effects of conventional and ultrasonic deep cold rolling processes on Ti-6Al-4V, *Mater. Sci. Tech.* 24 (2008) 1378 – 1384.
49. P.S. Prevey, R.A. Ravindranath, M. Shepard, T. Gabb, Case studies of fatigue life improvement using low plasticity burnishing in gas turbine engine applications, *J. Eng. Gas Turb. Power* 128 (2006) 865 – 872.
50. C.Y. Seemikeri, P.K. Brahmanekar, S.B. Mahagaonkar, Low plasticity burnishing: an innovative manufacturing method for biomedical applications, *J. Manuf. Sci. E. – T. ASME* 130 (2008) 021008/1 – 8.

51. P. Prevey, D. McNulty, J. Carr, P. Sade, A. Craft, Fatigue strength enhancement of Ti-6Al-4V ELI femoral distal stems using low plasticity burnishing, Proc. ASM MPMD (Materials & Processes for Medical Devices) Conf. and Expo. (2009) Minneapolis, MN.
52. J.A. Disegi, C. Sax, Effect of low plasticity burnishing on the fatigue strength of spinal rods, Proc. ASM MPMD (Materials & Processes for Medical Devices) Conf. and Expo. (2009) Minneapolis, MN.
53. A. Schuh, C. Zeller, U. Holzwarth, W. Kachler, G. Wilcke, G. Zeiler, B. Eigenmann, J. Bigoney, Deep rolling of titanium rods for application in modular total hip arthroplasty, J. Biomed. Mater. Res. B (2006) DOI 10.1002/jbmb.
54. P.S. Prevey, D.J. Hornbach, N. Jayaraman, Controlled plasticity burnishing to improve the performance of friction stir processed Ni-Al bronze, Mater. Sci. Forum 539 (2007) 3807 – 3813.
55. C.M. Gill, N. Fox, P.J. Withers, Shakedown of deep cold rolling residual stresses in titanium alloys, J. Phys. D Appl. Phys. 41 (2008) 174005 (5pp).
56. N. Tsuji, S. Tanaka, T. Takasugi, Evaluation of surface-modified Ti-6Al-4V alloy by combination of plasma-carburizing and deep rolling, Mater. Sci. Eng. A 488 (2008) 139 – 145.
57. N. Tsuji, S. Tanaka, T. Takasugi, Effect of combined plasma-carburizing and deep rolling on notch fatigue property of Ti-6Al-4V alloy, Mater. Sci. Eng. A 499 (2009) 482-488.
58. I. Nikitin, M. Besel, Correlation between residual stress and plastic strain amplitude during low cycle fatigue of mechanically surface treated austenitic stainless steel AISI 304 and ferritic-pearlitic steel SAE 1045, Mater. Sci. Eng. A 491 (2008) 297 – 303.
59. I. Nikitin, M. Besel, Residual stress relaxation of deep-rolled austenitic steel, Scripta Mater. 58 (2008) 239 – 242.
60. I. Nikitin, I. Altenberger, Comparison of the fatigue behavior and residual stress stability of laser-shock peened and deep rolled austenitic stainless steel AISI 304 in the temperature range 25-600 °C, Mater. Sci. Eng. A 465 (2007) 176 – 182.
61. P. Juijerm, I. Altenberger, Effective boundary of deep rolling treatment and its correlation with residual stress stability of Al-Mg-Mn and Al-Mg-Si-Cu alloys, Scripta Mater. 56 (2007) 745 – 748.
62. N. Jayaraman, D.J. Hornbach, P.S. Prevey, Mitigation of fatigue and pre-cracking damage in aircraft structures through low plasticity burnishing, Proc. ASIP (2007) Palm Springs, CA.

63. J.E. Scheel, D.J. Hornbach, P.S. Prevey, Safe life conversion of aircraft aluminum structures via low plasticity burnishing for mitigation of corrosion related failures, Dept. Defense Corros. Conf. (2009) Gaylord National, Washington DC.
64. L.N. Lopez, A. Lamikiz, J.A. Sanchez, J.L. Arana, The effect of ball burnishing in heat treated steel and Inconel 718 milled surfaces, *Int. J. Adv. Manuf. Tech.* 32 (2007) 958 – 968.
65. C.Y. Seemikeri, P.K. Brahmkar, S.B. Mahagaonkar, Investigations on surface integrity of AISI 1045 using LPB tool, *Tribol. Int.* 41 (2008) 724 – 734.
66. D.S. Rao, H.S. Hebbar, M. Komaraiah, U.N. Kempaiah, Investigation on the effect of ball burnishing parameters on surface hardness and wear resistance of HSLA dual-phase steels, *Mater. Manuf. Process.* 23 (2008) 295 – 302.
67. M. Pourbaix, Atlas of electrochemical equilibria in aqueous solutions, 2nd ed., Houston, Texas, USA (1974).
68. F. Witte, V. Kaese, H. Haferkamp, E. Switzer, A. Meyer-Lindenberg, C.J. Wirth, H. Windhagen, In vivo corrosion of four magnesium alloys and the associated bone response, *Biomaterials* 26 (2005) 3557 – 3563.
69. M.P. Staiger, A.M. Pietak, J. Huadmai, G. Dias, Magnesium and its alloys as orthopedic biomaterials: a review, *Biomaterials* 27 (2006) 1728 – 1734.
70. D.L. Miller, T. Goswami, A review of locking compression plate biomechanics and their advantages as internal fixators in fracture healing, *Clin. Biomechanics* 22 (2007) 1049 – 1062.
71. H.K. Tönshoff, T. Friemuth, J. Winkler, C. Podolsky, Improving the characteristics of magnesium workpieces by burnishing operations, *Magnesium Alloys and Their Applications* (2000) 406 – 411.
72. B. Roseler, C.A. Schiller, Current-potential correlated noise measurement (CorrELNoise): a new technique for the evaluation of electrochemical noise analysis, *Mater. Corros.* 52 (2001) 413-417.
73. F. Witte, J. Fischer, P. Maier, C. Blawert, M. Stormer, M. Hort, Magnesium-hydroxyapatite composites as an approach to degradable biomaterials, In: *Proc. 7th Int. Conf. Magnesium Alloys and Their Applications*, K.U. Kainer, Ed., Wiley-VCH Verlag GmbH & Co. (2007) 958 – 964.
74. X.N. Gu, Y.F. Zheng, L.J. Chen, Influence of artificial biological fluid composition on the biocorrosion of potential orthopedic Mg-Ca, AZ31, AZ91 alloys, *Biomed. Mater.* 4 (2009) 065011 (8pp).

75. C.L. Liu, Y.J. Wang, R.C. Zeng, X.M. Zhang, W.J. Huang, P.K. Chu, In vitro corrosion degradation behavior of Mg-Ca alloy in the presence of albumin, *Corros. Sci.* 52 (2010) 3341 – 3347.

CHAPTER 3

MACHINING CHARACTERISTICS OF HIGH SPEED DRY MILLING OF BIODEGRADABLE MAGNESIUM-CALCIUM ALLOY FOR ORTHOPEDIC IMPLANTS

Abstract

Degradable metallic biomaterials have attracted a great attention lately for orthopedic fixation applications. Binary magnesium-calcium (Mg-Ca) alloys have emerged as a promising choice to avoid stress shielding and second surgery inherent in permanent metallic biomaterials such as stainless steel, titanium, and cobalt alloys. In addition, a Mg-based implant provides biocompatibility and sufficient strength. Machining is often very necessary to make geometric features of Mg implants. In this paper, efficient and ecologic machining of a novel Mg-Ca (0.8 wt%) alloy at cutting speeds up to 2800 m/min has been conducted using polycrystalline diamond (PCD) inserts. The mechanisms of material adhesion, flank built-up (FBU) formation, tool wear, and chip ignition were investigated with the aid of a developed on-line optical inspection system. Chip morphology produced at different combinations of cutting parameters, i.e. cutting speed, feed, and depth-of-cut are also characterized in terms of crystal slip systems.

3.1. Introduction

The development of biodegradable implants has been one of the important areas in biomedical engineering. Biodegradable and biocompatible implants can gradually be dissolved

and absorbed in the human organism after implantation. Compared with a traditional permanent implant made of steel, titanium, and cobalt alloys, a biodegradable material will represent an appropriate solution for potential local inflammation and physical irritation induced by stress shielding [1-5] and the need for additional surgery to remove permanent implants. Current biodegradable implants are mainly made of polymers such as poly-L-Lactic acid. However, these polymer-based implants usually have low mechanical strength which has driven researchers to seek for biodegradable metallic substitutes. Magnesium (Mg) and its alloys are among the most interested options.

Mg is an element essential to human body. Intake of a certain amount of Mg (300~400 mg/day) is normally required for the human body's metabolic activities [6]. The direct corrosion product of Mg, Mg^{2+} , would be easily absorbed or consumed by the human body. No side effect of Mg^{2+} overdose has been found in human body [7,8].

Hydrogen evolution and alkalization resulting from Mg corrosion are the most critical obstacles in using Mg as an implant material. A straightforward strategy to tackle these difficulties is to reduce the corrosion rate. A biodegradable Mg implant needs to corrode at a controllable rate. Alloying is one of the possible solutions to reduce the corrosion rate of a Mg implant in human body. A concern with the alloying approach is biocompatibility of alloying elements. Alloying elements must not generate toxic, carcinogenic, or mutagenic products.

The previous studies on biomedical Mg alloys are mainly focused on the Mg-Al [7-12] and Mg-RE [10] alloy systems. Aluminum (Al) and Rare Earth (RE) elements seem not to be the best alloying elements [13]. Recently, calcium (Ca) has become a promising alloying element in non-commercial binary Mg-Ca alloys for biodegradable implants [13-20]. It is well known that Ca is a major component in human bone and also essential in chemical signaling with cells [21].

Ca has a low density (1.55 g/cm^3) which endues the Mg-Ca alloy system with the advantage of similar density to bones. In this context, Ca in Mg-Ca alloys will produce hydroxyapatite (HA) as corrosion product on the surface of the implant. HA mineral is a naturally occurring form of Ca apatite with the formula $\text{Ca}_{10}(\text{PO}_4)_6(\text{OH})_2$ and has close resemblance to the chemical and mineral components of teeth and bone. As a result of this similarity it stimulates bone cells to attach to the implant surface and make proper bonding [18, 22].

The other possible approach to control the corrosion rate of Mg alloys is mechanical surface treatment using different types of manufacturing processes. High speed machining (HSM) without applying coolant has been considered and studied as an effective and ecologic way of making parts for automotive, aerospace, and medical applications. High speed machining for Mg alloys is defined as machining with cutting speeds between 600 to 5000 m/min based on being a finish cut or a rough cut [23, 24]. Denkena et al [15] sought to adjust the degradation kinetics of Mg-Ca (3.0wt%) alloy through modifying surface (e.g. topography) and subsurface (e.g. residual stresses) characteristics by applying turning and deep rolling processes. They explored the space of process parameters to adopt a specific degradation profile appropriate for the specific medical application. They faced with the fact that for same amount of depth-of-cut and feed, lower cutting speed shows lower corrosion rate. That was attributed to higher cutting forces and consequently higher and deeper compressive residual stresses generated by lower cutting speeds. In their study, better surface finish produced at a lower feed rate did not show a significant influence on corrosion resistance.

Bach et al [25] studied the effects of milling parameters and cutting material on surface integrity and corrosion performance of two sand-cast Mg alloys EQ21 and WE43 for structural applications especially in automotive industry. Lower feed rates for a constant cutting speed

resulted in harder layers close to surface, which has a longer exposure to thermo-mechanical loads and higher chances for microstructural changes. In this regard, thermal conductivity of the alloy itself was mentioned as a key parameter for heat conduction rate of the machined surface. Higher cutting speeds for a constant feed rate produces a smoother surface due to thermally induced reduction of the material strength on the shear plane. It was found that PCD inserts produce more rough surfaces than by the cemented carbides. However, aggressive salt spray testing results showed rougher surfaces would have higher weight loss and corrosion rate.

3.2. Machining of biodegradable magnesium alloys

The bulk work in machining of Mg and its alloys has been limited to automotive industry in the last two decades. The increased concerns about energy consumption and global warming has forced automotive industry and research institutes to look for different alternatives to meet technical needs of modern world with less fuel consumption and consequently less CO₂ emission. In this context, manufacturing structural parts using light weight metals such as Al and Mg alloys seemed very appealing. Recommendations of machining guidelines for Mg castings in any heat treatment condition have been established [26, 27]. Mg alloys have the lowest density among the metallic materials used in construction so far and offer a potential of up to 30 percent weight reduction even over Al alloys [28, 29, 30]. Low corrosion resistance of Mg alloys has been the biggest barrier in using them for constructional applications. On the other end of the spectrum, high corrosion rate has emerged as an interesting key property of Mg alloys for medical applications especially orthopedics to make biodegradable implants [15, 25].

Machining of Mg alloys is characterized by low power requirements, long tool life, short-breaking chips, high surface qualities, low mechanical and thermal loads on the tool and the possibility of dry machining [27]. Although, dry machining of Mg alloys makes it an ecologic manufacturing process on the other hand. It may result in an increased adhesive effects on the tool flank face and the flank built-up (FBU). Attaching and detaching of FBU from flank face results in high dynamic cutting forces and even chatter which will reduce dimensional accuracy, lower surface quality, or break the cutting tool [31]. The formation of FBU causes a higher friction and heat generation which can enhance the danger of chip inflammation and make a safety hazard.

Mg ignites if the melting point is exceeded throughout the material's volume. This is especially dangerous when the materials volume is small such as the chips made by finishing with small depth-of-cut and feed rate. For safe and ecologic machining of Mg alloys, different cutting tools and coatings have been investigated in literature. High-performance cutting which intuitively brings up high-speed machining may be achieved by optimizing a tooling system, i.e. tool material, tool shape, coating thickness, and coating structure to avoid adhesive effects and flank build-up.

Tönshoff et al [29, 32, 33] studied the influence of tool material/coating on adhesive effects between tool and workpiece. They examined four different sets of carbide tools without coating, with TiN and PCD coatings, and with only a solid PCD tip soldered to the carbide body, respectively. Sand casted bars of AZ91 were cut using a lathe machine. FBU was observed on uncoated and TiN-coated carbide tools. PCD tipped tools could not generally avoid the FBU formation since workpiece material eventually gets into contact with the bare carbide and adheres to it. No Mg adhesion on the flank occurred using PCD coated carbide tools due to the

lower friction between PCD coating and Mg. In addition, the higher thermal conductivity of PCD causes lower heat generations and faster heat conduction away from the cutting edge, respectively. However, material adhesion could occur on rake face of all tools at certain cutting conditions. The best surface quality may be obtained with PCD coated tools due to the low possibility of FBU formation. They found for short cutting lengths ($l_c \approx 10$ m), cutting speeds in the range of 300-2400 m/min have negligible effect on cutting forces and surface roughness regardless of what tool material/coating is being used. Moreover, they predicted chip temperature will increase if a small depth-of-cut in combination with a small feed is chosen.

Mg in the molten state is flammable when exposed to oxygen. Fang et al [34] conducted an experimental study of the cutting temperature in high speed dry milling of AZ91 Mg alloy. Micro grain tungsten carbide inserts were used. Thermocouples were embedded into the workpiece to measure the mean flank temperature rise. They assumed that the mean flank temperature is likely not to be less than cutting temperature on rake face when the undeformed chip thickness is on the same order of the cutting edge radius. The validity of their assumption was rationalized by examining the produced chips to find burn marks. They found higher cutting speeds cause higher temperatures and smaller undeformed chip thicknesses lead to dramatic increase in specific cutting force and temperature.

To study the effect of abrasion on tool material/coating, Tönshoff et al [29] and Friemuth et al [30] machined a Mg-based metal matrix composite (MMC) to combine the adhesive effects during cutting of standard Mg alloys with the high mechanical load caused by a ceramic reinforcement component. They reported that TiN-coated tools were destroyed immediately by the impact of ceramic particles. PCD coatings showed a good wear resistance until the diamond film was chipped away after cutting length of 370 m and PCD-tipped tools gave the best result

by having 0.2 mm wear land width after cutting length of 11000 m. Pedersen et al [35] used TiCN/TiN coated carbide tools to study finish turning of a SiC reinforced magnesium MMC. They got both continuous and semi-continuous chips and observed that the abrasive wear of the flank face reduced by increasing the depth-of-cut for a given volume of material removal. The surface roughness was within the range of 0.2 to 3.0 μm .

Videm et al [23] studied the effect of alloying elements and heat treatment on the high speed machinability of five commercial Mg alloys with aluminum content in the range of 2 to 9 %. Depth-of-cut and feed were kept fixed at 0.4 mm and 0.1 mm/rev, respectively, and samples were turned using carbide inserts with cutting speeds in the range of 400 – 1750 m/min. They found critical cutting speed, which FBU will form above that, decreases by increasing the amount of β -phase ($\text{Mg}_{17}\text{Al}_{12}$) and cutting temperature. Using the same experimental setup, Tomac et al [36] investigated the effect of manganese (Mn) amount in Mg-Al alloys on FBU formation. Mn in small amounts is added to increase corrosion resistance and to remove iron and certain other impurities. In the presence of Al, manganese combines with it and produces very hard MnAl particles. They observed sparks due to FBU and theorized that those are consequences of temporary and local heat generation caused by friction between the hard particles and tool/workpiece.

Adjusting cutting parameters, using PCD inserts, applying coolant are different alternatives to reduce the cutting temperature. Machining with coolants demands additional costs for the purchase, storage, and disposal and causes difficulties when recycling the chips [30, 37]. In contact with water-based coolants, Mg alloys tends to have chemical reactions and forms hydrogen, which is extremely flammable. Oil-based lubricants introduce the danger of oil mist

explosions [38, 39]. Consequently machining of Mg alloys should be performed under dry conditions in order to guarantee ecological-friendly as well as economical processes [29, 36].

This paper deals with an experimental study of high speed diamond face milling of the novel lab-made Mg-Ca (0.8wt%) biomaterial. Machining experiments are done without using coolant to make the process ecological. This study focuses on chip formation, flank built-up formation, tool wear, and chip ignition. An optical monitoring system has been developed and integrated into the CNC milling machine for on-line inspection of the wear process. PCD inserts are used to take advantage of PCD's high thermal conductivity and low chemical affinity with Mg alloy to reduce the chances of chip ignition, flank built-up formation, and also to increase the tool life.

3.3. Experimental procedure of high speed face milling

3.3.1. Mg-Ca0.8 material preparation

The binary alloying system of Mg and Ca is the basis for making biodegradable implants out of Mg [13-20]. The alloy Mg-Ca0.8 used in this study contains 0.8wt% of Ca as main alloying element. Due to the inherent poor plasticity of Mg, which comes from its hexagonal lattice structure [29], many efforts have been made to improve its plasticity by adding 0.8wt% Ca which gives a high elongation at rupture of about 15%. Higher amount of Ca will decrease the alloy's ductility while it will increase its corrosion resistance [16, 17]. Moreover, researchers have found Mg-Ca0.8 very promising for biomedical applications through in-vitro and in-vivo

tests [14, 15, 18]. On the other words, there has been some sort of trade-off between corrosion resistance, ductility, and in-vivo function of the Mg alloy in selecting Ca amount.

The Mg-Ca0.8 alloy was prepared in a 0.04 m³ (40 liter) crucible using pure Mg of the ASTM grade 9980A and Mg-Ca (30wt%) master alloy. Pure Mg ingots were melted down at 650°C. Then the melt was heated to 710 °C and Mg-Ca (30wt%) hardener was added in the required quantity in order to obtain the target alloy composition. After settling for 0.5 hours, the alloy was cast into two ingots. The ingots were machined into round bars. The cylindrical samples were cut with SiO₂ abrasive cutting wheel and then face milled to make 38 mm × 13 mm disks. The disks were face milled using carbide inserts, 2400 m/min surface cutting speed, 0.05 mm/rev feed, and 0.2 mm depth-of-cut.

The maximum solubility for Ca in Mg in the solid state is 1.34 wt% at 516.5 °C based on Mg-Ca phase diagram shown in figure 3.1 and goes down to amounts less than 0.8wt% at ambient temperature. The extra amount of Ca precipitates as Mg₂Ca phases on grain boundaries and sporadically inside the grains (figure 3.1). Therefore, the matrix will have very low amount of Ca at room temperature. This is especially the case if the cooling rate after processing is relatively low, e.g. in sand casting. The melting point within the alloy's different phases varies from 516.5 to 650 °C, depending on the local Ca content.

3.3.2. Experimental set-up and test plan

High speed face milling tests were carried out on a 3 axis Cincinnati Arrow 500 CNC machine with a main power of 18 KW and a maximum spindle speed of 8000 rpm. No coolant was applied throughout the tests. Nine ISCAR PCD tipped milling inserts, ADKW 1505-75RM PDR (grade ID5), were clamped in an ISCAR HM90 F90A-15 face mill of 127 mm diameter.

Resulting angles at the cutting edges were axial rake 12° , axial relief 6° , radial rake 8° , and radial relief 10° . Flank built-up formation and tool wear were on-line monitored using the integrated optical tool wear inspection system (figure 3.2). This system is equipped with an illuminator on the top and an OPTIXCAM microscope camera at the bottom which takes the image of object online and sends it to a computer for image processing. Flank built-up formation and/or tool wear can be detected and/or measured online without the need to uninstall the inserts. Figure 3.2 shows one insert image taken by the optical system. All nine inserts were inspected visually using scanning electron microscopy to ensure cutting edge unison. Self-aligning mechanism embedded in the design of inserts guarantees the presence of same cutting geometry for all the inserts after installation on face mill.

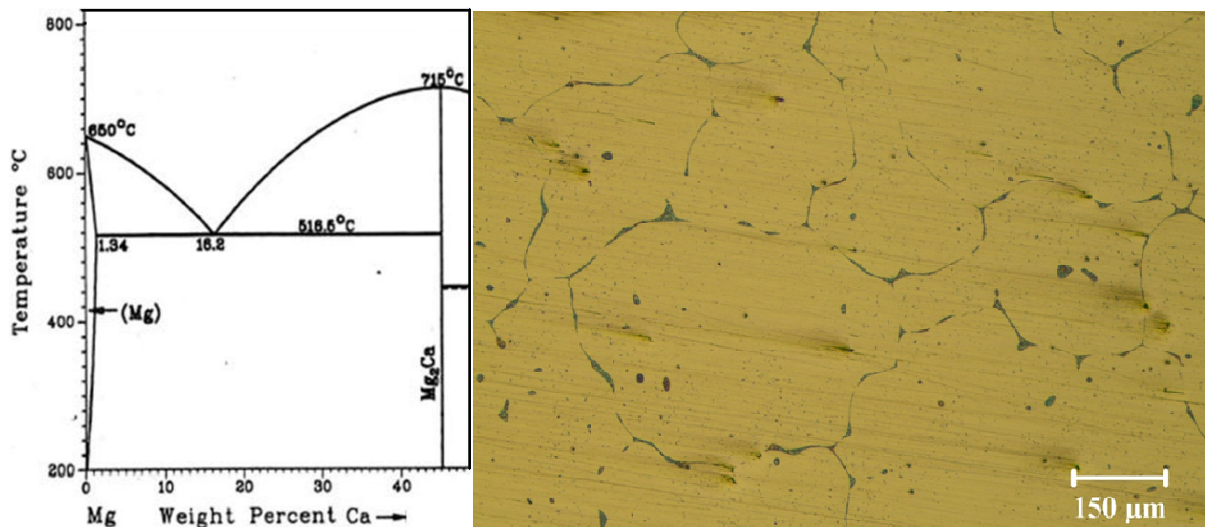


Fig. 3.1 Phase diagram of Mg-Ca alloy [40] and microstructure of Mg-Ca_{0.8}

Three sets of experiments were planned to isolate and study the effects of cutting speed, feed, and depth-of-cut in high speed dry face milling of Mg-Ca_{0.8} samples with the PCD tipped inserts. Each set has five different combinations of cutting parameters with only one varying parameter depending on which parameter's effect was being experimented on that set (Table 3.1). The cutting speed, feed, and depth-of-cut vary in the range of 1200 – 2800 m/min, 0.05 – 0.4 mm/rev, and 0.1 – 0.5 mm, respectively.

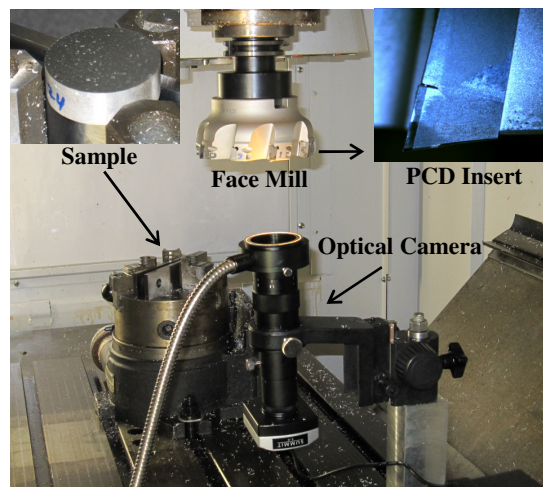


Fig. 3.2 High speed machining set-up with on-line optical inspection system

3.4. Results and discussions

3.4.1. Tool geometry and chip morphology

As is shown in figure 3.3, PCD inserts are made of a solid polycrystalline diamond blank soldered to a carbide body. These inserts have a side cutting edge of 240 μm length, a 45° lead

angle, and a 5 μm corner edge radius. This geometry of PCD inserts results in a specific chip cross section shown in figure 3.4b. Each cutting insert starts with zero chip thickness when it enters the workpiece and ends with a chip thickness equal to feed per tooth when it leaves the workpiece (figure 3.4a). Examining the geometry of actual chips under scanning electron microscope (figures 3.4c and 3.4d) reveals a very good agreement with the theoretically expected geometry in figure 3.4b. High speed dry face milling of Mg-Ca_{0.8} produces continuous chips with many turns and twists in three-dimensional view which make the electron microscopy of chips a difficult task considering the small chip cross sections. As such, in three-dimensional perspectives, which are the case in all SEM images of chips, some dimensions may look expanded or contracted based on the taken viewpoint.

Table 3.1 Experimental plan of high speed face milling

	Sample #	Cutting speed [m/min]	Feed [mm/rev]	Depth of cut [mm]
Cutting speed	1	1200	0.2	0.2
	2	1600	0.2	0.2
	3	2000	0.2	0.2
	4	2400	0.2	0.2
	5	2800	0.2	0.2
Feed	6	2400	0.05	0.2
	7	2400	0.1	0.2
	8	2400	0.2	0.2
	9	2400	0.3	0.2
	10	2400	0.4	0.2
Depth of cut	11	2400	0.2	0.1
	12	2400	0.2	0.2
	13	2400	0.2	0.3
	14	2400	0.2	0.4
	15	2400	0.2	0.5

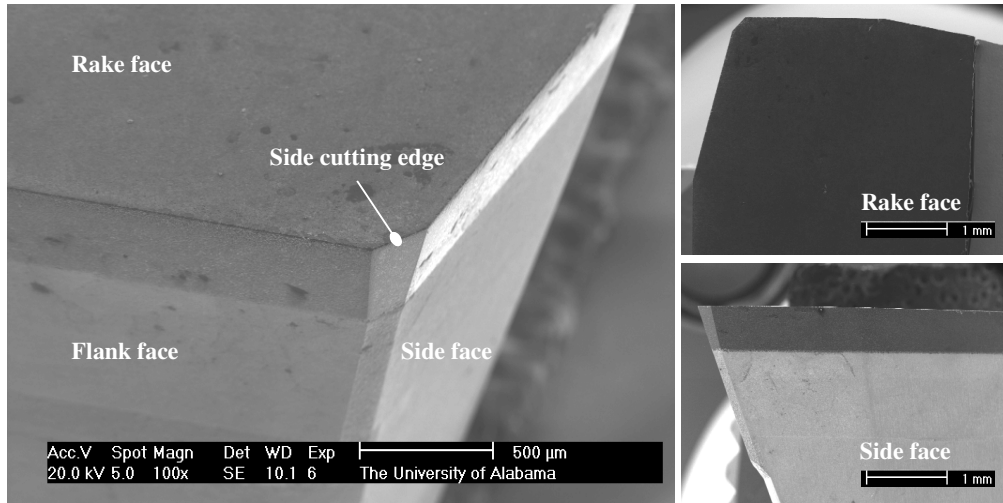


Fig. 3.3 SEM images of a fresh PCD insert

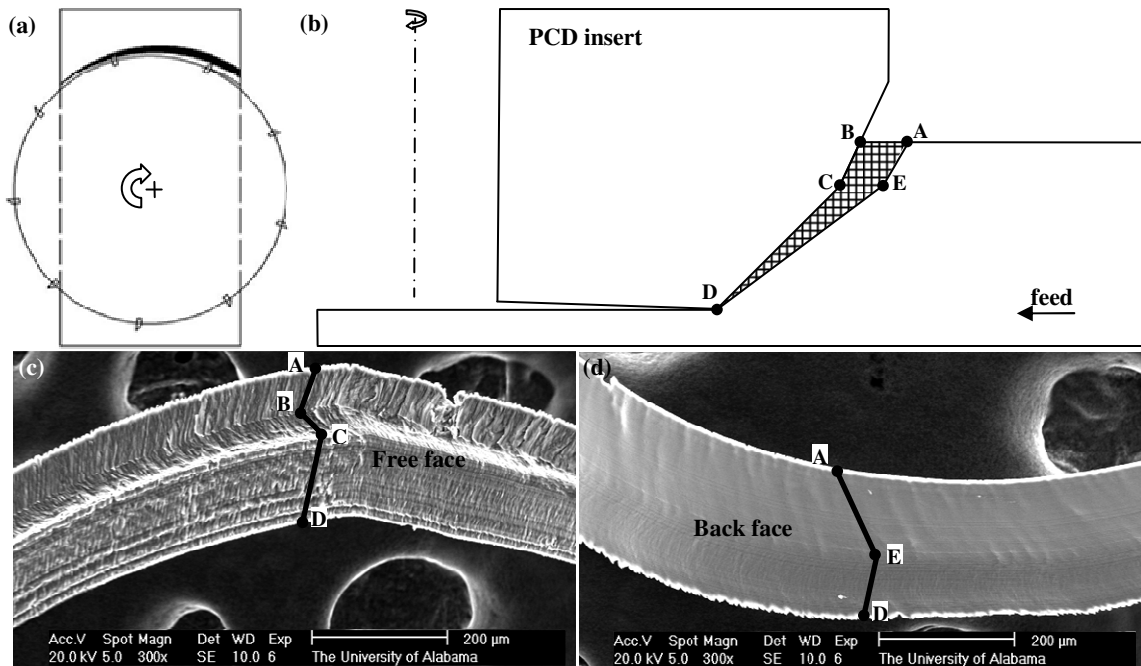


Fig. 3.4 Theoretical (a, b) and actual (c, d) geometry of chip in face milling of Mg-Ca_{0.8} alloy

The HCP lattice structure of the Mg crystal only offers the base plan to slip under stress at room temperature. At temperatures greater than 220°C twelve additional planes are activated [24]. This increase in number of slip systems at high cutting temperatures could be an explanation to improved ductility of Mg-Ca0.8 and the resultant continuous chips rather than short breaking chips [23, 24, 27, 29, 30, 33, 36, 37] observed in machining of Mg-Al alloys used in automotive industry such as AM20, AM50, AM60, and AZ91. Although these alloys will probably experience the same number of increase in slip systems at high cutting temperatures, but as a matter of fact they have more alloying element than Mg-Ca0.8 alloy. Mg-Al alloys with 2 to 9 wt% Al will have more barriers in their dislocations' path than Mg-Ca (0.8wt%) alloy for the same number of slip systems. More alloying element in substitutional and/or interstitial form(s) will increase strain fields in both number and intensity. Dislocations will face with more obstacles to move on slip systems in the presence of these strain fields and eventually ductility will decrease. Hassel et al [17] observed this decrease in ductility with more Ca content in Mg-Ca alloys.

Figure 3.5 shows the morphology of chips' free (A, C, E) and back (B, D, F) sides obtained under different combinations of cutting speed, feed, and depth-of-cut based on experiment plan in Table 3.1. A₁/B₁ corresponds to sample one's cutting conditions in Table 3.1 and so on and so forth till E₅/F₅ which corresponds to sample 15 in Table 3.1. Generally, the chip's free side for all the cutting conditions shows a lamellar structure for the portion above the side cutting edge (line ABC in figure 3.4c) and an almost coherent structure for the portion formed by the side cutting edge itself (line CD in figure 3.4c). This lamella structure, which is correlated to low number of slip systems [24], is almost disappeared in C₁ and C₂ corresponding to samples 6 and 7, respectively, in Table 3.1. For these two sets of cutting conditions, we have

low feed and depth-of-cut as well as high cutting speed which causes to higher cutting temperature in comparison to the rest of cutting conditions in Table 3.1. Therefore, more slip systems will get a chance to be active and chip's free side morphology tends to be more coherent rather than lamellar. In contrast to the lamellar free side, the back side of chips in the vicinity of the inserts' rake face shows a very smooth and shiny morphology which is related to shearing action on the rake face and the constraint imposed on the material's flow by this face itself. However, some local melting marks, as in cases B2 and B3, are observed sporadically on the back sides which are dealt with in the next section.

3.4.2. Material adhesion and flank built-up

Microstructure of Mg-Ca0.8 alloy in figure 3.1 illustrates the presence of a different phase on grain boundaries. A closer look to this phase under optical microscope reveals that it has two different phases itself as is shown in figure 3.6. Knowing that cooling rates in most casting processes are not the stable thermo-dynamical rate, which phase diagrams like the one in figure 3.1 are built upon it, hence after primary Mg forms the bulk of grains, a Ca rich melt would be left on the boundaries which then solidifies to secondary Mg and intermetallic phase Mg₂Ca, bright and dark spots in the grain boundary, respectively (figure 3.6).

The primary Mg melts at 650 °C according to phase diagram in figure 3.1 and secondary Mg's melting happens at 516.6 °C. If during a cutting process the generated temperature passes melting point of secondary Mg then a semi-solid phase comprised of Mg₂Ca particles and melted secondary Mg will form on the grain boundaries, even though the bulk of grains are still solid. This fact facilitates grain boundary sliding which ultimately results in increased thermal

softening of the material and even increased chance of the whole grains being pulled out due to the cutting action right in the vicinity of the cutting edge.

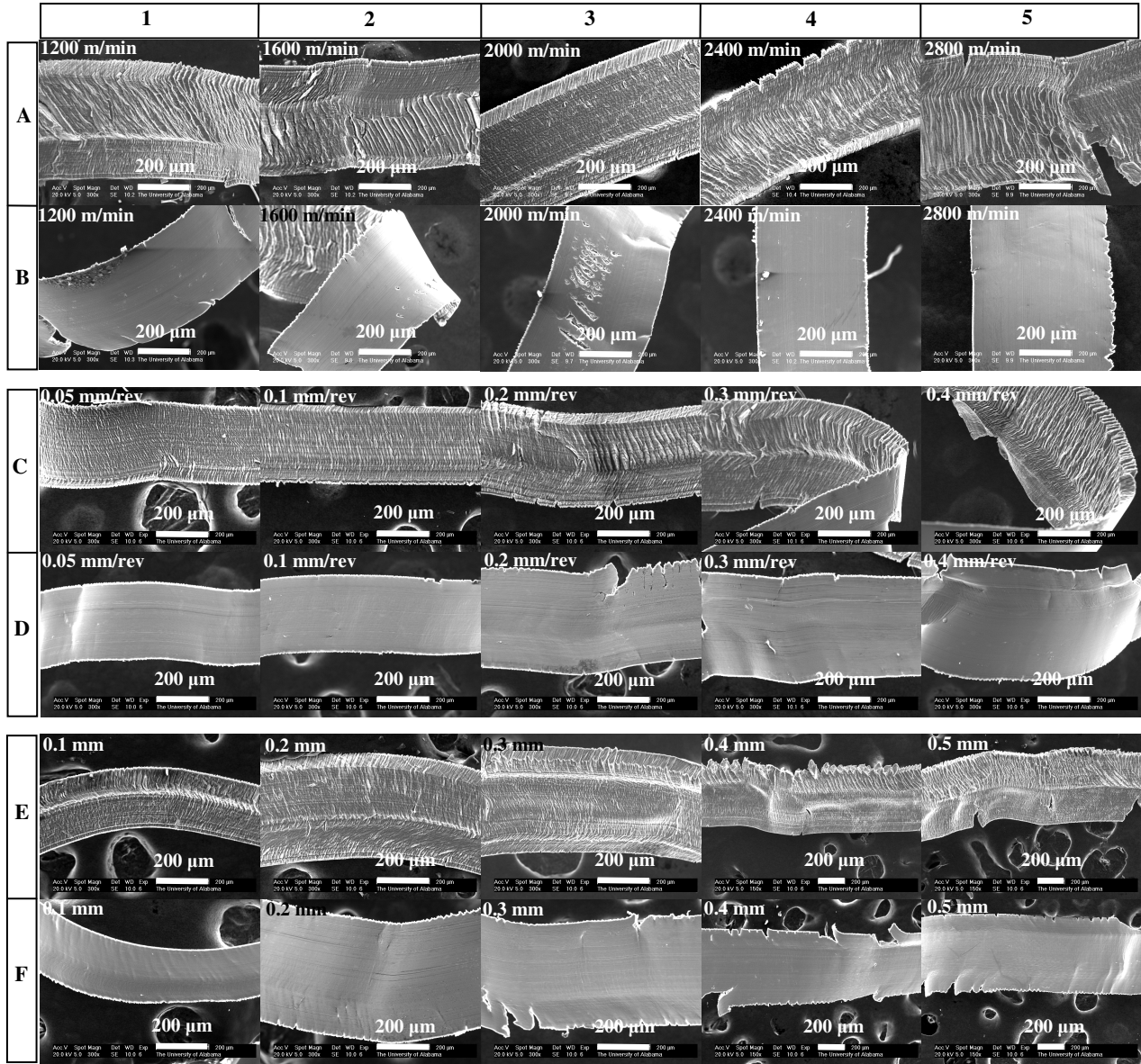


Fig. 3.5 Effect of cutting speed (A, B), feed (C, D), and depth-of-cut (E, F) on chip morphology (A, C, E free surface; B, D, F back surface)

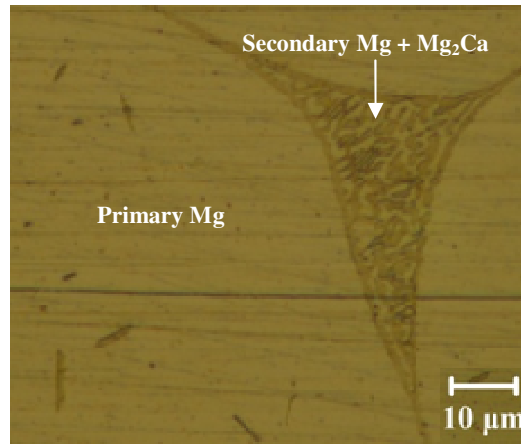


Fig. 3.6 Primary Mg phase on the bulk of grains and secondary Mg phase plus Mg_2Ca on the grain boundary

Mg_2Ca particles at grain boundaries are expected to be harder than Mg itself due to higher melting point which speaks on the fact that these particles have gotten stronger atomic bonds and consequently more resistance to indentation. Although the heat generated by plastic deformation in the cutting zone and friction at the tool/workpiece interface would be enough to make the semi-solid phase at grain boundaries, the presence of these hard phases could make the interaction more intense by adding high energy impacts of the hard particles to the scenario and generating more heat. They will accelerate the tool wear as well.

Theoretically, flank built-up formation happens in three stages which are similar to cutting other Mg alloys [23]. Stage I (initiation): thermally softened Mg-Ca0.8, a mixture of semi-solid in itself, flows on the rake face of the cutting inserts due to shear action. Despite the low chemical affinity between Mg and PCD materials, the presence of high pressure on the rake face during cutting will cause some material adhesion to the rake face called built-up layer (BUL) in figure 3.7. Stage II (development): hereafter, material is stacked up on the BUL and

results in a compact mass which is called stagnant zone or built-up edge. Stage III (formation): Built-up edge (BUE) can grow large enough to make a gap between the cutting edge and machined surface. Eventually, large cutting pressures will extrude the material between the flank face and machined surface which ultimately forms a FBU.

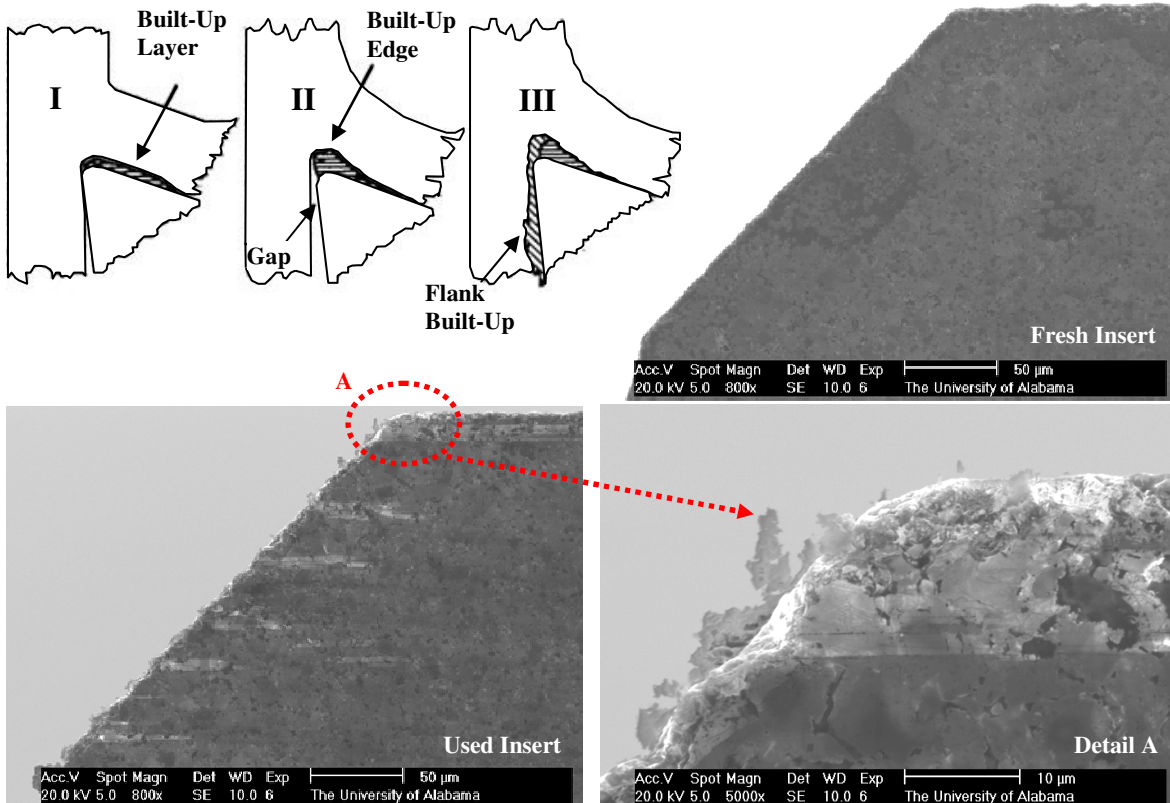


Fig. 3.7 Theoretical stages in FBU formation and rake face SEM images of fresh and used PCD inserts

Fresh and used cutting inserts are also shown in figure 3.7. The material adhesion to rake face along the side and horizontal cutting edges of the used insert are clearly visible. Thermal conductivity of Mg is about 150 W/(m.C) and by adding alloying elements it decreases more

[41]. This is almost Thirteen times smaller than the thermal conductivity of PCD material which is 2000 W/(m.C) [29]. Therefore, BUL can be a good thermal barrier making it easy for temperature to pave the almost 135 °C span between melting point of secondary Mg on the eutectic line and that of primary Mg and to cause BUL melting on the rake face. As soon as BUL melts, bare PCD comes into contact with the back face of the chip due to shear action and starts to carry the generated heat away which avoids the global melting of the chip to happen.

Therefore, BUL melting on the rake face is local and limited which can be verified by the limited melting marks on back face of the chips shown in figure 3.8a. The absence of any sparks or chip ignition during high speed dry face milling of Mg-Ca0.8 is another fact which strengthens the presence of limited local rather than global melting of the chips. FBU formation has the same dynamic nature as BUL does. It forms temporarily and interacts intensely with machined surface. This causes local irregular patterns on the machined surface (figure 3.8b) and also limited local melting which ultimately wipes off the FBU from flank face.

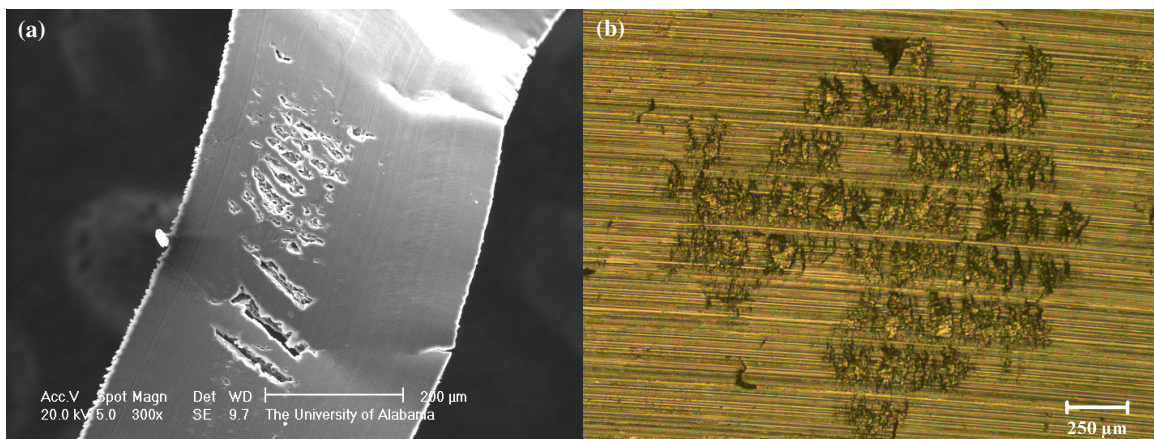


Fig. 3.8 Local melting marks on the back face of a chip (a) and local surface deterioration on the machined surface due to temporary FBU formation (b)

3.4.3. Abrasion and tool wear

The material adhesion and abrasion were monitored online with the aid of a developed optical system integrated in the CNC milling machine (figure 3.2). All the images in figure 3.9 are for the same PCD insert under different conditions. The other PCD inserts show almost the same trend regarding adhesion and abrasion on the flank face. All the tests in Table 3.1 were performed using the same set of PCD inserts and the flank faces were cleaned using cotton swab damped with acetone at the end of each test.

Figure 3.9a shows an insert in fresh condition and also after cutting all the 15 samples in Table 3.1. Comparative study of the two images reveals clearly that the flank face wear is practically negligible since PCD is a very hard material (10000 HV0.05) [29]. This hardness makes it very resistant to wear against abrasion by hard phases like Mg_2Ca . On the other hand, the cutting forces in cutting Mg alloys are low (about 30% smaller as compared with Al alloys) [24, 29, 30, 32, 33]. These facts make PCD inserts the first choice for cutting Mg alloys since the long tool life, due to high wear resistance, easily pays off for the initial costs and makes them economical in the long run with consistent surface and dimensional quality of the machined components.

The effect of cutting speed on material adhesion at flank face can be observed in figure 3.9b. For these images feed and depth-of-cut are fixed at 0.2 mm/rev and 0.2 mm, respectively. FBU may appear within short machining times if the cutting speed exceeds critical limit [36]. Starting with fresh flank face, cutting speed of 2000 m/min is definitely above the critical speed since considerable material adhesion is visible on flank face. More material adheres to flank face by increasing the cutting speed to 2800 m/min as is shown in figure 3.9b.

Figure 3.9c shows the effect of feed on material adhesion. Cutting speed and depth-of-cut are 2400 m/min and 0.2 mm, respectively. Starting with cleaned flank face, increasing feed from 0.2 mm to 0.4 mm doesn't show a significant increase in material adhesion. However, for fixed cutting speed and feed of 2400 m/min and 0.2 mm/rev, increasing the depth-of-cut from 0.2 mm to 0.5 mm shows a slightly more adhesion in figure 3.9d.

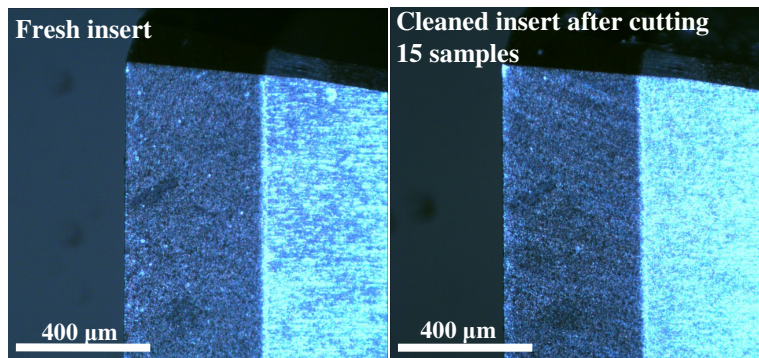


Fig. 3.9a Tool abrasion in high speed diamond face milling of Mg-Ca_{0.8} without coolant

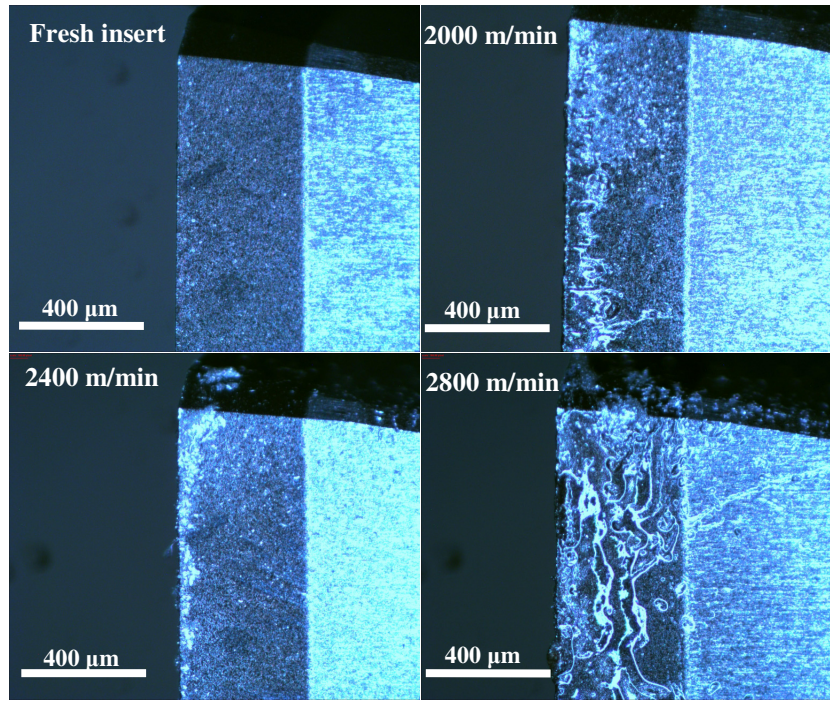


Fig. 3.9b Effect of cutting speed on flank face adhesion of PCD inserts

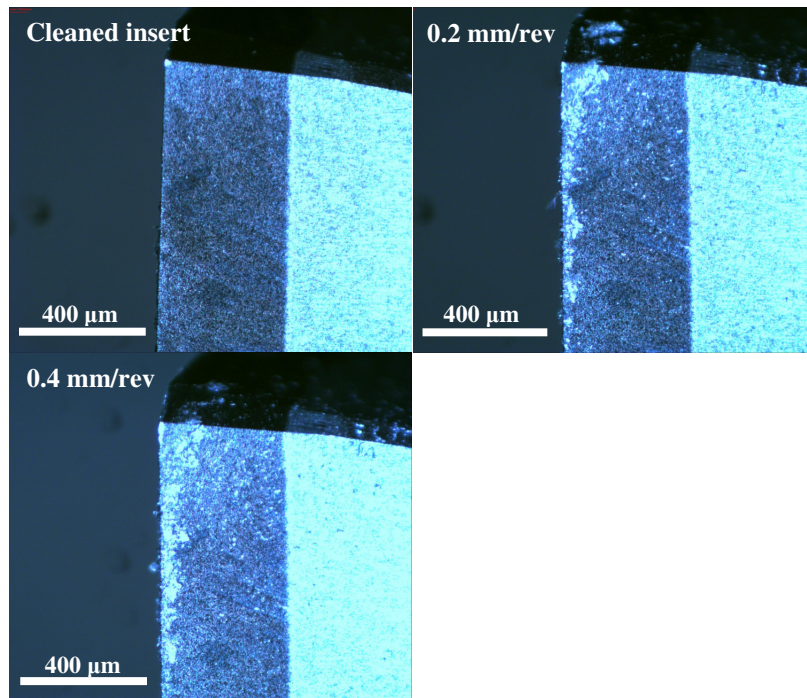


Fig. 3.9c Effect of cutting feed on flank face adhesion of PCD inserts

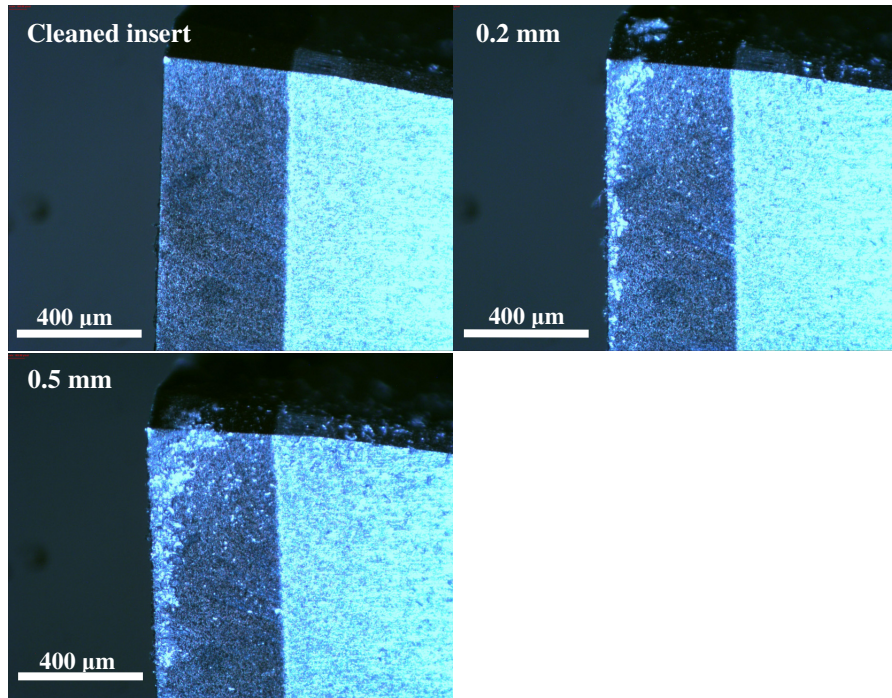


Fig. 3.9d Effect of cutting depth on flank face adhesion of PCD inserts

3.5. Conclusions

Biodegradable Mg-Ca_{0.8} alloy is dry milled in high speed range of 1200 to 2800 m/min using PCD tools. An optical monitoring system is integrated into the milling machine to in-situ inspect the material adhesion to flank face as well as possible wear due to abrasion. Followings are the conclusions of this experimental study:

- High speed dry face milling of Mg-Ca_{0.8} produces continuous chips. Chips free side is characterized by lamellar structure for the portion above the side cutting edge and almost coherent structure for the portion formed by the side cutting edge itself. Back side of the chips shows a very smooth and shiny morphology.

- Coherent portion of the chips free face is more dominant than lamellar portion under those combinations of cutting parameters which produce more cutting temperature. This might be due to increased number of active slip systems and ultimately ductility of Mg alloys at high temperatures.
- No chip ignition and/or spark are observed during the cutting process even at finish cutting conditions.
- Sporadic melting marks on back side of the chips along with the sporadic surface deteriorations indicate that there has been some flank built-up formation which has had a transient nature rather than a dominating fact which can ruin the surface topography and reduce surface integrity.
- Flank built-up (FBU) in cutting Mg-Ca0.8 alloy occurs in three stages of initiation, development, and formation similar to other Mg alloys. Built-up layer (BUL) initiates on rake face at stage I and then grows till it develops built-up edge (BUE) at stage II. Finally, BUE becomes extruded between flank face and machined surface to form FBU at stage III.
- The developed optical monitoring system proves itself a very useful technique to inspect material adhesion and tool abrasion. Cutting speed has the most significant effect on material adhesion at flank face. Material adhesion happens at cutting speeds above the critical speed even within short cutting time. No abrasion is observed on polycrystalline diamond inserts.

References

1. A. Gefen, Computational simulations of stress shielding and bone resorption around existing and computer-designed orthopaedic screws, *Medical & Bio. Eng. & Comp.* 40 (2002) 311-322.
2. J. Nagels, M. Stokdijk, P.M. Rozing, Stress shielding and bone resorption in shoulder arthroplasty, *J. Shoulder and Elbow Surgery* 12 (2003) 35-39.
3. H. Isaksson, A.L. Lerner, Mathematical modeling of stress shielding with bioresorbable materials for internal fracture fixation, *Bioengineering Conf.* (2003) 1041-1042.
4. A.G. Au, V.J. Raso, A.B. Liggins, A. Amirfazli, Contribution of loading conditions and material properties to stress shielding near the tibial component of total knee replacements, *J. Biomechanics* 40 (2007) 1410-1416.
5. A. Completo, F. Fonseca, J.A. Simoes, Strain shielding in proximal tibia of stemmed knee prosthesis: experimental study, *J. Biomechanics* 41 (2008) 560-566.
6. H.G. Seiler, *Handbook on toxicity of inorganic compounds*, 1st edition, CRC Press (1987).
7. G. Song, Control of biodegradation of biocompatible magnesium alloys, *Corrosion Science* 49 (2007) 1696-1701.
8. G. Song, S. Song, A possible biodegradable magnesium implant material, *Adv. Eng. Mater.* 9 (2007) 298-302.
9. B. Heublein, R. Rohde, V. Kaese, M. Niemeyer, W. Hartung, A. Haverich, Biocorrosion of magnesium alloys: a new principle in cardiovascular implant technology, *Heart* 89 (2003) 651-656.
10. F. Witte, V. Kaese, H. Haferkamp, E. Switzer, A. Meyer-Lindenberg, C.J. Wirth, H. Windhagen, In vivo corrosion of four magnesium alloys and the associated bone response, *Biomaterials* 26 (2005) 3557-3563.
11. C. Liu, Y. Xin, G. Tang, P.K. Chu, Influence of heat treatment on degradation behavior of bio-degradable die-cast AZ63 magnesium alloy in simulated body fluid, *Mat. Sci. & Eng. A* 456 (2007) 350-357.
12. H. Wang, Y. Estrin, H. Fu, G. Song, Z. Zuberova, The effect of pre-processing and grain structure on the bio corrosion and fatigue resistance of magnesium alloy AZ31, *Adv. Eng. Mater.* 9 (2007) 967-972.

13. Z. Li, X. Gu, S. Lou, Y. Zheng, The development of binary Mg-Ca alloys for use as biodegradable materials within bone, *Biomaterials* 29 (2008) 1329-1344.
14. B. Denkena, F. Witte, C. Podolsky, A. Lucas, Degradable implants made of magnesium alloys, *Proc. 5th Euspen Int. Conf.* (2005), Montpellier, France.
15. B. Denkena, A. Lucas, Biocompatible magnesium alloys as absorbable implant materials-adjusted surface and subsurface properties by machining processes, *Ann. CIRP* 56 (2007) 113-116.
16. T. Hassel, F.W. Bach, Production and properties of small tubes made from MgCa0.8 for application as stent in biomedical science, *Proc. 7th Int. Conf. Mg Alloys & Their App.* (2007) 432 – 437.
17. T. Hassel, F.W. Bach, C. Krause, Influence of alloy composition on the mechanical and electrochemical properties of binary mg-ca-alloys and its corrosion behavior in solutions at different chloride concentrations, *Proc. 7th Int. Conf. Mg Alloys & Their App.* (2007) 789 – 795.
18. N. Von Der Hoh, D. Bormann, A. Lucas, B. Denkena, C. Hackenbroich, A. Meyer-Lindenberg, Influence of different surface machining treatments of magnesium-based resorbable implants on the degradation behavior in rabbits, *Adv. Eng. Mater.* 11 (2009) B47-54.
19. Y.B. Guo, V. Brooks, Characterization of mechanical property and microstructure of biomedical magnesium alloy, *Proc. of ASM MPMD (Materials & Processes for Medical Devices) Conference and Exposition* (2009), Minneapolis, MN.
20. Y.B. Guo, M. Salahshoor, Process mechanics and surface integrity by high-speed dry milling of biodegradable magnesium-calcium implant alloys, *CIRP Ann. – Manuf. Tech.* 59 (2010) 151 – 154.
21. J.Z. Ilich, J.E. Kerstetter, Nutrition in bone health revisited: a story beyond calcium, *J. Am. College of Nutrition* 19 (2000) 715-737.
22. B. Aksakal, C. Hanyaloglu, Bioceramic dip-coating on Ti-6Al-4V and 316L SS implant materials, *J. Mat. Sci.: Materials in Medicine* 19 (2008) 2097-2104.
23. M. Videm, R.S. Hansen, N. Tomac, K. Tonnesen, Metallurgical considerations for machining magnesium alloys, *SAE Trans.* 103 (1994) 213 – 220.
24. G. Byrne, D. Dornfeld, B. Denkena, Advancing cutting technology, *Ann. CIRP* 52 (2003) 483 – 507.

25. F.W. Bach, B. Denkena, K. Weinert, P. Alpers, M. Bosse, N. Hammer, Influence of cutting and non-cutting processes on the corrosion behavior and the mechanical properties of magnesium alloys, Proc. 7th Int. Conf. Mg Alloys & Their App. (2007) 1076 – 1084.
26. B.D. Danilenko, Selecting the initial cutting parameters in machining magnesium alloys, Russian Eng. Res. 29(3) (2009) 316 – 318.
27. D.L. Hallum, Magnesium: lightweight, easy to machine, American Machinist 139(5) (1995) 48 – 51.
28. B. Denkena, J.C. Becker, C. Podolsky, A. Kuhlmann, Safe machining of magnesium parts by cutting and burnishing operations, Proc. 7th Int. Conf. Mg Alloys & Their App. (2007) 895 – 901.
29. H.K. Tönshoff, J. Winkler, The influence of tool coatings in machining of magnesium, Surface and Coatings Tech. 94-95 (1997) 610 – 616.
30. T. Friemuth, J. Winkler, Machining of magnesium workpieces, Adv. Eng. Mater. 1(3-4) (1999) 183 – 186.
31. M. Salahshoor, H. Ahmadian, Continuous model for analytical prediction of chatter in milling, Int. J. of Machine Tools and Manufacture 49 (2009) 1136 – 1143.
32. H.K. Tönshoff, T. Friemuth, J. Winkler, C. Podolsky, Improving the characteristics of magnesium work pieces by burnishing operations, Mg Alloys & Their App. (2000) 406 – 411.
33. H.K. Tönshoff, J. Winkler, C. Gey, Machining of light metals, Mat.-wiss. u. Werkstofftech 30 (1999) 401 – 417.
34. F.Z. Fang, L.C. Lee, X.D. Liu, Mean flank temperature measurement in high speed dry cutting of magnesium alloy, J. Mater. Proc. Tech. 167 (2005) 119 – 123.
35. W. Pedersen, M. Ramulu, Facing SiCp/Mg metal matrix composites with carbide tools, J. Mater. Proc. Tech. 172 (2006) 417 – 423.
36. N. Tomac, K. Tonnessen, Formation of flank build-up in cutting magnesium alloys, Ann. CIRP 40(1) (1991) 79 – 82.
37. J. Schmidt, J. Winkler, 1998, Machining of magnesium castings, Aluminium 74(6) (1998) 412 – 417.
38. C. Sanz, E. Fuentes, F. Obermair, L. Muntada, Efficient and ecological machining of magnesium hybrid parts, Proc. 7th Int. Conf. Mg Alloys & Their App. (2007) 916 – 921.

39. R. Schwerin, S. Joksch, Experiences with the machining of magnesium, Proc. 7th Int. Conf. Mg Alloys & Their App. (2007) 922 – 925.
40. T.B. Massalski, Binary alloy phase diagrams, 2nd Edition, ASM International 1 (1990) 927 – 928.
41. J. Zhou, Y. Yang, M. Lamvik, G. Wang, Determination of thermal conductivity of magnesium alloys, J. Cent. South Univ. Technol. 8(1) (2001) 60 – 63.

CHAPTER 4

SURFACE INTEGRITY OF BIODEGRADABLE ORTHOPEDIC MG-CA ALLOY BY HIGH SPEED DRY FACE MILLING

Abstract

Biodegradable magnesium-calcium (Mg-Ca) implants have the ability to gradually dissolve and be absorbed in human body after implantation. Since the implant surface is in direct interaction with body fluids, surface integrity of Mg-Ca implants are key factors influencing degradation rate of the biodegradable implants. Machining is often very necessary to make geometric features of implants. The effects of process parameters in dry high-speed face milling of Mg-Ca_{0.8} alloy on surface integrity characteristics, i.e. surface topography, surface roughness, microstructure, microhardness, and residual stresses, are investigated in this study. Polycrystalline diamond inserts are used to avoid material adhesion in milling Mg-Ca alloy. High cutting speeds of up to 2800 m/min and a broad range of feed and depth-of-cut values are selected to cover the regimes of finish and rough cutting. Average roughness value of 0.4 μm and shallow strain hardened depths are achieved. Little change of grain size can be observed in the near surface even for very slow feed value of 0.05 mm/rev. The surface residual stresses are measured to be highly compressive.

4.1. Introduction

Development of biodegradable implants has been one of the important areas in biomedical engineering. Biodegradable and biocompatible implants can be gradually dissolved and absorbed in the human organism after implantation. Compared with a traditional permanent implant made of steel, titanium, and cobalt alloys, a biodegradable implant will provide an appropriate solution for prevention of revision surgery, and other negative effects such as local inflammation and permanent physical irritation. Furthermore, conventional metallic implants are too stiff and will cause stress shielding effect [1-5]. Biodegradable implants made of polymers such as poly-L-Lactic acid usually have low mechanical strength for load carrying applications and cannot prevent misalignments between fragments of a fractured bone. This has driven researchers to seek for biodegradable metallic substitutes. Magnesium (Mg) and its alloys are among the most interesting options due to their close modulus of elasticity to that of bone. Mg-Ca alloys are biocompatible and do not generate toxic, carcinogenic, or mutagenic products [6,7,8].

High speed machining (HSM) without applying coolant has been considered and studied as an effective and ecologic way of making parts in automotive and aerospace applications. High speed machining of Mg alloys is defined as machining with cutting speeds between 600 to 5000 m/min based on being a finish cut or a rough cut [9,10]. The majority of work in machining of Mg and its alloys has been conducted for automotive industry through the period of last two decades. Increasing concerns about energy consumption and global warming has forced automotive industry and research institutes to look for different alternatives to meet technical needs of modern world with less fuel consumption and consequently less CO₂ emission. In this context, manufacturing structural parts using light weight metals such as Al and Mg seemed very

appealing and recommended machining guidelines for magnesium castings in any heat treatment condition have been established [11,12]. Mg alloys have gotten the lowest density among the metallic materials used in construction so far and offer a potential of up to 30 percent weight reduction even over Al alloys [13,14,15]. Low corrosion resistance of Mg alloys has been the biggest barrier in using them for constructional applications. On the other end of the spectrum, high corrosion rate has emerged as an interesting key property of Mg alloys for medical applications specially orthopedics to make biodegradable implants [16,17].

Denkena et al [16] sought to adjust degradation kinetics of Mg-Ca3.0 alloy through modifying surface properties by turning and deep rolling processes. They explored the space of process parameters to adopt a specific degradation profile appropriate for the specific medical application. They found that for same amount of depth-of-cut and feed, lower cutting speed shows lower corrosion rate and they related that to higher cutting forces and consequently higher and deeper compressive residual stresses generated by lower cutting speeds. In their study, the better surface finish at a lower feed rate did not show a significant influence on corrosion resistance.

Bach et al [17] studied the effects of milling parameters and cutting tool material on surface integrity and corrosion performance of two sand-cast Mg alloys EQ21 and WE43 meant for structural applications especially in automotive industry. Lower feed rates for a constant cutting speed resulted in harder layers in near surface related to longer exposure to thermo-mechanical loads and higher chances for micro-structural changes. In this regard, thermal conductivity of the alloy itself was mentioned as a key parameter in transferring rate of the generated heat away from the surface area. Higher cutting speeds at a constant feed rate gave rise to a smoother surface due to thermally induced reduction of the material strength on the shear

plane and the increased easiness of cut. They ended up with more surface roughness using polycrystalline diamond (PCD) inserts than cemented carbides. Aggressive salt spray test results showed rougher surfaces would have higher weight loss and corrosion rate.

Tönshoff et al [14,18,19] studied the influence of tool material/coating on adhesive effects between tool and workpiece. They examined four different sets of carbide tools without coating, with TiN and CVD diamond coatings, and with only a solid PCD tip brazed to the carbide body, respectively. Sand casted bars of AZ91-hp were cut using a lathe machine. Flank built-up (FBU) was observed with uncoated and TiN-coated carbide tools. PCD tipped tools could not generally avoid the FBU formation since workpiece material eventually gets into contact with the bare carbide and adheres to it. No adhesion of magnesium on the flank occurred using CVD diamond coated carbide tools related to lower friction between CVD diamond coating and Mg, and higher thermal conductivity of PCD (2000 W/m•C) which cause lower heat generations and faster heat conduction away from the cutting edge, respectively. However, they reported material adhesion to rake face of all tools. The best surface quality obtained with CVD diamond coated tools due to the absence of FBU. They found for short cutting lengths ($l_c \approx 10$ m), cutting speeds in the range of 300-2400 m/min have negligible effect on cutting forces and surface roughness regardless of what tool material/coating is used.

This paper deals with an experimental study of high speed dry face milling of lab-made Mg-Ca0.8 alloy. All the machining experiments are done without using coolant to make the process ecological. A special attention has been paid to the effects of machining parameters on surface integrity characteristics. Polycrystalline diamond (PCD) inserts are used to take advantage of PCD's high thermal conductivity and low chemical affinity with Mg in order to reduce the chances of chip ignition and FBU formation, but to increase tool life. The generated

surface integrity characteristics including surface topography, surface roughness, microhardness, microstructure, and residual stresses are examined and discussed.

4.2. Fabrication and microstructure of Mg-Ca0.8 alloy

The Mg-Ca0.8 used in this investigation was fabricated with the same procedure explained in section 3.3.1. Microstructure of the fabricated alloy is shown in figure 3.1.

4.3. Experimental conditions of high speed dry milling

The utilized experimental setup is explained in section 3.3.2 and shown in figure 3.2. This setup was used to investigate the effect of various cutting conditions in Table 3.1 on surface integrity of the machined samples.

4.4. Results and discussion

4.4.1. Surface topography and roughness

Nikon optical microscope was used to detect the effect of different cutting conditions on the surface topography. Surface topography of the machined surfaces is shown in figure 4.1. Surface roughness R_a values were measured with a contact stylus instrument (SLOAN DEKTAK II) with scan length of 2 mm perpendicular to feed marks in figure 4.1. For each set of cutting conditions, roughness measurements repeated three times. Average roughness values together

with corresponding max-min error bars are shown in figure 4.2. Surface cutting speed and depth-of-cut variations do not show a considerable effect on generated surface profile and ultimately roughness value. On the other hand, higher feeds lead to theoretically predictable increase of surface roughness from 0.2 μm up to 0.75 μm . Generally, high speed dry face milling of Mg-Ca0.8 alloy produces smooth surface with average R_a value of 0.4 μm .

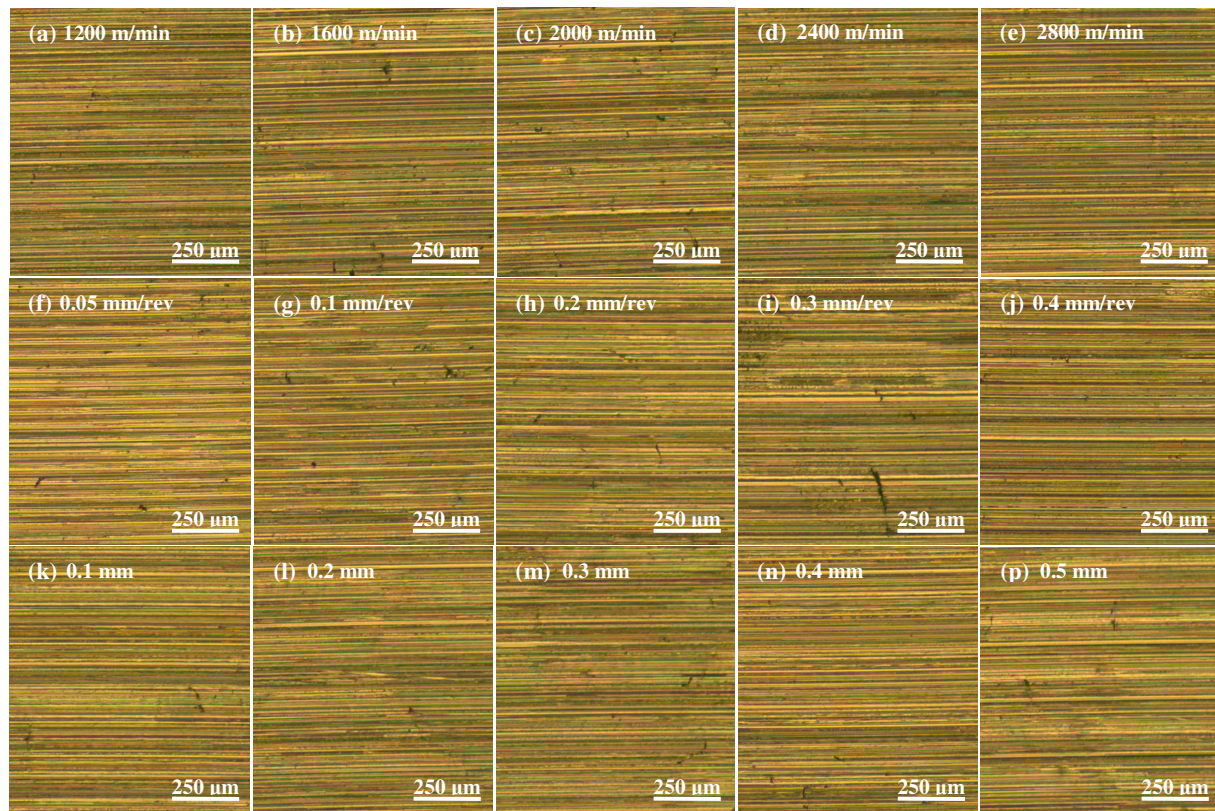


Fig. 4.1 Effect of cutting speed (a, b, c, d, e), feed (f, g, h, i, j), and depth-of-cut (k, l, m, n, p) on surface topography

The presence of any material adhesion on the machined surface can be a sign of FBU formation which may adversely affect the surface integrity. Such deteriorations are observed

sporadically on the machined surfaces as shown in figure 3.8. This may seem in contradiction with the high quality surfaces presented in figure 4.1 with average roughness value of about 0.4 μm (figure 4.2). A possible explanation, that may relieve this contradiction, is the kinetics of FBU formation which has not received enough attention so far. For high speed dry face milling of Mg-Ca_{0.8} with PCD inserts, FBU formation mechanism theorized in ref. [9] needs to include another step occurring after FBU formation, and that is FBU detachment from the tool. The developed FBU results in severe interactions around cutting edge zone and as a result, high amounts of heat will be generated. Low thermal conductance of Mg compared to PCD and insufficient time for thermal diffusion in high cutting speeds traps the generated heat in FBU.

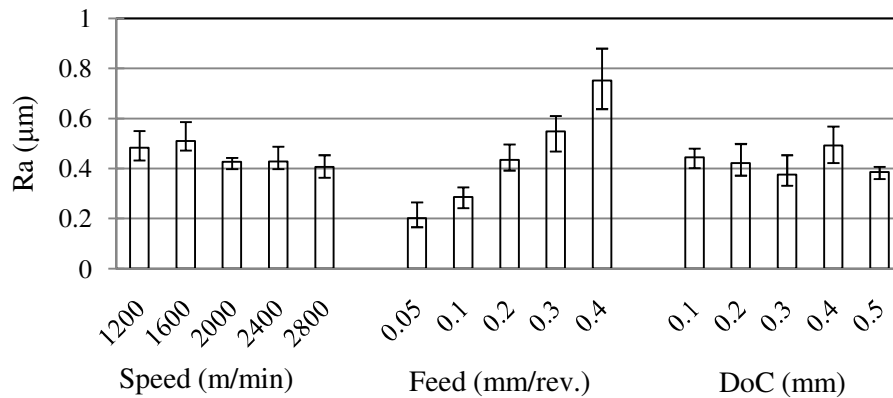


Fig. 4.2 Effect of cutting parameters on surface roughness

The extremely low heat content of magnesium [12] as well as high amounts of generated heat will ultimately cause FBU melting. However, this melting will be local and limited to FBU since as soon as FBU and its thermal barrier effect are removed, PCD will begin to conduct the

heat very quickly away from the cutting edge zone and will avoid global melting of chips and chip ignition to occur. Sporadic, limited deterioration marks on the machined surface (figure 3.8b), local melting marks on chips' back side (figure 3.8a), and the absence of sparks and chip ignition support the local, transient nature of FBU melting. Considering low chemical affinity between Mg and PCD plus the high thermal conductance of PCD, the high surface qualities observed in cutting Mg-Ca_{0.8} speaks on the fact that FBU formation is very slow and shortly after formation, it will be wiped off of the flank face due to local, limited melting as explained.

4.4.2. Microstructure and microhardness profile

Cutting processes often lead to changes of the microstructure in terms of reshaping and resizing of the grains or even phase transformation in near surface due to thermal effects present in cutting regimes. The intensity of this influence can vary based on the selected cutting parameters. Subsurface optical micrographs are presented in figure 4.3 to study the possible effects of cutting speed, feed, and depth-of-cut on microstructure. Fine grain structures which are usually observed in thermo-mechanical processes occur due to dynamic recrystallization (DR). As is well known, DR needs a minimum amount of temperature and deformation in order to happen. Deformation and dense tangles of dislocations will accumulate energy in grains. This energy will serve as driving force for nucleation of new grains at boundaries of the old ones and the temperature will facilitate atomic scale mechanisms and migrations during nucleation.

Examining the images shown in figure 4.3 reveals the fact that no dynamic recrystallization has happened in high speed dry face milling of Mg-Ca_{0.8} samples under different cutting conditions. There are extra large grains close to the machined surfaces. They

cannot be produced due to grain growth mechanism which often occurs after recrystallization since they will not have enough time for that due to high cutting speeds.

If recrystallization has not happened then either or both of the prerequisites for DR, i.e. enough deformation or/and temperature, would have not been provided. High thermal conductivity of PCD inserts is a fact that can rule out the presence of deep thermal gradients in the cutting zone. This is supported by the absence of dominant FBU, sparks, and chip ignition. Therefore, even if we assume the presence of high amounts of plastic deformation and strain hardening to provide appropriate circumstances for nucleation at old grain boundaries, still atomic migrations to nucleation sites would not occur or would linger too much.

However, microhardness profiles shown in figure 4.4 show that the plastic deformation has not gone too deep below the surface since below 12 μm the microhardness stabilizes at about 50 HK. The microhardness profiles in figure 4.4 are measured using Knoop indenter at 10 gr load and 15 s dwell time. Generally, hardness value can carry information about the intensity and extent of the plastic deformation. Dislocations and their movement on slip systems cause plastic deformation to happen. Dislocations' density simultaneously increases when they move which raises the chances of getting tangled with other dislocations. Grain boundaries may also block dislocations, but since grains are big for Mg alloys and grain boundary density is low they contribute much less in immobilizing dislocations.

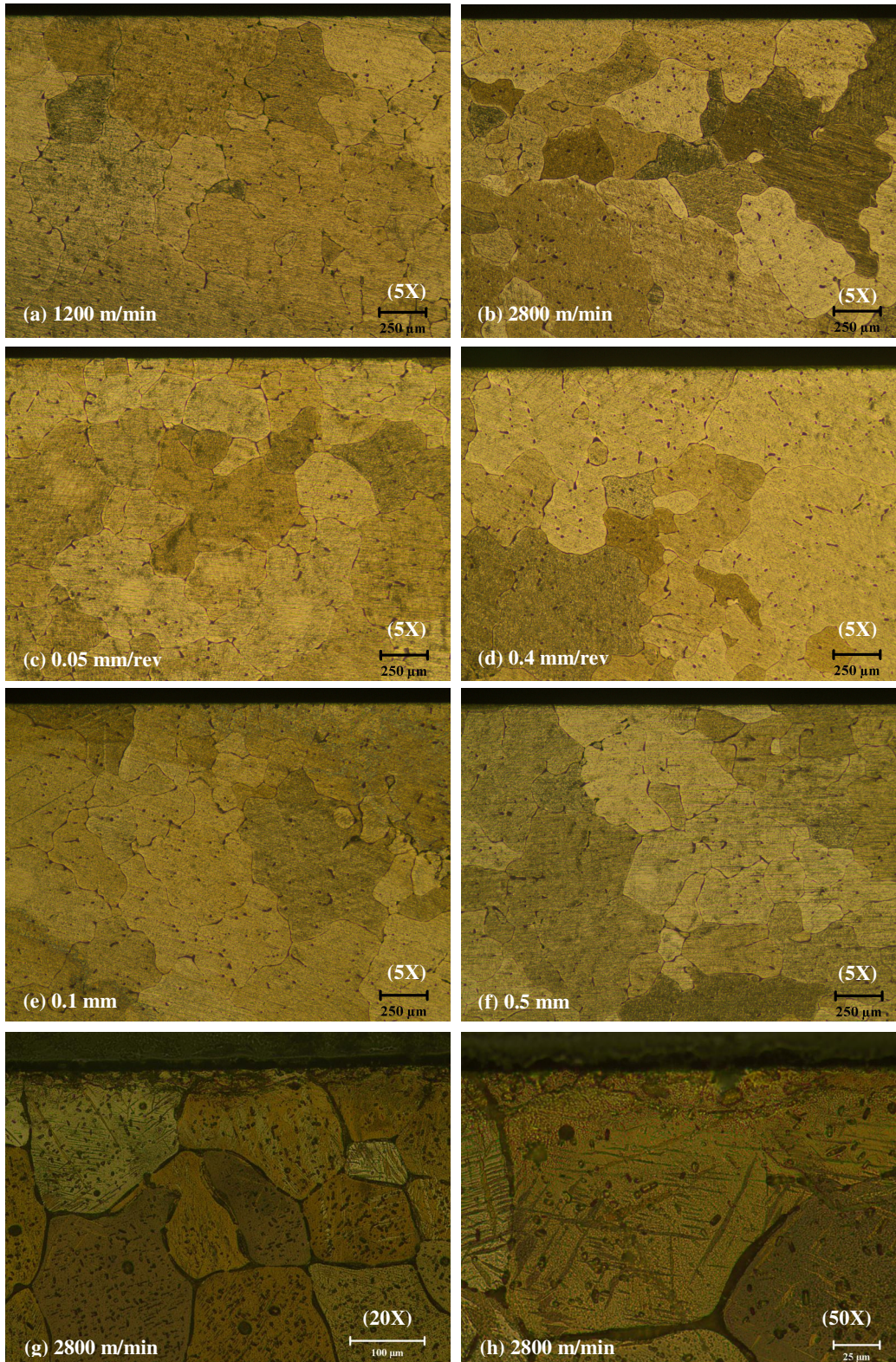


Fig. 4.3 Effects of cutting speed (a,b), feed (c,d), and depth-of-cut (e,f) on subsurface microstructure along with typical higher magnification images (g,h)

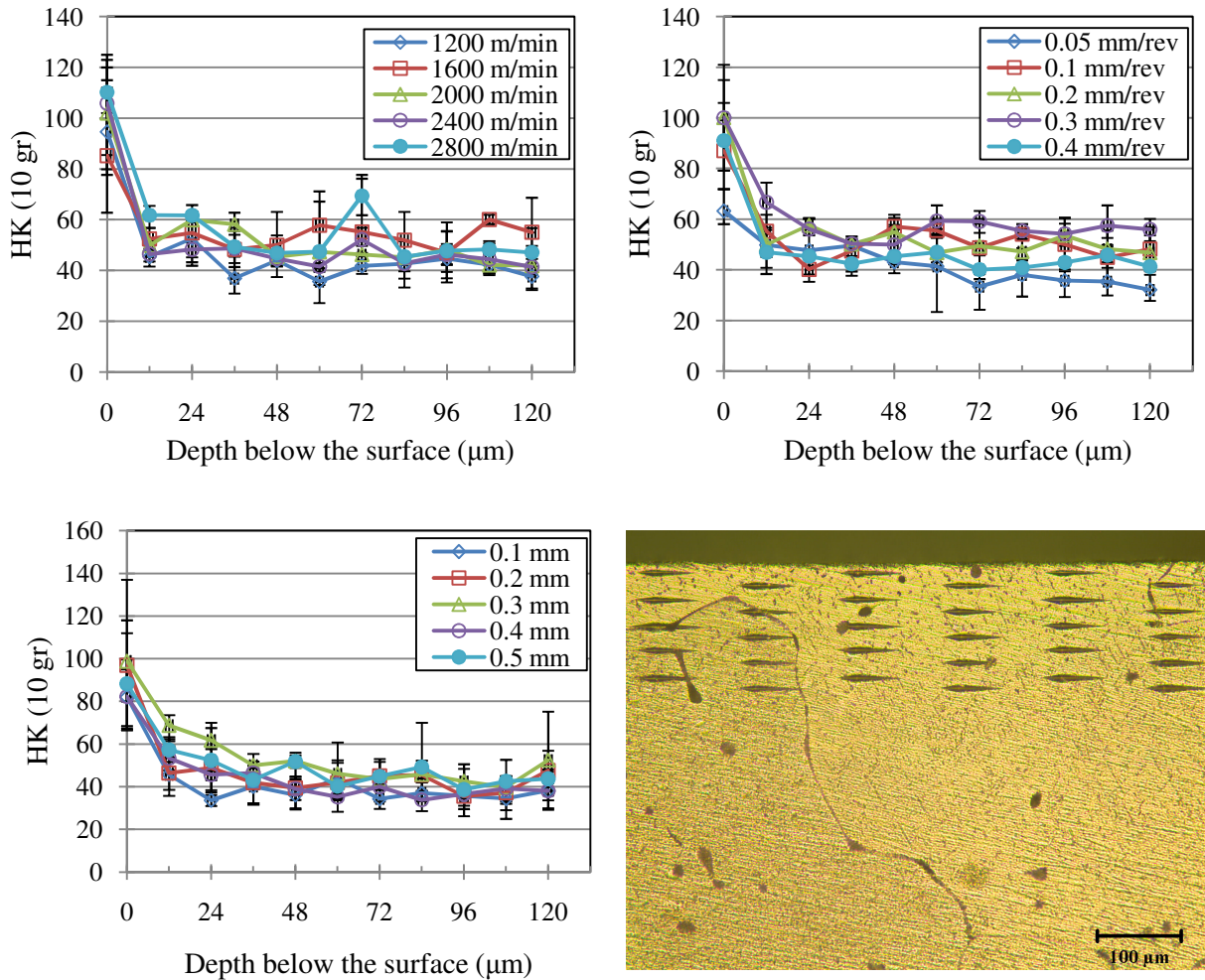


Fig. 4.4 Effect of cutting parameters on microhardness profile and microdent pattern

Strain hardening is the result of decreased mobility in dislocations. On the other hand, hardness testing is nothing but making an indent permanently on the target surface and calculating the hardness value based on the size of the indent. Therefore, as the material becomes more strain hardened its hardness value also increases. Strain hardening depth of less than 12 μm in figure 4.4 is much smaller than huge grain sizes in figure 4.3. This speaks on the fact that not

only the required temperature is not provided for DR, as discussed before, but also the extent of deformed zone is not big enough to cover more than one grain and to drive the nucleation to start.

Figure 4.4 also shows the pattern of indents on subsurface zone. At each depth microhardness measurement is repeated three times. The hardness values reported in figure 4.4 are average values with max-min error bars. This scatter may be caused by two factors. First, as is visible from dents' pattern, some dents are on the grain boundaries or have some overlap with small porosities which affect the hardness value, and second, even though extreme care was taken to make the polished subsurface plane parallel to horizon but since the polishing was performed manually some amount of tilt is expected. This fact will make the diagonal of the dents look slightly longer or shorter than what really is and consequently the reported microhardness values will have some amount of error.

The microhardness values at depth zero in figure 4.4 are measured on the machined surface as is visible from dents' pattern in figure 4.5. Surface microhardness is measured in both parallel and normal to feed mark directions and is repeated five times in each direction. However, the surface hardness in parallel direction is reported as zero depth hardness value in figure 4.4 to keep the consistency with the fact that subsurface dents are also parallel to feed mark direction, since samples are sectioned parallel to the feed marks. There is some amount of directionality in surface microhardness and it is different in parallel and normal to feed mark directions (figure 4.5). Surface hardness values in figure 4.5 are average values.

Figure 4.5 also shows the effect of different cutting parameters on surface microhardness in parallel and normal to feed mark directions. Generally, hardness in cutting direction is higher than that in feed direction. While increase in cutting speed and feed raise the hardness in parallel

direction, depth-of-cut has relatively less effect on average hardness. Large scatter in measurements, shown by max-min error bars in figure 4.5, are due to presence of feed marks on the machined surface. The surface hardness is the least for the smallest feed rate and this might be due to lower ploughing, flaking, or superficial material adhesion effects.

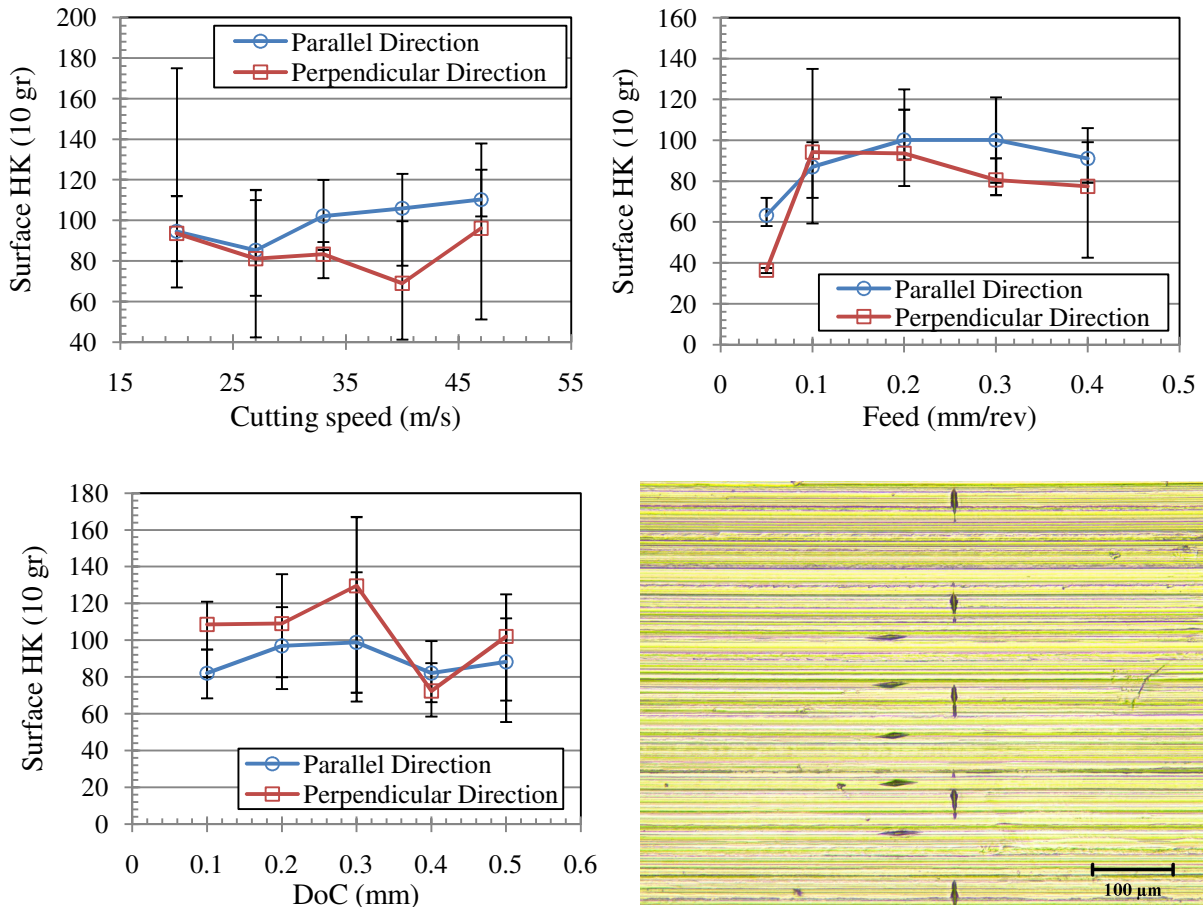


Fig. 4.5 Effect of cutting conditions on surface microhardness in parallel and normal to feed directions

4.4.3. Residual stresses

Normal residual stresses on the machined surfaces are measured using the 4-axis Bruker D8 XRD machine. Co-K α rays with 1.7889 Å wavelength and 6.93 keV energy are generated applying 40 kV and 35 mA power rating to X-ray tube. Generated X-rays are collimated and directed onto samples' surface with the 0.8 mm diameter collimator. Diffracted X-rays emerging from samples are detected by HI-STAR area detector located at 15 cm distance from the goniometer center. The highest intensity peak in diffraction profile shown in figure 4.6 happens at $2\theta = 42.89^\circ$ which belongs to $(10\bar{1} 1)$ pyramidal planes. Therefore, this peak was chosen to minimize the noise effects of known, e.g. surface roughness (figure 4.1) and other unknown factors. However, it is acknowledged that small Bragg angles may cause error to some extent in measured residual stresses. Meanwhile, comparative study of residual stresses using higher Bragg angles and different radiation sources will be explored in future work. The distance between these planes are used as an internal gauge to measure residual strains and ultimately residual stresses according to the $\sin^2\psi$ method. Since X-rays inter-react only with near surface layers of the samples (a few microns in depth) the stress state is assumed to be plane stress ($\sigma_3 = 0$) and uniform within the diffracting volume. Modulus of elasticity and Possion's ratio are taken as of polycrystalline Mg-Ca0.8, i.e. 45 GPa and 0.33, respectively, and assumed that they are isotropic within the diffracting volume.

For each cutting parameters' set in Table 3.1, three measurements are performed. The average values for in-plane normal stresses with max-min error bars are shown in figure 4.7. The observed scatter in measured data might be due to presence of feed marks on the surface as shown in figure 4.1 and nonuniformity of strain along their profile. The other possibility could be the large grain structure on the vicinity of the machined surface which makes the assumption of

treating diffracting volume as an ideal polycrystalline with certain deviation from reality due to lack of sufficient grains in the radiation area by a 0.8 mm collimator. The effect of grain structure on diffraction rings is visible in figure 4.6 for $(10\bar{1}1)$ prismatic planes ring. This coarse grain structure makes this ring a continuous ring with some bright spots on it rather than a continuous and uniformly bright ring.

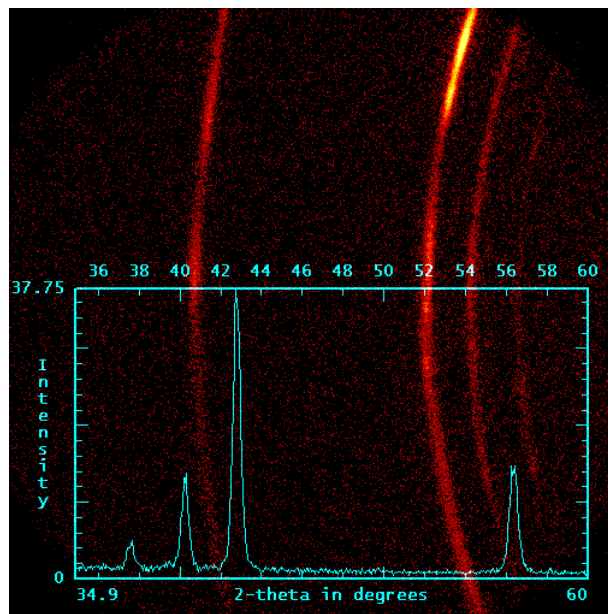


Fig. 4.6 2D frame and integrated diffraction profile

All normal residual stresses are measured to be compressive (figure 4.7) which is expected to slow down the corrosion rate of the implant in human body fluid [16]. The initial residual stresses were not measured. However, all the samples experienced same deformation history before machining. Therefore, for the purpose of this study which is to compare the cutting process effects on surface integrity, it is expected that the initial residual stress state

would not affect the relative trends of residual stress by a cutting process. The link between bio-degradation and surface integrity is beyond the scope of this study and will be addressed in future investigations. Basically, no special trend in residual stresses is visible by changing the cutting parameters in high speed dry face milling of Mg-Ca0.8 alloy.

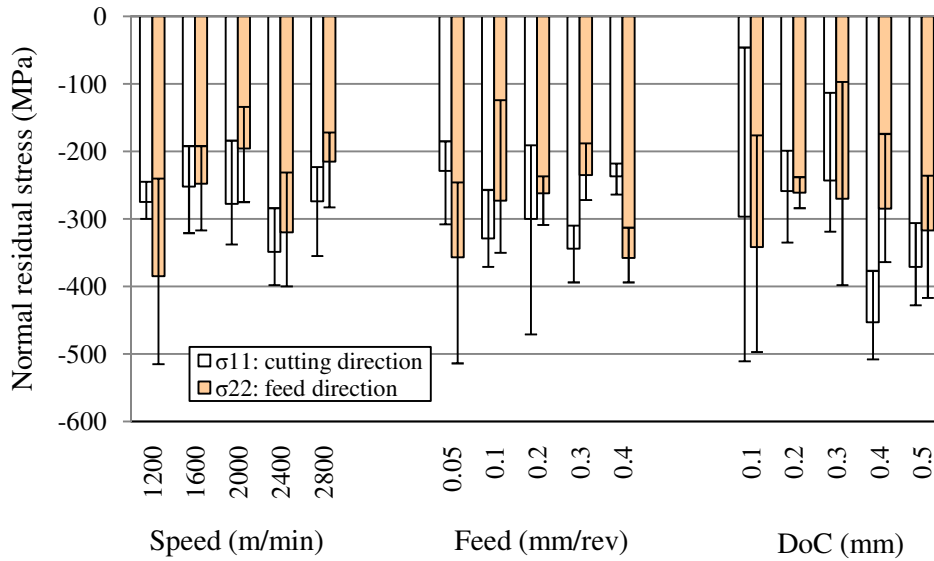


Fig. 4.7 Effect of cutting parameters on normal residual stresses

4.5. Conclusions

Lab made Mg-Ca0.8 orthopedic implant alloy has been dry milled at high cutting speeds of 1200 – 2800 m/min. The effects of different combinations of process parameters on surface integrity of this biomedical material are investigated. The summaries of this research are as follows:

- Regular feed marks pattern is dominating scene in surface topography micrographs with average roughness of 0.4 μm . Surface roughness increases with increasing feed amount.
- The machined surface is clean in general. The sporadic surface deteriorations suggest that there could be a little transient flank built-up formation on the cutting tool, but it has little effect on surface topography and surface integrity.
- Grain refinement was not observed in the near surface. The large grains are cut through, which is very different from machining steel and super alloys.
- Strain hardening depth is very shallow and subsurface microhardness profile stabilizes after 12 μm depth. Anisotropic surface microhardness shows directionality with regard to cutting direction.
- Normal residual stresses are measured to be all highly compressive which could be beneficial to corrosion resistance of Mg-Ca orthopedic implants.

References

1. A. Gefen, Computational simulations of stress shielding and bone resorption around existing and computer-designed orthopaedic screws, *Medical & Bio. Eng. & Comp.* 40 (2002) 311-322.
2. J. Nagels, M. Stokdijk, P.M. Rozing, Stress shielding and bone resorption in shoulder arthroplasty, *J. Shoulder and Elbow Surgery* 12 (2003) 35-39.
3. H. Isaksson, A.L. Lerner, Mathematical modeling of stress shielding with bioresorbable materials for internal fracture fixation, *Bioengineering Conf.* (2003) 1041-1042.
4. A.G. Au, V.J. Raso, A.B. Liggins, A. Amirfazli, Contribution of loading conditions and material properties to stress shielding near the tibial component of total knee replacements, *J. Biomechanics* 40 (2007) 1410-1416.

5. A. Completo, F. Fonseca, J.A. Simoes, Strain shielding in proximal tibia of stemmed knee prosthesis: experimental study, *J. Biomechanics* 41 (2008) 560-566.
6. H.G. Seiler, *Handbook on toxicity of inorganic compounds*, 1st ed., CRC Press, 1987.
7. G. Song, Control of biodegradation of biocompatible magnesium alloys, *Corrosion Sci.* 49 (2007) 1696-1701.
8. G. Song, S. Song, A possible biodegradable magnesium implant material, *Adv. Eng. Mater.* 9 (2007) 298-302.
9. M. Videm, R.S. Hansen, N. Tomac, K. Tonnesen, Metallurgical considerations for machining magnesium alloys, *SAE Trans.* 103 (1994) 213 – 220.
10. G. Byrne, D. Dornfeld, B. Denkena, Advancing cutting technology, *Ann. CIRP* 52 (2003) 483 – 507.
11. B.D. Danilenko, Selecting the initial cutting parameters in machining magnesium alloys, *Russian Eng. Research* 29 (2009) 316 – 318.
12. D.L. Hallum, Magnesium: lightweight, easy to machine, *American Machinist* 139 (1995) 48 – 51.
13. B. Denkena, J.C. Becker, C. Podolsky, A. Kuhlmann, Safe machining of magnesium parts by cutting and burnishing operations, *Proc. 7th Int. Conf. Mg Alloys & Their App.* (2007) 895 – 901.
14. H.K. Tönshoff, J. Winkler, The influence of tool coatings in machining of magnesium, *Surface and Coatings Tech.* 94-95 (1997) 610 – 616.
15. T. Friemuth, J. Winkler, Machining of magnesium workpieces, *Adv. Eng. Mater.* 1 (1999) 183 – 186.
16. B. Denkena, A. Lucas, Biocompatible magnesium alloys as absorbable implant materials-adjusted surface and subsurface properties by machining processes, *Ann. CIRP* 56 (2007) 113-116.
17. F.W. Bach, B. Denkena, K. Weinert, P. Alpers, M. Bosse, N. Hammer, Influence of cutting and non-cutting processes on the corrosion behavior and the mechanical properties of magnesium alloys, *Proc. 7th Int. Conf. Mg Alloys & Their App.* (2007) 1076 – 1084.
18. H.K. Tönshoff, T. Friemuth, J. Winkler, C. Podolsky, Improving the characteristics of magnesium work pieces by burnishing operations, *Mg Alloys & Their App.* (1999) 406 – 411.

19. H.K. Tönshoff, J. Winkler, C. Gey, Machining of light metals, Mat.-wiss. u. Werkstofftech 30 (1999) 401 – 417.

CHAPTER 5

CUTTING MECHANICS IN HIGH SPEED DRY MACHINING OF BIOMEDICAL MAGNESIUM-CALCIUM ALLOY USING INTERNAL STATE VARIABLE PLASTICITY MODEL

Abstract

Magnesium Calcium (Mg-Ca) alloys have become attractive orthopedic biomaterials due to their biodegradability, biocompatibility, and congruent mechanical properties with bone tissues. However, process mechanics of cutting biomedical Mg-Ca alloys is poorly understood. Mechanical properties of the biomedical magnesium alloy at high strain rates and large strains are determined by using the split-Hopkinson pressure bar testing method. Internal state variable (ISV) plasticity model is implemented to model the material behavior under cutting regimes. A finite element analysis (FEA) model has been developed to study the chip formation during high speed dry cutting of Mg-Ca_{0.8} alloy. Continuous chip formation predicted by finite element simulation is verified by high speed dry face milling of Mg-Ca_{0.8} using polycrystalline diamond (PCD) inserts. Chip ignition as the most hazardous aspect in machining Mg alloys does not occur in high-speed dry cutting with sharp PCD tools. The predicted temperature distribution well explains the reason for the absence of chip ignition in high speed dry cutting of Mg-Ca_{0.8} alloy. In addition, sporadic surface deterioration and void marks on the back face of chips are explained.

5.1. Introduction

Traditional orthopedic methods use permanent metallic implants made of stainless steel, titanium, or cobalt-chromium alloys to bring bone traumas back to their original anatomical configuration and to hold them in place before the start of healing process. Durable implants are stiffer than bone and permanently protect the healing bone against mechanical exposure. This effect called stress shielding [1-3] hinders stabilization of the bone tissue which needs mechanical loads to obtain and maintain its rigidity and ultimately causes artificial osteoporosis. Moreover, permanent implants are foreign objects in human anatomy and always carry the risk of local inflammation. To avoid those negative effects, annually many revision surgeries with all their personal, medical, social and economical consequences have to be performed to remove the implants after one or two years.

Development of biodegradable implants is one of the important areas in medical science. Degradable, biocompatible implants can gradually dissolve and become absorbed in human organism after implantation. A biodegradable material will offer an appropriate solution for inflammatory discomfort, permanent physical irritation, stress shielding and the revision surgery associated with durable implants. Current biodegradable implants are mainly polymeric which have an unsatisfactory strength in load carrying applications. This has led researchers to seek for metallic biodegradable substitutes.

Clinical studies on biocompatibility of magnesium-calcium (Mg-Ca) alloys have brought very appealing results. These alloys do not generate any toxic, carcinogenic, or mutagenic products and so their dissolution inside human anatomy is acceptable from physiological point of view [4-8]. However, rapid corrosion of Mg-Ca alloys produces a great amount of dissolved Mg cations, a large volume of hydrogen, and a remarkable increase in local pH value which will

cause significant imbalance in physiological reactions. To develop Mg-Ca alloys as a successful orthopedic material, corrosion rate of these alloys should be adjusted to match the local absorption rate of corrosion by-products and the healing rate of bone tissue.

While the bulk material of the biomedical device is often important for integrity and mechanical success, the device surface is at the interface with biology. In this context, modifying a biomaterial surface [9,10] in order to elicit or inhibit a biological response seems very promising approach to tackle the above mentioned issue in Mg-Ca alloys. High speed machining (HSM) without applying coolant is an advanced surface treatment process which has been considered as an effective and ecologic way of making parts in automotive, aerospace, and medical device industries. HSM for Mg alloys is defined as machining with cutting speeds between 600 to 5000 m/min based on having a finish or rough cut [11,12].

Machining of Mg alloys is characterized by low power requirements, long tool life, short-breaking chips, high achievable surface qualities, low mechanical and thermal loads on the tool, and the possibility of dry machining [13,14]. Machining with coolants demands additional costs for the purchase, storage, and disposal and also causes difficulties when recycling the chips [15,16]. In contact with water-based coolants, magnesium tends to have chemical reactions and forms hydrogen which is extremely flammable. Oil-based lubricants introduce the danger of oil mist explosions [17,18]. Dry machining of magnesium alloys makes it a green and economic manufacturing process due to the elimination of cutting fluids [17].

Although the possibilities of oil mist or hydrogen gas explosions are avoided by dry machining, however, it may result in an increased adhesive effect at the cutting tool and a fire hazard [19]. In particular at high cutting speeds, the formation of flank build-up (FBU) on cutting tools have been reported [20]. This will cause higher friction and increased danger of

chip inflammation. Magnesium ignites if the melting point is exceeded throughout the material volume. This is especially dangerous, when the material volume is small, e.g. in chips during finishing operations with small depths of cut and small feed rates. Moreover, attachment and detachment of FBU from flank face results in high dynamic cutting forces and even chatter which will reduce dimensional accuracy, lower surface quality, or even break the tool [21].

Safe and high performance dry machining of Mg alloys will be achievable by optimizing tool material, tool geometry, coating thickness, and coating structure to avoid adhesive effects and FBU formation. In turning AZ91 alloy, no adhesion on flank face occurs using carbide tools coated with polycrystalline diamond (PCD) alloy compared to uncoated and TiN-coated carbide tools [22,23]. That is related to lower friction between PCD coating and Mg plus the higher thermal conductivity of PCD which cause lower heat generation and faster heat conduction from the cutting edge zone, respectively. Adhesive effects are combined with abrasion effect of high mechanical load caused by ceramic reinforcements in Mg based metal matrix composites (MMCs) [24]. TiN-coated carbide tools are destroyed immediately by the impact of hard ceramic particles. However, PCD-coated carbide tools show a better wear resistance [15,22].

FBU formation depends not only on physical and geometrical properties of cutting tool and its coatings but also on the metallurgical microstructure and heat treatment history of the specific Mg alloy being cut. The amount of $Mg_{17}Al_{12}$ phase or β -phase on grain boundaries increases by adding more aluminum (Al) to Mg-Al alloys. At fixed depth-of-cut and feed, the critical cutting speed above which FBU forms decreases by increasing amount of β -phase [11]. Manganese (Mn) is usually added to Mg-Al alloys in small amounts to increase their corrosion resistance. Mn combines with Al and produces very hard MnAl particles. The sporadic, high

energy impacts between these particles and cutting tool generate local, temporary heat and FBU which causes sparks during machining [20].

Cutting parameters are the only option left which can be tuned to avoid FBU formation if the cutting tool and the workpiece material are already selected. Cutting temperature controls FBU formation and is highly dependent on chosen cutting parameters. Tönshoff et al [25] implemented an analytical formula to calculate chip temperature in cutting Mg alloys and predicted it will increase if a small depth-of-cut and feed are chosen. Salahshoor and Guo [26] used FEA method to study the effect of cutting parameters on chip temperature in orthogonal cutting of Mg-Ca0.8 alloy. The stress-strain data, obtained from split-Hopkinson pressure bar (SHPB) test under various strain rates, were directly applied in the FE model. Therefore, the FEA predictions may be erroneous under different strain rates happening in cutting operation. This issue is addressed in this paper by incorporating a material plasticity model which enables the FE simulation to predict mechanical behavior of the material under different conditions than the SHPB test. Fang et al [27] measured the cutting temperature in high speed dry milling of AZ91 alloy. Undeformed chip thickness was in the same order as cutting edge radius, i.e. micromachining. They found higher cutting speed causes higher temperature.

The objectives of this study are to compute chip temperature in cutting novel Mg-Ca0.8 biomaterial using FEA method, to predict chip morphology, and to explore the opportunity of FBU formation. An internal state variable (ISV) plasticity model [29] is implemented in FE model to enhance its capability in predicting mechanical behavior of this material under cutting regimes. Stress-strain data obtained from split-Hopkinson pressure bar test (SHPB) are used along with a nonlinear square fitting technique to extract the parameters of the ISV model. Experiments are performed to study chip morphology and FBU formation in actual cutting. In

addition to temperature, von Mises stress and equivalent plastic strain distributions along with cutting forces are computed to gain a better understanding on cutting mechanics of this special alloy. It is important to note that some parametric evaluations and understanding are difficult to achieve experimentally.

5.2. Material model

5.2.1. Split Hopkinson pressure bar (SHPB) test

SHPB test [30] was applied to obtain the mechanical behavior of the Mg-Ca0.8 biomaterial under high strain rate loadings common in metal cutting processes. This test is built upon the one-dimensional stress wave propagation theory to calculate the strain rate in the specimen and ultimately the average true strain and true stress. The theory has a few assumptions [31] which must be satisfied in order to have a valid SHPB test results. First of all, stress wave propagation in SHPB bars should be one-dimensional. This assumption was met via following a few provisions: a) SHPB bars were made of maraging steel to have homogeneous and isotropic bars; b) they were centerless ground to have uniform cross section over the entire length and a straight neutral axis; c) stress level in propagating wave was kept below the elastic limit of the bars material via controlling the impact velocity; d) Bars were designed long and slender (12.7 mm in dia., 122 and 244 mm in length) to maintain a uniform axial stress distribution over the entire cross section; e) data corrections were made to accommodate for dispersion effects existing in finite diameter bars.

Specimen-bar interfaces are assumed to remain plane at all time during the test. Tungsten carbide discs were applied at the mentioned interfaces to achieve that goal. In one-dimensional stress wave propagation theory, deformation happens uniformly in the specimen implying that friction and inertia effects are assumed to be minimum and negligible. Specimen-bar interfaces were lubricated with oil-based molybdenum disulfide to reduce friction effect. Longitudinal and radial inertial effects were accounted for in specimen design stage [30-32]. They were designed as cylinders with 3.3 mm dia. and 7.62 mm thickness to minimize inertial effects.

Having force/stress equilibrium, uniaxial compression state, and constant strain rate, all the time during deformation, is another assumption made in one-dimensional stress wave propagation theory. Figure 5.1 shows strain-time and stress-strain plots of Mg-Ca_{0.8} alloy under quasi-static loading condition. It is visible that strain-time plot will be a straight line passing through origin under constant strain rate, uniaxial compression condition when the specimen is in force/stress equilibrium. Therefore, the stress-strain plot is valid through the whole range of strain values.

However, strain-time plots are not straight lines through the whole deformation time period under dynamic loading conditions as is shown in figure 5.2. Constant strain rates are not achieved unless after about 3% strain. The time spent at the beginning of the deformation up to 3% strain is called “ringing-up” time and is the time required to have about four reverberations of stress wave inside the specimen before gaining force/stress equilibrium. Hence, in order to establish the equilibrium condition faster, it is desirable to design SHPB samples as thin as possible of course without compromising the requirements for minimum inertial effects. Indeed, although the non-equilibrium condition in specimen during the initial phase of loading can be minimized but cannot be eliminated completely in SHPB test [31].

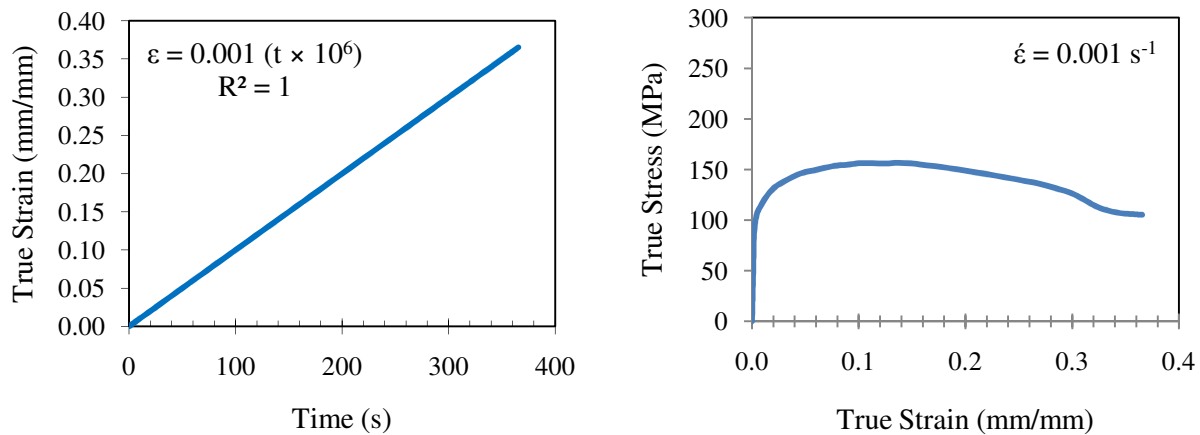


Fig. 5.1 Strain-time and stress-strain data in quasi-static compression testing [30]

Presence of non-linear portion in strain-time plot under dynamic loading condition implies that small strain measurements are unreliable due to non-equilibrium condition. For the same reason, high rate elastic modulus of Mg-Ca0.8 alloy cannot be measured by HSPB test. To avoid the propagation of this unreliability in finite element (FE) simulations, stress-plastic strain plot is used instead of stress-strain plot (figure 5.3). Elastic modulus of 45 GPa obtained from quasi-static compression test is implemented in FE simulations to account for elastic behavior prior to initial yield. Moreover, figure 5.4 clearly shows that for this material the effect of strain rate on flow stress is not considerable until above 600/s strain rate. Therefore, selected strain rates in figure 5.3 are successfully representing the work hardening effect of strain rate on stress-strain data.

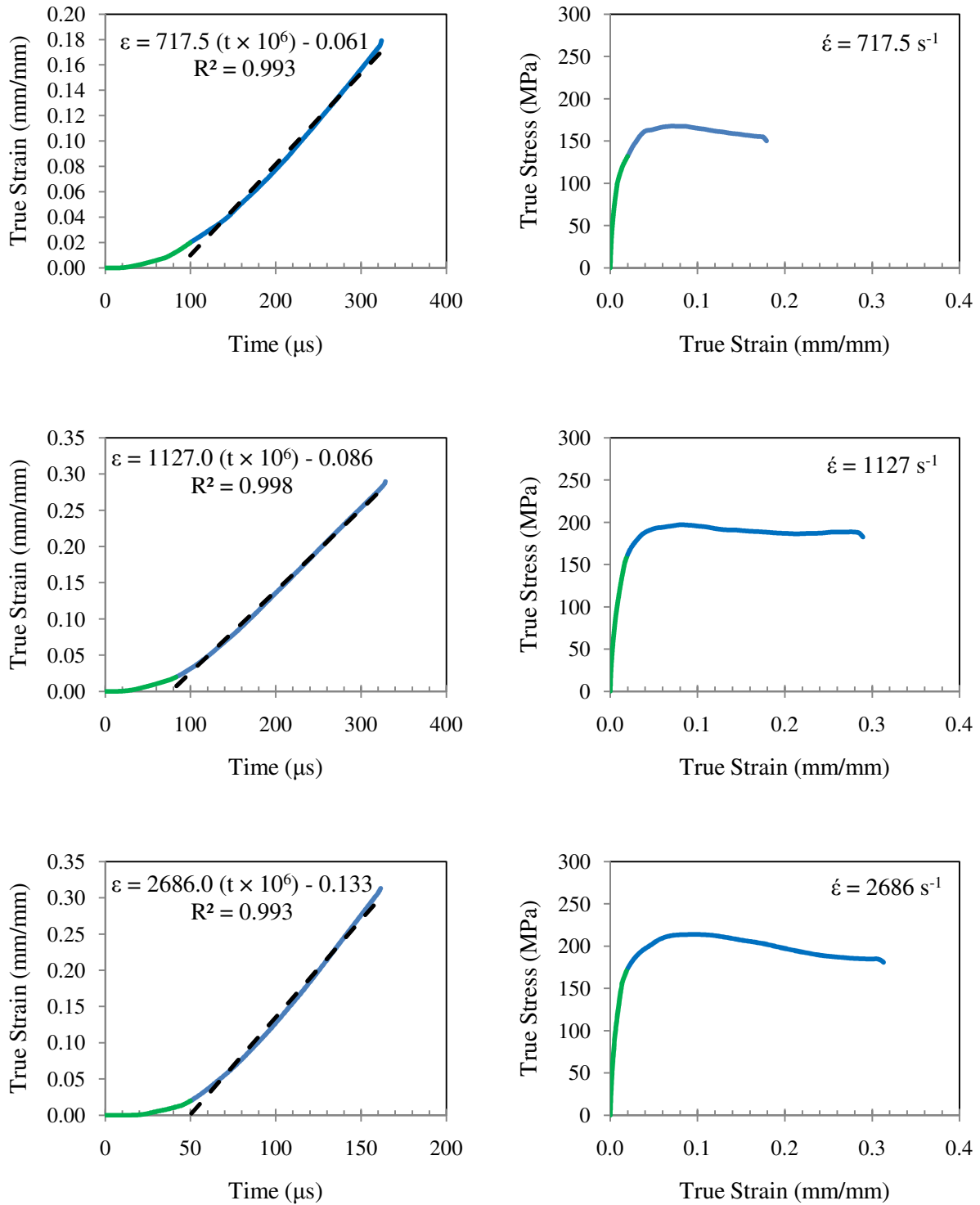


Fig. 5.2 Strain-time and stress-strain data in SHPB testing at various loading rates

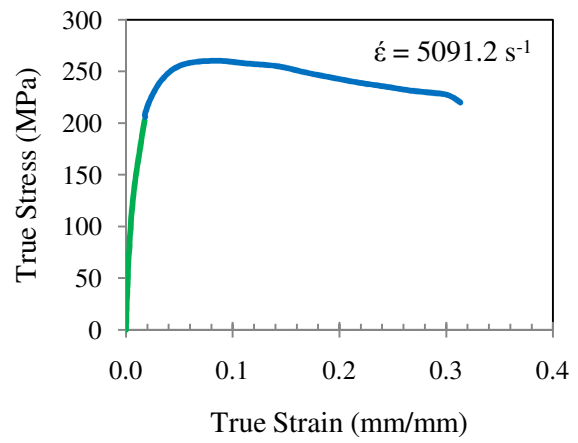
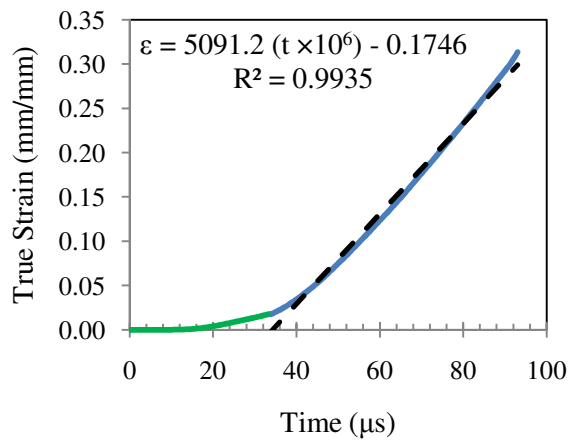
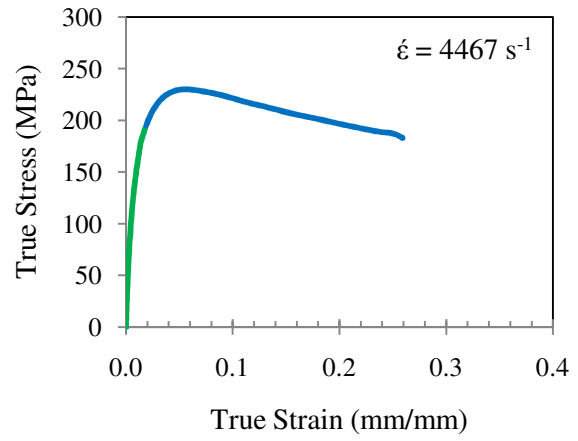
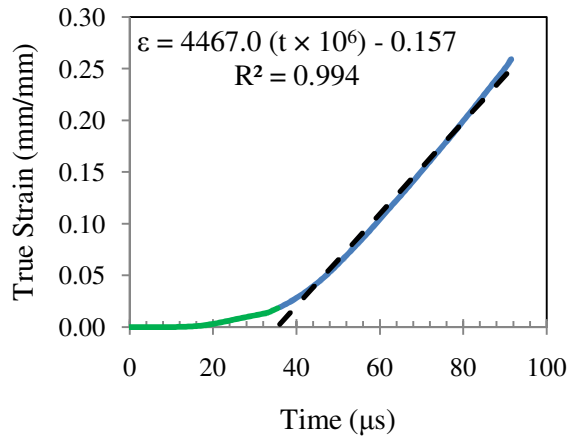


Fig. 5.2 (Contd.) Strain-time and stress-strain data in SHPB testing at various loading rates

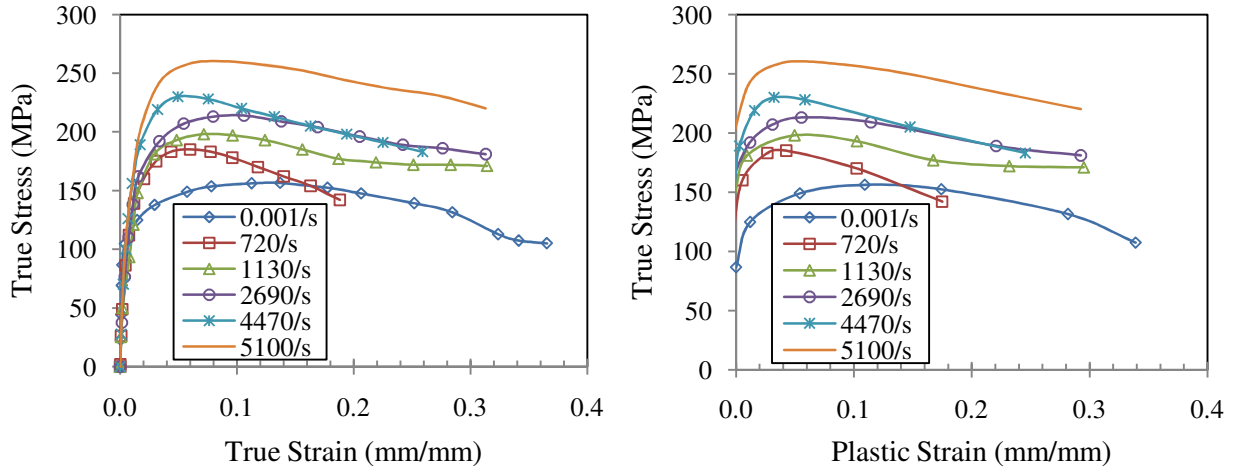


Fig. 5.3 Stress-strain and stress-plastic strain [30]

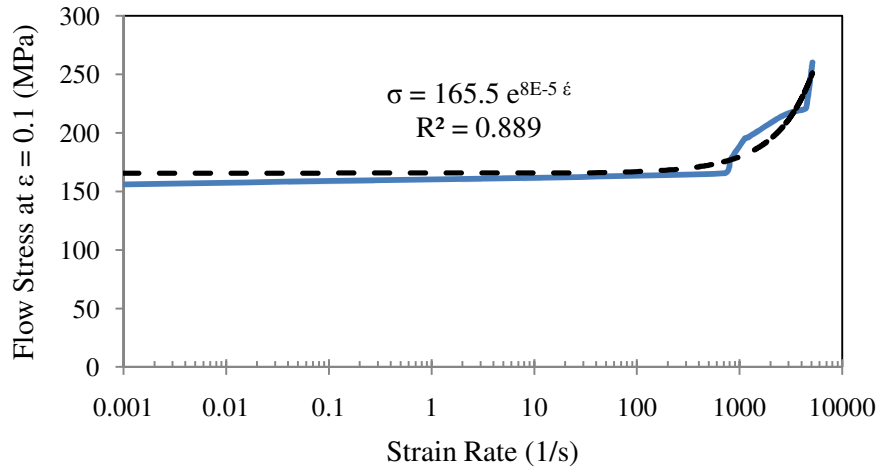


Fig. 5.4 Effect of strain rate on flow stress

5.2.2. Internal state variable (ISV) plasticity model

The ISV plasticity model developed by Bammann, Chiesa, and Johnson [29] introduces internal state variables to describe the deformation state of the material. The kinematics of the model is based on the multiplicative decomposition of the deformation gradient to elastic, deviatoric plastic, volumetric plastic (damage), and thermal portions. The constitutive model is formulated with respect to stress free configuration and can be written as follow for uniaxial tension and compression

$$\sigma = \alpha + \kappa + Y(\theta) + V(\theta) \sinh^{-1}(|\dot{\epsilon}|/f(\theta)) \quad (5.1)$$

$$\alpha = \sqrt{h \dot{\epsilon}/(r_d \dot{\epsilon} + r_s)} \tanh(\sqrt{h (r_d \dot{\epsilon} + r_s)/\dot{\epsilon}} \epsilon) \quad (5.2)$$

$$\kappa = \sqrt{H \dot{\epsilon}/R_d \dot{\epsilon} + R_s} \tanh(\sqrt{H \dot{\epsilon} (R_d \dot{\epsilon} + R_s)/\dot{\epsilon}} \epsilon) \quad (5.3)$$

Where $f(\theta)$ and $V(\theta)$ describe the rate dependence of the initial yield stress as a function of temperature θ . The evolution equations of internal state variables α and κ are motivated from dislocation mechanics. Dynamic recovery due to dislocation cross slip and thermal recovery due to diffusion controlled vacancy assisted climb of dislocations are taken into account in deriving the evolution equations. These equations are in hardening minus recovery format. α represents kinematic hardening and captures the softening effect, termed as Bauschinger effect, due to unloading. κ represents isotropic hardening and captures the continued hardening at large strains. The use of internal state variables and the evolution equations enable the prediction of strain rate history and temperature history effects as well.

The temperature dependence of the hardening and recovery functions results in the prediction of thermal softening during adiabatic temperature rises. The model has used nine

temperature dependent functions to describe the inelastic response. They can be classified into three groups. Those associated with the initial yield, the hardening functions, and the recovery functions. The rate-independent yield stress $Y(\theta)$, the rate-dependence of initial yield stress $f(\theta)$, and the magnitude of rate-dependence of yield stress $V(\theta)$ are assumed to be of the forms

$$V(\theta) = C_1 \exp(-C_2 / \theta) \quad (5.4)$$

$$Y(\theta) = C_3 \exp(C_4 / \theta) ([1 + (\tanh(C_{19}(C_{20} - \theta)))] / 2) \quad (5.5)$$

$$f(\theta) = C_5 \exp(-C_6 / \theta) \quad (5.6)$$

The three functions of $r_d(\theta)$, $h(\theta)$, and $r_s(\theta)$ describe the kinematic hardening and recovery, which can be thought of as the center of yield surface. The functions of $R_d(\theta)$, $H(\theta)$, and $R_s(\theta)$ describe the isotropic hardening and recovery, which can be thought of as the radius of the yield surface.

$$r_d(\theta) = C_7 \exp(-C_8 / \theta) \quad (5.7)$$

$$h(\theta) = C_9 - C_{10}\theta \quad (5.8)$$

$$r_s(\theta) = C_{11} \exp(-C_{12} / \theta) \quad (5.9)$$

$$R_d(\theta) = C_{13} \exp(-C_{14} / \theta) \quad (5.10)$$

$$H(\theta) = C_{15} - C_{16}\theta \quad (5.11)$$

$$R_s(\theta) = C_{17} \exp(-C_{18} / \theta) \quad (5.12)$$

The material constants (C_1 - C_{20}) in equations 5.1 to 5.12 are determined by fitting the ISV model to stress-strain data obtained from quasi-static and dynamic compression tests. A nonlinear square fitting technique is utilized to extract the parameters since it is difficult to find the twenty parameters of the ISV model simultaneously by conventional curve fitting techniques [33,34]. The fitting technique requires the material's test data in stress-strain format as the input along with the testing temperatures and strain rates. Material constants are estimated by fine tuning until the predicted stress-strain curves match the experimental ones. The fitted constants for Mg-Ca0.8 biomaterial are listed in Table 5.1. Since nonlinear square fitting technique gives a local rather than global optimum, another set of constants may be possible for this material. However, a very slight difference between different sets of material constants is expected since the residue (fitting error) was kept as small as possible. Nevertheless, the found set of material constants always represents the material properties with an acceptable accuracy.

Table 5.1 ISV material constants of Mg-Ca0.8 alloy at compression test mode

ISV parameter	Material constant	ISV parameter	Material constant
C1 (MPa)	0.5	C11 (s/MPa)	5.0×10^{-5}
C2 (K)	200	C12 (K)	0.0
C3 (MPa)	90	C13 (1/MPa)	0.1
C4 (K)	20	C14 (K)	0.0
C5 (1/s)	1.0×10^{-7}	C15 (MPa)	28000
C6 (K)	0.0	C16 (MPa/K)	0.0
C7 (1/MPa)	0.2	C17 (s/MPa)	500
C8 (K)	-300	C18 (K)	-850
C9 (MPa)	2000	C19	0.15
C10 (MPa/K)	0.0	C20 (K)	300

5.3. Simulation scheme of high speed dry cutting

It is fundamental to gain knowledge about field variables (i.e. temperature, stress, strain) distribution in order to obtain an understanding of metal cutting mechanics. Due to complex nature of metal cutting process, doing so would be very cumbersome if not impossible through measurements. In this context, finite element method is a powerful tool aiding researchers in metal cutting field. A finite element model is developed here to simulate chip formation process in high speed cutting of Mg-Ca0.8 alloy. The general purpose FE code ABAQUS is used to make the simulation more cost effective.

The developed FE mesh for orthogonal metal cutting process is shown in figure 5.5. Tool is assumed to be rigid and constrained to move horizontally at the specified cutting speed. Chip layer size is considered to be much smaller than the workpiece thickness in out of plane direction to facilitate the plane strain condition. Lower left and right edges of the workpiece are fixed in both directions. Bottom edge is modeled applying semi-infinite elements to avoid stress bounce back. Frictional contacts between tool/chip and tool/workpiece are modeled by the stick-slip friction model [35] in which frictional shear stress in sticking region approaches shear stress limit τ_{\max} . The friction coefficient is selected to be 0.1 in the sliding region due to the low chemical affinity between PCD tools and Mg alloys.

The chip layer (depth-of-cut) is modeled by 20 layers of elements and the rest of workpiece by 27 layers, each having 200 elements along the cutting path. Workpiece has 1200 μm height and 3000 μm length. The length is sufficient to reach the steady state condition before cutting tool passes the left edge. A varying mesh density is used around the cutting edge to accommodate for the size effect and severe deformation gradient. Since PCD tool is much harder

than Mg alloys, it is modeled as a rigid surface. The cutting edge radius r is $10\ \mu\text{m}$ representing a sharp cutting edge. Rake angle α and clearance angle λ are 12° and 6° , respectively.

The ISV plasticity model of Mg-Ca0.8 alloy was implemented in the simulation via modified user defined subroutine VUMAT. Thermal expansion, specific heat, and mass density are $26\ \mu\text{m}/\text{m.K}$, $1010\ \text{J}/\text{kg.K}$, $1750\ \text{kg}/\text{m}^3$, respectively. In metal cutting, heat is generated due to plastic work done in the primary and secondary shear zones. During high speed machining of Mg-Ca0.8 alloy with PCD tool, heat generated due to local energy dissipation can cause local heating in the active plastic zones and along the sliding frictional interface before diffusing away. The temperature rise in the chip due to this fact can be approximated with the adiabatic heating condition. In this study, the percentage of plastic and frictional work transformed into heat is taken as 90% and is assumed that all the generated heat stays the chip.

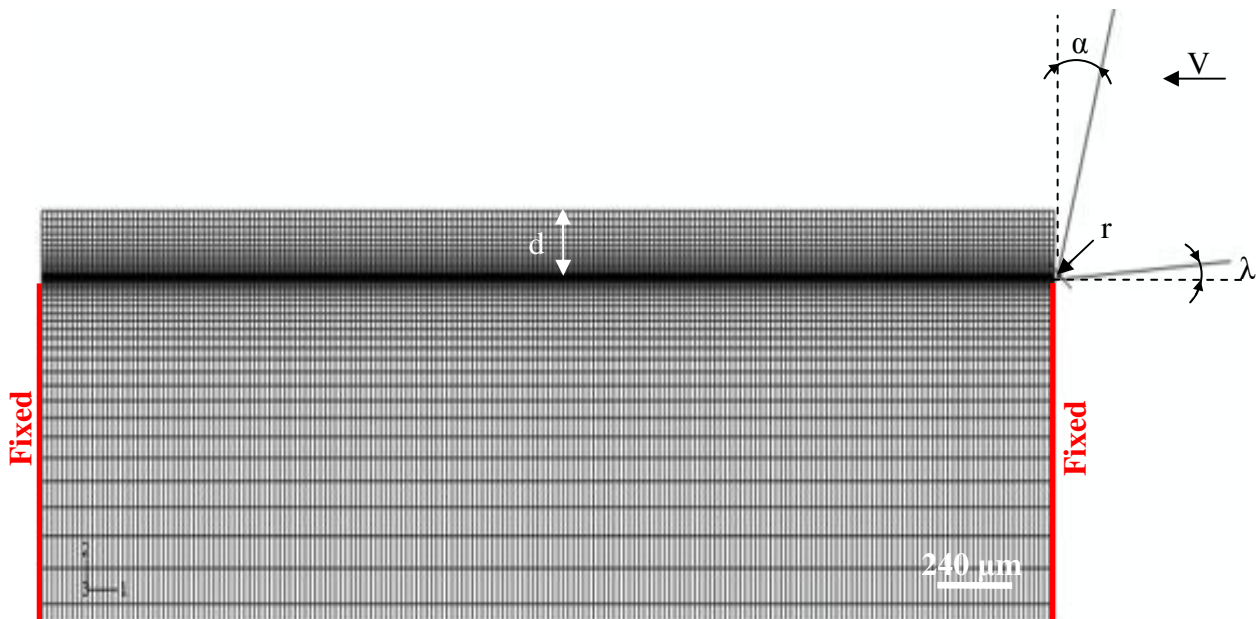


Fig. 5.5 FE mesh of chip formation simulation in orthogonal cutting of Mg-Ca0.8 alloy

A total of five simulation cases have been performed covering five cutting speeds of 1200, 1600, 2000, 2400, and 2800 m/min at 200 μ m depth-of-cut. This allows for a parametric evaluation of the effects of cutting speed on temperature, stress, and strain fields. Steady state cutting was ensured for each simulation case by tracing the cutting forces.

5.4. Cutting experiments

5.4.1. Material

The material used in this study is magnesium-calcium alloy with 0.8 weight percent calcium (Mg-Ca0.8). This binary alloy is not commercialized and is custom made for research purposes. Different researchers have tried to experiment different concentrations of Ca and they have found Mg-Ca0.8 very promising for biomedical applications through in-vitro and in-vivo tests [7,8,10,28]. The Mg-Ca0.8 alloy was prepared with the procedure explained in section 3.3.1. The hardness of ground and polished cylindrical samples with mirror surface finish was measured to be 42 HV.

5.4.2. Experimental setup and test plan

The experimental setup explained in section 3.3.2 and shown in figure 3.2 was utilized for this investigation. A set of experiments were planned to study the effect of cutting speed in high speed dry face milling of Mg-Ca0.8 samples with the PCD tipped inserts. The cutting speed varies in the range of 1200 – 2800 m/min (Table 5.2).

Table 5.2 Cutting parameters used in numerical/experimental study

Cutting speed [m/min]	Feed [mm/rev]	Depth of cut [mm]
1200	0.2	0.2
1600	0.2	0.2
2000	0.2	0.2
2400	0.2	0.2
2800	0.2	0.2

5.5. Results and discussions

5.5.1. Cutting forces

Time histories of cutting and thrust force variations are shown in figures 5.6a and 5.7a. Both force components increase rapidly and become stable about a mean value in first few seconds of the simulation. Therefore, steady state cutting is secured. Cutting forces are affected by two opposing mechanisms during cutting process: work hardening and thermal softening. Indeed, these mechanisms influence the resistance of material against plastic deformation. Work hardening is due to decreased mobility of dislocations under progressive plastic deformation. Thermal softening is caused by heat generation from plastic and frictional works. Hence, while one mechanism hardens the material, the other softens it and the balance between these mechanisms will determine the resultant cutting forces.

Higher cutting speed is parallel to faster material deformation and higher strain rate in the cutting zone. Work hardening and thermal softening effects become stronger under higher strain rates. However, making any prejudgment about the way cutting forces will change with the cutting speed can be erroneous by considering hardening and softening effects separately.

Numerically computed cutting and thrust forces in figures 5.6b and 5.7b show that increasing cutting speed in 1200 to 2800 m/min range has a slight increasing effect on both force components. Observed force fluctuations presented by error bars in figures 5.6b and 5.7b could be due to temperature fluctuations caused by highly distorted elements during chip formation progress and their deletion.

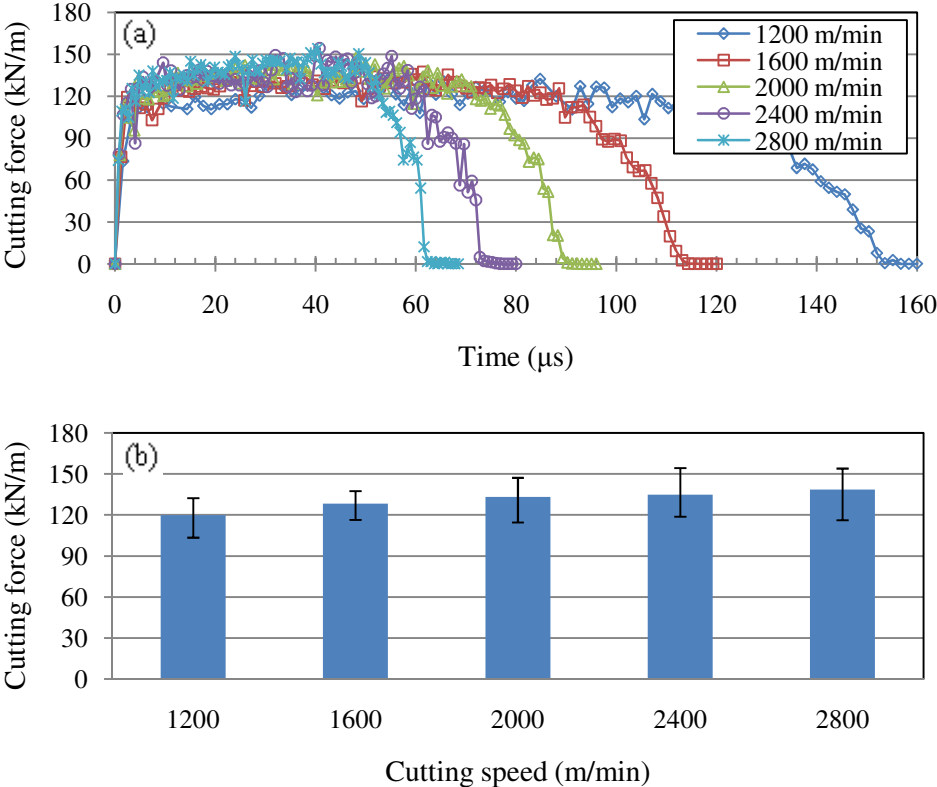


Fig. 5.6 Effect of cutting speed on cutting force: (a) time history, (b) bar chart

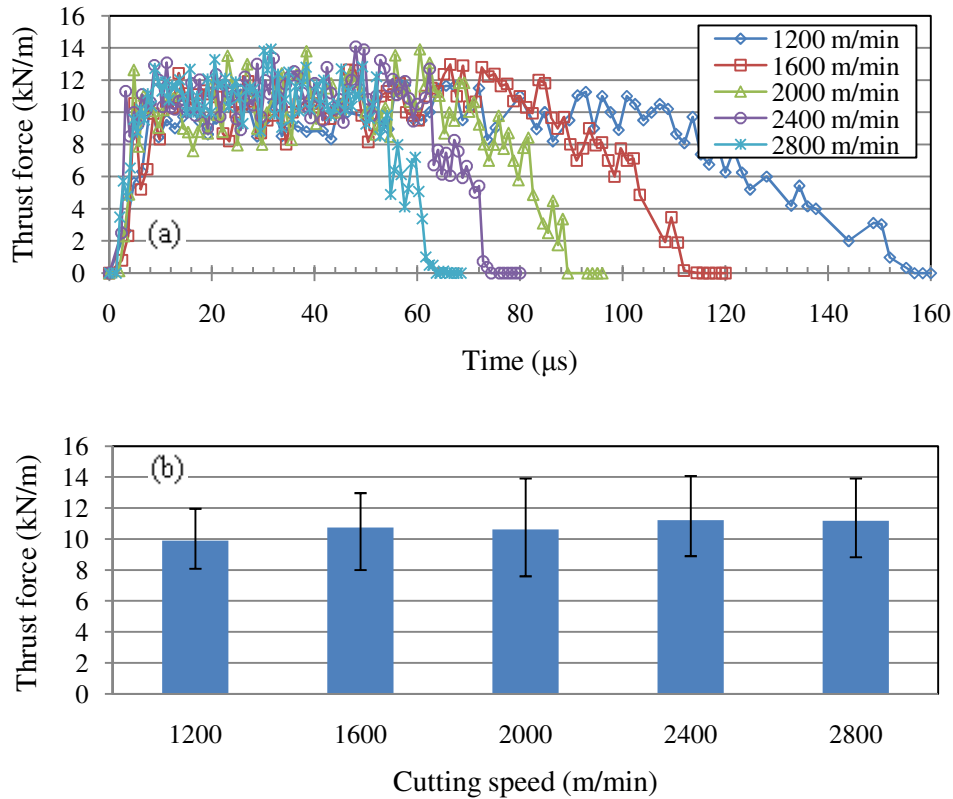


Fig. 5.7 Effect of cutting speed on thrust force: (a) time history, (b) bar chart

5.5.2. Temperature distribution and chip morphology

Temperature contours are shown in figure 5.8. There are two factors which should be considered in studying these contour plots: the size of the area covered with certain temperature and the temperature itself. It is noticeable that the predicted maximum temperature is close to 600 °C (melting point of Mg) in all simulation cases. It should be pointed out that heat conductions between the tool/workpiece and workpiece/environment were not incorporated, the predicted temperatures would be the upper bound of machining temperatures in practice at the

cutting conditions. It implies that material melting and chip ignition would not happen for the concerned machining conditions.

The maximum temperature occurs on the back face of the formed chip in the vicinity of the tool rake face. Temperature drops rapidly to about 450 °C in moving 1 μm towards the opposite face of the formed chip as is shown in temperature gradients of figure 5.8. That is only 0.5% of the formed chip thickness and rest of the chip stays between 150 °C to 450 °C during cutting. Therefore, 99.5% of the formed chip remains in solid state during cutting since eutectic temperature of Mg-Ca_{0.8} alloy is 516.6 °C [36]. This predicts that no chip ignition and fire hazard will occur in cutting Mg-Ca_{0.8} alloy since Mg chips will ignite if the melting point is exceeded throughout the chip volume. This is confirmed experimentally since no spark or chip ignition happened during cutting.

The observed random void marks on back face of the chips (figure 5.9a) shows the effect of bulk material voids on chip surface. If they are indeed the melting marks, then the whole region instead of those occurring at scattering spots should show similar voids because the temperature at the back face is the more or less the same. An examination on the machined chips shows that the random void marks appear only on very few chips produced not by highest cutting speed. In addition, no BUE was found at the concerned machining conditions. Since the bulk material has large grain size and random voids, it is believed that the void marks on the chips are just random material voids instead of melting marks.

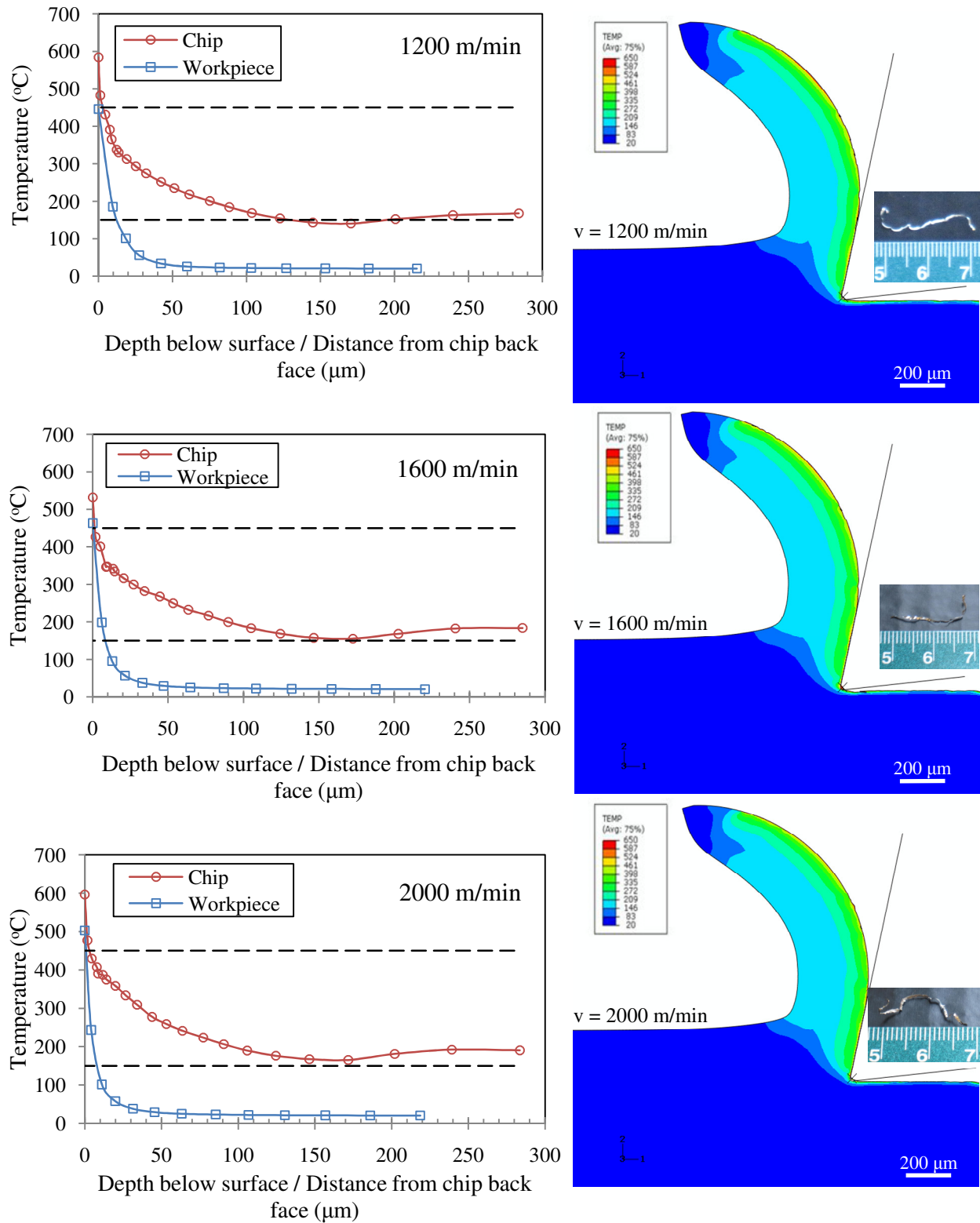


Fig. 5.8 Effect of cutting speed on chip morphology and temperature distributions

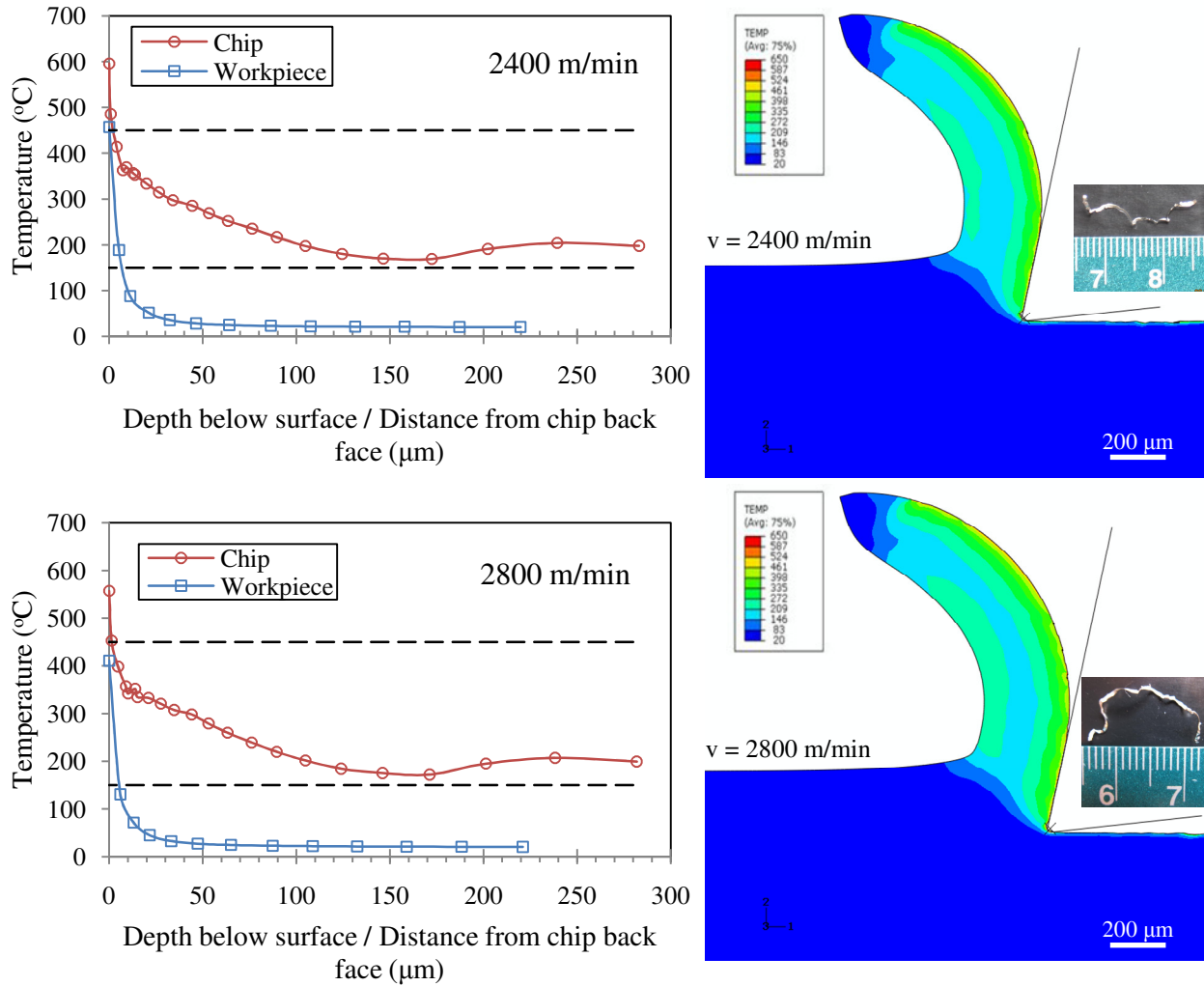


Fig. 5.8 (Contd.) Effect of cutting speed on chip morphology and temperature distributions

Sporadic deterioration on machined surface (figure 5.9c) was also observed on a few locations on the machined surfaces. But the sporadic deterioration is not melting marks but adhered tiny chips momentarily smeared by the tool cutting. If it is the local surface adhesion on the machined surface due to temporary FBU formation as described in the paper, then it is expected to observe very rough surface before the occurrence of FBU adhesion because of the

cyclic formation nature of FBU. The FBU will abrade machined surface before it is torn away from the tool flank, the surface becomes very rough as a result. But the rough and not uniform surface around the sporadic deterioration marks is not observed in figure 5.9b. An examination on the tool flank face (figure 5.9d) shows residues of the smeared tiny chips (not BUE) which support the explanation of momentary smearing of chips on the machined surface.

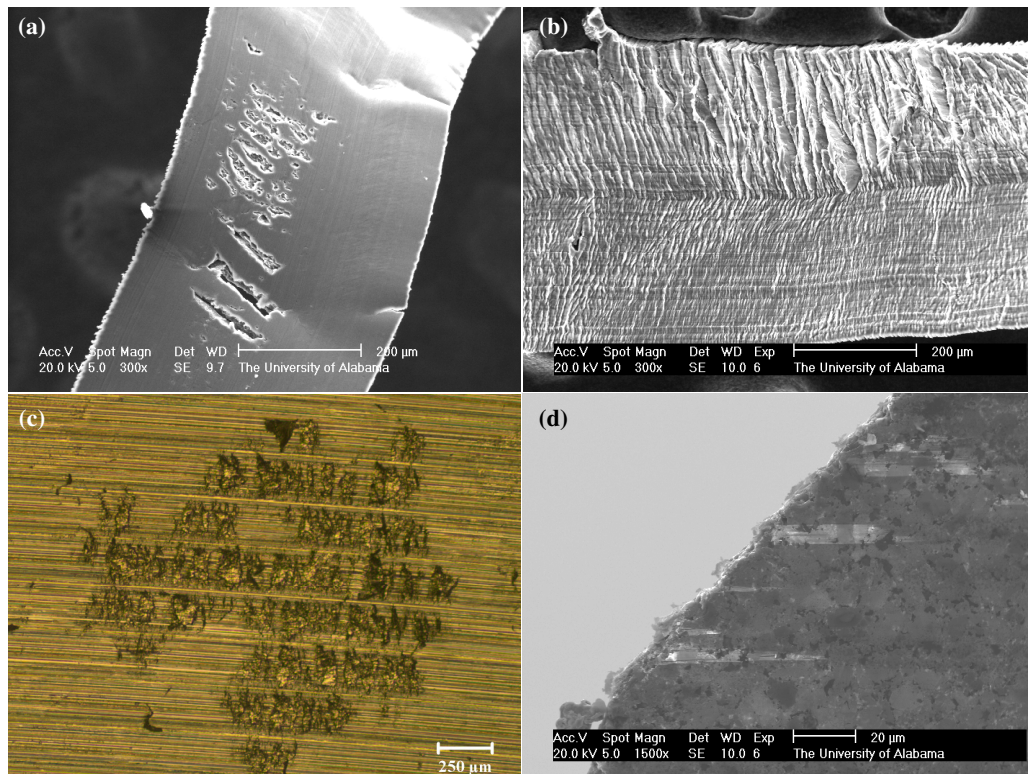


Fig. 5.9 (a) Influence of random material voids on chip back face; (b) Chip morphology; (c) Random surface deterioration due to chip adhesion; (d) slight chip adhesion on tool flank face

The presence of primary and secondary shear zones is well predicted in this simulation. In the primary shear zone, the temperature is close to 110 °C whereas in the secondary zone it is around 450 °C. This verifies the fact that in the secondary zone at the tool/chip interface, the

material experiences more severe deformation and, therefore, higher temperature. It is also predicted in figure 5.8 that chip formation in high speed cutting of Mg-Ca0.8 alloy will be continuous which is in agreement with experimental observations. Moreover, the transient temperature gradient in workpiece is predicted to start at about 450 °C on machined surface and to cool down to 20 °C at depth 50 μm.

5.5.3. Stress distribution

Contour plots of von Mises stress are shown in figure 5.10 where the unit for stress is Pa. Plastic flow behavior can be studied from von Mises stress distribution. It is visible that stress contours in the chip ahead of the tool tip have the highest values and are aligned in a left forward direction forming the primary “shear” zone. Shear zone is assumed to be a thin straight plane in classical theory of cutting [37], however, in practice [38-41] and as is predicted here, plastic deformation deviates from this assumption and shear happens in a zone thicker than the ideal shear plane. In cutting soft materials like Mg-Ca0.8 (42 HV), the shear zone will tend to be pie-shaped as shown in figure 5.11. Shaw [38] has implemented the geometrical approach, illustrated in figure 5.11, to measure a definite shear angle in such cases. The equivalent shear angle defined in this way is claimed to represent a good first approximation. The equivalent shear angle calculated by the explained method and from the contour plots of figure 5.10, is 40.2°. Knowing rake angle (12°), depth-of-cut (200 μm), and chip thickness (270 μm) from contour plots, the Merchant’s shear angle is calculated to be 40.6° which is in good agreement with calculated equivalent shear angle. For any rake angle, there is a shear angle at which the mean chip thickness is equal to the undeformed chip thickness. For 12° rake angle case, this occurs at about 51° [39,41].

Typical values of shear angle found in machining many other metals are between 10° to 35° [41]. There are two possible explanations for the shear angle (40°) being out of this range in this study. First is the friction at tool/chip interface. When tool face friction is decreased there is a corresponding increase in shear angle and an accompanying decrease in the thickness of the chip. This is the case in this study and PCD inserts are used deliberately with the knowledge that there is low chemical affinity between the two materials and consequently low friction. Second is the property of the work material. Different ductility in materials will bring about different shear angles in their cutting processes. For example, the chip thickness ratio is low in cutting copper, the shear angle is small, and the chip moves slower on the rake face while in cutting aluminum alloys larger shear angle and consequently thinner, and faster moving chip exists [39]. Back to figure 5.10, The peak stress contour initiates from the point ahead of the cutting edge and ends on the free surface of the pie-shaped shear zone. The comparison between figures 5.8 and 5.10 shows that the peak contour occurs in the same region as low temperature contour of 110°C . This means thermal softening in the primary shear zone is not significant. In addition, the peak stress contour region gets wider by increasing cutting speed.

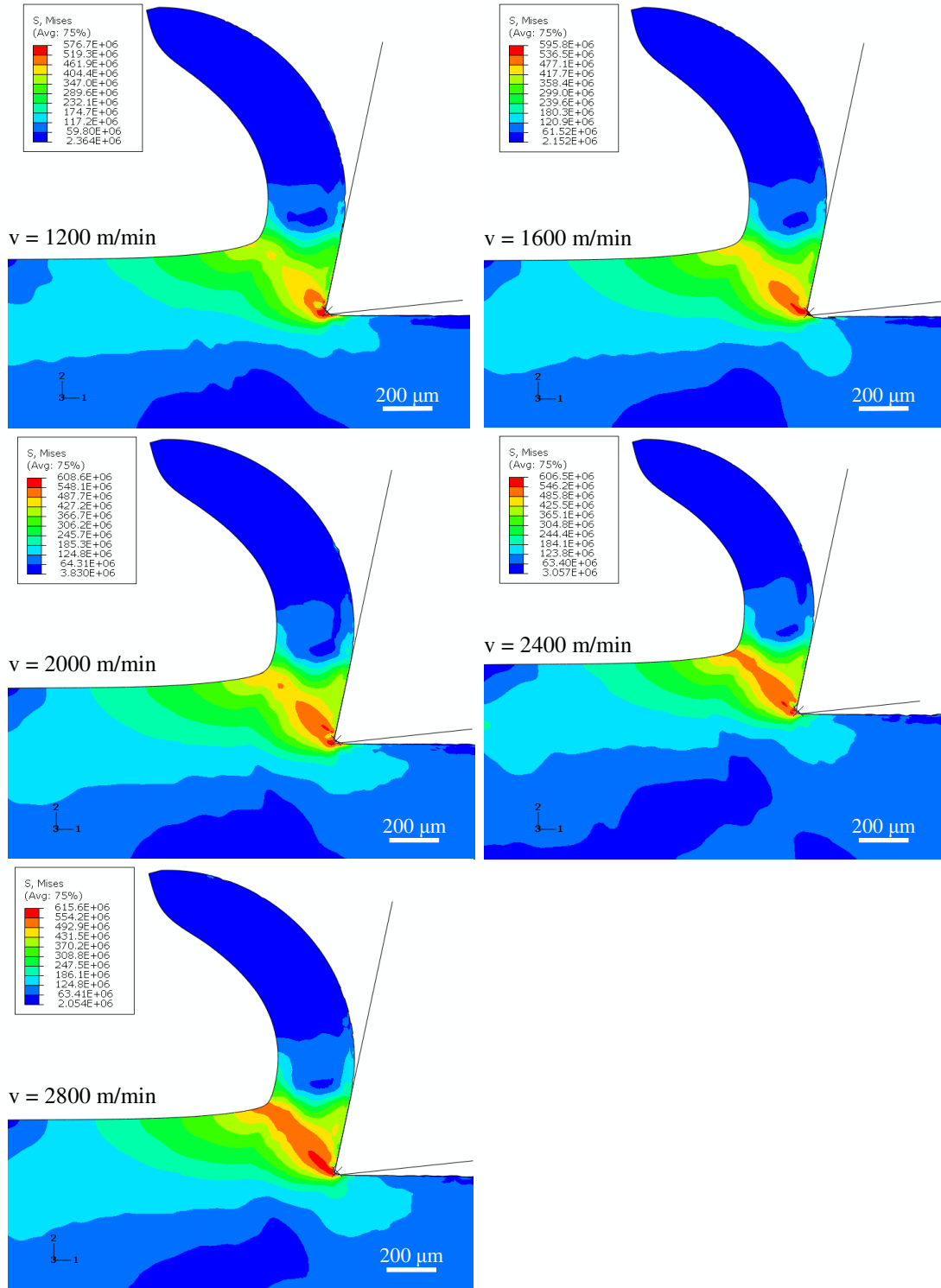


Fig. 5.10 Effect of cutting speed on von Mises stress contour

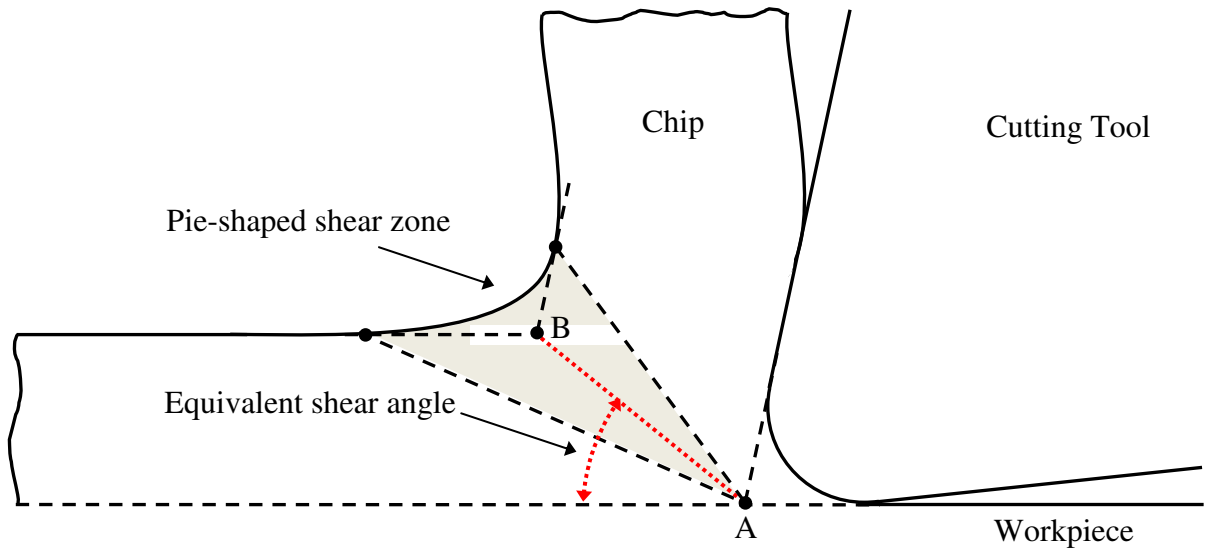


Fig. 5.11 Pie-shaped shear zone in cutting soft materials and equivalent shear plane (AB)

5.5.4. Strain distribution

The contours of equivalent plastic strain (PEEQ) are shown in figure 5.12. Comparing figures 5.8 and 5.12 shows that regions of high plastic deformation are consistent with high temperatures. This is in accordance with the classical understanding of metal cutting that the larger the plastic deformation, the more the dissipated energy as heat. It is also observed that equivalent plastic strain in the secondary shear zone is much larger than plastic strain in the primary shear zone.

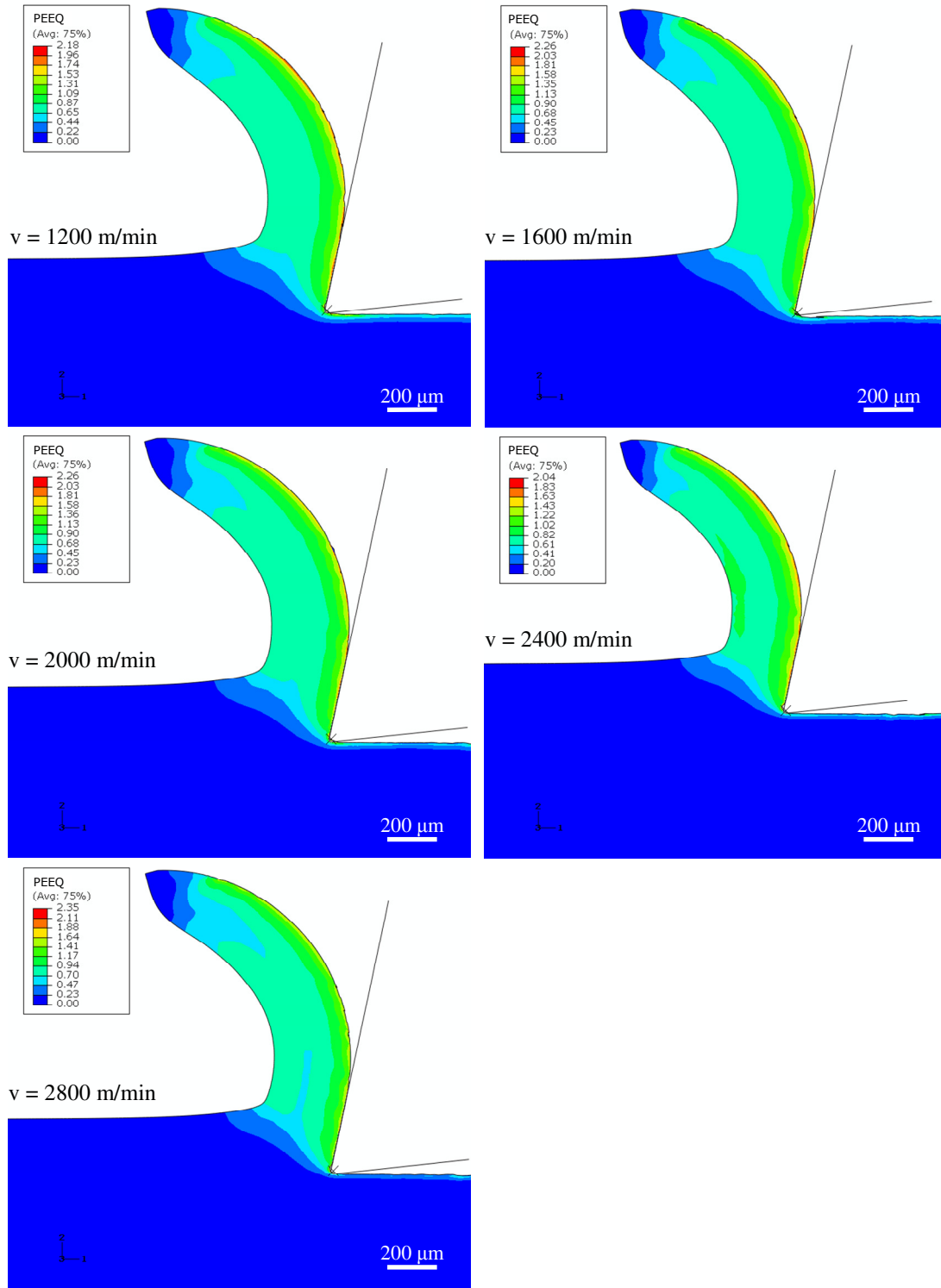


Fig. 5.12 Effect of cutting speed on equivalent strain (PEEQ) contour

5.6. Conclusions

A finite element analysis model has been developed to study the cutting mechanics of a novel Mg-Ca biomaterial under high speed regime. Complex mechanical behavior of the biomaterial during cutting was incorporated into FE simulations utilizing internal state variable (ISV) plasticity model. ISV material parameters were extracted by fitting the ISV model to a set of experimental data from quasi-static and dynamic SHPB tests. Followings are the conclusions of this study:

- Work hardening effect of strain rate on stress-strain of Mg-Ca_{0.8} is not considerable until above 600/s strain rate. Small strain measurements (up to 3% strain) in SHPB test are not stable due to non-equilibrium condition.
- The predicted continuous chip is consistent with the experimental observation.
- It is predicted that only 1 μ m (~0.5%) of the formed chip thickness will be above eutectic line (516.6 °C) in high speed cutting of Mg-Ca_{0.8} alloy.
- Chip ignition and sparks did not happen in high speed dry cutting of Mg-Ca_{0.8} alloy. The numerical predictions suggest that the chip volume stays in solid state during cutting considering heat conduction to the environment and within the workpiece.
- Sporadic void marks on the chip back face are due to the porosity of the bulk material, while the random surface deterioration on machined surfaces is as result of smearing of tiny chips by the cutting tool.
- Peak stress contour region (primary shear zone) becomes wider by increasing cutting speed. Thermal softening in the primary shear zone is not significant.

- Equivalent plastic strain and temperature is much larger in the second shear zone than the primary zone. This is aligned with classical understanding that the larger the plastic deformation, the more the dissipated energy as heat.

References

1. A. Gefen, Computational simulations of stress shielding and bone resorption around existing and computer-designed orthopaedic screws, *Medical & Bio. Eng. & Comp.* 40 (2002) 311-322.
2. J. Nagels, M. Stokdijk, P.M. Rozing, Stress shielding and bone resorption in shoulder arthroplasty, *J. Shoulder and Elbow Surgery* 12 (2003) 35-39.
3. H. Isaksson, A.L. Lerner, Mathematical modeling of stress shielding with bioresorbable materials for internal fracture fixation, *Bioengineering Conf.* (2003) 1041-1042.
4. H.G. Seiler, *Handbook on toxicity of inorganic compounds*, 1st edition, CRC Press (1987).
5. G. Song, Control of biodegradation of biocompatible magnesium alloys, *Corrosion Science* 49 (2007) 1696-1701.
6. G. Song, S. Song, A possible biodegradable magnesium implant material, *Adv. Eng. Mater.* 9 (2007) 298-302.
7. Z. Li, X. Gu, S. Lou, Y. Zheng, The development of binary Mg-Ca alloys for use as biodegradable materials within bone, *Biomaterials* 29 (2008) 1329-1344.
8. B. Denkena, F. Witte, C. Podolsky, A. Lucas, Degradable implants made of magnesium alloys," *Proc. 5th Euspen Int. Conf.*, Montpellier, France (2005).
9. Y.B. Guo, M. Salahshoor, Process mechanics and surface integrity by high speed dry milling of biodegradable magnesium-calcium implant alloys, *Ann. CIRP* 59 (2010) 151-154.
10. N. Von Der Hoh, D. Bormann, A. Lucas, B. Denkena, C. Hackenbroich, A. Meyer-Lindenberg, Influence of different surface machining treatments of magnesium-based resorbable implants on the degradation behavior in rabbits, *Adv. Eng. Mater.* 11 (2009) B47-54.

11. M. Videm, R.S. Hansen, N. Tomac, K. Tonnesen, Metallurgical considerations for machining magnesium alloys, SAE Trans. 103 (1994) 213 – 220.
12. G. Byrne, D. Dornfeld, B. Denkena, Advancing cutting technology, Ann. CIRP 52 (2003) 483 – 507.
13. B.D. Danilenko, Selecting the initial cutting parameters in machining magnesium alloys, Russian Eng. Research 29 (2009) 316 – 318.
14. D.L. Hallum, Magnesium: lightweight, easy to machine, American Machinist 139 (1995) 48 – 51.
15. T. Friemuth, J. Winkler, Machining of magnesium workpieces, Adv. Eng. Mater. 1 (1999) 183 – 186.
16. J. Schmidt, J. Winkler, Machining of magnesium castings, Aluminium 74/6 (1998) 412 – 417.
17. C. Sanz, E. Fuentes, F. Obermair, L. Muntada, Efficient and ecological machining of magnesium hybrid parts, Proc. 7th Int. Conf. Mg Alloys & Their App. (2007) 916 – 921.
18. R. Schwerin, S. Joksch, Experiences with the machining of magnesium, Proc. 7th Int. Conf. Mg Alloys & Their App. (2007) 922 – 925.
19. B. Denkena, J.C. Becker, C. Podolsky, A. Kuhlmann, Safe machining of magnesium parts by cutting and burnishing operations, Proc. 7th Int. Conf. Mg Alloys & Their App. (2007) 895 – 901.
20. N. Tomac, K. Tonnesen, Formation of flank build-up in cutting magnesium alloys, Ann. CIRP 40/1 (1991) 79 – 82.
21. M. Salahshoor, H. Ahmadian, Continuous model for analytical prediction of chatter in milling, Int. J. of Machine Tools and Manufacture 49 (2009) 1136 – 1143.
22. H.K. Tönshoff, J. Winkler, The influence of tool coatings in machining of magnesium, Surface and Coatings Tech. 94-95 (1997) 610 – 616.
23. H.K. Tönshoff, T. Friemuth, J. Winkler, C. Podolsky, Improving the characteristics of magnesium work pieces by burnishing operations, Mg Alloys & Their App. (1999) 406 – 411.
24. W. Pedersen, M. Ramulu, Facing SiCp/Mg metal matrix composites with carbide tools, J. of Materials Processing Tech. 172 (2006) 417 – 423.
25. H.K. Tönshoff, J. Winkler, C. Gey, Machining of light metals, Mat.-wiss. u. Werkstofftech 30 (1999) 401 – 417.

26. M. Salahshoor, Y.B. Guo, Numerical modeling and simulation of high speed machining biomedical magnesium calcium alloy, Proc. of ASM MPMD (Materials & Processes for Medical Devices) Conference and Exposition, Minneapolis, MN (2009).
27. F.Z. Fang, L.C. Lee, X.D. Liu, Mean flank temperature measurement in high speed dry cutting of magnesium alloy, J. of Materials Processing Tech. 167 (2005) 119 – 123.
28. B. Denkena, A. Lucas, Biocompatible magnesium alloys as absorbable implant materials-adjusted surface and subsurface properties by machining processes, Ann. CIRP 56 (2007) 113-116.
29. D.J. Bammann, M.L. Chicsa, G.C. Johnson, Modeling large deformation and failure in manufacturing processes, Theor. App. Mech. (1996) 359-376.
30. V.S. Brooks, An experimental study on the mechanical properties and microstructures of biodegradable magnesium-calcium alloy, M.Sc. Thesis, The University of Alabama, Alabama, USA (2009).
31. B.A. Gama, S.L. Lopatnikov, J.W. Gillespie Jr, Hopkinson bar experimental technique: a critical review, Appl. Mech. Rev. 57 (2004) 223-250.
32. E.D.H. Davies, S.C. Hunter, The dynamic compression testing of solids by the method of split Hopkinson pressure bar (SHPB), J. Mech. Phys. Solids 11 (1963) 155-179.
33. J.F. Lathrop, BFIT-A program to analyze and fit the BCJ model parameters to experimental data, SANDIA Labs Report, SAND97-8218 (1996).
34. Y.B. Guo, W. Wen, M.F. Horstemeyer, An internal state variable plasticity based approach to determine loading history effects in manufacturing processes, Int. J. Mech. Sci. 47 (2005) 1423-1441.
35. Y.B. Guo, C.R. Liu, 3D FEA modeling of hard turning, J. Manuf. Sci. Eng. 124 (2002) 189-199.
36. T.B. Massalski, Binary alloy phase diagrams, ASM International (1990) 927-928.
37. M.E. Merchant, Mechanics of the metal cutting process. I. orthogonal cutting and a Type 2 chip, J. Appl. Phys. 16 (1945) 267-275.
38. M.C. Shaw, Metal cutting principals, Clarendon Press, Oxford (1984) 18-46.
39. E.M. Trent, P.K. Wright, Metal cutting, 4th ed., Butterworth-Heinemann, Boston (2000) 12-30.
40. S. Kalpakjian, S.R. Schmid, Manufacturing engineering and technology, 4th ed., Prentice Hall, New Jersey (2001) 537-544.

41. J.T. Black, Mechanics of chip formation, ASM Handbook Vol. 16, Machining, ASM Int., Materials Park, OH (2000) 5-10.

CHAPTER 6

COMPUTATIONAL MODELING AND EXPERIMENTAL STUDY OF RESIDUAL STRESSES IN HIGH SPEED MACHINING OF BIODEGRADABLE MAGNESIUM-CALCIUM ALLOY

Abstract

Magnesium-Calcium alloys have become attractive biodegradable orthopedic biomaterials recently. Residual stresses are proven to be very influential on degradation rate of these alloys in human anatomy. Due to time and cost inhibitive reasons, development of finite element models to predict residual stress profiles under various cutting regimes is highly desirable. In this context, a finite element model of orthogonal cutting without explicit chip formation is developed by adopting plowing depth approach in order to predict process induced residual stresses in high speed dry cutting of MgCa0.8 using diamond tools. Mechanical properties of Mg-Ca0.8 biomaterial at high strain rates and large strains are determined using split-Hopkinson pressure bar test. Internal state variable (ISV) plasticity model is implemented to model the material behavior under cutting regimes. The residual stress evolution process and effects of plowing speed and plowing depth on residual stress profiles are studied. Residual stress measurements are performed utilizing X-ray diffraction technique for validation purposes.

6.1. Introduction

The in-service performance of machined components substantially depends on *surface integrity*, particularly residual stresses at or near the machined surface. Residual stresses directly influence deformation, static and dynamic strength, chemical resistance, electromagnetic, optical, acoustical, and thermal properties of mechanical and electrical components [1]. They are generated by individual or combined effects of mechanical, thermal, and metallurgical impacts in machining processes. Machining process parameters determine the intensity of the mentioned impacts and ultimately the magnitude, penetration depth, profile shape, and type of the induced residual stresses. Therefore, understanding the correlation between process parameters and induced residual stresses is a fundamental step towards realizing the manufacturing for performance concept. However, measuring a residual stress profile using popular x-ray diffraction technique normally takes hours to be accomplished even with the utilization of computerized systems, the slope method for material removal, and position sensitive detectors (PSDs) for capturing diffracted x-rays. In an effort to study process parameter-residual stress correlations more economically and efficiently, researchers have sought to develop predictive models to calculate induced residual stress profiles in machining processes since three decades ago.

Sasahara et al [2] studied the effect of cutting sequence from roughing to finishing on residual stress and strain, cutting forces, and shear angle using finite element method. They found that tensile residual stress layer made by one pass roughing (250 μm depth of cut) is removed by subsequent fine machining pass (100 μm depth of cut) and compressive stress replaces tensile stress at the surface. Adding two more fine machining passes caused surface layer to become tensile again, shear angle to decrease, and cutting forces to increase. Effects of

temperature and strain rate which are important factors in determining residual stresses were neglected.

Liu and Guo [3] investigated the effect of sequential cuts and tool-chip friction on residual stresses in a machined layer. Physical state of the machined layer after first cut, i.e. residual stresses and strains, was applied as initial condition for the second cut. The work hardening caused by the first cut had significant effect on the residual stress distribution in the second cut. Tensile residual stresses from the first cut became more compressive after second cut. Moreover, the work hardening from the first cut caused slight increase in shear angle and decrease in chip thickness. However, no significant change in cutting and thrust forces was observed between the two cuts. Residual stress predictions were sensitive to friction modeling and higher friction coefficients at tool-chip interface resulted in more compressive residual stresses [4].

Jacobus et al [5] developed a plane strain thermoelastoplastic model of metal flow under the flank of the cutting tool to predict the full in-plane biaxial residual stress profiles existing at and beneath the newly formed surface. They utilized two coordinate systems to understand the differences in the residual stress profiles in orthogonal and oblique cutting. Inclination angle showed significant effect in the workpiece coordinate frame. However, no significant effect of inclination angle was evident in tool coordinate system. Measured normal stresses were tensile at the surface and dropped down to a compressive state with increasing depth into the material regardless of tool or workpiece coordinate system. The presented thermomechanical rationale indicated that the observed profiles were the result of both thermal and mechanical mechanisms. The thermal mechanism led to the development of tensile residual stresses in the heat affected zone (HAZ) layer and the mechanical mechanism led to tensile plastic deformation below HAZ

layer. Compressive plastic strains in HAZ layer result in tensile residual stresses in that layer, and vice versa. Tool edge and normal to tool edge directions turned out to be principal directions for residual stresses in tool coordinate system regardless of inclination angle of the cutting edge with respect to the feed direction. Later, Jacobus et al [6] extended this model to accommodate for the more complex process geometry associated with turning and the three dimensional nature of thermal conduction in turning. Both prediction and experiment showed that increase in feed and depth of cut lead to increase in workpiece temperatures and, subsequently, to increase in the tensile character of the residual stresses at and near the surface.

Sasahara et al [7] modeled the face turning operation too. This process is three-dimensional in nature due to involvement of the tool nose. They combined residual stress predictions of the conventional orthogonal cutting model with those of a plane strain indentation model, in which tool nose indents the workpiece, to account for three dimensional nature of the face turning. They used the proposed combined model as a first approximation to evaluate the effects of cutting conditions on surface residual stresses. Both numerical and experimental results showed that nose radius and feed rate significantly affect surface residual stresses while the effect of depth of cut is negligible.

Zong et al [8] accounted for thermal influence of the diamond tool in their orthogonal turning model. They considered the generated heat from both friction and plastic deformation in their model. Heat transfer was handled through conduction and convection, however, radiation was neglected in their coupled thermal mechanical analysis. They also found that the tool edge geometry is the dominant factor affecting the residual stresses. Outeiro et al [9] developed a three-dimensional finite element model for turning operation. The difference between prediction and measurement for cutting force was less than 5%, however, the predicted feed and radial

forces were significantly different from measured values. They did not use their model to predict residual stresses.

Schulze et al [10] investigated the influence of the cutting edge radius on residual stresses using an orthogonal model for micro-cutting. The chip formation process was incorporated into the model by continuous remeshing. Surface residual stresses were overestimated by about 50% for all the investigated cutting edge radii. This nonconformity was partly attributed to short cutting length in the model and its subsequent influence on temperature distribution.

Ee et al [11] used a remeshing scheme in their orthogonal cutting model to simulate material flow in the vicinity of the rounded cutting edge without the use of a separation criterion. In this model, the viscoplastic material is allowed to deform and flow around the tool tip to form the chip and the machined surface. Applying chip-workpiece separation criterion is a major weakness of FE models developed to calculate residual stresses in the machined surface because it drastically alters the deformation process near the tool tip [3,11]. Strenkowski and Carroll [12] introduced an effective plastic strain based chip separation criterion and found that variation of the threshold for effective plastic strain causes change in the residual stresses. Caruso et al [13] used a stress based criterion. They defined a bonded contact interface between the chip layer and the workpiece as initial condition. Chip separation achieved when the local stress at specified distance ahead of the tool tip along the chip-workpiece interface reached the specified critical value. The predicted surface residual stresses were smaller than measured values by this model.

So far, all the numerical studies have included chip formation process and very often the chip is left on the model during the cool down or relaxation phase before extracting residual stress profiles. However, machined surfaces are without chips in practical cases. In order to avoid the possible thermo-mechanical influence of the chip on residual stresses, the overall

dimensions of the finite element model should be considered larger to compensate for those effects. On the other hand, very fine mesh around the cutting edge and machined surface is required to provide adequate spatial resolution in order to capture sharp strain, strain rate, temperature, and residual stress gradients. Inconsistency in spatial resolution has caused seemingly contradictory results in numerical/experimental studies of residual stresses in the past [9]. Larger and more refined models translate into more digital storage, computational time, and expensive simulations. Guo et al [14] proposed a new modeling approach without chip formation based on the concept of plowed depth. This approach avoids the severe element distortion inherent in traditional cutting models with chip formation, does not require a chip separation criterion, and provides enough spatial resolution to capture sharp deformation gradients. Meanwhile, it still reflects the realistic stagnation phenomenon (section 3) in cutting. This modeling approach is adopted in the present study.

Previous studies have shown that residual stress state after cutting is strongly influenced by material properties [10]. For instance, a higher initial yield strength results in more compressive residual stresses while higher strain hardening leads to more tensile residual stresses at the surface. Therefore, separate studies are needed to investigate the material specific residual stress state after cutting. Magnesium-calcium (Mg-Ca) alloys have emerged as very appealing biomaterials recently particularly for orthopedic applications [15,16]. As compared to currently available orthopedic materials, they do not cause stress shielding, there is no need for second surgeries to excise them since they are both biodegradable and biocompatible, and they have enough mechanical strength to be used in load carrying applications. However, these alloys degrade quickly in body environment and there is a dire need for alternatives to control their degradation rate. Denkena and Lucas [17] were able to decrease this rate by a hundred times

using machining to adjust surface integrity particularly residual stresses. In this context, it is critical to develop numerical models which can predict residual stresses under various machining conditions in order to facilitate development of these novel biodegradable materials.

The objective of this study is to predict process-induced residual stress profiles in cutting novel Mg-Ca_{0.8} biomaterial using FEA method. To meet this objective: (i) an FE model without explicit chip formation is developed; (ii) an internal state variable plasticity model is implemented to enhance the capability for predicting mechanical behavior of the material under prevalent cutting regimes; (iii) residual stress measurements are performed for validation purposes. Moreover, noticing the difficulty of some parametric evaluations experimentally, the effects of plowing speed and plowing depth on residual stress profiles are studied using the developed FE model.

6.2. Materials model

Workpiece material usually experiences large strains, high strain rates, high temperatures, Bauschinger effect, and complex loading histories throughout a cutting operation at various length scales. A dislocation based internal state variable (ISV) plasticity model developed by Bammann et al [18] and explained in section 5.2.2 is used to describe the complex thermomechanical deformation state of the material.

6.3. Residual stress prediction model

Guo et al [14] introduced a novel hybrid modeling approach without explicit chip formation to predict cutting-induced residual stresses. This modeling approach is built upon the concept of plowed depth and material stagnation ahead of the cutting edge. As is shown in

schematic figure 6.1, material flows towards the cutting edge until it reaches to the material stagnation zone in the vicinity of point P . The presence of stagnation zone in cutting has been shown both experimentally [20] and numerically [11,21]. Material flow splits into upward and downward streams at stagnation zone. Upward stream forms chip and downward stream forms the machined surface. The formed chip leaves the rake face of the cutting tool at point A and at point B , tool loses contact with machined surface. Plowed depth δ is a fraction of uncut chip thickness d located between ideal material separation line BD and actual separation line PC . This depth of material becomes squashed by the cutting edge and experiences high transient stresses, large strains and strain rates at high temperatures with severe gradients. It is legitimately hypothesized that the plowed layer is the key element contributing to residual stress generation in near surface zone of machined surfaces. Therefore, the chip forming stream of material flow above the actual separation line PC is neglected in the proposed numerical modeling approach.

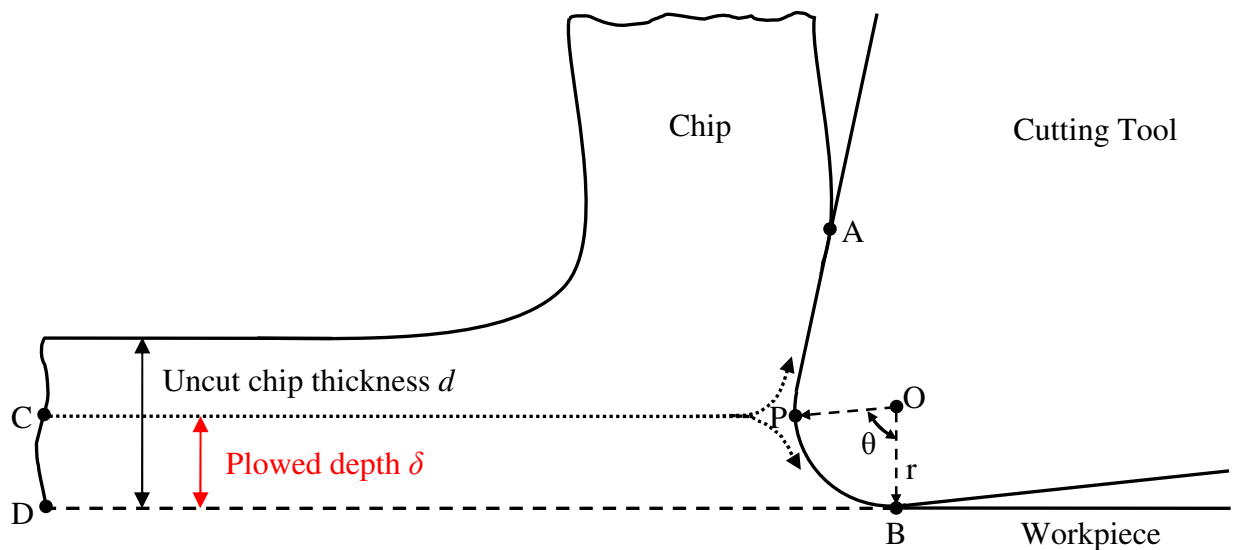


Fig. 6.1 Schematic of plowed depth and material stagnation in a cutting process [14]

The plowed depth δ depends on cutting edge geometry and workpiece material. It is calculated using $\delta = r \times (1 - \cos \theta)$ where r is cutting edge radius and θ is stagnation angle. A wide range of published work has shown that the stagnation angle varies from 20° to 50° for most cutting edge geometry and work materials. The stagnation angles used in this study are 20° , 26° , and 32° corresponding respectively to 0.6, 1.0, and 1.5 μm plowed depth. Higher stagnation angles caused severe element distortion in the converged mesh shown in figure 6.2 and ultimately simulations failed despite the fact that adaptive mesh was used in near surface layers of the model. This may indicate that the upper limit of stagnation angle is about 32° for this combination of Mg-Ca0.8 (wt%) alloy and tool geometry. However, the later statement needs to be verified experimentally.

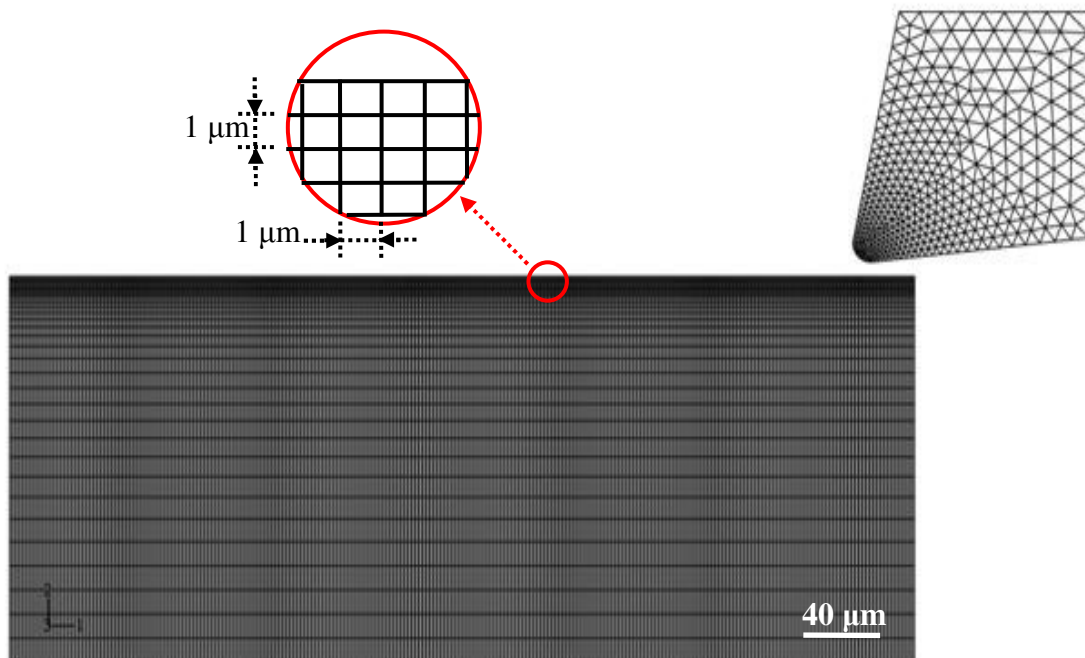


Fig. 6.2 FE mesh of residual stress prediction simulation using plowed depth concept

Figure 6.2 represents the 2-dimensional orthogonal cutting of Mg-Ca0.8 (wt%) alloy. The cutting edge radius r is 10 μm representing a sharp cutting edge. Rake angle α and clearance angle λ are 12° and 6° , respectively. Cutting temperature of chip/workpiece system is determinative of the generated residual stresses. On the other hand, realistic computation of cutting temperature involves considering thermal interactions of chip/workpiece system with environment through convection, radiation, and conduction. In this context, both tool and workpiece are meshed using plane strain elements with temperature degree of freedom. The tool is constrained to move horizontally at a constant speed after initial vertical penetration into the workpiece surface till it reaches the plowed depth amount. The overall dimensions of the workpiece are set to be $500 \mu\text{m} \times 200 \mu\text{m}$ to avoid both size and edge effects and also to provide efficient computation time. The bottom layer of the workpiece is modeled with semi-infinite elements to prevent stress bounce back. Workpiece mesh becomes finer moving towards the surface and elements in the first 10 layers are as small as $1 \mu\text{m}$. The initial temperature of tool and workpiece is 20°C .

Inelastic deformation and friction at tool/workpiece interface generate heat during cutting process. The dominant heat transfer mode, especially in dry cutting, is conduction and the total dissipated heat due to convection and radiation is about 20% [22]. The tool/workpiece interface is assumed to be perfectly conductive due to intimate contact between adjacent surfaces under high cutting pressures. However, tool and workpiece will receive different shares of the generated heat depending on their thermal properties (Table 6.1). Heat flux partition of tool and workpiece are calculated using following equations [22]

$$R_W = 1 / \left(1 + 1.5 \times (\lambda_T / \lambda_W) \times \sqrt{\alpha_W / \alpha_T} \right) \quad (6.1)$$

$$R_T = 1 - R_W \quad (6.2)$$

$$\alpha = \lambda / (c_p \times \rho) \quad (6.3)$$

Where R_i is heat partition of component i [%], λ_i is thermal conductivity of component i [W/m.K], α_i is thermal diffusivity of component i [m²/s], c_p is specific heat [J/Kg.K], ρ is mass density [Kg/m³]. Subscripts W and T refer to workpiece and tool respectively. Substituting appropriate values from Table 6.1 into equations 1 to 3 result in $R_w = 11\%$ and $R_T = 89\%$ meaning 89% of the generated heat diffuses into PCD tool and only 11% stays in the chip/workpiece system. Guo et al [14] modified the VUMAT subroutine to include frictional heat in addition to inelastic deformation heat as well as heat transfer between chip/workpiece system and surrounding environment in numerical analysis of cutting. This subroutine used in this study, implements ISV plasticity model of the workpiece mechanical behavior and elastic properties of the PCD tool (Table 6.2).

Table 6.1 Thermal properties of PCD tool and Mg-Ca0.8 alloy

Material	C_p [J/Kg.K]	λ [W/m.K]	α [m ² /s]	β [μ m/m.K]
PCD ^[23]	509	2000	1.12×10^{-3}	1.18
Mg-Ca0.8	1010	72	4.07×10^{-5}	26

Table 6.2 Elastic properties of PCD tool and Mg-Ca0.8 alloy

Material	ρ [Kg/m ³]	E [GPa]	ν
PCD ^[23]	3500	1220	0.20
Mg-Ca0.8	1750	45	0.33

A total of seven simulation cases (Table 6.3) were performed to study the effect of plowed depth and cutting speed on induced residual stresses. Each simulation case consists of two-step analysis. At first step, tool plows the workpiece surface which is accomplished in ABAQUS/Explicit. Transient mechanical state of the workpiece including stresses, strains, and temperatures is computed in a dynamic coupled temperature-displacement analysis. At step two, computed transient mechanical state is imported into ABAQUS/Standard and the workpiece is cooled down to room temperature. As such, transient stresses relax till residual stresses develop at room temperature.

Table 6.3 Cutting speed and plowed depth in residual stress prediction cases

Cutting speed V [m/min]	Plowed depth δ [μm]
1200	0.6, 1.0, 1.5
1600	0.6
2000	0.6
2400	0.6
2800	0.6

6.4. Cutting setup and residual stress measurements

Disc-shaped samples made of lab-made Mg-Ca0.8 alloy were face milled in a 3 axis Cincinnati Arrow 500 CNC machine. No coolant was applied throughout the tests. Nine diamond tipped milling inserts were clamped in a 127 mm diameter face mill. Resulting angles at the cutting edge were axial rake 12° and axial relief 6° . The cutting speed was in 1200-2800 m/min range while the depth of cut and feed were held constant at 200 μm and 200 $\mu\text{m}/\text{rev}$, respectively. A detailed description of the experimental setup is given in section 3.3.2. Cutting-induced

residual stresses on the machined surfaces were measured using 4-axis Bruker D8 XRD machine and $\sin^2\psi$ method. X-rays with $\lambda = 0.1542$ nm wavelength were generated applying 35 mA and 40 kV power to X-ray tube with copper target. X-rays were collimated and directed onto the sample's surface using 0.8 mm diameter collimator. An area detector located 15 cm far from the goniometer's center collected diffracted X-rays. $\{1\ 2\ \bar{3}\ 3\}$ crystallographic planes corresponding to $2\theta = 118.48^\circ$ angle were used to measure residual strains. The stress state was assumed to be plane stress ($\sigma_3 = 0$) and uniform within the diffracting volume. Modulus of elasticity ($E = 45$ GPa) and Poisson's ratio ($\nu = 0.33$) of the polycrystalline Mg-Ca_{0.8} were used in computing residual stresses and they were assumed to be isotropic within the diffracting volume. Electropolishing technique was implemented to remove the material layer by layer in order to measure subsurface residual stresses.

6.5. Simulation results and discussions

6.5.1. Machining forces

The computed plowing and thrust force time histories are shown in figure 6.3. Plowing and thrust forces are aligned in “1” and “2” directions, respectively, in figure 6.2. Both force components become stable around an average value after a few micro seconds. This implies that steady state cutting condition is established in the simulations. As can be seen in figure 6.4, higher cutting speeds result in larger plowing and thrust forces. Work hardening and thermal softening are two rival mechanisms playing role in determining material resistance against plastic deformation and consequently machining forces. Work hardening tends to increase the

forces while thermal softening tends to decrease them. The observations made from figure 6.4 indicate that work hardening is more prominent than thermal softening in high speed dry cutting of Mg-Ca_{0.8} alloy using diamond tool. Moreover, thrust force is almost three times larger than plowing force regardless of the cutting speed.

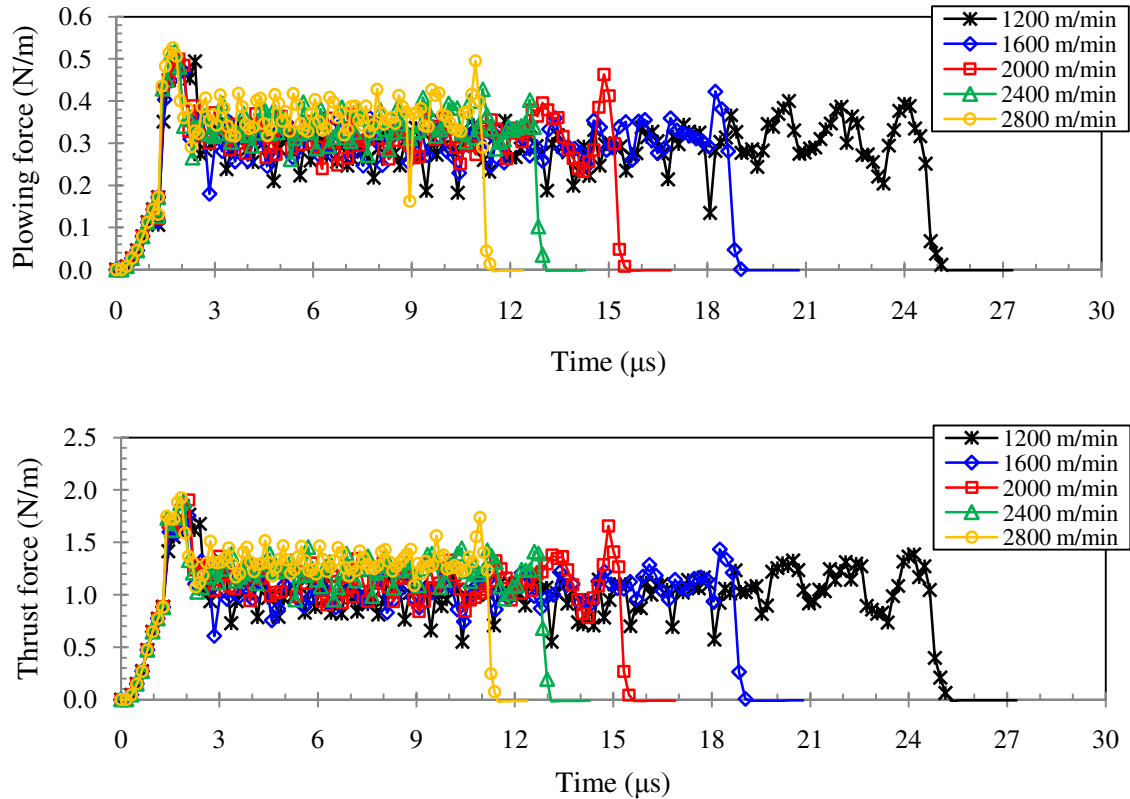


Fig. 6.3 Time histories of plowing and thrust forces under various cutting speeds ($\delta = 0.6$ mm)

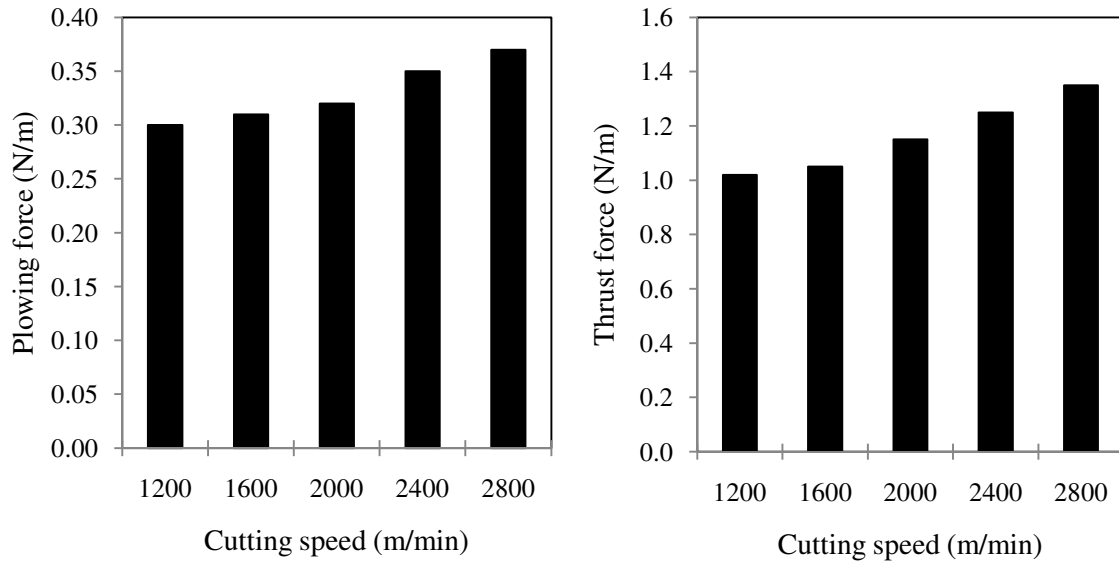


Fig. 6.4 Effect of cutting speed on plowing and thrust forces ($\delta = 0.6$ mm)

6.5.2. Residual stress evolution

Figure 6.5 shows how stresses along a straight, in-depth path evolve to eventually become residual stresses at and near the machined surface. Transient profile refers to stress distribution right below the cutting edge while cutting process is under progress. There is a sharp stress gradient in the first $12 \mu\text{m}$ below the surface during the cutting. Due to fast cutting speeds, generated heat does not have enough time to diffuse away. As such, considerable thermal strains are superimposed on mechanical strains to stretch the surface layers. However, layers below the HAZ zone constrain the stretching and cause large compressive stresses at or near the surface while the cutting is in progress. When the cutting/plowing is over, significant portion of the thermal strains are relaxed since the generated heat has had more time to spread around in the surrounding media. Therefore, surface layers tend to shrink. On the other hand, according to

Hertzian contact theory maximum contact pressure and mechanical deformation has happened below the surface. This means that subsurface material layers are mechanically stretched due to compressing action of the thrust force. At the end of the cutting process, the tendency of the HAZ layer to shrink faces with some constraint by the plastically stretched subsurface layers. This causes more tensile stresses at closer to surface layers and more compressive stresses at deeper layers in the material. Giving the machined surface more time in order to cool down to room temperature leads to more shrinkage tendency in HAZ layer. This causes even more tensile *residual* stresses at the surface and in about 5 μm below the surface. At this point, residual stress profile has established its characteristic *hook* shape as is shown in figure 6.5.

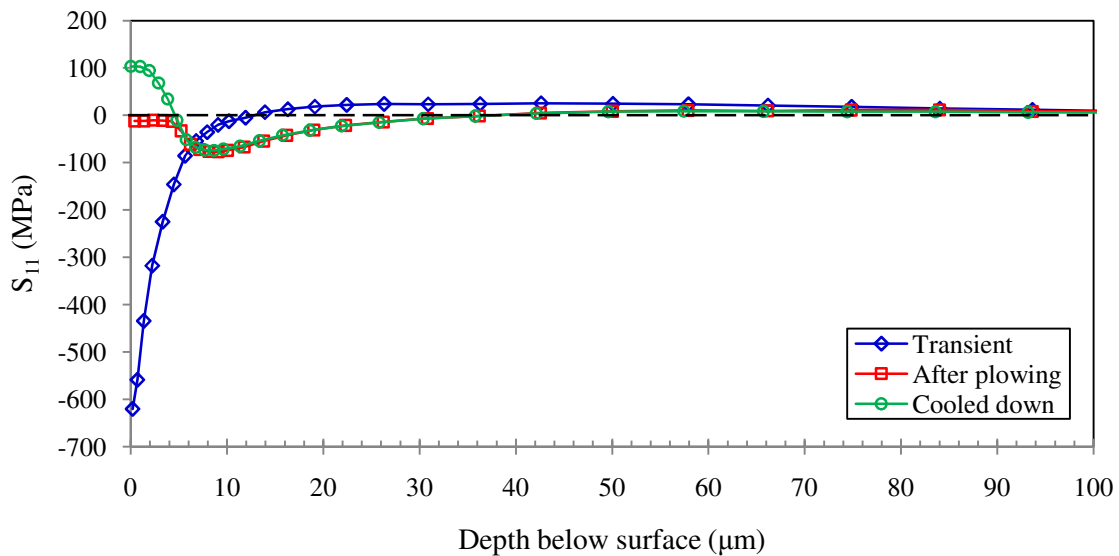


Fig. 6.5 Residual stress evolution in machined Mg-Ca0.8 surface ($V = 1200$ m/min; $\delta = 0.6$ μm)

6.5.3. Cutting speed effect on residual stress profile

Figure 6.6 shows residual stress profiles at machined surface layer developed under different cutting speeds. To analyze our observation in figure 6.6, it would be helpful if we go back and pay attention to the process by which the machined surface is formed in figure 6.1. Each material element located in plowed-depth layer experiences an extrusion like deformation as it approaches to cutting edge and becomes part of the machined surface past point *B*. This deformation field would govern the machined surface formation process regardless of the rate by which the deformation takes place. However, material elements would require more energy to experience same amount of deformation under higher rate than they would under lower rate. That translates into more heat generation under higher cutting speeds, considering the fact that majority of the inelastic deformation energy dissipates into heat. Therefore, cutting speed effect on residual stress profile has more of a thermal rather than mechanical nature. In this context, it is expected to observe more tensile residual stresses at machined layer under higher cutting speeds. However, the predicted results in figure 6.6 does not support this expectation and cutting speed shows almost effect less on residual stress profiles in cutting Mg-Ca_{0.8} using diamond tool. The missing piece should be something that suppresses thermal effect of the cutting speed. A possible way is taking out the generated heat from the deformation field fast enough to avoid thermal softening and subsequent excessive stretching in subsurface layers. Revisiting Table 6.1 reveals that this potential possibility could be an occurring reality. Diamond has super heat conduction property and acts as a heat sink which suppresses thermal effect of cutting speed on residual stress profiles.

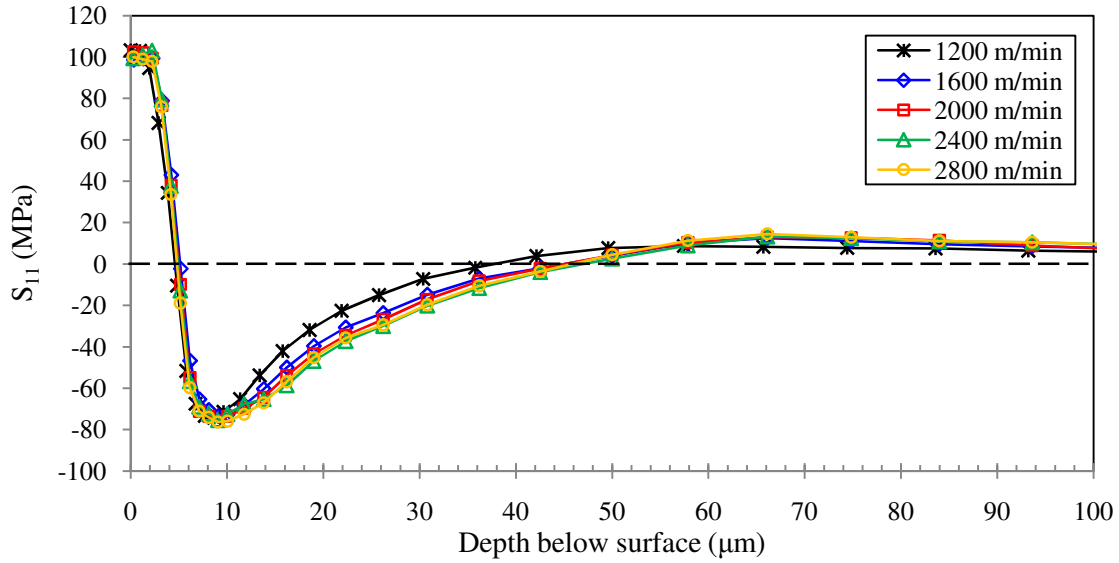


Fig. 6.6 Effect of cutting speed on residual stress profiles of machined Mg-Ca0.8 ($\delta = 0.6 \mu\text{m}$)

6.5.4. Plowing depth effect on residual stress profile

Figure 6.7 shows the effect of plowing depth on residual stress profiles in the machined surface layer of the Mg-Ca0.8 workpiece. Increasing plowed depth from $\delta = 0.6 \mu\text{m}$ to $\delta = 1.5 \mu\text{m}$ (almost three times increase) shows marginal influence on the tensile portion of the residual stress profiles as opposed to more noticeable influence on compressive portion of the profiles. This speaks on the fact that plowing depth has more of a mechanical rather than thermal effect on residual stress profiles. It is predicted that deeper plowing will shift the location of the maximum compressive stress to deeper subsurface layers and will increase the total thickness of the compressively stressed layers ($\sim 70 \mu\text{m}$ for $\delta = 1.5 \mu\text{m}$). However, magnitude of the maximum subsurface residual stress decreases with increasing the plowing depth.

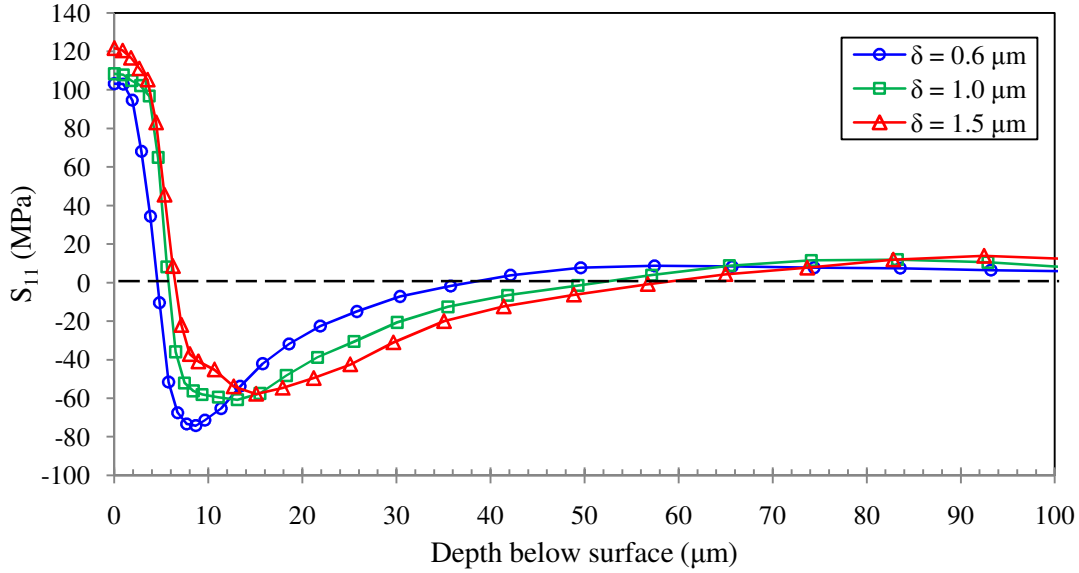


Fig. 6.7 Effect of plowing depth on residual stress profiles of machined Mg-Ca0.8 ($V = 1200$ m/min)

6.6. Experimental validation and discussion

Figure 6.8 shows measured residual stresses at and near the machined Mg-Ca0.8 surface along with the predicted profile. There is a noticeable difference between measurement and prediction at the surface. This might be partially due to the presence of feed marks on the actual machined surface which are neglected in the numerical model. Meanwhile, taking into account the inherent uncertainty of the X-ray diffraction method, there is a reasonable agreement among prediction and measurements at subsurface layers. Uncertainty in the measurement and neglecting surface roughness in the model are among the contributing error sources for observed discrepancies in figure 6.8. Another source of error would be the deformation patterns by which each of the measured and predicted residual stresses are created. While predictions are extracted from an orthogonal cutting model, measured values are caused by a three-dimensional face

milling operation. Although details like cutting geometry, effective cutting parameters, corner radius, and cutting sequence set the three-dimensional cutting considerably apart from the orthogonal cutting, both operations follow same fundamental mechanics in generating the finished surface [7]. “The finished surface is generated through elastic-plastic deformation in front of the cutting tool as the tool edge separates chips from the machining surface”. In this context, orthogonal modeling could be used as a first approximation for three-dimensional operation to analyze the effects of process parameters on residual stress profiles particularly in the subsurface as is shown in figure 6.8.

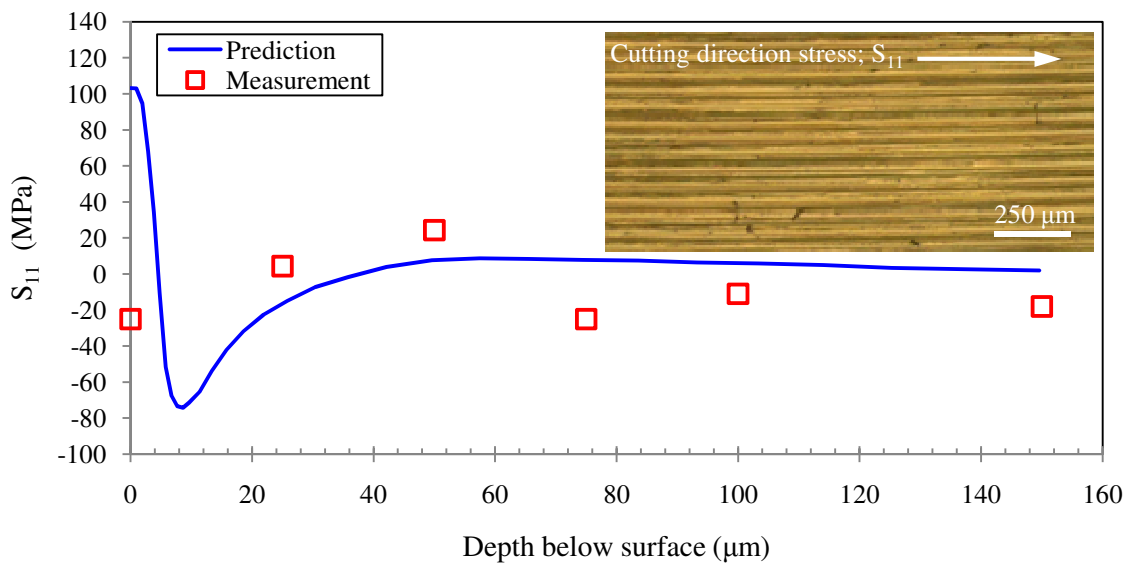


Fig. 6.8 Residual stress predictions and measurements ($V = 1200 \text{ m/min}$; $\delta = 0.6 \text{ } \mu\text{m}$)

It is also noticed that there is a sharp gradient of residual stress in the first 20 μm below the machined surface by prediction which would be either overlooked in measurements for

efficiency and economical reasons or considerably erroneous, if not impossible, to measure due to the size effect of the interacting volume of the material with the X-rays (5 ~ 20 μm deep [1]). Therefore, the possibility of having very fine spatial resolution would and should remain as a key characteristic of numerical techniques to make them viable in competing with measurement techniques.

6.7. Conclusions

A finite element model without explicit chip formation is developed to predict process-induced residual stress profiles in orthogonal cutting of the novel Mg-Ca_{0.8} biomaterial. Complex thermomechanical behavior of the material is captured applying an internal state variable plasticity model. The key findings of this study are as follow:

- Higher cutting speeds result in larger plowing and thrust forces. Thrust force is almost three times larger than plowing force regardless of the cutting speed.
- Work hardening is more prominent than thermal softening in high speed dry cutting of the Mg-Ca_{0.8} alloy using diamond tool.
- Residual stresses evolve from a transient, highly compressive, and L-shaped profile to a stable, hook-shaped profile which starts with tensile stresses at the surface and reaches to more moderate compressive residual stresses at deeper subsurface layers.
- Super hear conduction property of the diamond tool suppresses the thermal effect of the cutting speed and avoids the change in residual stress profiles with respect to the cutting speed.

- Deeper plowing shifts the maximum compressive stress location to deeper subsurface layers and increases the thickness of the subsurface layer which is covered by compressive residual stresses.
- The predictions are good first approximation of the measured residual stresses particularly at subsurface layers.

References

1. E. Brinksmeier, J.T. Cammett, W. König, P. Leskovar, J. Peters, H.K. Tönshoff, Residual stresses-measurement and causes in machining processes, *Ann. of the CIRP* 31 (1982) 491-510.
2. H. Sasahara, T. Obikawa, T. Shirakashi, FEM analysis of cutting sequence effect on mechanical characteristics in machined layer, *J. Mater. Process. Tech.* 62 (1996) 448-453.
3. C.R. Liu, Y.B. Guo, Finite element analysis of the effect of sequential cuts and tool-chip friction on residual stresses in a machined layer, *Int. J. Mech. Sci.* 42 (2000) 1069-1086.
4. X. Yang, C.R. Liu, A new stress-based model of friction behavior in machining and its significant impact on residual stresses computed by finite element method, *Int. J. Mech. Sci.* 44 (2002) 703-723.
5. K. Jacobus, R.E. DeVor, S.G. Kapoor, Machining-induced residual stress: experimentation and modeling, *J. Manuf. Sci. E. – T. ASME* 122 (2000) 20-31.
6. K. Jacobus, R.E. DeVor, S.G. Kapoor, R.A. Peascoe, Predictive model for the full biaxial surface and subsurface residual stress profiles from turning, *J. Manuf. Sci. E. – T. ASME* 123 (2001) 537-546.
7. H. Sasahara, T. Obikawa, T. Shirakashi, Prediction model of surface residual stress within a machined surface by combining two orthogonal plane models, *Int. J. Mach. Tool. Manu.* 44 (2004) 815-822.
8. W.J. Zong, D. Li, K. Cheng, T. Sun, Y.C. Liang, Finite element optimization of diamond tool geometry and cutting-process parameters based on surface residual stresses, *Int. J. Adv. Manuf. Tech.* 32 (2007) 666-674.

9. J.C. Outeiro, J.C. Pina, R. M'Saoubi, F. Pusavec, I.S. Jawahir, Analysis of residual stresses induced by dry turning of difficult-to-machine materials, *CIRP Ann. – Manuf. Techn.* 57 (2008) 77-80.
10. V. Schulze, H. Autenrieth, M. Deuchert, H. weule, Investigation of surface near residual stress states after micro-cutting by finite element simulation, *CIRP Ann. – Manuf. Techn.* 59 (2010) 117-120.
11. K.C. Ee, O.W. Dillon Jr., I.S. Jawahir, Finite element modeling of residual stresses in machining induced by cutting using a tool with finite edge radius, *Int. J. Mech. Sci.* 47 (2005) 1611-1628.
12. J.S. Strenkowski, J.T. Carroll, A finite element model of orthogonal metal cutting, *J. Eng. Ind. – T. ASME* 107 (1985) 349-354.
13. S. Caruso, J.C. Outeiro, D. Umbrello, R. M'Saoubi, Modeling and experimental validation of the surface residual stresses induced by hard machining of AISI H13 tool steel, *Int. J. Mater. Form.* 3 (2010) 515-518.
14. Y.B. Guo, S. Anurag, I.S. Jawahir, A novel hybrid predictive model and validation of unique hook-shaped residual stress profile in hard turning, *CIRP Ann. – Manuf. Techn.* 58 (2009) 81-84.
15. F.W. Bach, B. Denkena, K. Weinert, P. Alpers, M. Bosse, N. Hammer, Influence of cutting and non-cutting processes on the corrosion behavior and the mechanical properties of magnesium alloys, *Proc. 7th Int. Conf. Magnesium Alloys and Their Applications* (2007) 1076-1084.
16. N. von Der Hoh, D. Bormann, A. Lucas, B. Denkena, C. Hackenbroich, A. Meyer-Lindenberg, Influence of different surface machining treatments of magnesium-based resorbable implants on the degradation behavior in rabbits, *Adv. Eng. Mater.* 11 (2009) B47-54.
17. B. Denkena, A. Lucas, Biocompatible magnesium alloys as absorbable implant materials – adjusted surface and subsurface properties by machining processes, *Ann. of the CIRP* 56 (2007) 113-116.
18. D.J. Bammann, M.L. Chicsa, G.C. Johnson, Modeling large deformation and failure in manufacturing processes, *Theor. App. Mech.* (1996) 359 – 376.
19. D.J. Bammann, M.L. Chiesa, M.F. Horstemeyer, L.I. Weingarten, Failure in ductile materials using finite element methods, In: N. Jones, T. Wierzbicki (Eds.), *Structural crashworthiness and failure*, Elsevier, Essex, England (1993) 1-54.
20. W.B. Palmer, R.C.K. Yeo, Metal flow near the tool point during orthogonal cutting with a blunt tool, *Proc. 4th Int. Machine Tool Design & Res. Conf.* (1963) 61-71.

21. Y.B. Guo, Q. Wen, A hybrid modeling approach to investigate chip morphology transition with the stagnation effect by cutting edge geometry, Transactions of NAMRI/SME 33 (2005) 469-476.
22. W. Grzesik, P. Nieslony, A computational approach to evaluate temperature and heat partition in machining with multilayer coated tools, Int. J. Mach. Tool. Manu. 43 (2003) 1311-1317.
23. H.E. Spear, J.P. Dismukes, Synthetic diamond – emerging CVD science and technology, Wiley, NY (1994).

CHAPTER 7

PROCESS MECHANICS IN HYDROSTATIC BURNISHING OF BIOMEDICAL MAGNESIUM-CALCIUM ALLOY

Abstract

Magnesium-Calcium (Mg-Ca) alloys have received considerable attention recently in medical device manufacturing industry especially for making biodegradable bone implants. Hydrostatic burnishing has emerged as a promising manufacturing alternative to tailor surface integrity of implants with the ultimate goal of being able to adjust their corrosion rate. Hydrostatic burnishing mechanics is essential to understand the process. The process mechanics is further complicated by the normal force reduction due to unavoidable hydraulic pressure loss at the tip of the burnishing tool, and the penetration depth reduction due to elastic recovery of the workpiece material. The measured normal force, in this study, shows maximum 23% reduction compared to theoretical value. The normal force drop is not uniform but increases with increasing applied pressure. A 2D axisymmetric and semi-infinite finite element analysis (FEA) model has been developed and validated to predict the amount of elastic recovery after burnishing. The dynamic mechanical behavior of the material is simulated using the internal state variable (ISV) plasticity model and implemented in the FEA simulation using a user material subroutine. The simulated dent geometry agrees with the measured ones in terms of burnishing profile and depth. Simulation results suggest an 8% elastic recovery on average. Acoustic

emission (AE) signals are also recorded and the likely correlation with predicted residual stress, plastic strain, and temperature distributions are studied to achieve an in-process monitoring.

7.1. Introduction

Traditional orthopedic methods use permanent metallic implants made of stainless steel, titanium, or cobalt-chromium alloys to bring bone traumas back to their original anatomical configuration and to hold them in place during the healing process. Durable implants are stiffer than bone and permanently protect the healing bone against mechanical exposure. This effect called stress shielding [1-3] hinders stabilization of the bone tissue which needs mechanical loads to obtain and maintain its rigidity. Stress shielding will cause artificial osteoporosis, ultimately. Moreover, permanent implants are foreign objects in human anatomy and always carry the risk of local inflammation. To avoid those negative effects, annually many revision surgeries with all their personal, medical, social and economical consequences have to be performed to remove the implants after one or two years.

Development of biodegradable implants is one of the important areas in medical science. Degradable, biocompatible implants can gradually dissolve and become absorbed in human organism after implantation. A biodegradable material will offer an appropriate solution for inflammatory discomfort, permanent physical irritation, stress shielding and the revision surgery associated with durable implants. Current biodegradable implants are mainly polymeric which have an unsatisfactory strength in load carrying applications. This has led researchers to seek for metallic biodegradable substitutes.

Clinical studies on biocompatibility of magnesium-calcium (Mg-Ca) alloys have brought very appealing results. These alloys do not generate any toxic, carcinogenic, or mutagenic products and so their dissolution inside human anatomy is acceptable from physiological point of view [4-8]. However, rapid corrosion of Mg-Ca alloys causes them to lose their mechanical strength before the healing process is over and consequently to fail in serving the main purpose of their application which would be fixing the bone fragments. In order to develop Mg-Ca alloys as a successful orthopedic material, corrosion rate of these alloys should be adjusted in one way or another to match the healing rate of the bone tissue.

While the bulk material of the biomedical device is often important for integrity and mechanical success, the device surface is at the interface with biology. In this context, modifying a biomaterial surface [9,10] in order to elicit or inhibit a biological response, in this case degradation rate, seems very promising approach to tackle the above mentioned issue in Mg-Ca alloys. Hydrostatic burnishing is a novel surface treatment process which has attracted a considerable attention lately in orthopedic device research. Denkena et al [11] tried to control the corrosion of magnesium implants by hydrostatic burnishing and ultimately to achieve adaptable degradation profile for various medical applications. Schuh et al [12] evaluated hydrostatic burnishing of titanium alloy rods as a possible alternative to shot peening in treating the mating surfaces of Morse tapers in modular hip endoprostheses. Their motive was to avoid the contamination of shot peened surfaces leading to enhanced corrosion and third body wear. Seemikeri et al [13] studied the effect of hydrostatic burnishing process parameters i.e. number of passes, ball diameter, pressure, and speed on surface and subsurface characteristics and fatigue performance of AISI 316L steel which is most commonly used in prosthesis. Prevey et al [14] applied hydrostatic burnishing process to titanium distal stem tapers, used in a modular hip

construct, to provide increased fatigue strength and improved tolerance to fretting damage. Disegi et al [15] determined the effect of hydrostatic burnishing on the fatigue strength of spinal rods utilizing a cantilever fatigue testing procedure.

7.2. Hydrostatic burnishing

The center piece of this process is a smooth free-rolling ball supported in a spherical socket and pressed against the surface to deform the near surface zone of the workpiece. It is characterized by unique combination of three physical effects: (I) producing deep and stable compressive residual stresses; (II) work hardening in surface/subsurface and increasing microhardness; (III) burnishing and decreasing surface roughness and micronotches. Although application of hydrostatic burnishing in medical device field is quite new, it has earned increasing applications in automotive and aerospace industry to improve the fatigue life and corrosion resistance.

Literature survey on mechanical surface treatments reveals two processes named deep rolling (DR) and low plasticity burnishing (LPB) which are very similar and follow the hydrostatic burnishing concept explained above [16-24]. However, it is believed that DR produces more cold work than LPB [25]. The fatigue performance and wear resistance of Ti-6Al-4V alloy can be significantly improved by a combination of low-temperature plasma-carburizing and deep rolling [17,18]. Surface diffusion processes such as plasma-carburizing and nitriding have been used to improve tribological properties of titanium and its alloys. However, the improvement of fatigue strength by these processes has not been successful due to brittleness

introduced in the high-hardness surface layer and the disappearance of compressive residual stress and grain growth by heating.

Performing LPB right after end-milling and prior to typical marine environment corrosion increases the endurance limit of the aluminum alloy 7075-T6 over three times [26]. Titanium, iron, and nickel based aero-turbine engine alloys treated by LPB show higher and deeper compressive residual stresses with less amount of cold work as opposed to conventional shot peening (SP) process [25]. LPB can also be used as a maintenance technique for pre-damaged specimens since the depth of compression from LPB greatly exceeds the maximum corrosion pit depth. Therefore, failure from pitting or cracking is prevented and safe-life operation is ensured [27]. Several millimeters of compressed zone are achievable in this process. Applying LPB to friction stir welds in Ni-Al Bronze produces a deep compressed layer of 2.5 mm depth and a maximum subsurface residual stress of -1.0 GPa [28].

In a comparative study on the effect of SP and DR on fretting fatigue life of Aluminum 7075-T6, it turned out that, for high cycle fatigue, the effect of DR on fretting fatigue resistance was more profound than SP such that an increase of about 700% was observed for DR [19]. DR produces lower levels of cold work as opposed to SP. There is an emerging consensus that high levels of cold work leave a severely deformed surface layer with a high dislocation density that adversely affects the thermal and mechanical stability of compressive layer.

Residual stress relaxation is observed in deep cold rolled samples of Ti-6Al-4V alloy caused by low cycle, constant strain amplitude fatigue at loads and temperatures replicating the most extreme conditions in the compression stages of a gas turbine engine [20]. For room temperature low cycle fatigue (LCF), residual stress relaxation was less than 50% of the peak compressive residual stress. For high temperature exposure residual stress relaxation was less

than 40% of the peak compressive residual stress. For high temperature LCF, relaxation was greater than either thermal exposure or fatigue alone and about 70% of the peak residual stress. However, the depth of compressive residual stress was unaffected by relaxation.

Consecutive deep rolling and annealing as well as high temperature deep rolling of austenitic stainless steel (AISI 304) and ferritic-pearlitic steel (SAE 1045) produce more stable near-surface stress states during low cycle fatigue than conventional deep rolling at room temperature [21]. Between laser-shock peening (LSP) and deep rolling, the residual stress state and work hardening induced by LSP are less stable under isothermal cyclic loading at elevated temperatures [22]. Therefore, the fatigue lifetime of the deep rolled condition at elevated temperatures is higher due to more stable near-surface microstructures, e.g. nanocrystalline layers, deformation-induced phase transformation, and higher dislocation densities. The near-surface work hardening, characterized by the full width at half maximum (FWHM) values of the X-ray diffraction peaks, is the major factor influencing the fatigue lifetime of the deep-rolled aluminum alloys [23]. Work hardening states are considerably more stable than macroscopic residual stresses.

The ease of implementation in standard CNC machining centers offers the possibility of employing hydrostatic burnishing successively or simultaneously with cutting operations to selectively enhance performance of different components [24,29]. In other work to develop hybrid manufacturing technologies, Brinksmeier et al [30] used deep rolling to improve the machinability of STRIP-steels. This new manufacturing technology eliminates the thermal hardening and combines hardening and surface finishing in one step on the same machine tool. Therefore, there is no need to unclamp the workpiece which causes less distortion in the part and considerable economical savings.

Experimental and numerical study of contact mechanics can make a noticeable help in understanding the hydrostatic burnishing process. In this paper, the actual normal force has been measured. Theoretical value of this force calculated based on hydrostatics is greater than the measured one which is attributed to hydraulic pressure loss at the tip of the burnishing tool. An internal state variable model which incorporates strain rate and temperature sensitivity as well as damage is used to describe the material behavior under deformation [31]. For the first time, the parameters of this model are obtained for the novel Mg-Ca_{0.8} biomaterial. A 2D-axisymmetric, semi-infinite FEM model is developed for numerical study of the contact mechanics. The material model is implemented in numerical model using a user subroutine. Experimentally measured and numerically predicted dent profiles are compared to evaluate the performance of the applied material model and the FEM model itself. The amount of elastic recovery after tool removal is predicted. Actual normal force and elastic recovery amount are two critical values to know before moving further to simulate the hydrostatic burnishing process itself in any future work. Acoustic emission (AE) signals are recorded and the likely correlation with predicted residual stress, plastic strain, and temperature distributions are studied with an eye on obtaining an in-process monitoring tool.

7.3. Indentation using hydrostatic burnishing tool

7.3.1. Experimental plan and set-up

The burnishing tool used in this study is Ecoroll HG13. It has a 12.7 mm ceramic ball made of silicon nitride. This ceramic ball sits on a pressurized hydro-cushion produced by

Ecoroll HGP4.0 hydraulic unit. This unit is capable of producing pressures up to 40 MPa. Based on the technical data provided by manufacturer, a thin layer of pressurized oil will be between ball and its housing all the time and the ball can roll freely without having a chance to touch its housing. The housing has 10 mm of free stroke to accommodate for elevation changes on sample surface. The power carrying fluid is anti-wear, dual purpose oil Aries 15 which functions as both lubricant and coolant. The top plate of the fixture in figure 7.1 can freely slide vertically and transfer the normal force to the high accuracy compression load cell (Intertechnology Inc., Model 220 5T) underneath. The acoustic waves emitted during contact are acquired and processed using an AE sensor and Physical Acoustics Corp. PCI-2 based AE system. A thin layer of vacuum grease is applied at the interface of AE sensor and sample to fill any possible air gap while AE sensor is secured firmly against the sample.

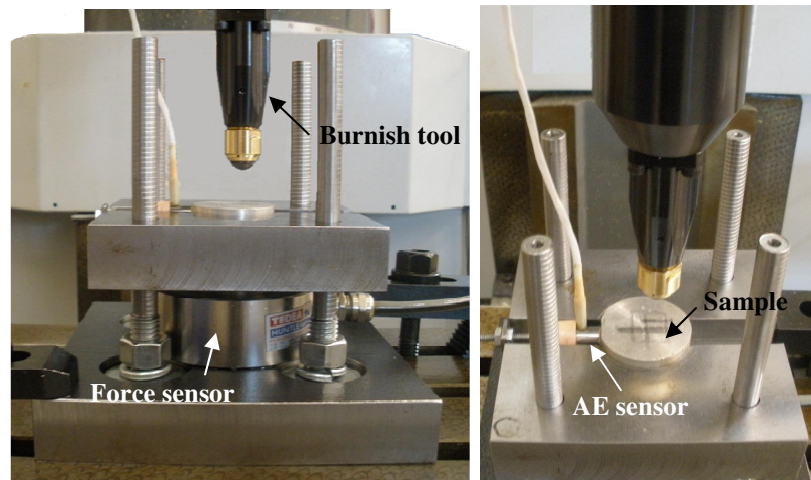


Fig. 7.1 Experimental setup of burnishing Mg-Ca alloy

All the setup shown in figure 7.1 is hooked up on a Bridgeport milling machine. The dents are fabricated following the map shown in figure 7.2. This map is designed to avoid the possible overlap of deformation fields associated with different dents. The small circles represent indents and are 1.25 mm in diameter. They are equally spaced in both X and Y directions. Coordinates of each dent and the amount of hydraulic pressure used to make them are summarized in Table 7.1.

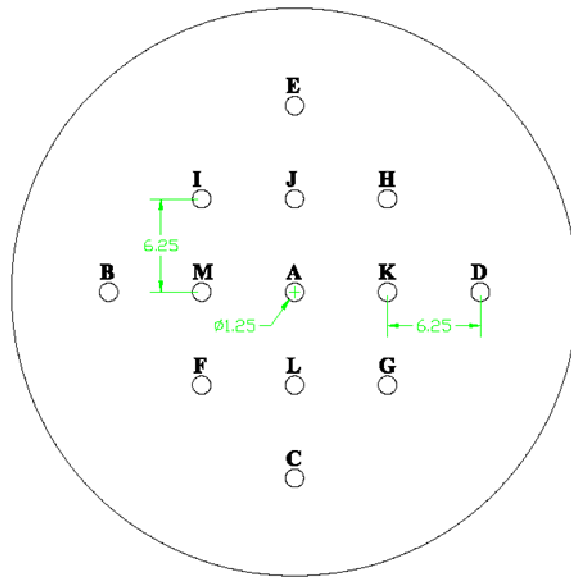


Fig. 7.2 Dent fabrication map

Table 7.1 Hydraulic pressure and coordinates of each dent

sequence	A	B	C	D	E	F	G	H	I	J	K	L	M
Pressure [MPa]	16	14	12	10	9	8	7	6	5	4	3	2	1
X coordinate [mm]	0	-12.5	0	12.5	0	-6.25	6.25	6.25	-6.25	0	6.25	0	-6.25
Y coordinate [mm]	0	0	12.5	0	-12.5	6.25	6.25	-6.25	-6.25	-6.25	0	6.25	0

7.3.2. Fabrication of novel Mg-Ca_{0.8} orthopedic biomaterial

The material used in this study was fabricated using the procedure explained in section 3.3.1. The cylindrical samples (38 mm dia. × 13 mm thickness) were face milled using carbide inserts at 2400 m/min surface cutting speed, 0.05 mm/rev feed, and 0.2 mm depth-of-cut. All the discs were polished afterwards.

7.4. Results and discussions

7.4.1. Dent geometry

Optical images of five dents made under different pressures are shown in figure 7.3. All these images are taken with 5X magnification. The dents corresponding to pressures above 6 MPa in Table 7.1 were so big that they did not fit into the image frame with 5× magnification which was the smallest available magnification. This is partly due to the large size of the ball itself. Besides, Mg-Ca_{0.8} behaves very ductile in compression mode. It shows 30% of strain at failure [32]. For the lowest hydraulic pressure, i.e. 1 MPa, the maximum contact pressure at dent center based on Hertz theory will be 1055 MPa which is well above the compressive yield stress of the material, i.e. 85 MPa. Therefore, the material will plastically deform. The contact pressure decreases by moving away from the dent center and becomes equal to materials yield stress at the dent perimeter before removing the tool. On the other words, the actual dent size while the tool is in contact with sample surface is larger than the one remains on sample after tool removal because it includes both elastic and plastic part of the deformation. The elastic part will recover upon tool removal and only the plastic part will be visible under optical microscope. Measured

2D profiles of the dents are shown in figure 7.4. The indentation was repeated on two samples and each dent was measured three times along diametric lines located 120° apart. Figure 7.4 shows average dent profile resulted from totally six measurements for each pressure. It also presents the most shallow (labeled by Min) and deepest (labeled by Max) measured profiles for each pressure. The maximum measurable depth is 55 μm for 6 MPa hydraulic pressure. Dents made with higher pressures have depth beyond the limit of Dektak IIA profiler which is 60 μm.

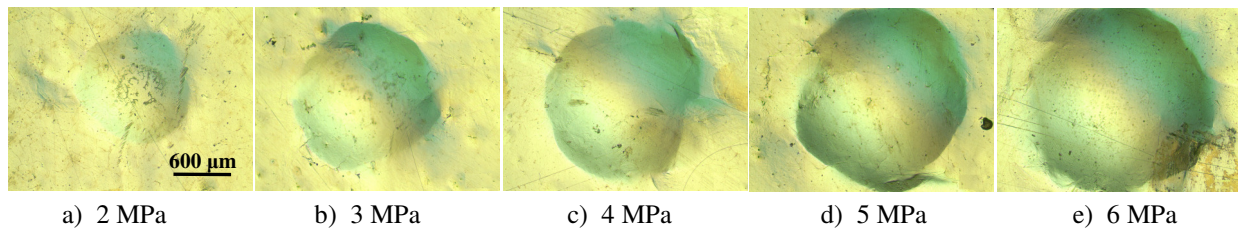


Fig. 7.3 Optical images of dents at different hydraulic pressures

7.4.2. Normal force vs. hydraulic pressure

The theoretical normal force can be calculated using hydrostatic principals. It will be equal to $\pi \times (d/2)^2 \times P$; d ball diameter, and P hydraulic pressure. The theoretically calculated and experimentally measured normal forces are shown in figure 7.5. The actual normal force is smaller than theoretical one. The amount of this discrepancy depends on the amount of hydraulic pressure. This discrepancy is attributed to the pressure loss at tip of the burnishing tool and seems to be the right reason since by increasing hydraulic pressure this discrepancy increases. On average, experimental force is 23% lower than theoretical one.

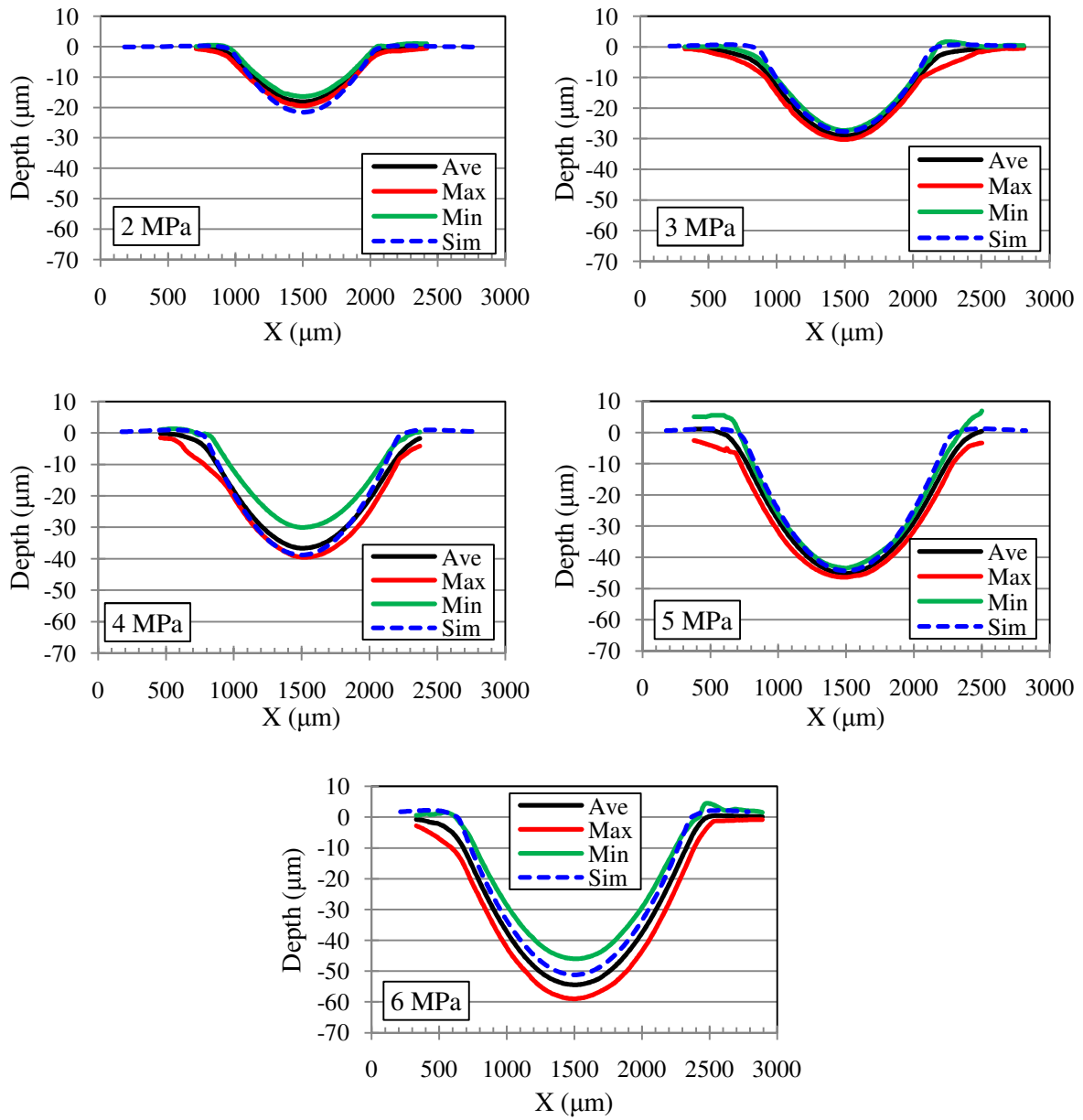


Fig. 7.4 Experimental and Simulated dent profiles

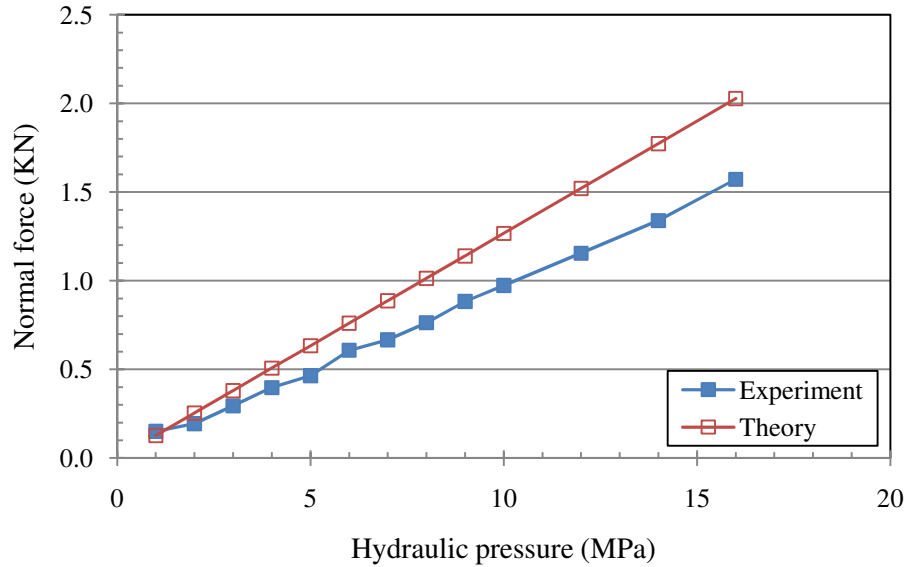


Fig. 7.5 Experimental and theoretical normal force at different hydraulic pressure

7.4.3. Penetration depth vs. hydraulic pressure

As expected, depth of penetration increases with increasing hydraulic pressure (figure 7.4). However, these depth values are the plastic part of the total indentations which remain after removal of burnishing tool. The elastic part, which is hard to measure if not impossible, recovers upon tool removal. The amount of elastic recovery, computed later using finite element analysis (FEA), is an important information to obtain in order to further perform displacement controlled FE analysis of the actual hydrostatic burnishing process.

7.4.4. Acoustic emission signals

The raw AE signals are processed after recording with the aid of Physical Acoustics Corp. PCI-2 based AE system. The time history of AE signals RMS for four different pressures

are shown in figure 7.6. Number of AE signals which have enough amplitude to cross the threshold value, set on 45 dB in this study, increases with increasing hydraulic pressure and they last longer. The frequency content of the AE signals gets wider as well. All these observations can be rationalized considering the fact that the main source of acoustic emission in metals is dislocation movements which ultimately cause plastic deformation. Both plastic and elastic part of deformation increase by applying higher hydraulic pressure and consequently normal force. This will be verified by FE analysis later.

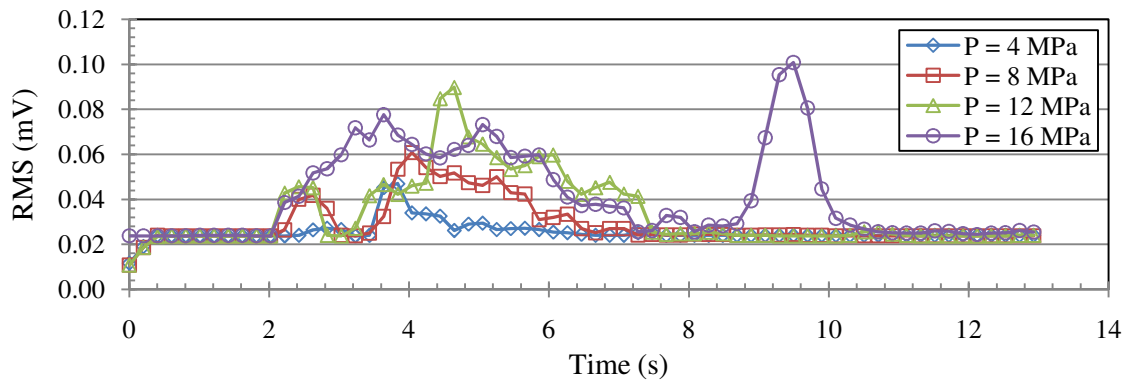


Fig. 7.6 Time history of AE signal's RMS

7.5. Simulation procedure

7.5.1. Mesh

A finite element model for simulating contact mechanics in hydrostatic burnishing of Mg-Ca_{0.8} biomaterial is developed in ABAQUS [33]. The 2D axisymmetric model is shown in figure 7.7. The ball is assumed to be rigid and constrained to move vertically under the specified

normal force measured experimentally in section 5.2. The workpiece domain is discretized using a combination of 4-node CAX4R and 3-node CAX3 axisymmetric finite elements and 4-node CINAX4 axisymmetric semi-infinite elements. The model has 6620 elements and 6691 nodes. After obtaining converged values for the interested output variables, the mesh is optimized to be finer right below the penetrating ball and coarser in far field. The high density mesh region includes elements as small as $10\ \mu\text{m}$ to provide the suitable spatial resolution for the output variables. Axisymmetric boundary condition is applied to the left edge of the mesh. Semi-infinite elements as quiet boundary along the back and bottom surfaces are implemented to allow for stress waves to pass through a non-reflective boundary.

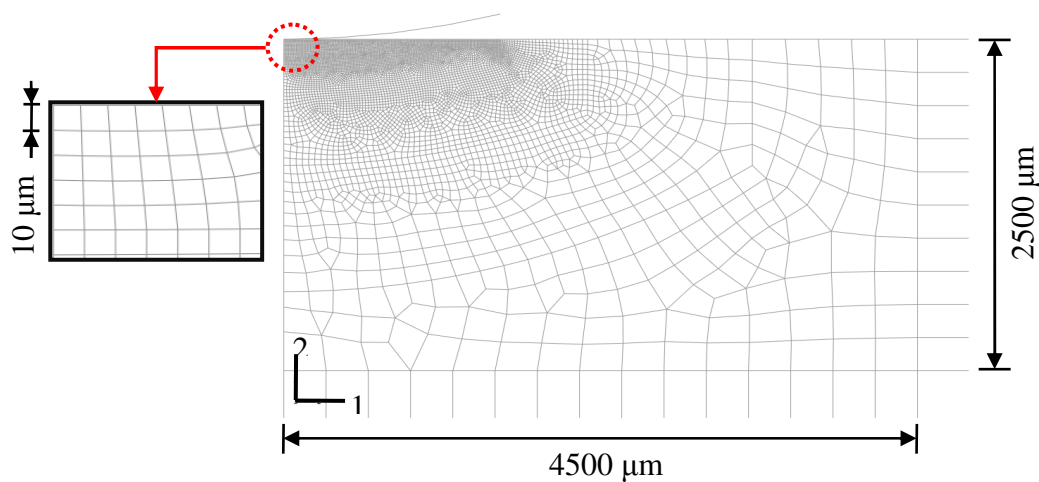


Fig. 7.7 Axisymmetrical FE simulation of indentation using hydrostatic burnishing tool

The friction coefficient in ball-workpiece interface is taken to be 0.01 to simulate highly lubricated interface due to the presence of hydraulic oil all the time through burnishing process.

To avoid the occurrence of highly distorted elements, Arbitrary Lagrangian-Eulerian (ALE) adaptive meshing is used on upper left corner of the workpiece. A total of five simulation cases are performed covering five hydraulic pressures 2, 3, 4, 5, and 6 MPa. This allows for a parametric evaluation of the effect of hydraulic pressure on the dent geometry, elastic recovery, residual stress, strain, and temperature.

7.5.2. Material model

The ISV plasticity model developed by Bammann, Chiesa, and Johnson [31], explained in section 5.2.2, is used to describe the deformation state of the material in this investigation.

7.6. Simulation results and discussion

7.6.1. Dent geometry

The simulated and measured dent profiles for various hydraulic pressures are shown in figure 7.4. Generally, there is a good agreement between measured and simulated profiles. As can be seen in figure 7.3, mouth opening of dents is not exactly circular which might be associated with anisotropy of the material properties. Considering this fact and also the inherent uncertainty in 2D profiling of a 3D dent using a mechanical stylus, the small discrepancy between simulated and experimental profiles and the observed variance in measured dent profiles (presented by Max and Min profiles) might be explained.

As is shown in figure 7.8, the actual depth of penetration is larger than the one measured after tool removal. This is due to elastic part of the deformation which recovers upon tool

removal. The amount of elastic recovery increases by increasing hydraulic pressure. This confirms the more energetic acoustic emissions detected by AE sensor under higher hydraulic pressures in section 7.4. On average, there is about 8% recovered deformation.

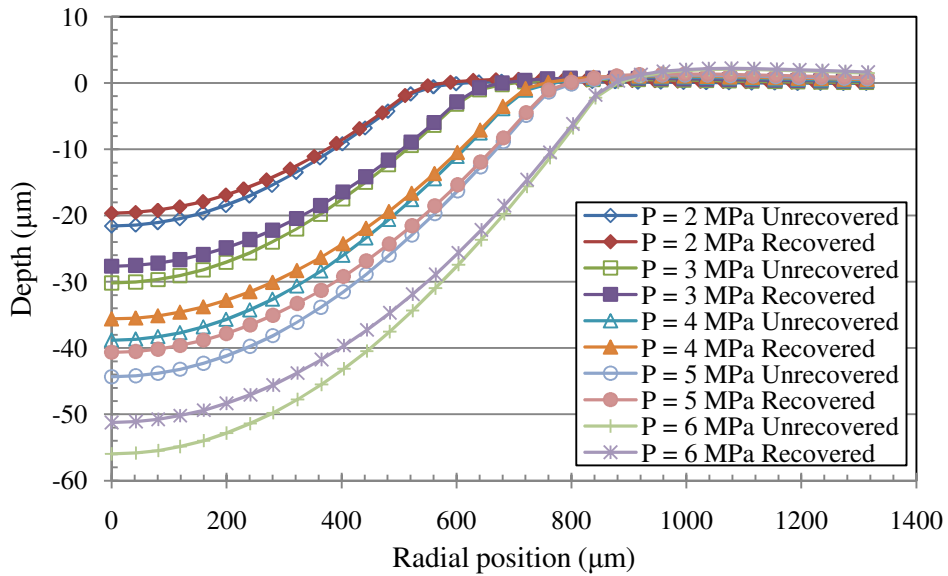


Fig. 7.8 Simulated half dent profiles before and after recovery

7.6.2. Temperature

Pressurized hydraulic oil leaks through the tip of the burnishing tool all the time during the process. This dual purpose oil serves as both lubricant and coolant. So, besides lubricating the contact between ball and sample, it carries away the heat generated due to plastic deformation. This means hydrostatic burnishing is an isothermal deformation process. As figure 7.9 shows, the maximum temperature rise is about 5 to 6 C° and happens at 250 μm depth for the

applied pressure range. As such, stress and strain distributions in following sections can be good approximations of residual stresses and strains.

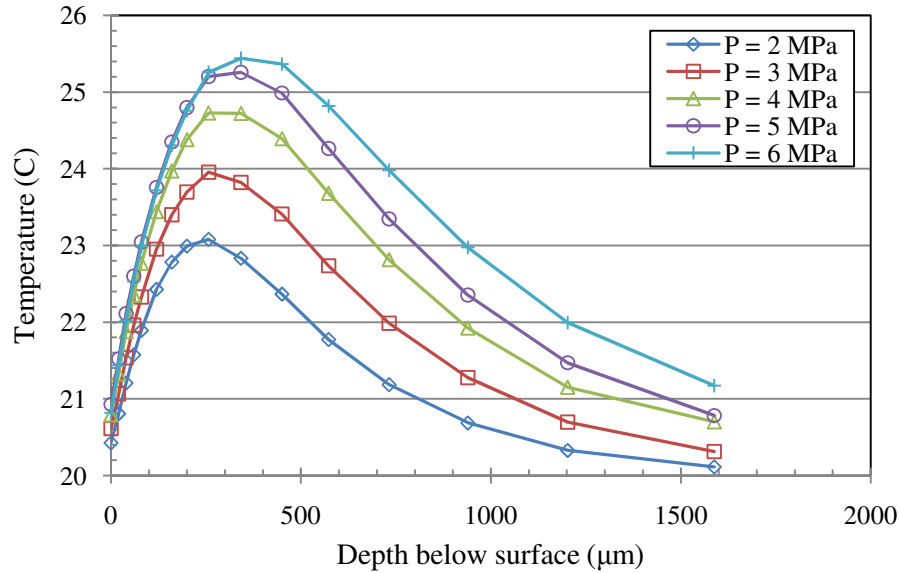


Fig. 7.9 Temperature distribution at different hydraulic pressures

7.6.3. Strains

The residual strain state along the axis of symmetry is composed of tensile strains in radial (LE11) and circumferential (LE33) directions, which are exactly identical in terms of magnitude and distribution due to axial symmetry, and a compressive axial strain (LE22). This is reasonable based on Poisson effect since by pushing the material downward along the axis of symmetry it will stretch out in the radial and circumferential directions. As is shown in figure 7.10, the maximum tensile and compressive residual plastic strains happen in about 250 µm depth. This is same as the depth in which maximum temperature happens in figure 7.9. This

correspondence indicates that plastic deformation is the main source of heat generation in this case and friction contribution is negligible. Presence of hydraulic oil which functions as both lubricant and coolant is the physical reason for that. Plastic deformation happens isothermally and that is the reason for only a few degrees rise in temperature. Although maximum tensile and compressive residual plastic strains do not penetrate any deeper than 250 μm by increasing hydraulic pressure, but their magnitude increases from 1.2% to 2.2% and from -2.4% to -4.4%, respectively.

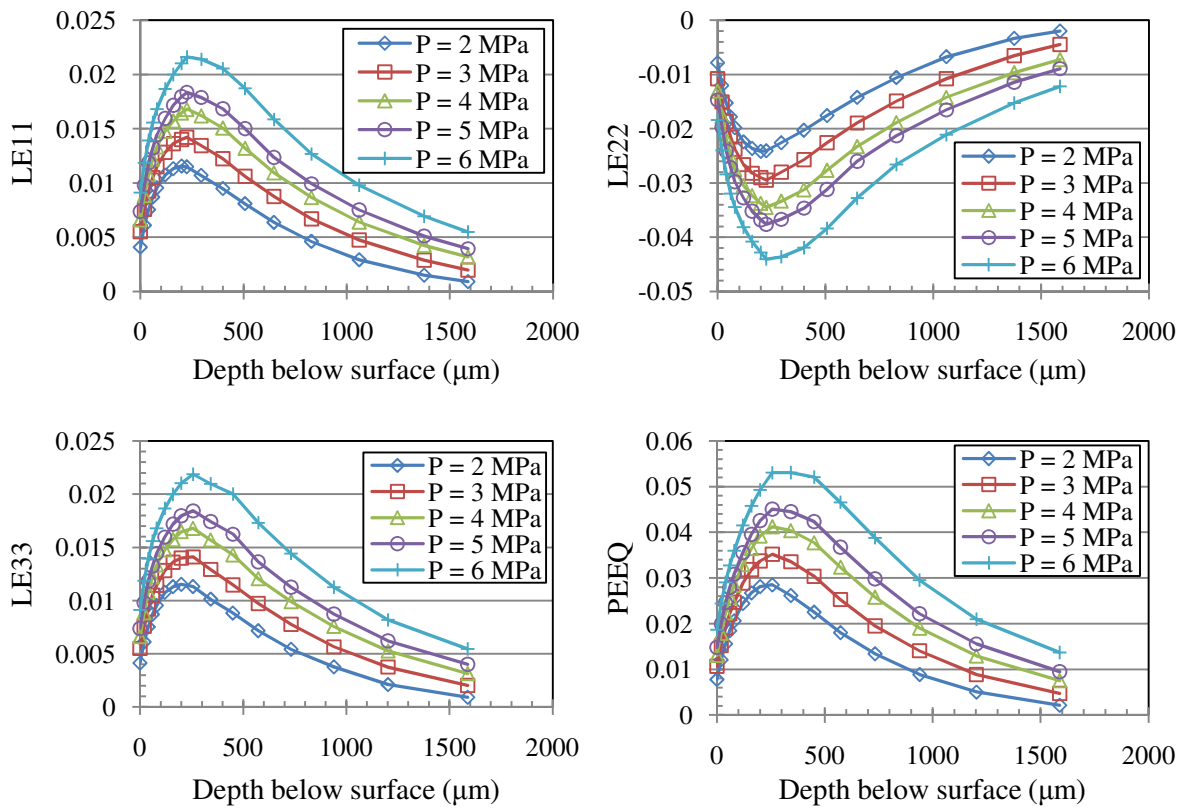


Fig. 7.10 Strain distributions at different hydraulic pressures

Effective plastic strain (PEEQ) in figure 7.10 represents this multi-axial strain state with an equivalent value in uniaxial tension test. It rises to 5.4% from 2.8% by increasing the hydraulic pressure. It is noticeable that the depth of plastically deformed zone is almost above 1.5 mm while a sharp gradient of strain distribution happens in the first 250 μm . This indicates the fact that deformation is concentrated close to surface in hydrostatic burnishing process.

7.6.4. Stresses

Residual stress state starts with pure tension at surface and ends up with pure compression below surface for 2, 3, and 4 MPa pressures. As figure 7.11 shows, all the residual stress components are tensile within the first 10 μm . Radial (S11) and circumferential (S33) components start to be compressive and remain compressive beyond 10 μm depth while axial stress (S22) is still tensile up to 200 μm depth. In a depth below 200 μm all stress components are compressive. For 5 and 6 MPa pressures, radial and circumferential components are always compressive while axial stress has the same profile as before. The maximum tensile stress of 17 MPa, in both radial and circumferential directions, happens on the surface under 2 MPa pressure. For the same pressure, the maximum axial tensile stress of 5 MPa occurs at 60 μm below surface. Radial and circumferential components like their strain counterparts are exactly same in terms of magnitude and distribution due to axial symmetry of the case.

While increasing hydraulic pressure does not show a significant influence on the magnitude of the maximum compressive residual stress in radial and circumferential directions (-83 MPa), but it increases the depth, in which maximum stress happening, from 600 μm to 1100 μm . This is not the same location that maximum radial and circumferential strains are happening which is the reason why this process is called low plasticity burnishing (LPB). As the simulation

results predict maximum radial and circumferential plastic strains are in 200 μm depth while maximum compressive stress counterparts are happening in locations 3 to 6 times deeper. Producing very deep compressive layers with comparatively shallow layers of highly deformed material is the unique characteristic of this process which affects the stability of compressive residual stresses and the fatigue performance of products under service load (both thermal and mechanical) [20,24,26-28].

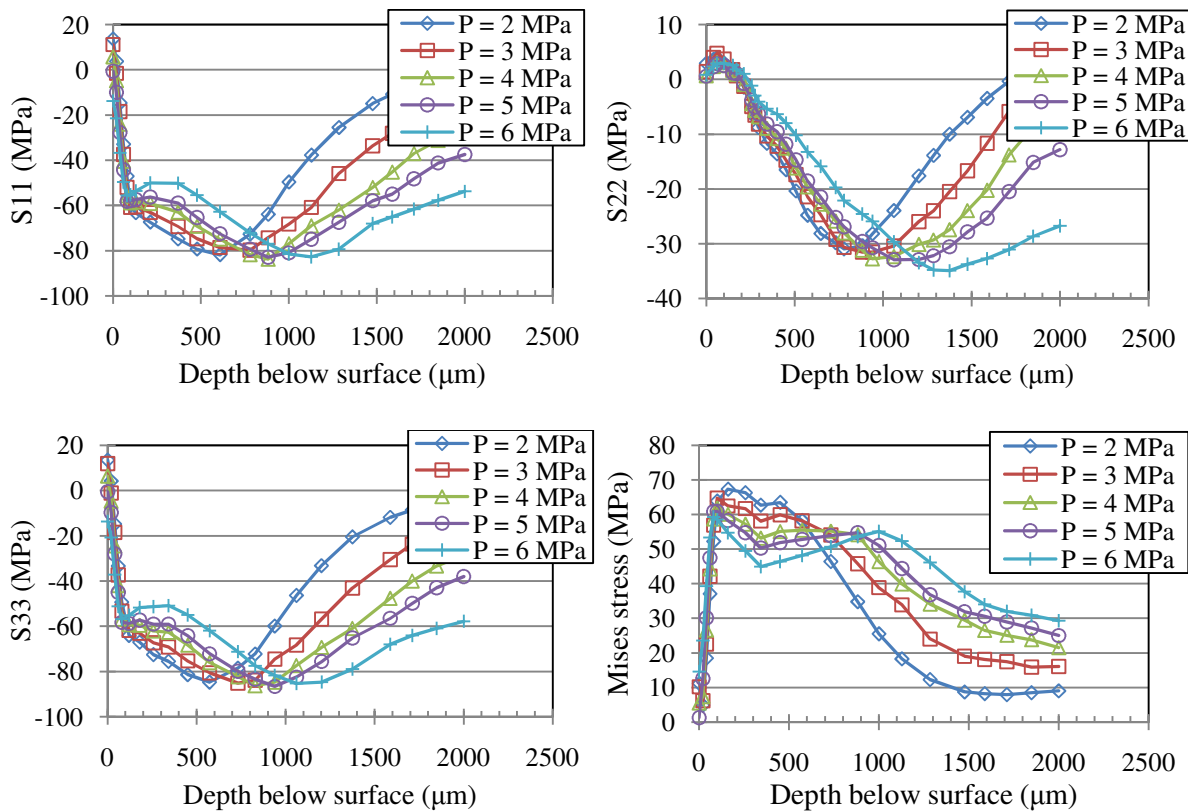


Fig. 7.11 Residual stress distribution at different hydraulic pressures

Maximum compressive axial stress occurs in deeper locations from 800 μm to 1400 μm by increasing the hydraulic pressure from 2 to 6 MPa. The change in magnitude of maximum axial stress is small and about -5 MPa starting from -31 MPa at 2 MPa pressure. The von Mises stress is the counterpart of PEEQ for multi-axial stress state. These two quantities represent a multi-axial state with an equivalent uniaxial state. In this case, even though the problem has a compressive nature but in terms of equivalent uniaxial representation it is a simple tension test noticing that both von-Mises stress and PEEQ are positive values.

While the general trend is increase in PEEQ and von Mises values with pressure, there is a deviation from general trend. From 100 μm to about 700 μm , Mises stress decreases with increasing depth and then rises again. It is in this region that higher hydraulic pressure produces smaller rather than larger von Mises, while it still causes larger PEEQ. The maximum von Mises happens in 100 μm depth and decreases from 68 MPa to 60 MPa with increasing pressure.

7.7. Conclusions

Numerical and experimental evaluations of process mechanics in hydrostatic burnishing of the novel Mg-Ca_{0.8} biomaterial are performed. Followings are the conclusions of this study:

- Actual normal force is lower than the one calculated based on theoretical principals of hydrostatics. It is attributed to pressure loss at the tip of the burnishing tool. This discrepancy increases with increasing hydraulic pressure. On average, actual normal force is 23% lower than theoretical value for Ecoroll HG13 tool used in this study.

- Internal state variable (ISV) plasticity model shows successful in predicting the novel Mg-Ca_{0.8} biomaterial mechanical behavior. The developed 2D axisymmetric FEM model can predict the dent geometry closely.
- Numerically predicted amount of elastic recovery shows increase with increasing hydraulic pressure. This is verified experimentally by recorded acoustic signals. The energy and frequency content of these signals get larger by increasing the hydraulic pressure. This is due to more acoustic emission under higher plastic and consequently elastic deformation. On average, there is 8% of elastic recovery for this biomaterial in the applied pressure range.
- The predicted in-depth distribution of temperature field shows about 5 to 6 C° increase in the applied pressure range. This validates the assumption of isothermal deformation in this application. The dual purpose oil leaks out all the time during hydrostatic burnishing. It lubricates and cools down the tool-workpiece interface simultaneously.
- The maximum axial tensile and radial compressive residual plastic strains are predicted to happen in depth of 250 μm. The depths of maximum residual plastic strains do not penetrate deeper by increasing hydraulic pressure but their magnitude almost doubles in the applied pressure range.
- The residual stresses are predicted to be all compressive below 200 μm depth while for some pressures there are small tensile residual stresses in the surface and also first 10 to 60 μm below surface. Increase in hydraulic pressure does not affect the magnitude of residual stresses but their depth. Radial and circumferential residual stresses (-83 MPa) are more compressive than axial ones (-33 MPa).
- There is high gradient of plastic strain (~ 4%) in first 250 μm depth. With respect to the high ductility that this biomaterial shows in compressive mode, this is a small amount of

deformation which happens in shallow depth comparing to 83 MPa compressive residual stresses in depth of 1000 μm . Producing large amounts of deep compressive layers by small amount of shallow deformation is a unique characteristic of hydrostatic burnishing process which is well predicted by the developed FEM model.

References

1. A. Gefen, Computational simulations of stress shielding and bone resorption around existing and computer-designed orthopaedic screws, *Medical & Bio. Eng. & Comp.* 40 (2002) 311-322.
2. J. Nagels, M. Stokdijk, P.M. Rozing, Stress shielding and bone resorption in shoulder arthroplasty, *J. Shoulder and Elbow Surgery* 12 (2003) 35-39.
3. H. Isaksson, A.L. Lerner, Mathematical modeling of stress shielding with bioresorbable materials for internal fracture fixation, *Bioengineering Conf.* (2003) 1041-1042.
4. H.G. Seiler, *Handbook on toxicity of inorganic compounds*, 1st edition, CRC Press, (1987).
5. G. Song, Control of biodegradation of biocompatible magnesium alloys, *Corrosion Science* 49 (2007) 1696-1701.
6. G. Song, S. Song, A possible biodegradable magnesium implant material, *Adv. Eng. Mater.* 9 (2007) 298-302.
7. Z. Li, X. Gu, S. Lou, Y. Zheng, The development of binary Mg-Ca alloys for use as biodegradable materials within bone, *Biomaterials* 29 (2008) 1329-1344.
8. B. Denkena, F. Witte, C. Podolsky, A. Lucas, Degradable implants made of magnesium alloys, *Proc. 5th Euspen Int. Conf.*, Montpellier, France (2005).
9. Y.B. Guo, M. Salahshoor, Process mechanics and surface integrity by high-speed dry milling of biodegradable magnesium-calcium implant alloys, *CIRP Ann.-Manuf. Tech.* 59 (2010) 151-154.
10. N. von Der Hoh, D. Bormann, A. Lucas, B. Denkena, C. Hackenbroich, A. Meyer-Lindenberg, Influence of different surface machining treatments of magnesium-based

- resorbable implants on the degradation behavior in rabbits, *Adv. Eng. Mater.* 11 (2009) B47-54.
11. B. Denkena, A. Lucas, Biocompatible magnesium alloys as absorbable implant materials-adjusted surface and subsurface properties by machining processes, *Ann. CIRP* 56 (2007) 113-116.
 12. A. Schuh, C. Zeller, U. Holzwarth, W. Kachler, G. Wilcke, G. Zeiler, B. Eigenmann, J. Bigoney, Deep rolling of titanium rods for application in modular total hip arthroplasty, *J. Biomed. Mater. Research Part B: Applied Biomaterials* (2006), DOI 10.1002/jbmb
 13. C. Y. Seemikeri, P. K. Brahmanekar, S. B. Mahagaonkar, Low plasticity burnishing: an innovative manufacturing method for biomedical applications, *J. Manuf. Sci. Eng.* 130 (2008) 021008/1-8.
 14. P. Prevey, D. McNulty, J. Carr, P. Sade, A. Craft, Fatigue strength enhancement of Ti-6Al-4V ELI femoral distal stems using low plasticity burnishing, *Proc. of ASM MPMD (Materials & Processes for Medical Devices) Conference and Exposition, Minneapolis, MN* (2009).
 15. J. A. Disegi, C. Sax, Effect of low plasticity burnishing on the fatigue strength of spinal rods, *Proc. of ASM MPMD (Materials & Processes for Medical Devices) Conference and Exposition, Minneapolis, MN* (2009).
 16. A. T. Bozdana, N. N. Z. Gindy, Comparative experimental study on effects of conventional and ultrasonic deep cold rolling processes on Ti-6Al-4V, *Mater. Sci. Tech.* 24 (2008) 1378-1384.
 17. N. Tsuji, S. Tanaka, T. Takasugi, Evaluation of surface-modified Ti-6Al-4V alloy by combination of plasma-carburizing and deep-rolling, *Mater. Sci. Eng. A* 488 (2008) 139-145.
 18. N. Tsuji, S. Tanaka, T. Takasugi, Effect of combined plasma-carburizing and deep rolling on notch fatigue property of Ti-6Al-4V alloy, *Mater. Sci. Eng. A* 499 (2009) 482-488.
 19. G. H. Majzoobi, K. Azadikhah, J. Nemati, The effects of deep rolling and shot peening on fretting resistance of Aluminum-7075-T6, *Mater. Sci. Eng. A* 516 (2009) 235-247.
 20. C. M. Gill, N. Fox, P. J. Withers, Shakedown of deep cold rolling residual stresses in titanium alloys, *J. Phys. D: Appl. Phys.* 41 (2008) 174005 (5pp).
 21. I. Nikitin, M. Besel, Correlation between residual stress and plastic strain amplitude during low cycle fatigue of mechanically surface treated austenitic stainless steel AISI 304 and ferritic-pearlitic steel SAE 1045, *Mater. Sci. Eng. A* 491 (2008) 297-303.

22. I. Nikitin, I. Altenberger, Comparison of the fatigue behavior and residual stress stability of laser-shock peened and deep rolled austenitic stainless steel AISI 304 in the temperature range 25-600 C, *Mater. Sci. Eng. A* 465 (2007) 176-182.
23. P. Juijerm, I. Altenberger, Effective boundary of deep-rolling treatment and its correlation with residual stress stability of Al-Mg-Mn and Al-Mg-Si-Cu alloys, *Scripta Materialia* 56 (2007) 745-748.
24. N. Jayaraman, D. J. Hornbach, P. S. Prevey, Mitigation of fatigue and pre-cracking damage in aircraft structures through low plasticity burnishing, *Proc. ASIP*, Palm Springs, CA (2007).
25. P. S. Prevey, R. A. Ravindranath, M. Shepard, T. Gabb, Case studies of fatigue life improvement using low plasticity burnishing in gas turbine engine applications, *J. Eng. Gas Turbines and Power* 128 (2006) 865-872.
26. P. S. Prevey, J. T. Cammett, The influence of surface enhancement by low plasticity burnishing on the corrosion fatigue performance of AA7075-T6, *Int. J. Fatigue* 26 (2004) 975-982.
27. J. E. Scheel, D. J. Hornbach, P. S. Prevey, Safe life conversion of aircraft aluminum structures via low plasticity burnishing for mitigation of corrosion related failures, *Department of Defense Corrosion Conf.*, Gaylord National, Washington DC (2009).
28. P. S. Prevey, D. J. Hornbach, N. Jayaraman, Controlled plasticity burnishing to improve the performance of friction stir processed Ni-Al bronze, *Mater. Sci. Forum* 539 (2007) 3807-3813.
29. B. Denkena, R. Meyer, B. Breidenstein, Development of combined manufacturing technologies for high-strength structure components, *Advanced Mater. Research* 22 (2007) 67-75.
30. E. Brinksmeier, M. Garbrecht, D. Meyer, Cold surface hardening, *CIRP Annals – Manuf. Tech.* 57 (2008) 541-544.
31. D. J. Bammann, M. L. Chicsa, G. C. Johnson, Modeling large deformation and failure in manufacturing processes, *Theor. App. Mech.* (1996) 359 – 376.
32. M. Salahshoor, Y. B. Guo, Numerical modeling and simulation of high speed machining biomedical magnesium calcium alloy, *Proc. of ASM MPMD (Materials & Processes for Medical Devices) Conference and Exposition*, Minneapolis, MN (2009).
33. ABAQUS User's Manual, 2008, HKS, Inc., Ver. 6.8, Providence, RI.

CHAPTER 8

SURFACE INTEGRITY OF BIODEGRADABLE MAGNESIUM-CALCIUM ORTHOPEDIC IMPLANT BY BURNISHING

Abstract

Magnesium-Calcium (Mg-Ca) alloy as an emerging biodegradable implant material has received considerable attentions in orthopedic fixation applications. The biodegradable Mg-Ca alloys avoid stress shielding and secondary surgery inherent with permanent metallic implant materials. They also provide sufficient mechanical strength in load carrying applications as opposed to biopolymers. However, the key issue facing a biodegradable Mg-Ca implant is the fast corrosion in the human body environment. The ability to adjust degradation rate of Mg-Ca alloys is critical in the successful development of biodegradable orthopedic materials. Burnishing as a low plastic deformation process is a promising technique to tune surface integrity of Mg-Ca implant surface for biodegradation control. However, the poor ductility of Mg-Ca alloys imposes a great challenge for burnishing. This study focuses on the basic understanding of surface mechanical behavior of burnished biodegradable Mg-Ca_{0.8} alloy. The effects of burnishing parameters, i.e., pressure, feed, speed, number of path, and burnishing pattern on surface integrity factors such as surface topography, roughness, microhardness, microstructure, and residual stresses are investigated. The burnished surfaces are shinier and smoother than the as-machined ones. The Mg-Ca alloy can be safely burnished at suitable burnishing conditions since no cracks at surface and in the subsurface. Microstructure including grain size does not show a

noticeable change after burnishing. The machined surfaces are harder than the burnished ones down to the deep subsurface (~200 μm) as opposed to shallow hardened depth (~50 μm) in cutting. Residual stresses are highly compressive especially at low burnishing pressure.

8.1. Introduction

The development of biodegradable orthopedic implants has been one of the important areas in biomedical engineering. Biodegradable and biocompatible implants can gradually be dissolved and absorbed in the human organism after implantation. Compared with a traditional permanent implant made of steel, titanium, cobalt alloys, a biodegradable material will represent an appropriate solution for potential local inflammation, permanent physical irritation, and the need for additional surgery to remove permanent implants. Furthermore, conventional metal implants are too stiff and will cause stress shielding effect [1-5]. Current biodegradable implants are mainly made of polymers such as poly-L-Lactic acid. However, these polymer based implants usually have low mechanical strength which has driven researchers to seek for biodegradable metallic substitutes. Magnesium (Mg) and its alloys are among the most interested options.

Magnesium is an element essential to human body. Intake of a certain amount of magnesium (300~400 mg/day) is normally required for the human body's metabolic activities [6]. The direct corrosion product of magnesium, Mg^{2+} , would be easily absorbed or consumed by the human body. No side effect of Mg^{2+} overdose has been found in human body [7,8].

Hydrogen evolution and alkalization resulting from Mg corrosion are the most critical obstacles in using magnesium as an implant material. A straightforward strategy to tackle these

difficulties is to reduce the corrosion rate. A biodegradable magnesium implant needs to corrode at a controllable rate. Alloying is one of the possible solutions to reduce the corrosion rate of Mg in human body. A concern with the alloying approach is biocompatibility of alloying elements. Alloying elements must not generate toxic, carcinogenic, or mutagenic products.

The previous studies on biomedical magnesium alloys are mainly focused on the Mg-Al [7,9-12] and Mg-RE [12] alloy systems. Aluminum (Al) and Rare Earth (RE) elements seem not to be the best alloying elements [13]. Recently, Calcium (Ca) has become a promising alloying element in non-commercial binary Mg-Ca alloys for biodegradable implants [13-19]. It is well known that Ca is a major component in human bone and Ca is also essential in chemical signaling with cells [20]. Ca has a low density (1.55 g/cm^3) which endues the Mg-Ca alloy system with the advantage of similar density to bones. In this context, Ca in Mg-Ca alloys will produce hydroxyapatite (HA) as corrosion product on the surface of the implant. HA mineral is a naturally occurring form of calcium apatite with the formula $\text{Ca}_{10}(\text{PO}_4)_6(\text{OH})_2$ and has close resemblance to the chemical and mineral components of teeth and bone. As a result of this similarity it stimulates bone cells to attack the implant surface and make proper bonding [19,21].

The other possible approach to control the corrosion rate of Mg alloys is mechanical surface treatment using different types of manufacturing processes. Burnishing as a novel surface treatment process has attracted a large attention lately. This process includes a spherical socket to support a smooth free-rolling ball that is pressed and rolled along the surface which deforms the workpiece surface into a state of compression. It is characterized by unique combination of three physical effects, which are production of deep and stable *compressive residual stresses*, *work hardening* or increase in surface/subsurface microhardness, and burnishing or decreasing surface roughness and micronotches. All these effects happen on close to surface layers. Burnishing can

be performed in conventional machine shop environments on CNC machine tools and in this context it is affordable and compatible with the manufacturing environment.

Denkena and Lucas [15] tried to control the corrosion of the magnesium implant in the organism by burnishing and ultimately to achieve adaptable degradation profile for various medical applications. Schuh et al. [22] evaluated burnishing of titanium alloy rods as a possible alternative to shot peening in treating the mating surfaces of Morse tapers of modular hip endoprostheses. Their motive was to avoid the contamination of shot peened surfaces which can lead to enhanced corrosion and third body wear. Seemikeri et al. [23] studied the effect of burnishing process parameters i.e. number of passes, ball diameter, pressure, and speed on surface and subsurface characteristics and fatigue performance of AISI 316L steel which is most commonly used in prosthesis. Prevey et al. [24] applied burnishing process to titanium distal stem tapers, used in a modular hip construct, to provide increased fatigue strength and improved tolerance to fretting damage. Disegi and Sax [25] determined the effect of burnishing on the fatigue strength of spinal rods utilizing a cantilever fatigue testing procedure.

The majority of burnished materials are high strength alloys. As a low plastic deformation process, burnishing could be a promising technique to tune surface integrity of Mg-Ca implant surface for biodegradation control. However, the poor ductility of Mg-Ca alloys imposes a great challenge for burnishing. The novelty of this study can be manifested by three aspects: a) The biodegradable Mg-Ca_{0.8} alloy; b) The synergistic cutting-burnishing process to tune surface integrity; and c) The fundamental understanding on surface mechanical behavior of burnished biodegradable Mg-Ca_{0.8} alloy. A special attention to whether surface and subsurface crack happens at high burnishing pressure and/or patterns was addressed due to the poor ductility of Mg alloys.

The specific objectives include the effects of burnishing parameters, i.e., pressure, feed, speed, number of path, and burnishing pattern on surface integrity factors such as surface topography, roughness, microhardness, microstructure, and residual stresses. The significance of this work is in several folds. First, since burnishing of medical device is in its scientific infancy, this study explores its process capabilities in processing light metallic biomaterials. Second, surface integrity characteristics of Mg-Ca_{0.8} biomaterial processed by burnishing are not understood at present, this research will be timely to address the fundamental issue. Lastly, the enhanced surface integrity is expected to significantly improve biodegradation performance of an Mg-Ca implant, which is beyond the scope of this work.

8.2. Background on surface integrity by burnishing

Although using burnishing in medical device manufacturing applications is new and there are not many of research results for that in literature, but its automotive and aerospace applications have been initiated earlier with more published research results. Prevey et al. [26] presented developed fatigue performance and residual stress data for titanium, iron, and nickel based aero-turbine engine alloys which are treated by burnishing. In comparison to conventional shot peening (SP) process, burnishing produces higher and deeper compressive residual stresses with less amount of cold work. Severe plastic deformation in SP makes compressive residual stresses less stable under mechanical and thermal loading which a typical part will be exposed to in aerospace applications. They believe more stable compressive residual stresses will be achieved by minimizing the amount of cold work produced to make them.

The ease of implementation in standard CNC machining centers offers the possibility of employing burnishing as an effective means of mitigating corrosion fatigue and pitting fatigue initiated failures in aircraft components without altering either material or design [27]. Applied locally to high stress fatigue prone locations in aging aircraft, burnishing could extend the service life of aircraft structural components, reduce the total cost of fleet ownership, and improve fleet readiness.

Prevey and Cammett [28] demonstrated that burnishing prior to typical marine environment corrosion, i.e. salt fog pitting or active corrosion fatigue in 3.5% NaCl solution, substantially improves the fatigue performance of the aluminum alloy 7075-T6 widely used in structural aircraft applications. These corrosions reduced the fatigue endurance limit of end-milled 7075-T6 to the half of its original fatigue strength. Performing burnishing right after end-milling increased the endurance limit over three times in the same corrosive environment.

It is shown that there is a maximum pit depth threshold for aircraft aluminums which is dependent on the surface treatment used. The depth of compression from burnishing greatly exceeds the maximum corrosion pit depth in the studied materials therefore preventing failure from pitting or cracking and ensuring safe-life operation. In this context, burnishing can be used as a repair treatment for pre-damaged specimens [29].

In other study, Prevey et al. [30] applied burnishing to friction stir processed Ni-Al Bronze to produce a depth of compression of 2.5 mm and a maximum subsurface magnitude of -150 ksi. The local heating produced by friction stir processing (FSP) can leave a fusion zone with reduced mechanical properties and a heat affected zone with tensile residual stresses that can be deleterious to fatigue performance.

Burnishing is a novel process and it needs an extensive study of the effect(s) of various process parameters, e.g. lateral feed, speed, force, ball diameter, tool path, lubricant, etc., on surface integrity and product performance to develop the required database for different materials. Lopez et al. [31] applied burnishing to reduce the roughness of surfaces obtained by ball-end milling of two materials, P20 low carbon steel (32 HRC) and the nickel alloy Inconel 718 (42 HRC, precipitation hardened). They concluded that using a large radial width of cut in end milling followed by small step over during burnishing can produce the acceptable final roughness. For same process parameters compressive cold work is greater and deeper in the Inconel 718 than in the steel. Seemikeri et al. [32] studied the effect of burnishing on surface integrity and fatigue life of AISI 1045 material in terms of evaluating the combined effects of burnishing process parameters, identifying the predominant parameter, establishing their order of significance, and setting the levels of different parameters to minimize surface roughness and/or maximize surface hardness and fatigue life. Rao et al. [33] did a similar experimental parametric study on HSLA dual-phase steel. Their result also indicated that burnishing parameters have significant effect on the surface hardness and wear resistance.

In surveying the literature on mechanical surface treatment processes, one will come across another process named deep rolling or shortly DR. This process, which is developed by Ecoroll, is very similar to the burnishing process developed by Lambda Technologies in terms of working principal [34], even though it is claimed that DR produces more cold work than burnishing [26]. High levels of cold work leave a severely deformed surface layer with a high dislocation density that adversely affects the thermal and mechanical stability of compressive layer. However, Gill et al. [35] report lower levels of cold work as a promising potential of DR

where they compare this process with shot peening (SP) in terms of compressive residual stress layers' depth and amount of cold work.

Bozdana and Gindyet [34] proposed a newly developed technique utilizing ultrasonic vibrations, named ultrasonic deep cold rolling (UDCR) process and present the experimental results on the treatment of Ti-6Al-4V using conventional deep cold rolling (CDCR) and UDCR processes. UDCR uses superimposed dynamic forces onto considerably reduced static forces applied on a part surface and it is believed to provide technological benefits for the treatment of thin walled aerospace components, such as turbine blades and discs, to be carried out without geometry distortion in addition to improved fatigue life and resistance to failure mechanisms which are common outcomes of CDCR.

Gill et al. [35] measured the level of residual stress relaxation in deep cold rolled samples of titanium alloys Ti-6Al-4V and IMI679, caused by low cycle, constant strain amplitude fatigue at both room and elevated temperature. They believe their experimental loads and temperatures replicate the most extreme conditions expected in the compression stages of a gas turbine engine. They observed that residual stress relaxation was limited to a depth of 400–500 μm and thus the depth of compressive residual stress was unaffected by relaxation. For room temperature low cycle fatigue (LCF), residual stress relaxation was less than 50% of the peak compressive residual stress. For high temperature exposure residual stress relaxation was less than 40% of the peak compressive residual stress. For high temperature LCF relaxation was greater than either thermal exposure or fatigue alone and about 70% of the peak residual stress.

Tsuji et al. [36] used deep rolling to induce compressive residual stress in plasma-carburized Ti-6Al-4V alloy sample. Plasma surface diffusion processes such as plasma-carburizing and nitriding have been used to improve tribological properties of titanium and its

alloys. However, the improvement of fatigue strength by these processes has not been successful due to brittleness introduced in the high-hardness surface layer and the disappearance of compressive residual stress and grain growth by heating. The fatigue properties and wear resistance of Ti-6Al-4V alloy modified by a combination of low-temperature plasma-carburizing and deep-rolling were significantly improved in comparison with those of the unmodified Ti-6Al-4V alloy. Knowing that fatigue fracture is normally affected by stress concentrators such as holes, grooves and fillets and also the fact that most engineering designs have notch-like features, in other study [37], they tried to investigate the effect of combined plasma-carburizing and deep rolling on notch fatigue property of Ti-6Al-4V alloy and noticed remarkable fatigue strength enhancement by subsequent deep-rolling.

Based on the fact that stress relaxation behavior and the stability of the residual stress during fatigue loading depend on the mechanical surface treatment method, Nikitin and Besel [38] used three different surface treatments and investigated their effects on the low cycle fatigue behavior of austenitic stainless steel (AISI 304) and ferritic-pearlitic steel (SAE 1045). They found that consecutive deep rolling and annealing as well as high temperature deep rolling produce more stable near-surface stress states than conventional deep rolling at room temperature. They measured the plastic strain amplitudes during fatigue loading and showed that they correlate well with the induced residual stress, its relaxation, and consequently the fatigue lifetime. In other study [39], they determined the thermal and mechanical fractions of residual stress relaxation during isothermal fatigue at elevated temperatures. They also investigated the fatigue behavior, stability of the residual stress state, and new-surface microstructure of laser-shock peened and deep rolled austenitic stainless steel AISI 304 in the temperature range 25–600 C at a cycling frequency of 5 Hz [40]. They found the residual stress state and work hardening

induced by laser-shock peening were less stable under isothermal cyclic loading at elevated temperatures as compared to the deep rolled condition. At elevated test temperatures, the fatigue lifetime of the deep rolled condition was higher than that of the laser-shock peened case due to more stable near-surface microstructures, e.g. nanocrystalline layers, deformation-induced martensite as well as higher dislocation densities. Juijerm and Altenberger [41] found that the near-surface work hardening is the major factor influencing the fatigue lifetime of the deep-rolled aluminum alloys. Their results showed work hardening states, characterized by the full width at half maximum (FWHM) values of the X-ray diffraction peaks, were considerably more stable than macroscopic residual stresses.

Brinksmeier et al. [42] came up with an innovative approach to improve the machinability of STRIP-steels using deep rolling. This new manufacturing technology eliminates the thermal hardening and combines hardening and surface finishing in one step on the same machine tool without unclamping the workpiece which causes less distortion in the part and considerable economical savings. In other work to develop combined or hybrid manufacturing technologies, Denkena et al. [43] visioned a project to develop combined tools which could do material cut and surface modification simultaneously. The ultimate goal is a selective surface enhancement of structural components through controlled manipulation of subsurface properties. They have targeted several millimeters of in depth affected zone. Deep rolling is one of the main processes they work on to combine with machining processes such as turning and milling.

This paper deals with an experimental study of burnishing of the novel lab made Mg-Ca_{0.8} alloy. The generated surface integrity characteristics including surface topography, roughness, microstructure, microhardness, and residual stresses are examined and discussed.

8.3. Burnishing experiment

8.3.1. Mg-Ca material

The binary alloying system of magnesium and calcium is the basis for making biodegradable implants out of magnesium [13,14-19]. The alloy Mg-Ca0.8 used in this study contains 0.8wt% of calcium as main alloying element. Due to the inherent poor plasticity of magnesium, which comes from its hexagonal lattice structure [44], it has been tried to improve its plasticity by adding 0.8wt% Ca which gives a high elongation at rupture of about 15%. Higher amount of Ca will decrease the alloy's ductility while it will increase its corrosion resistance [17,18]. Moreover, researchers have suggested Mg-Ca0.8 very promising for biomedical applications through in-vitro and in-vivo tests [14,15,19]. On the other words, there has been some sort of trade-off between corrosion resistance, ductility, and in-vivo function of the alloy in selecting Ca amount. The Mg-Ca0.8 alloy in this study was prepared using the procedure explained in section 3.3.1. The cylindrical samples (38 mm dia. × 12.7 mm thickness) were face milled using carbide inserts at 2400 m/min surface cutting speed, 0.05 mm/rev feed, and 0.2 mm depth-of-cut.

8.3.2. Experiment setup and plan

The burnishing tool used in this study is Ecoroll HG13. It has a ceramic ball on the tip made of silicon nitride 12.7 mm in diameter. This ceramic ball sits on a pressurized hydro cushion which is produced by Ecoroll HGP4.0 hydraulic unit. This unit is capable of producing pressures up to 40 MPa. Based on the technical data provided by manufacturer, a thin layer of pressurized oil will be between ball and its housing all the time during operation and the ball will

roll freely along the sample surface without having a chance to touch its housing. The housing has 10 mm of free stroke to accommodate for elevation changes on sample surface. The power carrying fluid is anti-wear, dual purpose oil Aries 15 which functions as both lubricant and coolant. The top plate of the fixture in figure 8.1 can freely slide vertically and transfer the force to the high accuracy compression load cell (Intertechnology Inc., Model 220 5T) underneath. All the setup shown in figure 8.1 is hooked up on a Bridgeport milling machine.

Four sets of experiments were planned to study the effects of burnishing pressure, lateral feed, burnishing speed, number of path, and burnish pattern on surface integrity characteristics of Mg-Ca_{0.8} biomaterial. The first three sets have different combinations of burnishing parameters with only one varying parameter depending on which parameter's effect was being experimented on that set (Table 8.1). The burnishing pressure, lateral feed, and burnishing speed vary in the range of 2 – 10 MPa, 0.04 – 0.2 mm, and 50 – 890 mm/min, respectively. The second burnish pass in the fourth set can be performed in two different ways as is shown in figure 8.2. Therefore the last set studies the number of pass and burnish pattern effects simultaneously.



Fig. 8.1 Experimental setup of burnishing

Table 8.1 Burnishing test plan

	Sample #	Pressure P [MPa]	Feed f [mm]	Speed V [mm/min]	Pass #	Pattern
Pressure effect	1	2	0.1	890	1	-
	2	4	0.1	890	1	-
	3	6	0.1	890	1	-
	4	8	0.1	890	1	-
	5	10	0.1	890	1	-
Feed effect	6	4	0.04	890	1	-
	7	4	0.06	890	1	-
	8	4	0.08	890	1	-
	9	4	0.1	890	1	-
	10	4	0.2	890	1	-
Speed effect	11	4	0.1	50	1	-
	12	4	0.1	150	1	-
	13	4	0.1	250	1	-
	14	4	0.1	500	1	-
	15	4	0.1	890	1	-
Path effect	16	4	0.1	890	2	A
	17	4	0.1	890	2	B

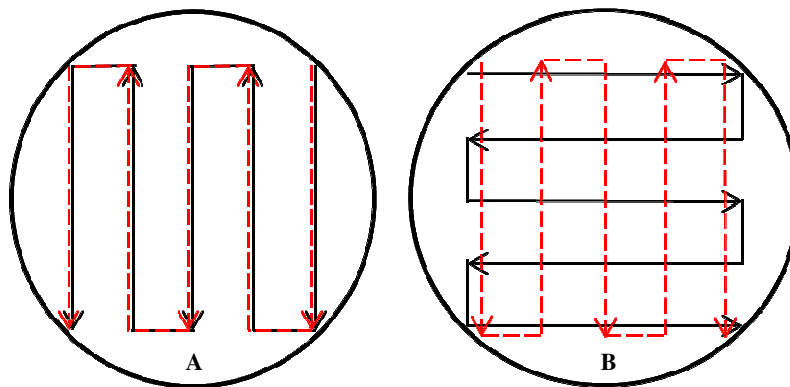


Fig. 8.2 Different burnish patterns; A – 2 parallel pass, B – 2 cross pass

8.4. Results and discussions

8.4.1. Surface topography

Optical images of the burnished surfaces are shown in figures 8.3a, 8.3b, 8.3c, and 8.3d. In general, cutting feed marks left behind from sample preparation stage are less sharp and defined as opposed to as machined case due to burnishing action of the burnishing tool. Starting with 2 MPa pressure at figure 8.3a, cutting feed marks are visible but not as defined as machined surface. Increasing the pressure up to 8 MPa improves the situation but does not eliminate the cutting feed marks totally. Further attempt to demolish cutting feed marks by increasing burnishing pressure will produce cracks along large grains (intragranular cracking) while cutting feed marks are still visible. This speaks on the fact that eliminating pre-existing surface topography left by cutting process at preparation stage is not achievable at least with the current geometry of burnishing ball at the tip of the burnishing tool. The large diameter burnishing ball cannot enter the small valleys made by cutting feed marks. As the result, cutting feed marks are actually hammered on their peaks rather than being burnished. Highly work hardened material at the vicinity of the feed mark profiles resist against further deformation as opposed to softer bulk material they are laid upon (figure 8.4a). As such, deformation proceeds at subsurface layers and produces a wavy surface like the one shown in figure 8.4b. Hence, the burnished surface consists of hammered cutting feed marks laid on waves generated by subsurface plastic deformation. This is clearly visible in the optical image presented in figure 8.4c.

Existing large grains in this alloy [45] makes grain boundaries a suitable location for crack nucleation under high burnishing pressures such as 10 MPa case in figure 8.3a. These cracks will get a chance to grow and propagate through the bulk material and eventually to cause

intragranular fracture under cyclic loads of patient's daily life. The other undesirable effect of applying high burnishing pressures is the possibility of having surface material folded upon itself as shown in figure 8.5 which is detrimental to fatigue life of the implant as well by providing another suitable location for crack nucleation.

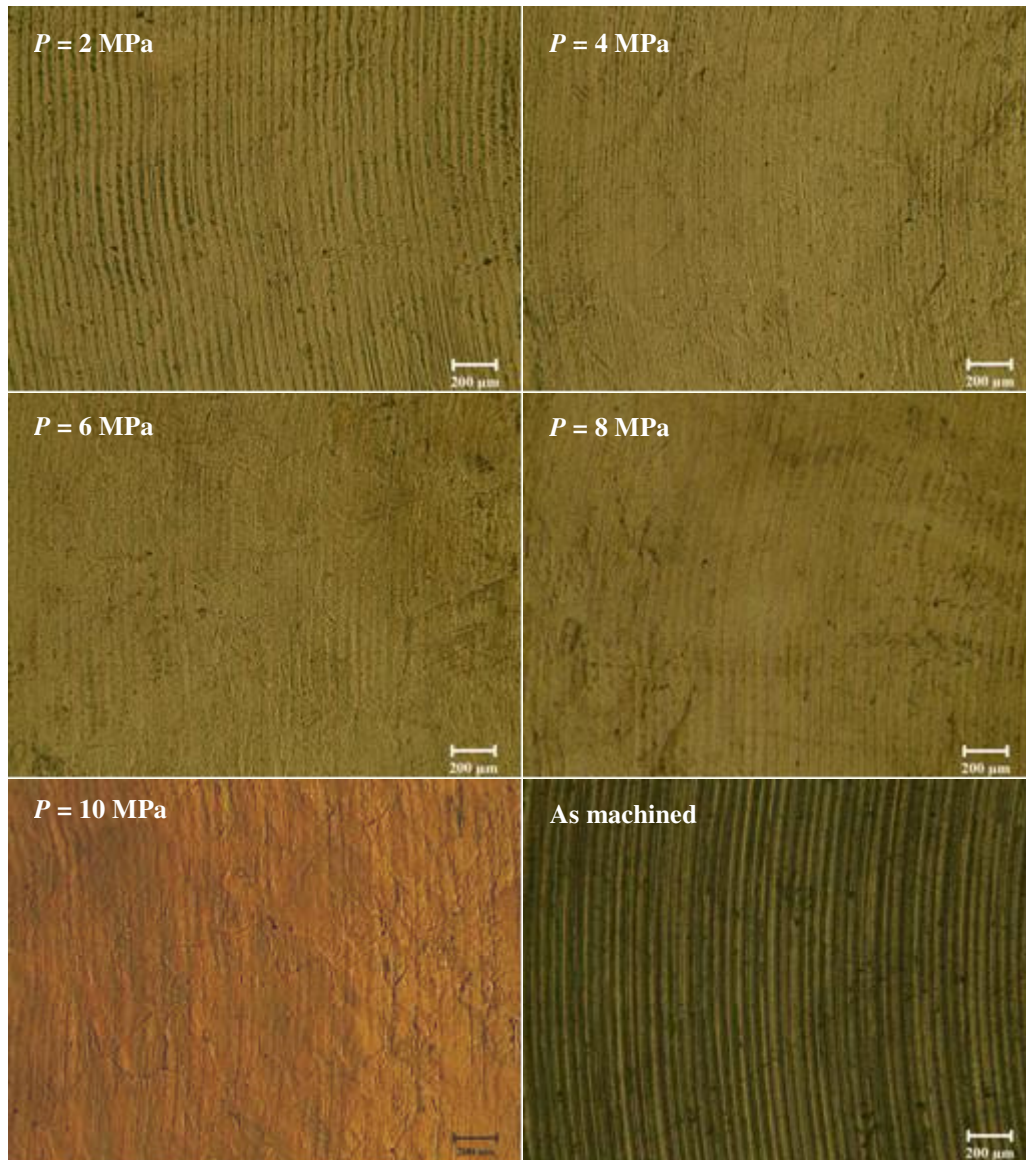


Fig. 8.3a Effect of burnishing pressure on surface topography ($f = 0.1 \text{ mm}$, $v = 890 \text{ mm/min}$)

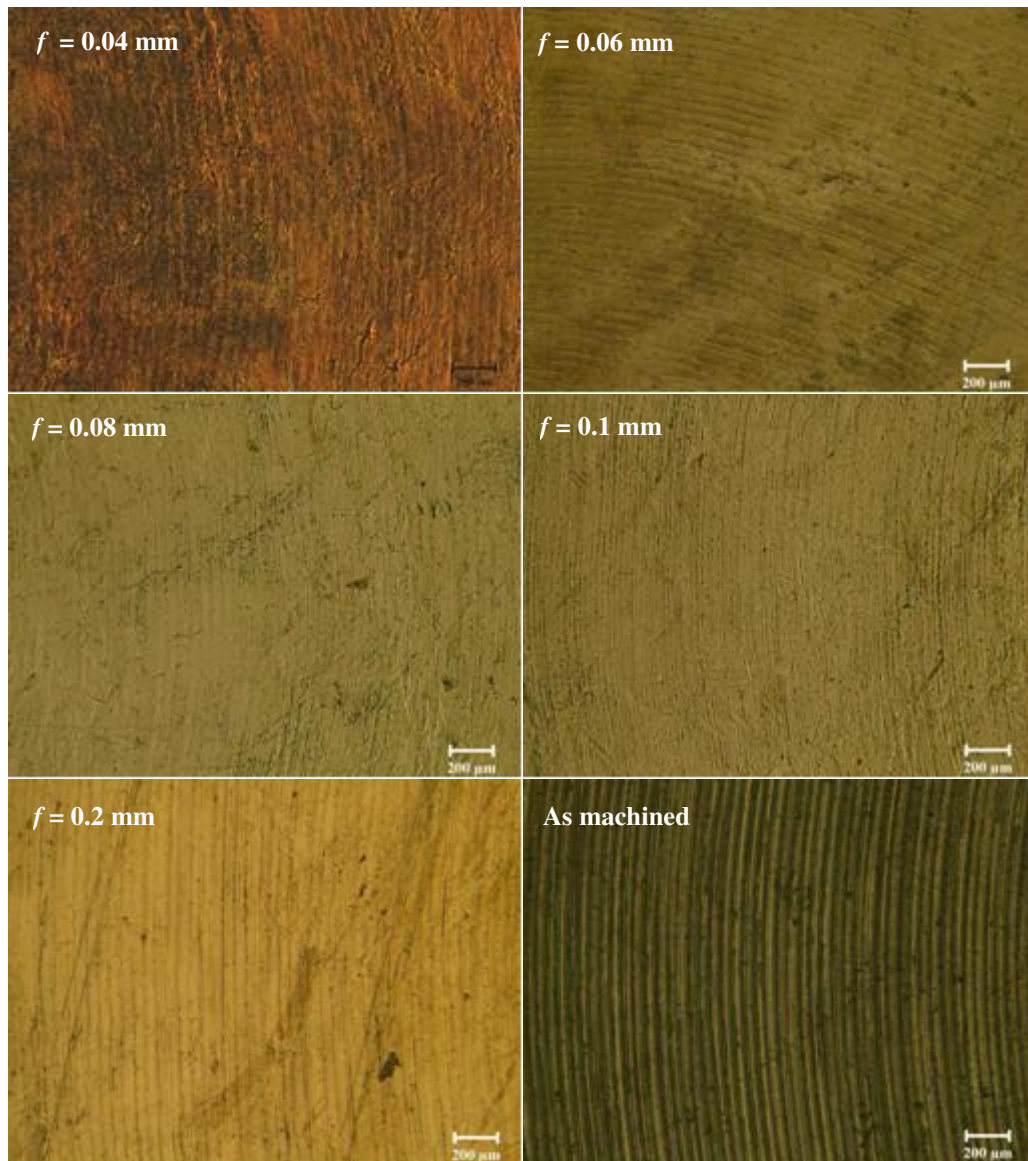


Fig. 8.3b Effect of lateral feed on surface topography ($P_h = 4 \text{ MPa}$, $v = 890 \text{ mm/min}$)

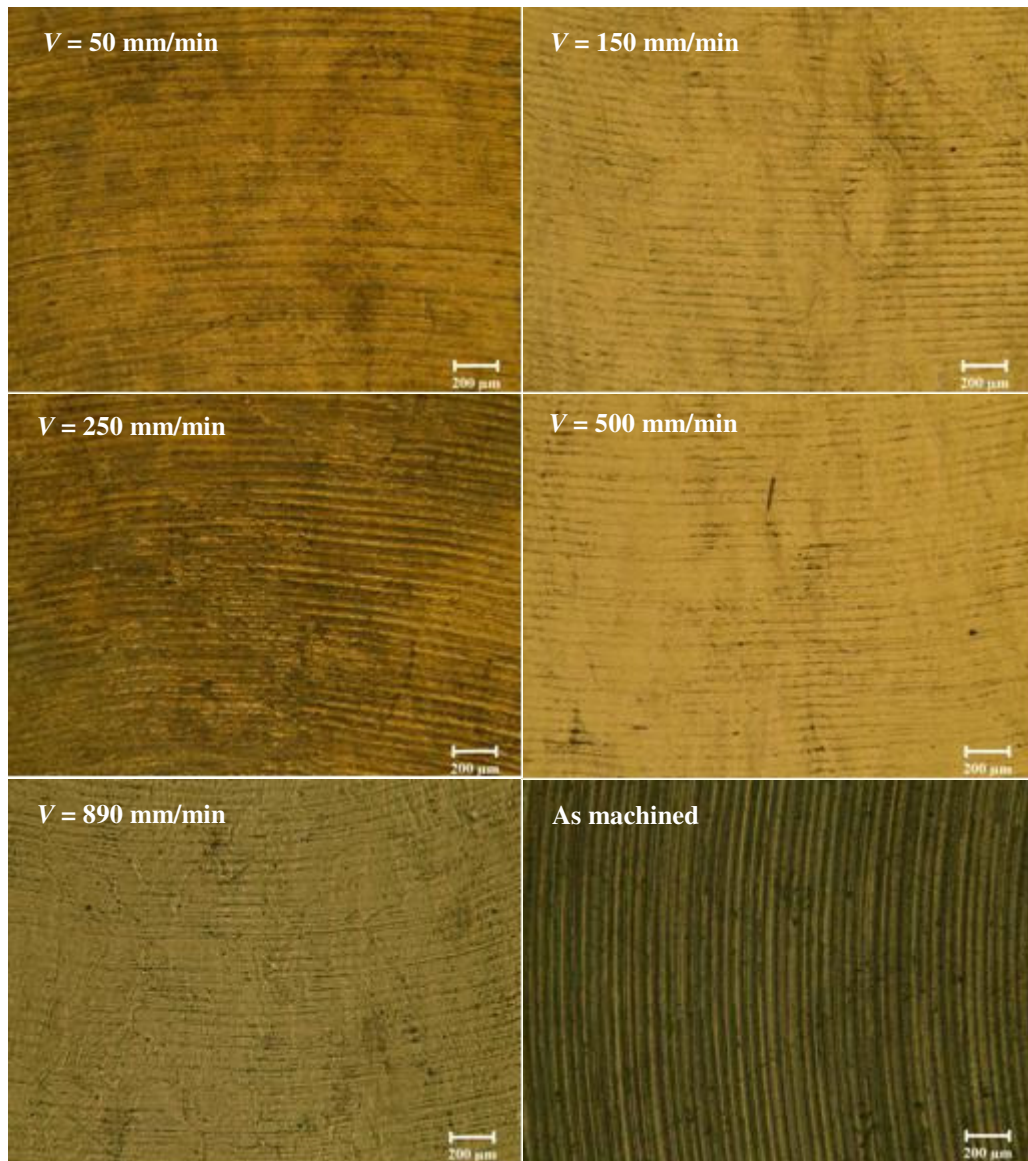


Fig. 8.3c Effect of burnishing speed on surface topography ($P_h = 4 \text{ MPa}$, $f = 0.1 \text{ mm}$)

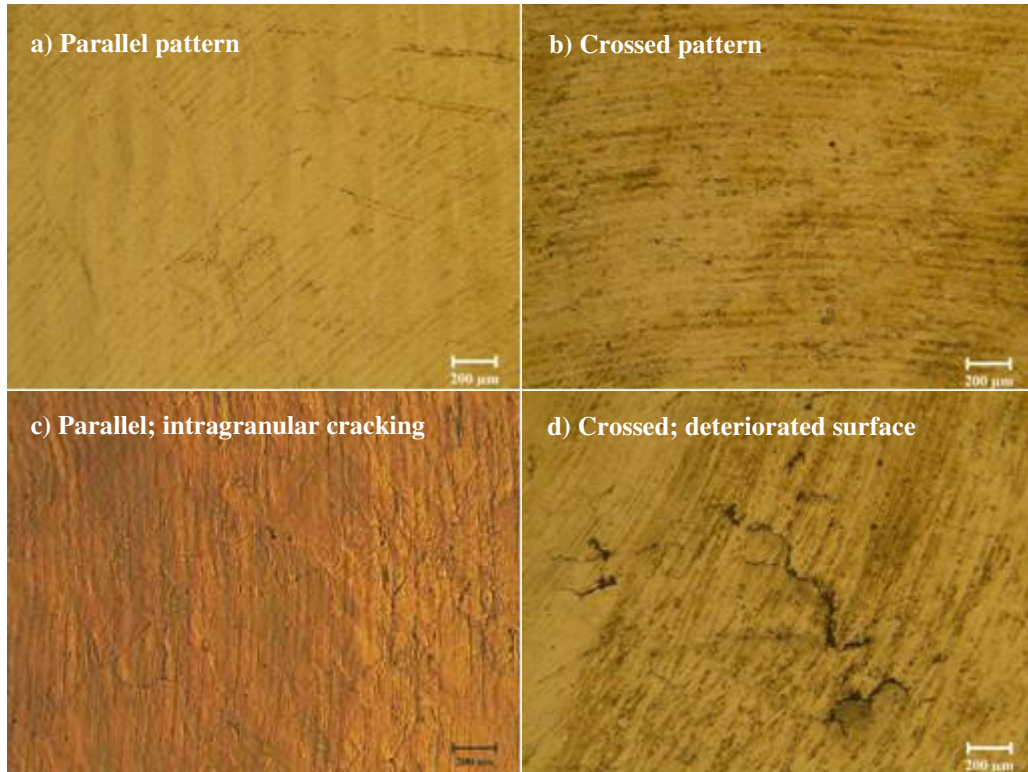


Fig. 8.3d Effect of burnishing pattern on surface topography
($P_h = 4 \text{ MPa}$, $f = 0.1 \text{ mm}$, $v = 890 \text{ mm/min}$)

Decreasing lateral feed of the burnishing ball under a middle pressure of 4MPa in figure 8.3b seems a better way to avoid surface deterioration while flattening the cutting feed marks. Lower feed increases the number of times each cutting mark will meet the burnishing ball. In first few encounters the cutting mark itself deforms and work hardens and then starts to transfer the deformation energy to the material underneath. As so, the cutting mark will be laid upon an already work hardened substrate for the rest of interactions between burnishing ball and cutting mark. This fact raises the possibility of being totally flattened for each cutting mark by the burnishing ball. This is clearly observable in figure 8.3b for different feed values. However, large diameter of burnishing ball compared to small feed values results in a very small curvature on

spherical profile of the ball at the contact area with the work material. This is to the extent that spherical-flat type of contact is literally replaced by flat-flat type. Therefore, it is quite hard to differentiate the effect of various lateral feed values compared to each other.

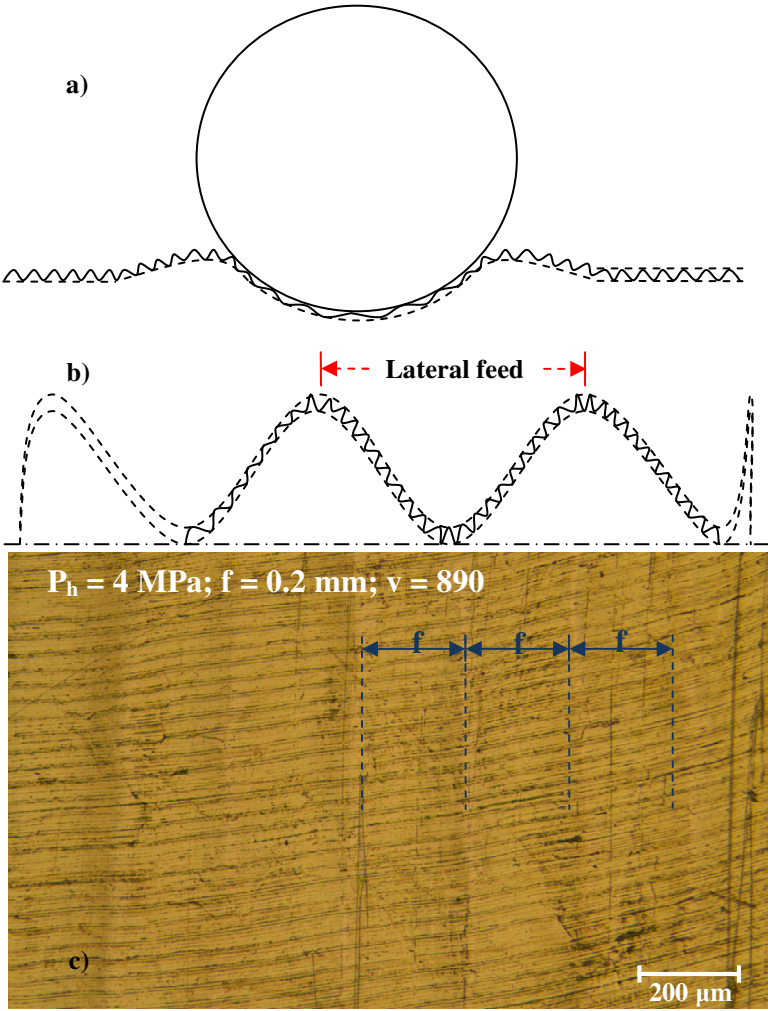


Fig. 8.4 Interaction between the pre-existing surface roughness and burnishing tool

Using slower burnishing speeds under a middle pressure of 4 MPa, as in figure 8.3c, is another better approach to eliminate cutting marks rather than applying high pressures which cause surface deteriorations. Burnishing speed determines the rate at which material deforms. Since straining any material to a certain amount will need larger stresses under higher strain rates, therefore resistance against deformation will increase under faster burnishing speeds. As so, slow burnishing of Mg-Ca0.8 will make it to appear softer in deformation and will increase the possibility of having the cutting marks completely flattened. The effects of lateral feed and speed on burnished surfaces will be quantified in next section using roughness value to determine which parameter is more effective in eliminating the pre-existing surface condition.



Fig. 8.5 Cold welds formed under high pressure ($P_h = 10$ MPa, $f = 0.1$ mm, $v = 890$ mm/min)

Adding another pass under a middle pressure of 4 MPa, as in figure 8.3d, with ultimate goal of flattening cutting marks could be another solution to surface deterioration under high

pressures. This can be accomplished in two different patterns as is shown in figure 8.2. Cutting marks are barely visible in both cases. The surface waviness present in parallel pattern is not observed in crossed pattern. This can be an advantage of crossed pattern over parallel pattern in dimensional accuracy sense of the final product. Except for some sporadic intragranular cracks in parallel pattern and peeling-off type anomalies in crossed pattern, adding an extra pass to already burnished surface seems successful in eliminating cutting marks. Applying lower pressure on second pass perhaps can avoid the occurrence of the before mentioned surface anomalies.

8.4.2. Surface roughness

Typical surface profiles after burnishing are shown in figure 8.6. Ideally, a surface profile will look like the one in figure 8.4b. It is composed of high frequency, low amplitude component laid upon a low frequency, high amplitude component. The former component is called “jaggedness” hereafter and represents pre-existing cutting marks. The later component is called “waviness” hereafter and represents the burnishing tracks. Frequency and amplitude of jaggedness depend on cutting feed and nose radius of the cutter in sample preparation stage. Lateral feed and burnishing ball radius determine the frequency and amplitude of waviness on the other hand. If cutting tool nose radius and burnishing ball radius are called geometry factors then surface roughness will depend on the feed to geometry factor ratio.

The smaller the feed to geometry factor ratio the smoother the processed surface will be. Although applying lower lateral feeds, slower burnishing speed, or more burnishing passes under middle pressure values can help to eliminated cutting marks and consequently jaggedness in burnishing process but it will save a lot of effort if smaller cutting feeds are used prior to that at first place.

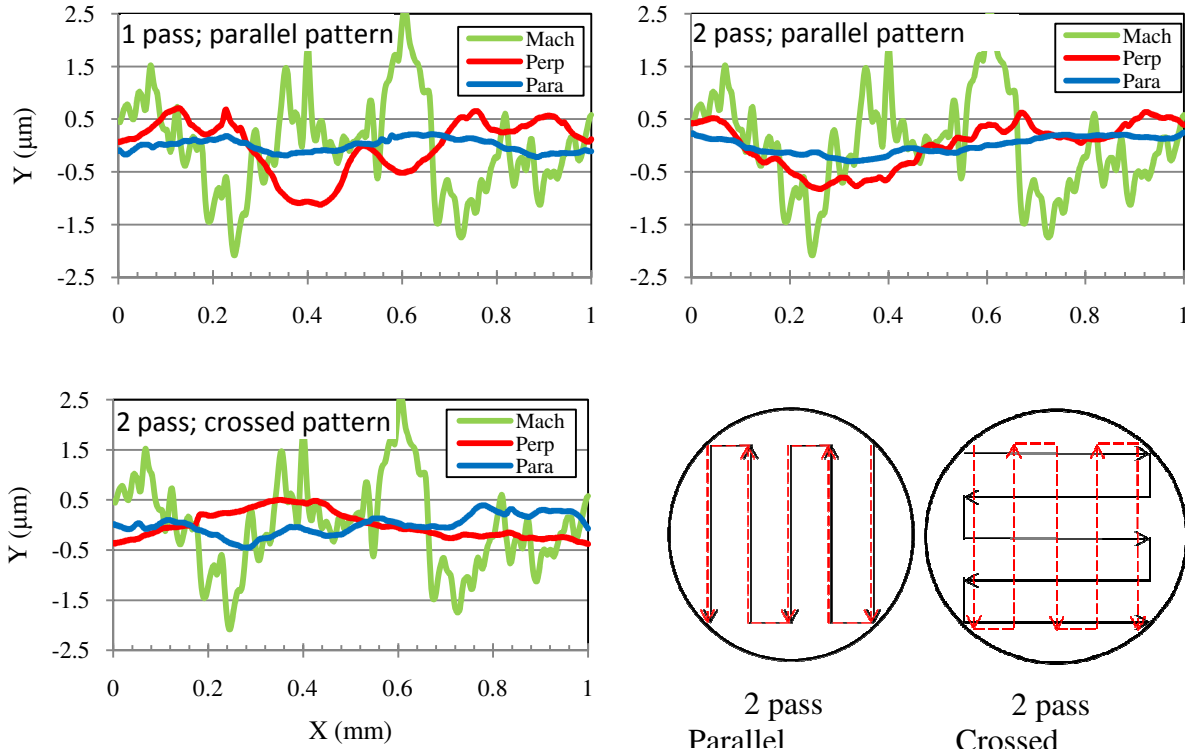


Fig. 8.6 Typical surface profiles ($P_h = 4 \text{ MPa}$, $f = 0.1 \text{ mm}$, $v = 890 \text{ mm/min}$)

The labels “Mach”, “Perp”, and “Para” refer to as-machined surface, perpendicular to burnish track, and parallel to burnish track respectively. The burnished surface profiles are less jagged than as-machined case and for that they look shinier and smoother. As-machined surface is dimmer due to high jaggedness which causes more scatter of the reflected light beams from the surface. Moreover, burnished surface profiles are not same in different directions and there is clear difference in parallel and perpendicular to burnish track directions. This directionality is due to the fact that lateral feed happens in perpendicular to burnish track direction. Parallel direction is the least jagged and waved compared to as-machined surface and perpendicular

direction. Perpendicular direction is not as jagged as machined surface but yet comparatively waved.

Burnishing pressure causes high directionality on surface profile. This is quantified in figure 8.7 by measured roughness value (R_a). This value for perpendicular direction is almost equal to the one for as-machined surface. Burnishing pressure does not seem to have an effect on perpendicular roughness expect for 10 MPa case which has even higher R_a value than as-machined case. This could be due to induced surface deteriorations under high pressure values.

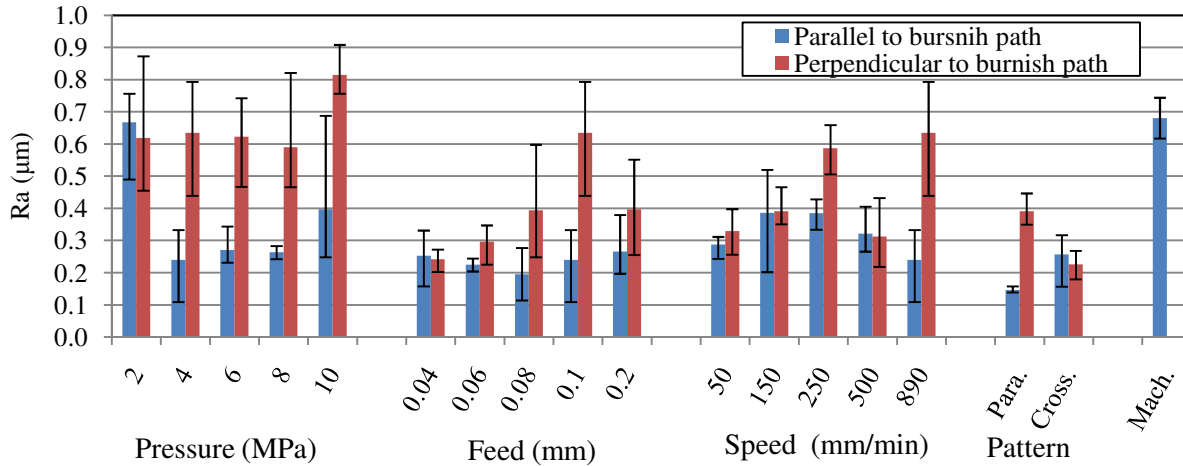


Fig. 8.7 Effects of burnishing pressure, feed, speed, and pattern on surface roughness

R_a value for parallel direction is less than as-machined surface by about half time. Rising burnishing pressure shows a slight increasing trend on parallel roughness. However, the lowest pressure (i.e. 2 MPa) is exceptional. This might be due to the fact that 2 MPa is not high enough

to modify the pre-existing roughness significantly. Low directionality in R_a value and the clearly visible cutting marks in figure 8.3a for 2 MPa case strengthen this possibility.

Directionality of surface profiles increases by applying larger lateral feeds. However, it is not as big as the effect of hydraulic pressure on roughness directionality (figure 8.7). Parallel roughness is almost one third of the as-machined case and does not change very much with feed. On the other hand, perpendicular roughness shows a rising trend with increasing feed and it is almost comparable to as-machined roughness under large lateral feeds.

Surface profiles and roughness values seem not to be directional under slow burnishing speeds and to be directional under fast burnishing speeds as is shown in figure 8.7. Parallel roughness is about half time less than as-machined case on average. It has a maximum of $0.4 \mu\text{m}$ at 250 mm/min speed. Perpendicular roughness shows a rising trend with increasing speed and is comparable to as-machined case roughness under fast speeds.

Number of passes and burnishing pattern have great influence on surface profiles in figure 8.6. Adding an extra pass to the existing one considerably decreases both roughness magnitude and its directionality. Directionality can be eliminated depending on which pattern is chosen to add the new pass. Perpendicular roughness is about three times bigger than parallel roughness in parallel burnishing pattern while this difference is almost vanished in crossed burnishing pattern. Roughness value of about $0.2 \mu\text{m}$ in crossed pattern is less than three times smaller than as-machined roughness.

As a general guideline and based on the above mentioned facts, small lateral feed, slow burnishing speed, and/or an extra pass with crossed pattern under a middle hydraulic pressure will be recommended to obtain the least rough surface in terms of magnitude and directionality. However, considering the importance of time and efficiency in global economy and engineering

slow burnishing speed and extra burnishing pass do not seem very appealing. Therefore, fast one-pass burnishing with a small lateral feed and under a middle hydraulic pressure will be the only economical way to obtain an isotropic and small roughness in burnishing of Mg-Ca_{0.8} biomaterial.

8.4.3. Microstructure

Typical microstructures of the material burnished under various process parameters are shown in figure 8.8. With respect to the fact that Mg-Ca_{0.8} is a lab-made alloy and does not exist in the market, obviously there is no established procedure for metallographic study of its microstructure. In that sense, it is useful to mention the procedure implemented in this study for metallographic analysis of the microstructures which is as follow:

Step 1: sectioning; this alloy is categorized as non-ferrous soft metal and for that a cut-off wheel made of SiC abrasive particles bonded together by Bakelite is used. Low cutting feed with water based coolant is applied to avoid thermal effects on microstructure,

Step 2: mounting; as a general rule of thumb it is a sound practice to avoid mounting as far as it is possible. This is respected in this study. If mounting is unavoidable then cold epoxy mounting should be used only. Hot mounting over 150 C° will change the microstructure,

Step 3: grinding; sand papers with following grit numbers are used sequentially: 800, 1200, and 2400. Samples are ground for 2 min on each sand paper with water based coolant and using 300 rpm speed,

Step 4: polishing; diamond pastes with following abrasive particle size are used sequentially on lecloth pads: 3 μm, 1 μm, and 0.25 μm. Samples are polished for 2 min on each

particle size with ethanol based diamond extender liquid and using 300 rpm speed. Samples were pressure rinsed using ethanol to avoid carrying larger size diamond particles to next polishing stage,

Step 5: fine polishing; samples are immersion etched in 5% Nital for 1 min and then rinsed with ethanol,

Step 6: etching; samples are etched in 98% picric acid for 2 min, rinsed with ethanol, and dried with pressurized air,

The binary alloying system of Mg and Ca produces Mg_2Ca phase in Mg rich side of the Mg-Ca phase diagram (figure 3.1). This intermetallic phase is dispersed inside the grains or precipitated at grain boundaries as is shown in un-etched micrograph of figure 3.1. The dark spots in figure 8.8 are mostly the Mg_2Ca filled locations inside the grains before etching. The aggressive etchant dissolves this intermetallic phase in itself at step 6 and leaves empty cavities behind which look as dark spots in 2D micrographs after etching. Very few of these spots could be pores made through sand casting process as well. The aggressive etchant was applied at step 6 to get as visible grain boundaries as possible since the near surface grain structure of the burnished material is significantly important in studying the effects of burnishing process on surface integrity characteristics. This extra clarity at grain boundaries caused over etching on inside grain regions and eventually the above mentioned dark spots. A less aggressive etchant of 100 ml ethanol + 18 ml distilled water + 6 ml glacial acetic acid + 12 gr picric acid 98% composition was also tried. Although, inside grain regions hardly become over etched with later etchant but the grain boundaries are not as visible even for higher etching time. All the optical micrographs in figure 8.8 are taken from sections cut parallel to burnish tracks. They all show

grain structure of the burnished Mg-Ca0.8 at different magnifications below the processed surface.

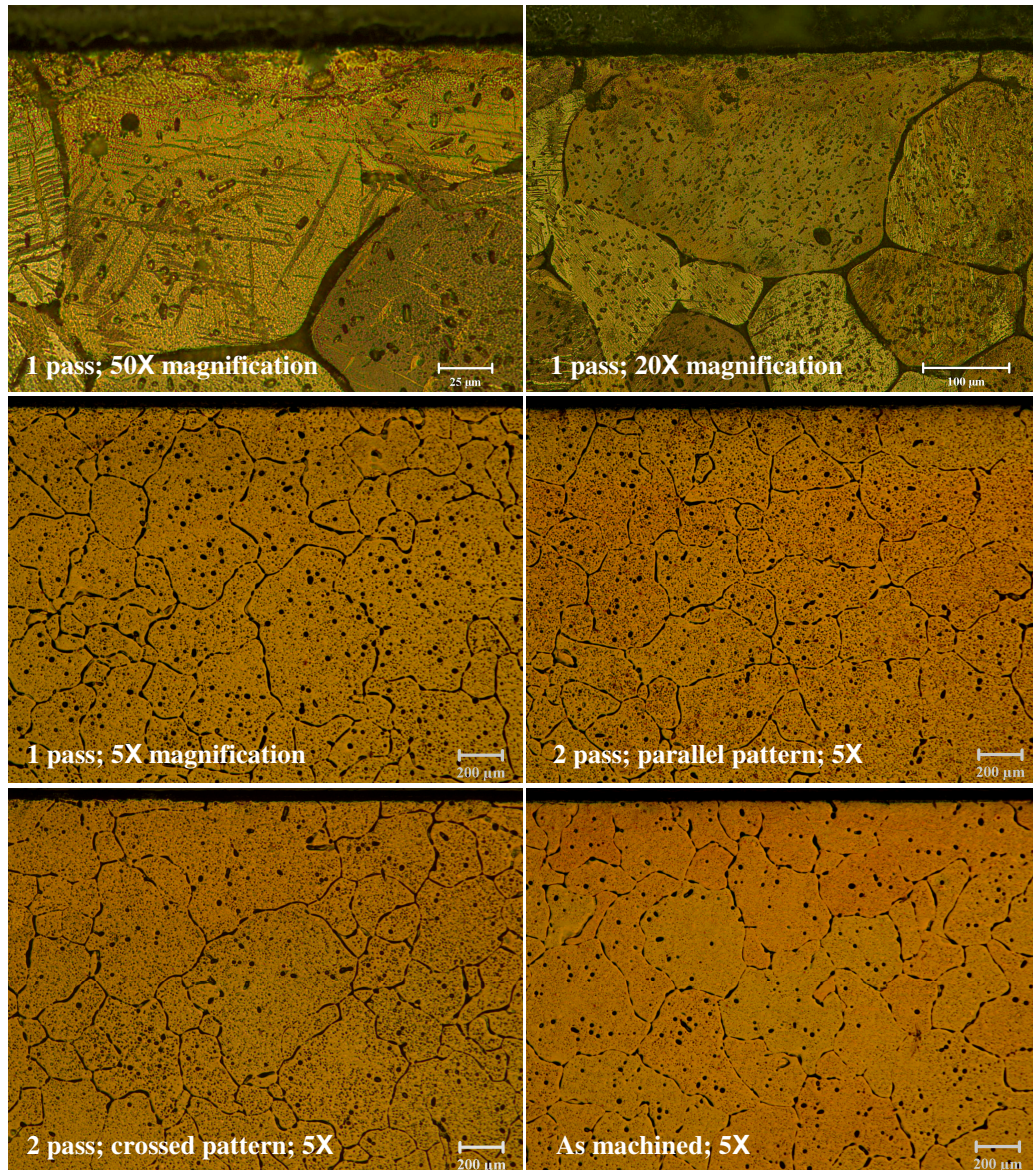


Fig. 8.8 Typical microstructures ($P_h = 4 \text{ MPa}$, $f = 0.1 \text{ mm}$, $v = 890 \text{ mm/min}$)

Generally, reshaping and resizing of the near surface grains and even phase transformation happen in metal forming processes. It was expected to observe a noticeable texture in grain structure near burnished surface in terms of having grains elongated in parallel to burnish track. However, comparison between optical micrographs of the burnished surfaces in figure 8.8 with as-machined case reveals no reshaping in the sense of making an obvious texture in grains as the result of burnishing process. Despite this fact, there is still this possibility that reshaping has occurred but then it has been vanished due to resizing later. Dynamic recrystallization and grain growth are the mechanisms that resizing of the grains in solid state occurs upon. Plastic deformation and temperature are key ingredients of these mechanisms. Plastic deformation produces dense tangles of dislocations which act as energy reservoirs inside grains. This energy will be the driving force to nucleate new grains at old grain boundaries.

However, the availability of high driving force alone cannot cause recrystallization and grain growth to happen since they need diffusion and migration of atoms which are highly temperature controlled processes. The dual purpose hydraulic oil which carries the pressure from HGP 4 hydraulic unit to the tip of the HG 13 burnishing tool acts as both lubricant and coolant. This pressurized fluid leaks out from the burnishing tool's tip and flows on the sample's surface all the time during burnishing. Therefore, temperature does not get a chance to rise while burnishing is under progress. With respect to this fact, recrystallization, grain growth, and even phase transformation which are all diffusion and consequently temperature controlled phenomena cannot resize the near surface grains. This speaks on the fact that observed grains in micrographs were existed before burnishing. Therefore, burnishing pressure, lateral feed, speed, number of burnish passes, and pattern do not have influence on microstructure in the range of values experimented and for the specific geometry of the burnishing tool used in this study.

8.4.4. Surface and subsurface microhardness

Measured surface microhardness values are reported in figure 8.9. The first thing which attracts attention in this figure is the fact that as-machined surface hardness is almost two times bigger than burnished surface hardness. Hardness is directly related to the extent of plastic deformation and work hardening which material experiences during a forming process. Whether or not cutting process produces more work hardening than burnishing process on the surface is the question which should be addressed after considering another fact. Among all burnished surfaces in figure 8.9 only one case has directionality in surface hardness as machined surface does, and that is the case with the lowest burnishing pressure (i.e. 2 MPa). This has to do with the presence of cutting marks. As mentioned in section 5.2, under this pressure cutting marks are still well defined and burnished surface has an isotropic roughness almost equal to the machined surface.

A closer look at indents on machined surface in figure 8.10 reveals the fact that cutting marks and the resulting roughness from their presence interact with indents and make dents diagonal smaller as opposed to that of a dent on an ideally flat surface obtained from polishing. Afterwards, the measured diagonal of the dents will be converted to corresponding hardness values using conversion tables. Therefore, presence of cutting marks will have a virtual hardening effect on processed surface. Regardless of this fact, it makes sense if machined surface is harder than burnished one since in machining atomic bonds need to be broken to form chips and hence deformation is more intense and localized than burnishing case where material simply goes through cold deformation.

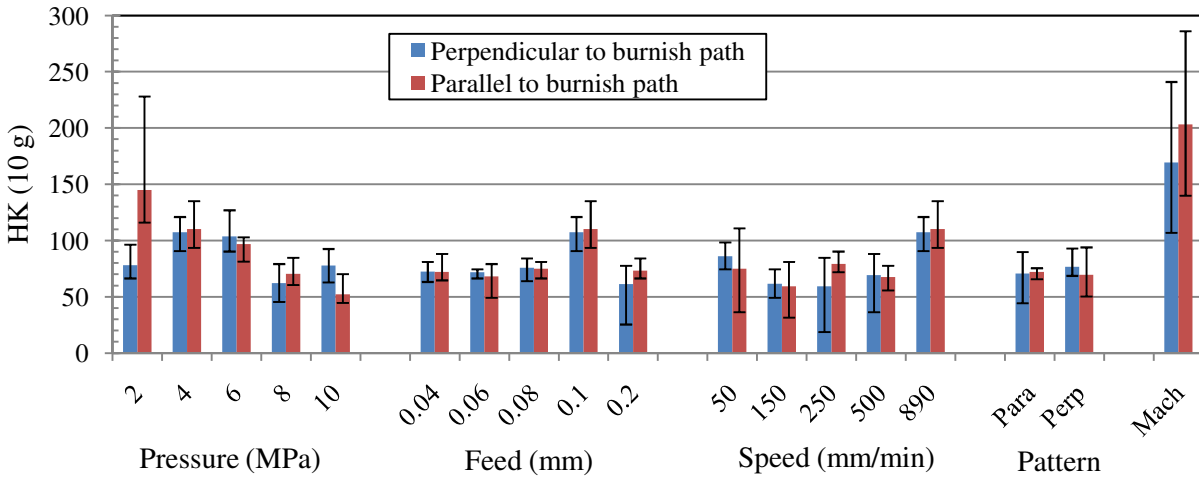


Fig. 8.9 Effect of burnishing parameters on surface microhardness

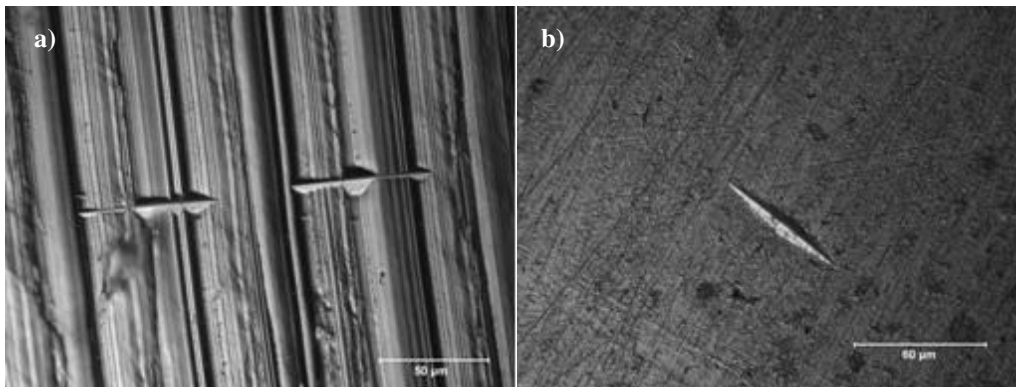


Fig. 8.10 Virtual hardening effect of cutting marks; a) machined surface, b) polished surface

Generally, surface hardness is isotropic under different combinations of burnishing parameters as is shown in figure 8.9 and does not change between parallel and perpendicular to burnish track directions. Increasing burnishing pressure causes surface hardness to decrease

while lateral feed, burnishing speed, and pattern are almost effect less. However, adding an extra pass decreases the surface hardness. Therefore, low pressure one-pass burnishing will result in highest surface hardness among the possible combinations of burnishing parameters.

Subsurface microhardness profiles are presented in figures 8.11a and 8.11b. As was expected, burnished material is harder than machined one in subsurface. This difference stays down to 500 μm depth and it is expected to drop down to bulk material's hardness of 29 HK at deeper layers. The ability to deform and work harden deep layers of material is the unique capability of the burnishing process. In contrast, machining is more concentrated in layers adjacent to the surface and subsurface microhardness drops to bulk hardness quickly in first 100 μm depth.

Burnishing pressure in figure 8.11a shows a considerable effect on hardness profile and it basically shifts upward by increasing the amount of burnishing pressure. Lateral feed and burnishing speed does not show a noticeable effect on hardness profile. Adding an extra pass in parallel pattern has more effect on hardness profile than in crossed pattern (figure 8.11b). Hence, the material should be burnished using either a high pressure value in one pass or a middle pressure value in two passes and parallel pattern to make the subsurface layers harder for a specific lateral feed and burnishing speed. However, considering the process time and efficiency applying higher burnishing pressure will be the only economical way to achieve harder subsurface layers.

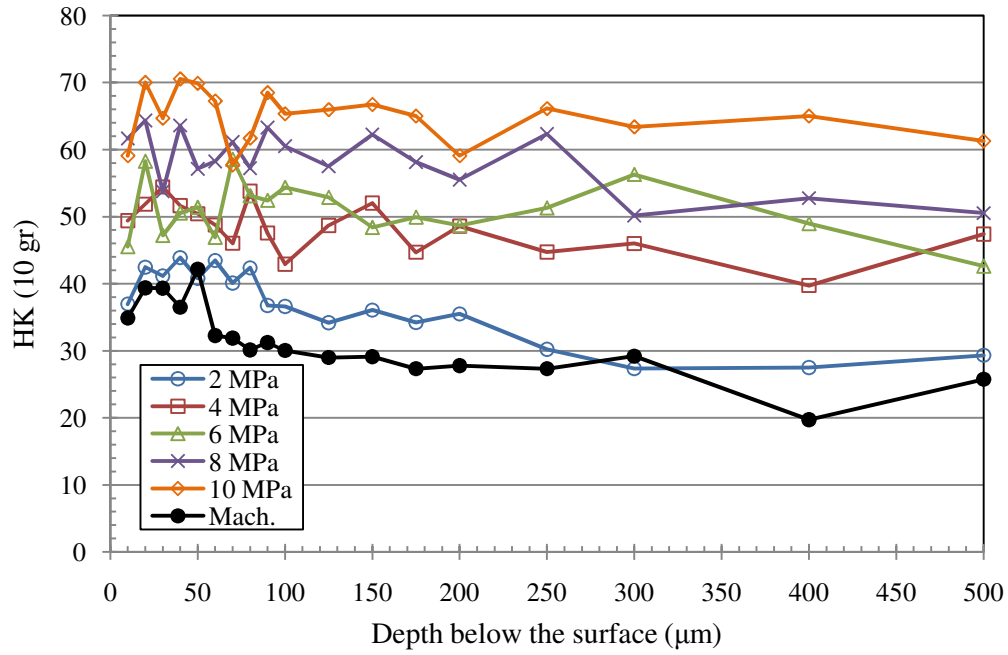


Fig. 8.11a Effect of burnishing pressure on subsurface microhardness
($f = 0.1$ mm, $v = 890$ mm/min)

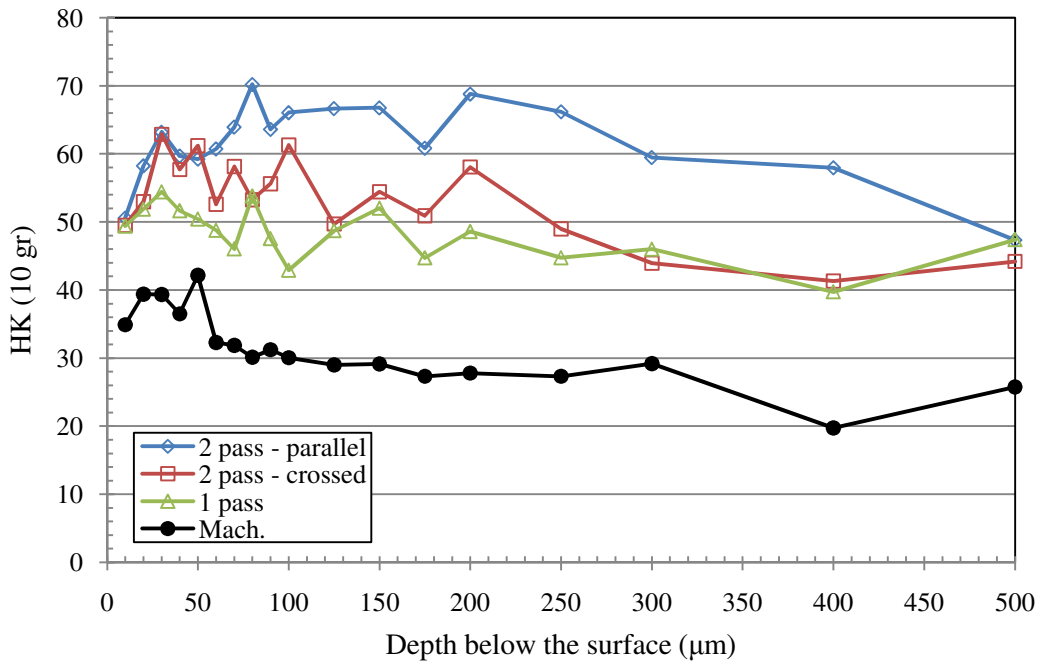


Fig. 8.11b Effects of burnishing pass and pattern on subsurface microhardness
($P_h = 4$ MPa, $f = 0.1$ mm, $v = 890$ mm/min)

8.4.5. Residual stresses

Residual normal stress components in parallel and perpendicular to burnish track directions along with Residual principal stress components are presented in figures 8.12a and 8.13b. 4-axis Bruker D8 XRD machine is used in residual stress measurements. X-rays with $\lambda = 0.1542$ nm wavelength are generated by applying 35 mA current and 40 kV voltage to X-ray tube with copper target. A collimator 0.8 mm in diameter collimates and directs the generated X-rays to the sample's surface. An area detector located 15 cm far from the goniometer's center detects diffracted X-rays produced as the result of interaction between colliding X-rays and crystallographic planes of the sample. Crystallographic interplanar spacings act as internal strain gauges. Strain changes these spacings and consequently corresponding diffraction angles based on Bragg's law. The shift in diffraction angles are used to calculate strains and then $\sin^2\psi$ method is applied to calculate residual stresses from strains.

In this study $\{1\ 2\ \bar{3}\ 3\}$ planes corresponding to $2\theta = 118.48^\circ$ are used to measure residual strains. The stress state is assumed to be plane stress ($\sigma_3 = 0$) since X-rays only interact with superficial layer of the sample. Besides, the stress state is taken to be uniform within the diffracting volume. Polycrystalline material's modulus of elasticity and Possion's ratio, i.e. 45 GPa and 0.33, are used in calculating residual stresses and they are assumed to be isotropic within the diffracting volume.

All the measured residual stresses are compressive as shown in figures 8.12a and 8.12b. In general, superficial residual stresses in figure 8.12a are anisotropic. Residual stress in parallel to burnish track is noticeably smaller than the one in perpendicular to burnish track in all but one case. This is opposite for cutting process and residual stress in parallel to cutting path is larger

than the one in perpendicular to cutting path. The anisotropy in superficial residual stresses is larger in burnished case as opposed to machined one.

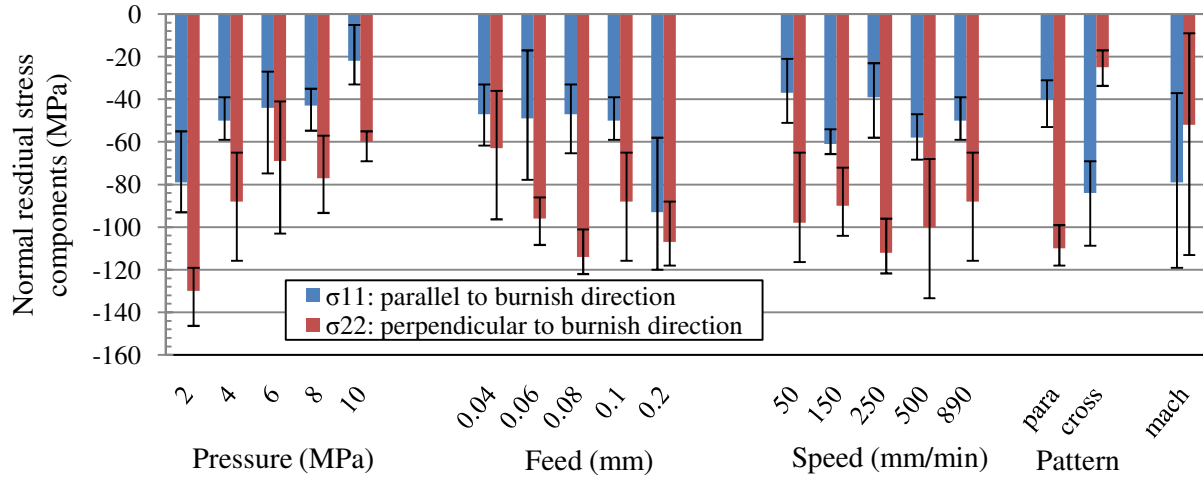


Fig. 8.12a Effect of burnishing parameters on normal residual stresses

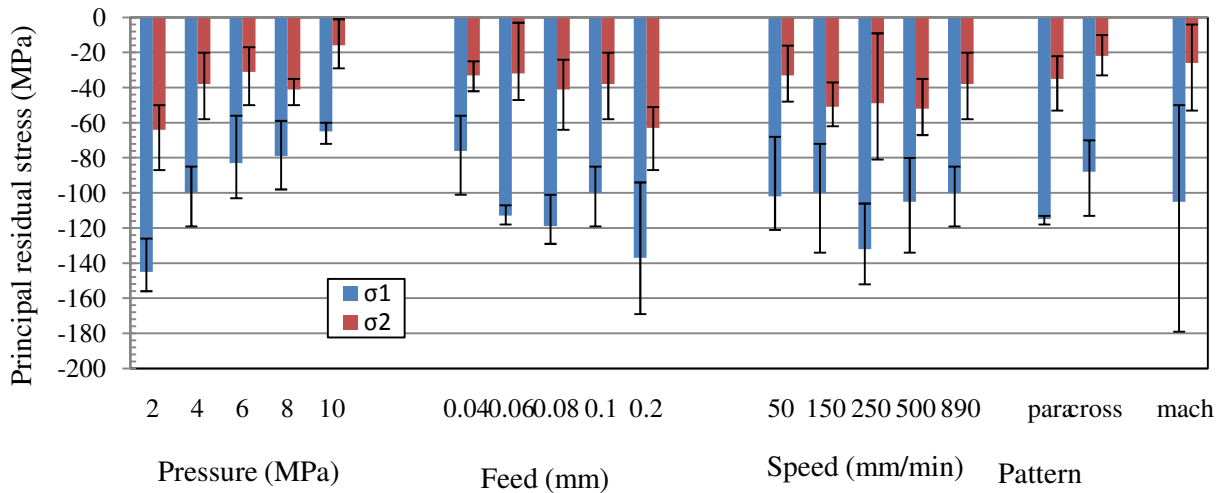


Fig. 8.12b Effect of burnishing parameters on principal residual stresses

Increasing burnishing pressure leads to smaller residual normal and principal stresses (figures 8.12a and 8.12b). Lateral feed has almost opposite effect and larger feed result in higher residual normal and principal stresses. Burnishing speed is almost effect less comparatively. Adding an extra pass in parallel pattern does not change the directionality but the magnitude of σ_{11} and σ_{22} meaning σ_{22} is still larger than σ_{11} and $\sigma_{22} - \sigma_{11}$ increases. If that extra pass is added in crossed pattern the directionality changes and σ_{11} will be greater than σ_{22} . Beside both principal components will be smaller than their counterparts in parallel pattern.

Machining process can produce compressive superficial residual stresses in the order of those for burnishing process as is visible in figure 8.12b. Low burnishing pressure, large lateral feed, and fast burnishing speed in one pass is the efficient and economical way to produce large compressive residual stresses. This combination of burnishing parameters will yield to $\sigma_{22} \approx 1.75 \sigma_{11}$ and $\sigma_1 \approx 2.25 \sigma_2$.

8.4.6. Statistical significance analysis

In figures 8.7, 8.9, and 8.12 effects of four burnishing factors on different response variables, i.e. roughness, hardness, and residual stresses are investigated. In figures 8.7, 8.9 and 8.12, each data bar represents average of measurements for the corresponding level and the error bars are demonstrating maximum and minimum recorded values. As is seen the error bars are large in some cases especially in figures 8.7 and 8.12 with three measurements for each level of the corresponding experimental factor. The data bars show changes as each experimental factor takes on different levels. However, these changes are not guaranteed to exist once the number of measurements increases for each level especially in the presence of wide range of uncertainty represented by large error bars. In order to find out how significant the observed changes are, a

one-way analysis of variance (one-way ANOVA) is run for each ordered pair of (factor, response variable). In each case, a null hypothesis is made that averages are same and then the F test is run to evaluate if the hypothesis is true. Another way to phrase the later statement is this: it is assumed that a factor is effect less on a response variable and then a factorial experiment is run to see if the assumption is true. Each run of F test yields a p -value which explains the probability of the hypothesis being true. If the p -value is less than 5% then the hypothesis is rejected and it is concluded that the effect of the factor on the response variable is statistically significant.

Figure 8.13 shows the calculated p -values for each ordered pair of (factor, response variable). This figure is a semi-log plot to accommodate for the large changes of p -value in the order of several magnitudes. There are eight response variables on X-axis and each is affected by four factors, i.e. pressure, feed, speed, and pattern. Each ordered pair represents fifteen measurements (three measurements for each level \times five levels for each factor) except than (pattern, response variable) pairs which represent six measurements (Table 8.1). These statistics are different in the hardness case and they are twenty five and ten, respectively. For this reason, statistical inferences for (pattern, response variable) pairs are not as strong as they are for the rest of the pairs.

The effect of feed, speed, and pattern on parallel to burnish track roughness is not significant statically. However, these factors affect perpendicular to burnish track roughness significantly. All factors except than pattern have influence on hardness statically. Feed and speed don't have influence on parallel and perpendicular to burnish track normal residual stresses. In case of principal residual stresses, burnishing pattern is also effect less in addition to feed and speed.

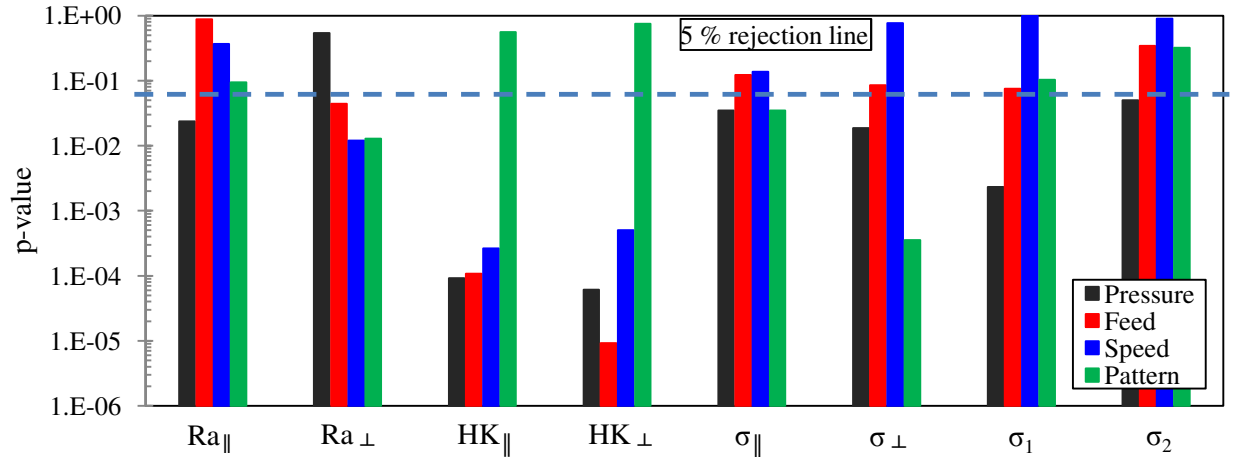


Fig. 8.13 Calculated p-values in the F test for one-way ANOVA (Ra roughness; HK hardness; σ residual stress; \perp perpendicular to burnish track; \parallel parallel to burnish track)

8.4.7. Discussion on the effect of surface integrity on degradation

It is a well known fact that corrosion performance of any material is directly affected by process-induced surface integrity and, therefore, the in-vivo degradation of biodegradable Mg-Ca_{0.8} implants is no exception to this general rule. Regarding to the effect of surface integrity on corrosion performance, it is necessary to consider the combined effects of surface integrity factors including surface finish, microstructure, microhardness, and residual stress, on degradation. Corrosion performance of a biodegradable orthopedic implant is not expected to be homogenous across the subsurface due to the distinct surface layer (about several hundreds of micron thickness) from the bulk material. The potential non-homogenous corrosion stems from the differences in grain structure, microhardness, and residual stresses which are hierarchically resulted from in-depth gradient of plastic deformation during the burnishing process.

It is expected that a smooth surface to provide less sites for corrosion reaction and also to decrease the chances of localized corrosion than a rough one. As shown in figures 8.6 and 8.7 for the burnished Mg-Ca_{0.8} surfaces, less corrosion pits would be expected than the as-machined surfaces.

On the microstructure side, grain boundaries are more prone to corrosion than bulk of grains with the assumption that grains are chemically homogeneous across their volume to avoid galvanic couples. Finer grain structure would mean higher density of these fertile sites for corrosion; however grain size across the subsurface seems to be negligibly influenced by burnishing as shown in figure 8.8. Therefore, the effect of microstructure on corrosion seems to be negligible.

Microhardness is an indirect index of deformation level and dislocation density at surface layer. High levels of cold work such as burnishing leave a severely deformed surface layer with a high dislocation density which results in higher hardness. Dense tangles of dislocations act as energy reservoirs and may aggravate the corrosion performance by providing the driving force for corrosion reaction. However, it should be pointed out that corrosion performance is encompassing two concepts: (i) *spontaneity* which is a thermodynamic concept and refers to likelihood of an electrochemical reaction to start; (ii) *rate* which is a kinetic concept and refers to how fast an electrochemical reaction will progress after it starts. In this context, improvement in corrosion performance of a biodegradable bone implant can be realized in two ways: (a) postponing the reaction until a good portion of the healing process is achieved; (b) decreasing the pace of reaction, even though it starts soon, so that healing rate can keep up with degradation rate. These alternatives are possible due to the fact that a spontaneous reaction does not necessarily mean a rapid reaction. Therefore, a high level deformation by burnishing could

increase the *spontaneity* or thermodynamic tendency of the corrosion reaction but there are still other surface integrity factors such as compressive residual stress to improve corrosion performance by controlling the kinetics.

Residual stresses can be beneficial or detrimental to corrosion performance depending on their nature. Tensile residual stresses aggravate corrosion performance while compressive residual stresses slower the kinetics and benefit the degradation performance. Considering the high compressive residual stress produced by burnishing at the sample surfaces, corrosion performance can be improved. In deed, Denkena and Lucas [15] have shown that corrosion performance can be improved by a factor of 100, approximately, by burnishing of another type of Mg-Ca alloy (Mg-Ca3.0).

The above discussions show that how surface integrity affects corrosion performance is a complex phenomena. The matter of fact is that corrosion performance is a collective influence of surface integrity factors. A full picture of how a burnished Mg-Ca0.8 surface will perform requires a comprehensive corrosion experiment to correlate process-induced surface integrity with corrosion performance. These intertwined effects of surface integrity factors on corrosion performance of burnished biodegradable Mg-Ca0.8 materials would have to be investigated in the near future.

8.5. Conclusions

Burnishing has been used in this study to improve surface integrity of the lab-made orthopedic material Mg-Ca0.8. The effects of various combinations of burnishing parameters on surface integrity characteristics were investigated. Followings are the major results:

- Cutting feed marks on the burnished surfaces are less sharp and defined as opposed to the as-machined ones due to burnishing action, but they cannot be completely flattened. High burnishing pressure not only eliminates pre-existing surface topography but may also produce intragranular cracks. Burnishing with smaller lateral feed, slower speed, and/or two passes in crossed pattern under middle pressure values can give better results in terms of eliminating cutting feed marks while avoiding surface deteriorations.
- Burnished surfaces are less modulated than machined surface and for that they look shinier and smoother. Burnished surface roughness is anisotropic and burnishing pressure causes the highest anisotropy. Roughness is generally smaller in parallel to burnish track than that in perpendicular direction. Increasing lateral feed will increase roughness anisotropy. Small lateral feed, slow burnishing speed, and/or an extra pass with crossed pattern under a middle pressure is recommended to obtain the least roughness in terms of magnitude and anisotropy.
- Burnishing does not have influence on microstructure in the range of parameter values experimented and for the specific geometry of the burnishing tool used in this study.
- Machined surfaces are about two times harder than the burnished ones. The burnished surfaces show higher hardness in subsurface down to the very deep subsurface as opposed to shallow hardened depth in machined sample. Surface hardness is isotropic. Increasing burnishing pressure causes surface hardness to decrease while lateral feed, burnishing speed, and pattern are almost effect less. However, adding an extra pass decreases the surface hardness.
- Burnishing pressure shows a considerable effect on subsurface hardness and it increases under higher pressures. Lateral feed and burnishing speed does not show a noticeable effect

on subsurface hardness profile. Adding an extra pass in parallel pattern has more effect on subsurface hardness than crossed pattern.

- Surface residual stresses are compressive and anisotropic. The anisotropy in burnishing is higher than that in machining. Residual stress parallel to the burnish track is noticeably smaller than the one perpendicular to burnish track direction. Low burnishing pressure, large lateral feed, and fast burnishing speed in one pass is recommended to produce highly compressive residual stresses in burnishing. In this combination of burnishing parameters $\sigma_{22} \approx 1.75 \sigma_{11}$ and $\sigma_1 \approx 2.25 \sigma_2$.

References

1. A.G. Au, V.J. Raso, A.B. Liggins, A. Amirfazli, Contribution of loading conditions and material properties to stress shielding near the tibial component of total knee replacements, *J. Biomech.* 40 (2007) 1410 – 1416.
2. A. Completo, F. Fonseca, J.A. Simoes, Strain shielding in proximal tibia of stemmed knee prosthesis: experimental study, *J. Biomech.* 41 (2008) 560 – 566.
3. A. Gefen, Computational simulations of stress shielding and bone resorption around existing and computer-designed orthopaedic screws, *Med. & Bio. Eng. & Comp.* 40 (2002) 311 – 322.
4. H. Isaksson, A.L. Lerner, Mathematical modeling of stress shielding with bioresorbable materials for internal fracture fixation, *Bioeng. Conf.* (2003) 1041 – 1042.
5. J. Nagels, M. Stokdijk, P.M. Rozing, Stress shielding and bone resorption in shoulder arthroplasty, *J. Shoulder and Elbow Surg.* 12 (2003) 35 – 39.
6. H.G. Seiler, *Handbook on toxicity of inorganic compounds*, 1st ed., CRC Press (1987).
7. G. Song, Control of biodegradation of biocompatible magnesium alloys, *Corros. Sci.* 49 (2007) 1696 – 1701.

8. G. Song, S. Song, A possible biodegradable magnesium implant material, *Adv. Eng. Mater.* 9 (2007) 298 – 302.
9. B. Heublein, R. Rohde, V. Kaese, M. Niemeyer, W. Hartung, A. Haverich, Biocorrosion of magnesium alloys: a new principle in cardiovascular implant technology, *Heart* 89 (2003) 651 – 656.
10. C. Liu, Y. Xin, G. Tang, P.K. Chu, Influence of heat treatment on degradation behavior of bio-degradable die-cast AZ63 magnesium alloy in simulated body fluid, *Mat. Sci. & Eng. A* 456 (2007) 350 – 357.
11. H. Wang, Y. Estrin, H. Fu, G. Song, Z. Zuberova, The effect of pre-processing and grain structure on the bio corrosion and fatigue resistance of magnesium alloy AZ31, *Adv. Eng. Mater.* 9 (2007) 967 – 972.
12. F. Witte, V. Kaese, H. Haferkamp, E. Switzer, A. Meyer-Lindenberg, C.J. Wirth, H. Windhagen, In vivo corrosion of four magnesium alloys and the associated bone response. *Biomaterials* 26 (2005) 3557 – 3563.
13. Z. Li, X. Gu, S. Lou, Y. Zheng, The development of binary Mg-Ca alloys for use as biodegradable materials within bone, *Biomaterials* 29 (2008) 1329 – 1344.
14. B. Denkena, F. Witte, C. Podolsky, A. Lucas, Degradable implants made of magnesium alloys, *Proc. 5th Euspen Int. Conf., Montpellier, France* (2005).
15. B. Denkena, A. Lucas, Biocompatible magnesium alloys as absorbable implant materials-adjusted surface and subsurface properties by machining processes, *Ann. CIRP* 56 (2007) 113 – 116.
16. Y.B. Guo, V. Brooks, Characterization of mechanical property and microstructure of biomedical magnesium alloy, *Proc. of ASM Materials & Processes for Medical Devices Conf. and Expo., Minneapolis, MN* (2009).
17. T. Hassel, F.W. Bach, Production and properties of small tubes made from MgCa0.8 for application as stent in biomedical science, In: K.U. Kainer, Ed., *Magnesium: Proc. 7th Int. Conf. Magnesium Alloys and Their Applications*, Wiley-VCH Verlag GmbH & Co. (2007) 432 – 437.
18. T. Hassel, F.W. Bach, C. Krause, Influence of alloy composition on the mechanical and electrochemical properties of binary mg-ca alloys and its corrosion behavior in solutions at different chloride concentrations, In: K.U. Kainer, Ed., *Magnesium: Proc. 7th Int. Conf. Magnesium Alloys and Their Applications*, Wiley-VCH Verlag GmbH & Co. (2007) 789 – 795.
19. N. von Der Hoh, D. Bormann, A. Lucas, B. Denkena, C. Hackenbroich, A. Meyer-Lindenberg, Influence of different surface machining treatments of magnesium-based

- resorbable implants on the degradation behavior in rabbits, *Adv. Eng. Mater.* 11 (2009) B47 – 54.
20. J.Z. Ilich, J.E. Kerstetter, Nutrition in bone health revisited: a story beyond calcium, *J. Am. College of Nutrition* 19 (2000) 715 – 737.
 21. B. Aksakal, C. Hanyaloglu, Bioceramic dip-coating on Ti-6Al-4V and 316L SS implant materials, *J. Mater. Sci.: Mater. Medicine* 19 (2008) 2097 – 2104.
 22. A. Schuh, C. Zeller, U. Holzwarth, W. Kachler, G. Wilcke, G. Zeiler, B. Eigenmann, J. Bigoney, Deep rolling of titanium rods for application in modular total hip arthroplasty, *J. Biomed. Mater. Res. Part B: Applied Biomaterials* (2006) doi:10.1002/jbmb.
 23. C.Y. Seemikeri, P.K. Brahmankar, S.B. Mahagaonkar, Low plasticity burnishing: an innovative manufacturing method for biomedical applications, *J. Manuf. Sci. Eng.* 130 (2008) 021008/1-8.
 24. P.S. Prevey, D. McNulty, J. Carr, P. Sade, A. Craft, Fatigue strength enhancement of Ti-6Al-4V ELI femoral distal stems using low plasticity burnishing, *Proc. of ASM Materials & Processes for Medical Devices Conf. and Expo., Minneapolis, MN* (2009).
 25. J.A. Disegi, C. Sax, Effect of low plasticity burnishing on the fatigue strength of spinal rods, *Proc. of ASM Materials & Processes for Medical Devices Conf. and Expo., Minneapolis, MN* (2009).
 26. P.S. Prevey, R.A. Ravindranath, M. Shepard, T. Gabb, Case studies of fatigue life improvement using low plasticity burnishing in gas turbine engine applications, *J. Eng. Gas Turbines and Power* 128 (2006) 865 – 872.
 27. N. Jayaraman, D.J. Hornbach, P.S. Prevey, Mitigation of fatigue and pre-cracking damage in aircraft structures through low plasticity burnishing, *Proc. ASIP, Palm Springs, CA* (2007).
 28. P.S. Prevey, J.T. Cammett, The influence of surface enhancement by low plasticity burnishing on the corrosion fatigue performance of AA7075-T6, *Int. J. Fatigue* 26 (2004) 975 – 982.
 29. J.E. Scheel, D.J. Hornbach, P.S. Prevey, Safe life conversion of aircraft aluminum structures via low plasticity burnishing for mitigation of corrosion related failures, *Department of Defense Corrosion Conf., Gaylord National, Washington DC* (2009).
 30. P.S. Prevey, D.J. Hornbach, N. Jayaraman, Controlled plasticity burnishing to improve the performance of friction stir processed Ni-Al bronze, *Mater. Sci. Forum* 539 (2007) 3807 – 3813.
 31. L.N. Lopez, A. Lamikiz, J.A. Sanchez, J.L. Arana, The effect of ball burnishing on heat treated steel and Inconel 718 milled surfaces, *Int. J. Adv. Manuf. Tech.* 32 (2007) 958 – 968.

32. C.Y. Seemikeri, P.K. Brahmkar, S.B. Mahagaonkar, Investigations on surface integrity of AISI 1045 using LPB tool, *Tribology International* 41 (2008) 724 – 734.
33. D.S. Rao, H.S. Hebbar, M. Komaraiah, U.N. Kempaiah, Investigations on the effect of ball burnishing parameters on surface hardness and wear resistance of HSLA dual-phase steels, *Mater. Manuf. Processes* 23 (2008) 295 – 302.
34. A.T. Bozdana, N.Z. Gindy, Comparative experimental study on effects of conventional and ultrasonic deep cold rolling processes on Ti-6Al-4V, *Mater. Sci. Tech.* 24 (2008) 1378 – 1384.
35. C.M. Gill, N. Fox, P.J. Withers, Shakedown of deep cold rolling residual stresses in titanium alloys, *J. Phys. D: Appl. Phys.* 41 (2008) 174005 (5pp).
36. N. Tsuji, S. Tanaka, T. Takasugi, Evaluation of surface-modified Ti-6Al-4V alloy by combination of plasma-carburizing and deep-rolling, *Mater. Sci. Eng. A* 488 (2008) 139-145.
37. N. Tsuji, S. Tanaka, T. Takasugi, Effect of combined plasma-carburizing and deep rolling on notch fatigue property of Ti-6Al-4V alloy, *Mater. Sci. Eng. A* 499 (2009) 482 – 488.
38. I. Nikitin, M. Besel, Correlation between residual stress and plastic strain amplitude during low cycle fatigue of mechanically surface treated austenitic stainless steel AISI 304 and ferritic-pearlitic steel SAE 1045, *Mater. Sci. Eng. A* 491 (2008) 297 – 303.
39. I. Nikitin, M. Besel, Residual stress relaxation of deep-rolled austenitic steel, *Scripta Materialia* 58 (2008) 239 – 242.
40. I. Nikitin, I. Altenberger, Comparison of the fatigue behavior and residual stress stability of laser-shock peened and deep rolled austenitic stainless steel AISI 304 in the temperature range 25-600 C, *Mater. Sci. Eng. A* 465 (2007) 176 – 182.
41. P. Juijerm, I. Altenberger, Effective boundary of deep-rolling treatment and its correlation with residual stress stability of Al-Mg-Mn and Al-Mg-Si-Cu alloys, *Scripta Materialia* 56 (2007) 745 – 748.
42. E. Brinksmeier, M. Garbrecht, D. Meyer, Cold surface hardening, *CIRP Ann.-Manuf. Tech.* 57 (2008) 541 – 544.
43. B. Denkena, R. Meyer, B. Breidenstein, Development of combined manufacturing technologies for high-strength structure components, *Adv. Mater. Res.* 22 (2007) 67 – 75.
44. G. Byrne, D. Dornfeld, B. Denkena, Advancing cutting technology, *Ann. CIRP* 52 (2003) 483 – 507.

45. Y.B. Guo, M. Salahshoor, Process mechanics and surface integrity by high speed dry milling of biodegradable magnesium-calcium implant alloys, *CIRP Ann.-Manuf. Tech.* 59 (2010) 151 – 154.

CHAPTER 9

FINITE ELEMENT ANALYSIS OF HYDROSTATIC BURNISHING USING INTERNAL STATE VARIABLE PLASTICITY MODEL

Abstract

Hydrostatic burnishing is mainly a ceramic ball supported by a pressurized cushion of hydraulic oil and pushed against the workpiece surface. As the ball rolls along the surface it produces a unique combination of three physical effects in the surface layer: i) work hardening and increased hardness, ii) burnishing and decreased roughness, and iii) increased compressive residual stresses. This process has gained an increasingly great attention in automotive, aerospace, and especially medical device manufacturing industries. However, most of the research in hydrostatic burnishing has been performed experimentally and there is still lack of numerical studies providing fundamental understanding of the mechanics and the way process parameters interact with surface integrity characteristics particularly surface roughness and residual stresses. In this study, the dynamic mechanical behavior of the material is simulated using internal state variable (ISV) plasticity model. A semi-infinite, two-dimensional, plane strain FE model is developed and the ISV material model is incorporated into it using a user defined material subroutine. The effects of burnishing pressure and feed on surface roughness and residual stresses are investigated. The simulation results are validated with experimental measurements of residual stresses and surface roughness.

9.1. Introduction

Hydrostatic burnishing has been used in automotive and aerospace industries for about three decades now. Burnished surface layers of IN 718, Ti-6Al-4V, stainless steels, and Aluminum 7075-T6 have yielded longer fatigue life due to simultaneous presence of high hardness, low roughness, and large, deep compressive residual stresses [1-4]. However, application of this surface treatment technique in medical device manufacturing industry, particularly making biodegradable orthopedic implants, is in its infancy. Schuh et al [5] studied burnishing of titanium alloy rods as possible alternative to shot peening in treating mating surfaces of Morse tapers in modular hip endoprostheses. The motive in their study was to avoid the contamination of shot peened surfaces which could ultimately lead to enhanced corrosion and third body wear. Seemikeri et al [6] investigated the effects of burnishing process parameters, i.e. number of passes, ball diameter, pressure, feed, and speed on surface integrity and fatigue performance of AISI 316L steel which is most commonly used in prosthesis. Disegi and Sax [7] investigated the effect of burnishing on fatigue strength of spinal rods. While metallic orthopedic materials such as titanium, stainless steel, and cobalt-chromium alloys are suitable for replacement applications due to their high corrosion resistance but in fixation cases, where bone fragments are only needed to be kept in their original anatomical configuration till the healing process is over, some side effects such as stress shielding, local inflammation, and physical irritation brings about the necessity for second surgeries to excise the implants rather than leaving them inside human body. To avoid second surgeries and also side effects such as artificial osteoporosis, researchers have triggered an initiative to find metallic biodegradable substitutes for traditional orthopedic materials which have closer Young's modulus to that of bone and are composed of biocompatible ingredients. Preliminary in-vitro and in-vivo studies

have proven magnesium-calcium (Mg-Ca) alloys very promising in terms of biocompatibility and biodegradability [8-12]. However, degradation rate of these alloys is faster than healing rate of fractured bones. Mechanical surface treatment is an approach some researchers have been followed recently to adjust degradation kinetics [11,12]. Denkena and Lucas [12] applied burnishing process to generate high levels of compressive residual stress (~ -100 MPa) at subsurface layers (~ 1000 μm deep) of Mg-Ca3.0 implants. They were able to reduce corrosion rate of the biodegradable material by a factor of 100 approximately. Hence, studying burnishing mechanics and the way process parameters interact with surface integrity characteristics, especially residual stresses and surface roughness, is vital in order to achieve adaptable degradation kinetics for various medical applications. Finite element analysis is a powerful tool which could provide researchers with the mentioned insight.

9.2. FE analysis of burnishing: literature review

Skalski et al [13] modeled burnishing process as a boundary-initial-value problem. The tool was rigid and the workpiece (normal and toughened steel 45) was an elastic-plastic body with only isotropic hardening. The material model was further simplified by linearization of the constitutive equation. The changes in loads and deformations in time were analyzed in the incremental procedure corresponding to quasi-static loading. Therefore, the effects of deformation speed and strain rate were neglected. They used displacement controlled finite element method to solve the developed boundary value problem but prior to that they had simplified the burnishing process further by assuming a cylindrical shaped tool rather than spherical one. Ultimately after all the simplifications which were stronger on material properties

than tool geometry, they concluded tool geometry, i.e. radius of the cylinder, has stronger influence on normal force, concentration of stresses under the tool, and depth of plasticized zone.

Black et al [14] used steady-state, plane-strain slipline field to model the burnishing of a relatively soft material by the *sliding* (rather than *rolling*) of a hard wedge along the surface. The main purpose of their work was to derive analytical equations for estimating the burnishing force, the depth of the burnished layer and the plastic strains in this layer. The analysis was further simplified by treating the workpiece as a rigid-perfectly plastic material, and neglecting the effect of speed (strain rate and temperature) on the process. The method was also unable to estimate the residual stresses resulted from burnishing on the surface.

Zhuang and Wicks [15] proposed a three-dimensional (3D) finite element model to simulate the multipass burnishing process and to predict the effects of process parameters on the resultant residual stress field. The interaction between ball and the IN 718 plate was a surface-to-surface moving frictionless rolling contact and the constitutive material model was a non-linear isotropic/kinematic hardening model. Disregarding temperature and large strain dependencies, the evolution of kinematic hardening was formulated as strain hardening, proportional to inelastic strain rate, minus dynamic recovery. Isotropic hardening was considered to be independent from strain rate. The predicted compressive residual stresses were underestimating the experimental results. However, the shape of the profile and location of the maximum residual stress were well predicted. Despite these observations, there is a significant issue that this model fails to address and that is the minimum number of passes required before establishing the steady state deformation. On the other words, the predicted residual stress profile could be a transient one if the steady state condition has not achieved yet. This issue directly relates to the overall dimensions of the workpiece model and consequently computational time which has been the

biggest challenge in developing 3D models of burnishing so far and were not addressed in Zhuang and Wicks' paper. Moreover, it is not clear if they have considered the rolling force drop due to normal oil leakage at the tip of burnishing tools.

Beres et al [16] performed 2D and 3D finite element analysis of the burnishing process. However, since 3D modeling was very time consuming (~ 6days), only some preliminary attempts were done using 3D models, while the majority of the study was performed using much more efficient 2D models (~ 24 hrs). The basic elastic-viscoplastic material model was assumed for Ti-6Al-4V ($E = 118 \text{ GPa}$) material. Beres et al performed parametric studies of the effect of ball elasticity ($E \approx 3 \times 118 \text{ GPa}$) on the stress-strain distributions and noticed that the difference between load-indentation curves obtained using rigid and elastic ball models did not exceed 3%, while the computer running time for the model with elastic ball was significantly larger. Therefore, it was concluded that the initial burnishing simulations could be simplified by modeling the burnishing ball as a rigid body. In all the 2D plane strain simulations, the rigid ball (actually *cylinder*) was first pressed into the workpiece for a given indentation depth (*displacement controlled*) and then it was rolled, friction-free, along the surface. Hence, their 2D models were unable to predict the effect of burnishing feed on residual stresses. The 3D simulations were capable of considering that effect but they were run for only two passes separated 500 μm apart. This brings about the lack of steady state deformation issue as it did in [15]. Compared to experimental results, 2D models well predicted the shape of residual stress profiles and also the location of maximum stresses. However, the difference between predicted and measured maximum values varied by 11%. The discrepancy was stronger on the surface and predicted surface value was less compressive than measured one.

Bouزيد et al [17] analyzed the evolution of surface roughness in burnishing using finite element method. They had defined an analytical model for burnished surface roughness as a function of burnishing feed, ball penetration depth, and pre-existing roughness from turning. Ball penetration depth was calculated using i) Hertz contact theory and assuming the workpiece material (AISI 1042 steel) has pure elastic behavior; and ii) finite element method and assuming the workpiece material has elastic-plastic behavior. The elastic-plastic material model considered isotropic hardening law with nonlinear expansion of the von Mises yield surface and without kinematic hardening. The ball was modeled as elastic body. Since small burnishing force of 150 N was applied, Bouزيد et al studied only the case where penetration depth was smaller than initial surface roughness. In a similar work, Korzynski [18] developed an analytical model to predict the amount of load necessary to produce penetration depth about the height of pre-existing roughness ridges. The goal was to smoothen the ground surface of steel pieces even more; as such inducing compressive residual stresses or increasing surface hardness was not a concern. It was found that load, radius of the ball, initial height of the roughness ridges, and the spacing between them are the most influential parameters in determining the amount of penetration depth.

Klocke et al [19] developed a 3D FE model for simultaneous roller burnishing of thin-walled structures (1 mm thick) in order to predict the effects of rolling force and burnishing feed (or overlap/coverage) on induced compressive residual stresses. Thermal effects and the influence of velocity were neglected based on previously published experimental results. Simultaneous roller burnishing is application of two hydrostatic burnishing tools at the same time on both sides of a thin-walled structural feature to prevent bending and deflection. Klocke et al emphasized that burnishing is a sequence of small successive forming processes (i.e. stretch

forming and upsetting) which include change in loading direction and for that reason a non-linear isotropic/kinematic strain hardening law should be used to capture the resulting complex material behavior, particularly Bauschinger effect, correctly. It was believed that laws built upon isotropic hardening alone, are not capable of capturing these effects. However, they did not provide any information about the formulation of the applied material model. Presence of high residual stress gradients in near surface layers ($\sim 500 \mu\text{m}$ depth in IN 718 and Ti-6Al-4V) requires considering a high mesh density and consequently a very high computational time especially for 3D models. Knowing this fact, their model presented only a small portion of the entire thin-walled feature to make the simulations computationally efficient. As such, sensitivity analyses to avoid edge effects and to guarantee steady state deformation are necessary. However, Klocke et al did not discuss this issue. Residual stresses were measured using hole drilling technique (0.8 mm dia.). Simulated profiles of residual stresses had less spatial resolution (1 data/50 μm depth) compared to measured ones (1 data/10 to 20 μm depth) and that is because the finest hexahedral elements were 50 μm in lateral size for computational efficiency purpose. Low spatial resolution of computed field variables and high computational times are disadvantages of 3D models. Besides, there were significant discrepancies between simulated profiles and measured ones especially for Ti-6Al-4V and in first 100 μm depth.

Yen et al [20] developed 2D plane strain and 3D finite element models for burnishing and compared the simulation results against each other as well as published experimental measurements in terms of material flow, surface roughness, and surface layer residual stresses. They considered several pre-existing conditions such as initial surface roughness, residual strains, and residual stresses induced by a cutting process preceding burnishing in their models. Their material model was a form of power law. Even though the model had strain hardening

exponent (0.3 for AISI 52100; 62 HRC) but was not capturing strain hardening properly and was showing an elastic-perfectly plastic type behavior. Simulations were displacement-controlled and the rigid ball's in-depth movement was modeled by a polynomial curve. As opposed to 2D model of Beres et al [16], their 2D model was able to consider the effects of not only burnishing speed but also feed. Moreover, the ball does indentation rather than rolling on the surface. They used theoretically calculated normal force in their 3D simulations to extract force-penetration characteristic curve and so overestimated the normal force by neglecting the force-drop due to oil leakage at the tool's tip. They performed necessary analysis to make sure that steady state deformation is achieved in 2D simulations. However, due to excessively large computational time (> 26 hrs per one path) and the required storage capacity, the steady state burnishing was compromised by performing only seven passes rather than required ten passes. Further analyses proved their 3D model was undersized. They concluded that overall the 2D model gives better results compared to the 3D model in terms of residual stress prediction. However, the 3D model showed more realistic surface deformation and material flow where the simplified 2D model represented a series of indenting cycles. Moreover, cutting-induced residual stresses and strains did not show significant effect on after burnish residual stresses.

Sartkulvanich et al [21] further developed the 2D FE model of burnishing presented by Yen et al [20] to study the effects of burnishing parameters (i.e. pressure and feed rate) on surface roughness and residual stresses. The inhomogeneous mechanical behavior of the material in surface layer and bulk substrate as the result of pre-burnish cutting was determined by a combination of instrumented ball indentation test and FEM inverse analysis rather than conventional tension/compression tests. However, their constitutive model for surface layer material was not strain-rate dependent and therefore the FE models could not consider the effects

of burnishing speed. The required penetration depths for displacement-controlled 2D simulations were extracted from load-penetration characteristic curve computed using a 3D model. The effect of pressure loss, at the tool tip due to oil leakage, on normal force was considered in the simulations. Pre-existing surface layer conditions such as surface roughness and residual stresses were measured and considered in simulations as well. The results showed that initial residual stresses from pre-burnish cutting have insignificant effect on residual stresses obtained after burnishing. This conclusion is in agreement with experimental results of Röttger [22]. Predictions of subsurface residual stress profiles with the 2D FE model were in good agreement with experimental measurements by x-ray diffraction. However, there were some discrepancies between computed and measured residual stresses especially in feed-direction and in first 200 μm depth. Burnishing pressure had the most influence on surface roughness and residual stresses.

In the wake of observed discrepancies between predicted and measured surface integrity characteristics, i.e. surface roughness and residual stresses, the need for improving current FE models and developing new ones are still being recognized. Although burnishing is a 3D process, the use of 3D FE model to analyze the effect of various process parameters on surface integrity is limited by the fact that an extremely large computational time is required to run a steady state burnishing simulation which carries enough spatial resolution or mesh density in near surface zone. Therefore, 2D FE model is more practical and has yet the capability to study the effects of burnishing parameters (i.e. pressure, feed, speed, and ball diameter) on surface finish and residual stresses. Because of the overall good predictions made by 2D model of Yen et al [20], this model is further developed in this study by (a) implementing an internal state variable (ISV) plasticity model which captures isotropic hardening, kinematic hardening, Bauschinger effect, strain rate sensitivity, temperature sensitivity, and damage and (b) applying semi-infinite element

layers to avoid edge effects and bounce back of field variables at boundaries. A separate semi-infinite, 2D-axisymmetric FE model is developed to extract the load-penetration characteristic curve for rigid 12.7 mm burnishing ball and Mg-Ca0.8 (42 HV) workpiece material. The parameters of the ISV model are extracted for the novel biodegradable biomaterial. Initial surface roughness and actual normal force are measured and applied in the FE model. The effects of burnishing pressure and feed on surface roughness and residual stresses are studied. Residual stresses are measured using x-ray technique and are used to validate the predictions along with post-burnish roughness measurements.

9.3. Internal state variable (ISV) plasticity model

The ISV plasticity model developed by Bammann, Chiesa, and Johnson [23] is used to describe the deformation state of the material (see section 5.2.2). The material constants are determined by fitting the ISV model to stress-strain data obtained from quasi-static and dynamic compression tests [24-26]. Split Hopkinson Pressure Bar (SHPB) test was applied to obtain mechanical behavior of Mg-Ca0.8 biomaterial under dynamic loading condition.

9.4. Hydrostatic burnishing experiments

The burnishing tool used in this study is Ecoroll HG13. It has a ceramic ball on the tip made of silicon nitride and is 12.7 mm in diameter. This ceramic ball sits on a pressurized hydro cushion which is provided by Ecoroll HGP4.0 hydraulic unit. This unit is capable of producing pressures up to 40 MPa. Based on the technical data provided by manufacturer, a thin layer of

pressurized oil will be between ball and its housing all the time during operation and the ball will roll freely along the sample surface without having a chance to touch its housing. The housing has 10 mm of free stroke to accommodate for elevation changes on sample surface. The power carrying fluid is anti-wear, dual purpose oil Aries 15 which functions as both lubricant and coolant. The top plate of the fixture in figure 9.1 can freely slide in vertical direction and transfer the force to the high accuracy compression load cell (Intertechonology Inc., Model 220 5T) located underneath. All the setup shown in figure 9.1 is hooked up on a 3 axis Cincinnati Arrow 500 CNC milling machine. Two sets of experiments were planned to study the effects of burnishing pressure and lateral feed on surface roughness and near surface residual stresses of Mg-Ca_{0.8} (42 HV) biomaterial after burnishing. Burnishing pressure and lateral feed vary in 2 – 10 MPa and 0.04 – 0.2 mm ranges, respectively (Table 9.1). Samples used in burnishing tests were circular disks (38 mm dia. × 13 mm thickness) which were face milled prior to burnishing using carbide inserts at 2400 m/min surface cutting speed, 0.05 mm/rev feed, and 0.2 mm depth-of-cut.



Fig. 9.1 Experimental setup of burnishing

Table 9.1 Burnishing parameters used in numerical/experimental study

Pressure P [MPa]	Feed f [mm]	Speed V [mm/min]
2	0.1	890
4	0.04, 0.06, 0.08, 0.1, 0.2	890
6	0.1	890
8	0.1	890
10	0.1	890

9.5. Residual stress measurement procedure

Residual stresses are measured using X-ray diffraction technique [27,28]. 4-axis Bruker D8 XRD machine is used for this purpose. X-rays with $\lambda = 0.1542$ nm wavelength are generated by applying 35 mA and 40 kV power to X-ray tube with copper target. X-rays are collimated and directed onto the sample's surface by 0.8 mm diameter collimator. An area detector located 15 cm far from the goniometer's center detects diffracted X-rays which are produced as the result of interaction between colliding X-rays and crystallographic planes of the sample. Diffraction spectrum of Mg-Ca_{0.8} alloy is shown in figure 9.2. Diffraction happens when incident X-rays hit a family of crystallographic planes which satisfy the Bragg's law $n\lambda = 2d \sin\theta$. Each peak in diffraction pattern represents a certain family of such diffracting planes.

Interplanar spacing of crystallographic planes can be considered as internal strain gauges. Strain changes the spacing and ultimately corresponding diffraction angle based on diffraction law. The shift in diffraction angle is used to measure strain. Residual stresses are then computed with $\sin^2\psi$ method. In this study, $\{1\ 2\ \bar{3}\ 3\}$ planes corresponding to $2\theta = 118.48^\circ$ are used to avoid erroneous data involved in using small Bragg angles [29]. The stress state is assumed to be plane stress ($\sigma_3 = 0$) since X-rays only interact with superficial layer of the sample. Besides, the

stress state is taken to be uniform within the diffracting volume. Polycrystalline material's modulus of elasticity and Poisson's ratio, i.e. 45 GPa and 0.33, are used in calculating residual stresses and they are assumed to be isotropic within the diffracting volume.

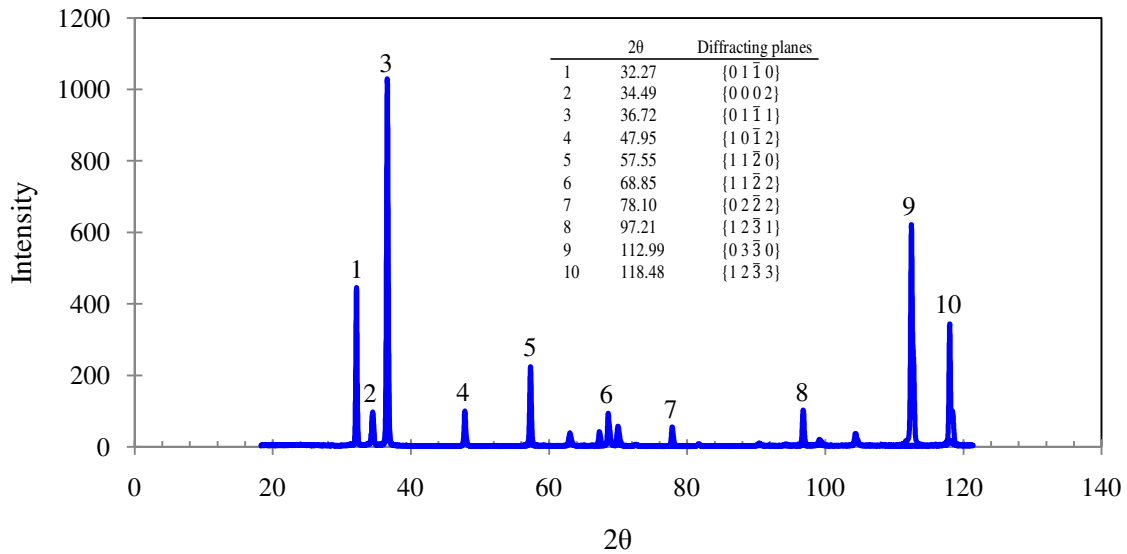


Fig. 9.2 Diffraction spectrum of Mg-Ca_{0.8} alloy

For measuring subsurface residual stresses, electro-polishing technique is utilized to remove the material layer by layer in order to reach to depths below the surface. This technique has much less effect on the microstructure and residual stresses than abrasive polishing. Figure 9.3 shows a schematic of the utilized polishing set-up. The electrolyte is composed of 800 ml ethanol 95%, 150 ml distilled water, and 60 ml perchloric acid 60% (ASTM E1558 – 99). Spinning action of the stirring beam causes the electrolyte to rise up in the stainless steel tube (cathode) till it reaches the sample surface. Moreover, the induced flow in the electrolyte will

assure uniformity of temperature and chemical composition in the electrolyte during the polishing process. Designated water cooling coil keeps temperature at 22 °C. Mask is a nonconductive polymeric material which isolates unwanted areas of the sample from being exposed to electrolyte. Figure 9.4 shows two-dimensional profile and topography of the electro-polished surface. If electrolyte composition, mask size, electrolyte flow rate, voltage, and temperature are already selected, polishing time will be the only parameter which controls the amount of removed material. The mathematical model relating depth of removed material to polishing time is shown in figure 9.5. This model predicts a constant material removal rate of 0.389 $\mu\text{m/s}$ for Mg-Ca_{0.8} alloy under aforementioned conditions.

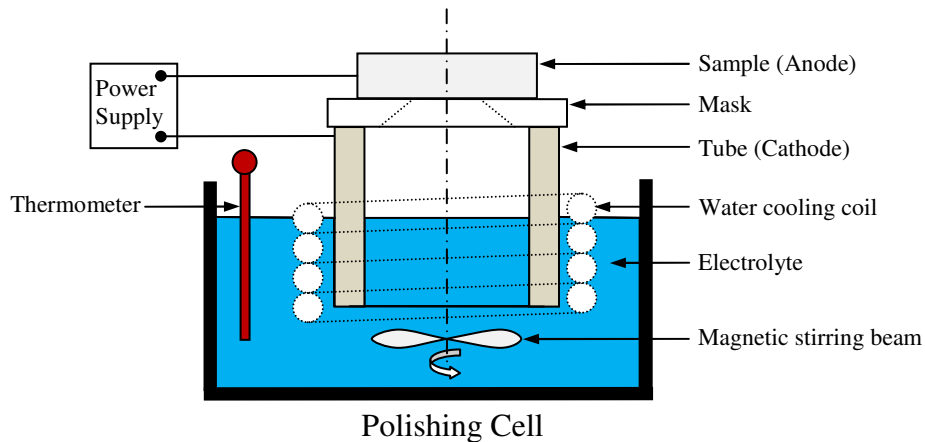


Fig. 9.3 Schematic diagram of the electro-polishing set-up

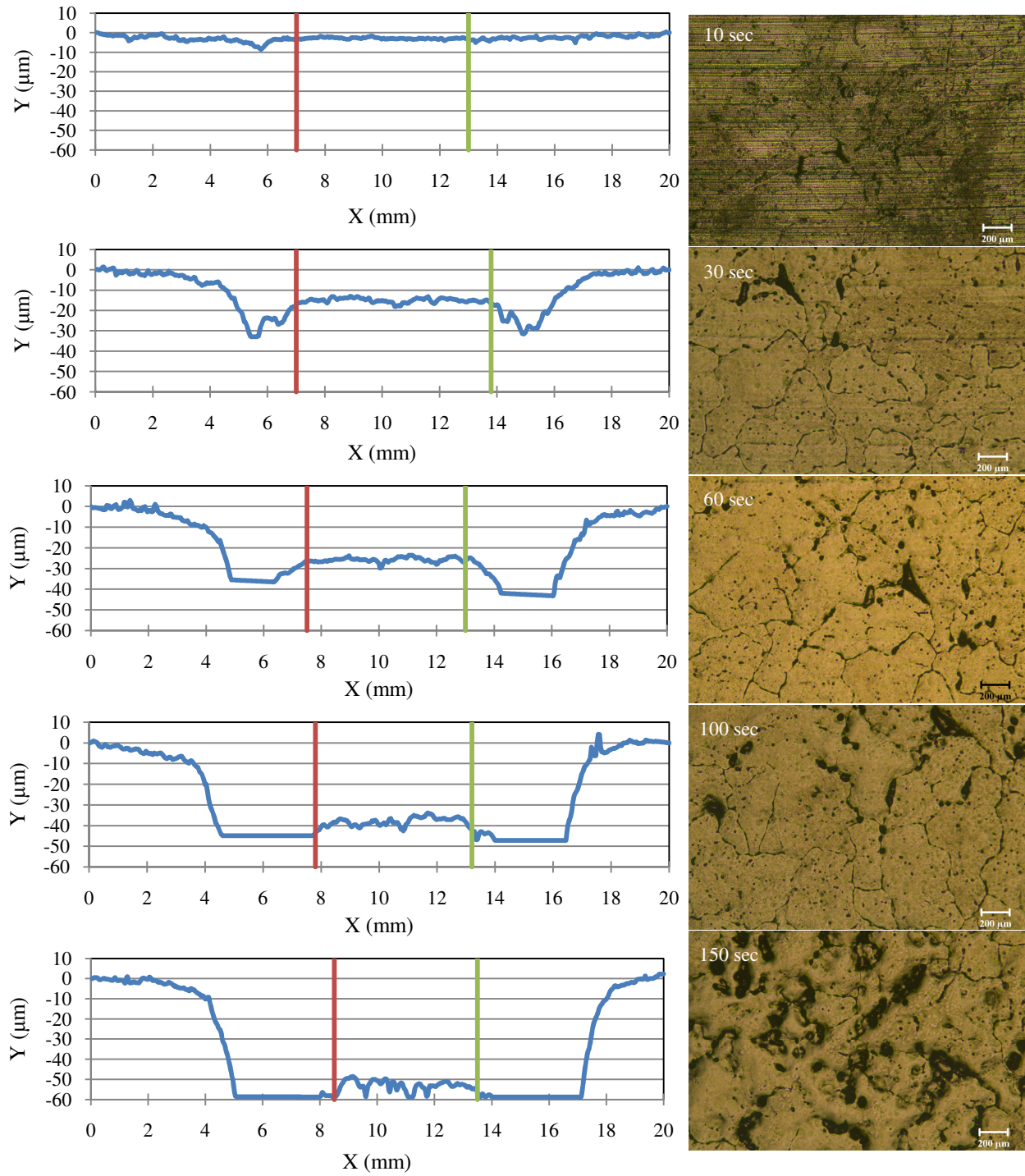


Fig. 9.4 Surface profile and morphology of the electro-polished area

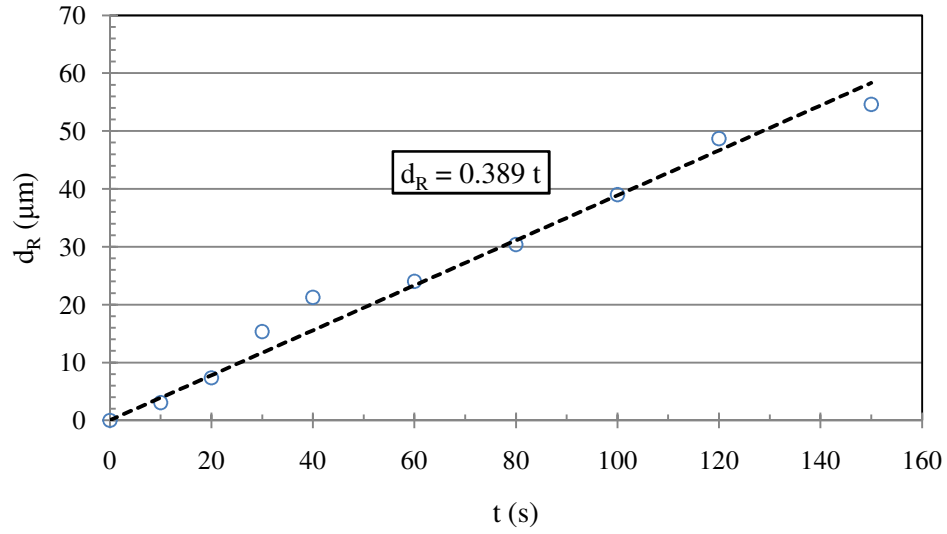


Fig. 9.5 Mathematical model of material removal dynamics in electro-polishing of Mg-Ca0.8

9.6. Simulation scheme

9.6.1. Pre-existing roughness left from face milling

Pre-existing surface roughness is considered in this numerical study to investigate the influence of pre-existing roughness on residual stresses and the influence of burnishing parameters on surface topography. The parameter used to quantify the surface topography condition is roughness depth (R_z) calculated from following equation:

$$Z_i = \max z_i - \min z_i \quad (9.1)$$

$$R_z = \frac{1}{N} (Z_1 + Z_2 + \dots + Z_N) \quad (9.2)$$

If the scanning length in surface roughness measurements is divided into N equal intervals then R_z is the average of Z_i values. Z_i is defined as the difference between peak and valley in each interval. Figure 9.6 shows the measured surface profile after face milling operation and an optical micrograph of the surface. The distance between cutting marks (cutting feed) is $50\ \mu\text{m}$ and knowing that scanning length is $1000\ \mu\text{m}$ there would be twenty intervals ($N=20$) in calculating R_z . The calculated roughness depth based on experimentally measured roughness profile in figure 9.6 is $1.43\ \mu\text{m}$.

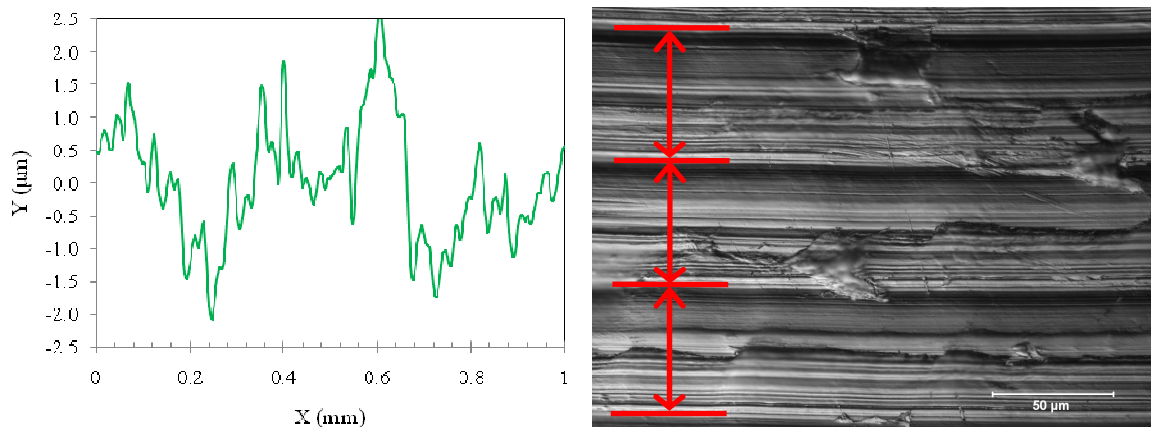


Fig. 9.6 Surface profile and optical micrograph of the face turned sample

9.6.2. Finite element model of burnishing

The developed 2D-plane strain FE model for studying the effects of pressure and feed on surface roughness and residual stresses in hydrostatic burnishing process is shown in figure 9.7. The general purpose FE code ABAQUS is used to make the simulations more cost effective. Since the ceramic ball is much harder than workpiece material, it is assumed to be rigid and its

movement is composed of a series of indentations which are separated by the amount of feed. The overall in-plane dimensions of the workpiece are 4.8 mm × 3 mm. These dimensions are designed to avoid boundary/edge effects, to provide enough length for establishing a steady-state deformation, and also to make sure of having efficient computations. There are two 1.4 mm margins of unburnished material at both ends of the workpiece to avoid boundary effects. Besides, semi-infinite elements along the sides and bottom face of the workpiece model are implemented to provide non-reflective boundaries for stress waves to pass through and so to avoid bounce back. The out-of-plane dimension of the workpiece is considered to be much larger than its thickness to facilitate the plane strain condition. The friction coefficient in ball-workpiece interface is taken to be 0.01 to simulate the highly lubricated interface existing in actual hydrostatic burnishing. The cooling function of the hydraulic oil has led to the assumption of isothermal deformation. The workpiece mesh becomes finer close to the surface to accommodate for the size effect and severe deformation gradients. Elements in the first 50 μm layer are as small as 5 μm and Arbitrary Lagrangian-Eulerian (ALE) adaptive meshing is used across this layer to prevent excessive distortion of elements and ultimately simulation failure. The ISV plasticity model of Mg-Ca_{0.8} alloy is implemented in the simulation via modified user defined material subroutine VUMAT.

The normal force in burnishing can be calculated theoretically applying hydrostatic principles [21]. However, the calculated normal force is larger than the measured one [30]. This discrepancy is attributed to pressure loss at the tip of the burnishing tool due to oil leakage and it grows larger by increasing hydraulic pressure. This pressure drop is considered in all the simulations through this study by using measured normal force rather than calculated one.

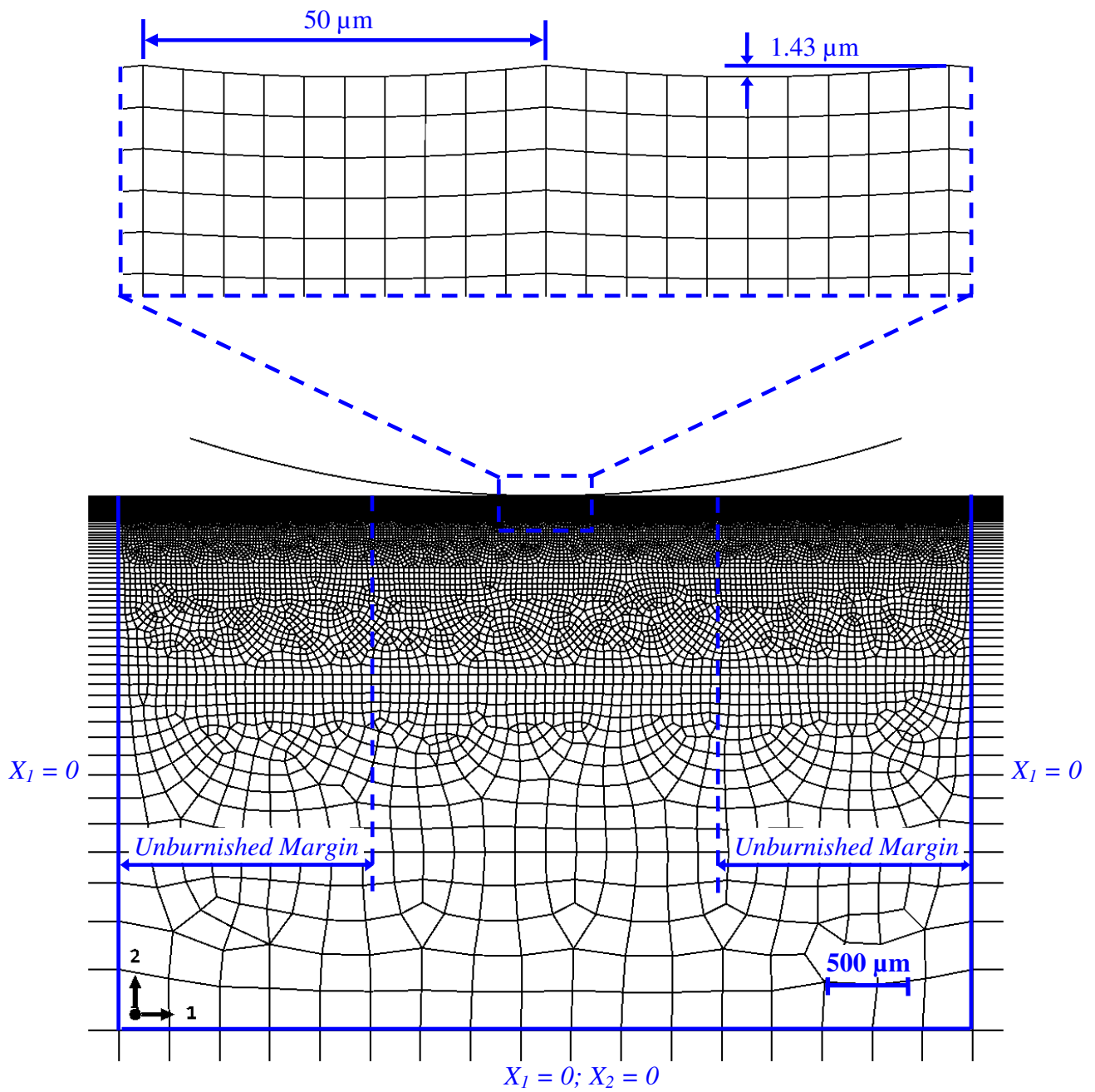


Fig. 9.7 2D plane strain FE model to simulate hydrostatic burnishing of Mg-Ca_{0.8} biomaterial

A total of nine simulations are performed covering different combinations of burnishing pressure and feed in Table 9.1 to evaluate effects of these process parameters on surface roughness and residual stresses. Steady state burnishing was insured for each simulation case by tracing normal contact stresses.

9.6.3. Load-penetration characteristic curve

Movement of the ball can be controlled by using two types of control curves: (i) the time variation of the normal force acting on the tool (force control) or (ii) the time variation of the vertical displacement of the tool (displacement control). However, force control method in 2D plane strain model fails for underestimating penetration depth and overestimating unloading time. The final penetration depth under plane strain condition (i.e. line contact) will actually be smaller than what it would be under realistic 3D condition (i.e. concentrated point contact) with the same applied normal force. Besides, force control method will overestimate the unloading time. The contact time during unloading the ball is expected to be considerably smaller than the loading contact time. These deviations from physics cause predictions for material flow, residual stress, and especially surface finish to deviate from corresponding measurements. Due to these shortcomings, Yen et al [20] and Sartkulvanich et al [21] believed it is more reasonable to build 2D simulations of burnishing process upon equal penetration depth using displacement control method. This thought is adopted for 2D plane strain simulations in this study as well.

Displacement control method will require information on maximum ball penetration depth for given hydraulic pressure (normal force). This depth value includes both elastic and plastic deformations. While plastic part of the deformation can be measured from the remaining dents but the elastic part will be recovered due to spring back and will not be measurable.

Therefore, indentation simulations are carried out to determine the relationship between normal force and ball penetration depth (i.e. characteristic curve). The developed 2D axisymmetric FE model is shown in figure 9.8. The ball is rigid and constrained to move vertically under the measured normal force.

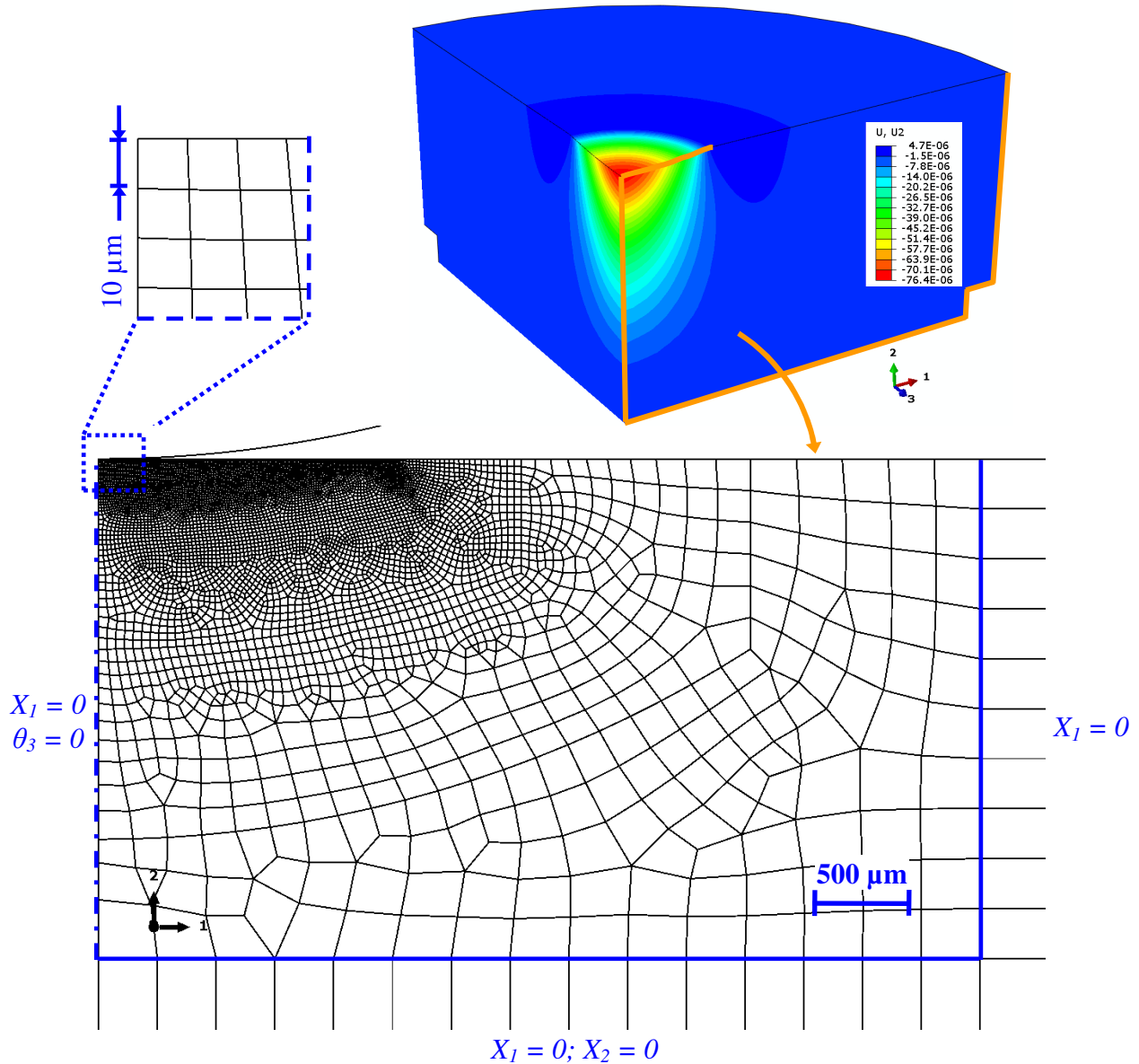


Fig. 9.8 2D axisymmetric FE model to obtain load-penetration characteristic curve

The overall dimensions of the workpiece are 4.5 mm × 2.5 mm and the mesh is optimized to be finer right below the penetrating ball and coarser in the far field. The high density mesh area includes elements as small as 10 μm to provide enough spatial resolution for the output variables. Axisymmetric boundary condition is applied to the left edge of the mesh. Semi-infinite elements are applied along the bottom and right faces of the model to provide non-reflective boundaries. Friction coefficient is 0.01 and ALE adaptive meshing is applied on the upper left corner of the mesh to avoid excessive distortion of elements. Figure 9.9 shows the obtained load-penetration depth characteristic curve.

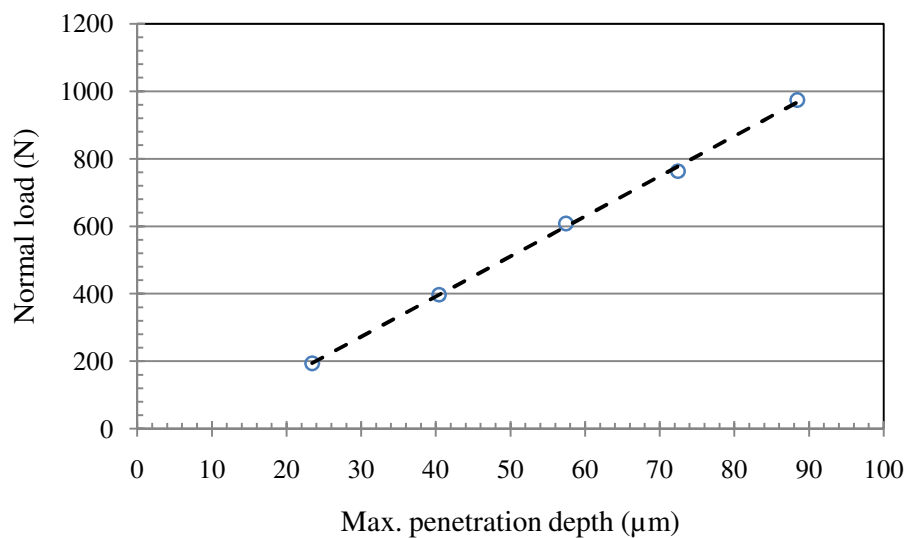


Fig. 9.9 Load-penetration characteristic curve in hydrostatic burnishing of Mg-Ca0.8 biomaterial

9.6.4. Displacement vs. time control curves

The displacement versus time control curves may be approximated by a second-order polynomial in the following form:

$$X_{2b}(t) = a t^2 + b t \quad (9.3)$$

Where X_{2b} is the vertical displacement of the ball, t is the burnishing time, and a and b are constants. These constants are determined in such a way that eqn. (9.3) satisfies following conditions

$$X_{2b}(0) = X_{2b}(t_c) = 0 \quad ; \quad X_{2b}(t_c/2) = d_{max} \quad (9.4)$$

Where t_c is the cycle/step time, and d_{max} is the maximum penetration depth obtained from 2D axisymmetric simulation. The cycle time t_c is approximated by [20]

$$t_c = K \cdot d_c / V_b \quad (9.5)$$

Where V_b is the burnishing speed, d_c is the contact area diameter obtained from 2D axisymmetric simulations, and K is the proportionality constant taken to be 0.001 in this study to make simulation times more manageable. Table 9.2 summarizes values of all parameters used to obtain displacement control curves in figure 9.10. Here, the effect of burnishing speed is considered implicitly by using eqn. (9.5).

Table 9.2 Parameters of second-order displacement polynomials

Pressure [MPa]	Normal load [N]	Penetration [μm]	Contact dia. [μm]	Step time [μs]	a [m/s^2]	b [m/s]
2	194	23.43	1198	80.8	-1.43×10^4	1.16
4	397	40.43	1520	103	-1.54×10^4	1.58
6	608	57.43	1762	119	-1.63×10^4	1.93
8	763	72.43	1906	129	-1.75×10^4	2.25
10	974	88.43	2092	141	-1.78×10^4	2.51

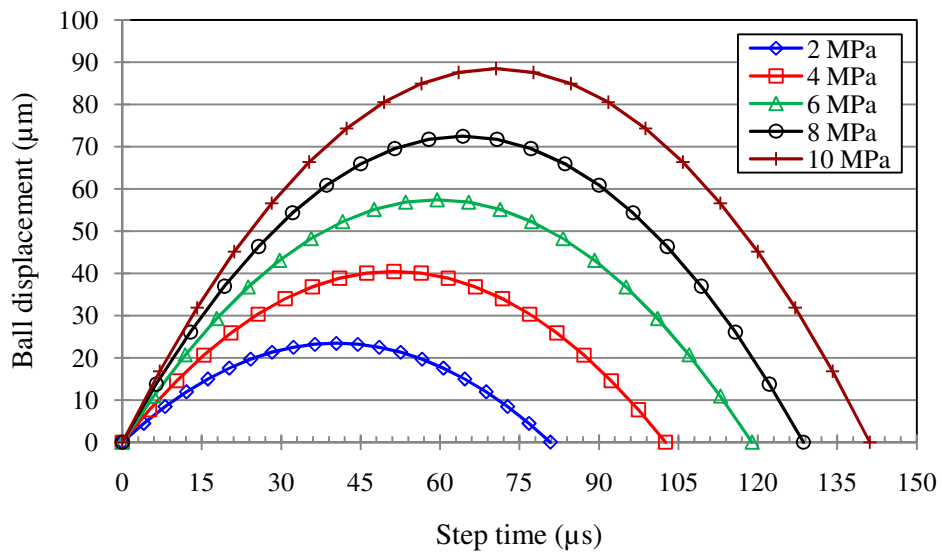


Fig. 9.10 Displacement vs. time control curves (burnishing speed $V_b = 890$ mm/min)

9.7. Results and discussion

9.7.1. Steady state burnishing

Number of indentation cycles needed to have steady state deformation in figure 9.7 varies depending on burnishing parameters. Figure 9.11 shows time histories of normal contact stress (S_{22}) at a representative point located half way through the burnished zone in figure 9.7 (i.e. $X_I = 2.4$ mm). Number of times that S_{22} spikes shoot beyond compressive yield stress (i.e. -85 MPa) is the number of indentation cycles needed to have full deformation history in a surface point. Burnishing under higher pressures will require more indentation cycles to establish the steady state deformation as is shown in figure 9.11a. However, larger feeds will require less cycles (figure 9.11b). Moreover, S_{22} spikes become smaller as deformation proceeds. This might be due to the fact that as deformation proceeds less unburnished material would be left to resist deformation and constancy of volume in plastic deformation would be satisfied easier.

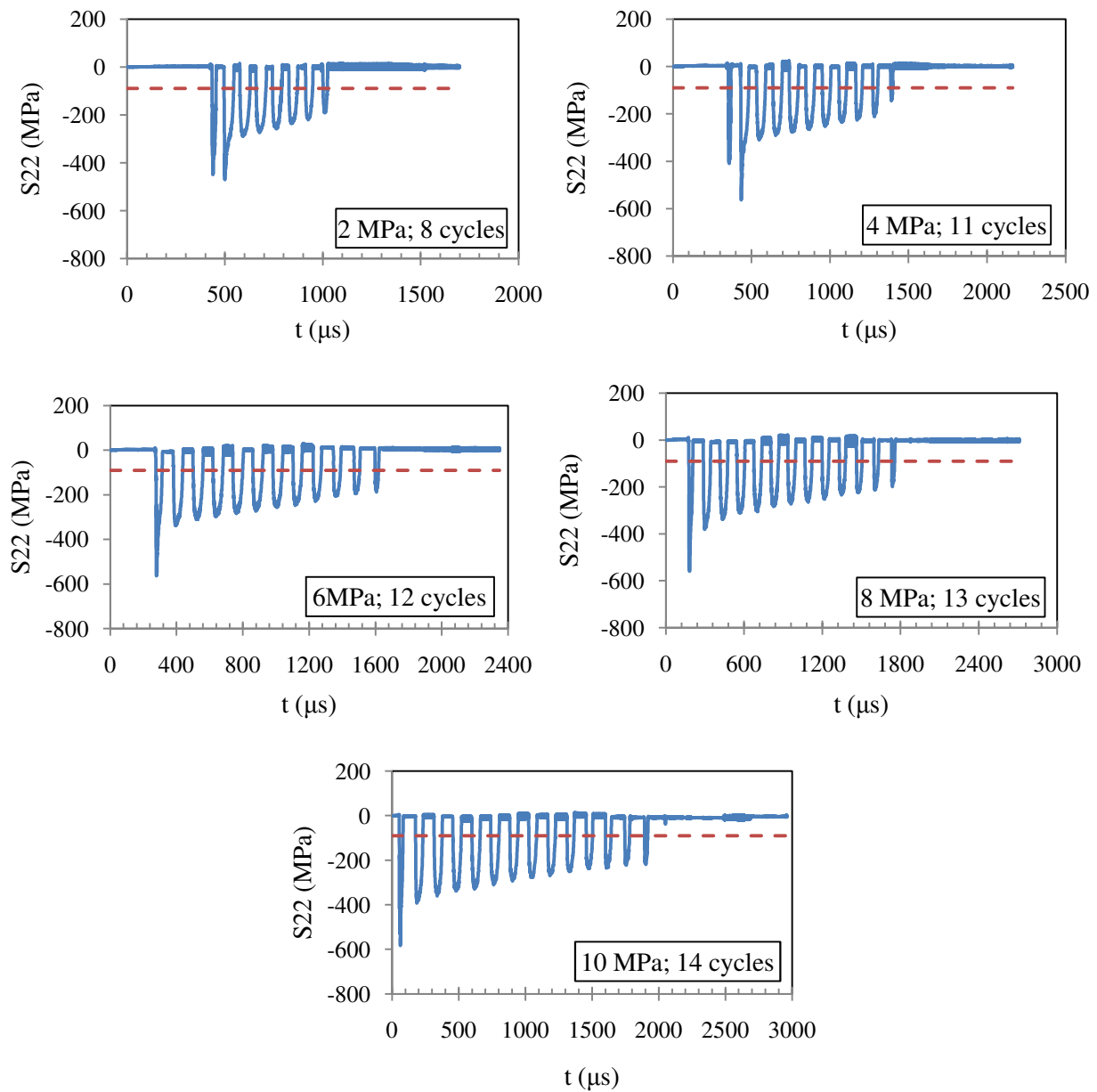


Fig. 9.11a Time history of contact stress at $X_1 = 2.4$ mm under different burnishing pressures ($f = 0.1$ mm; $V = 890$ mm/min)

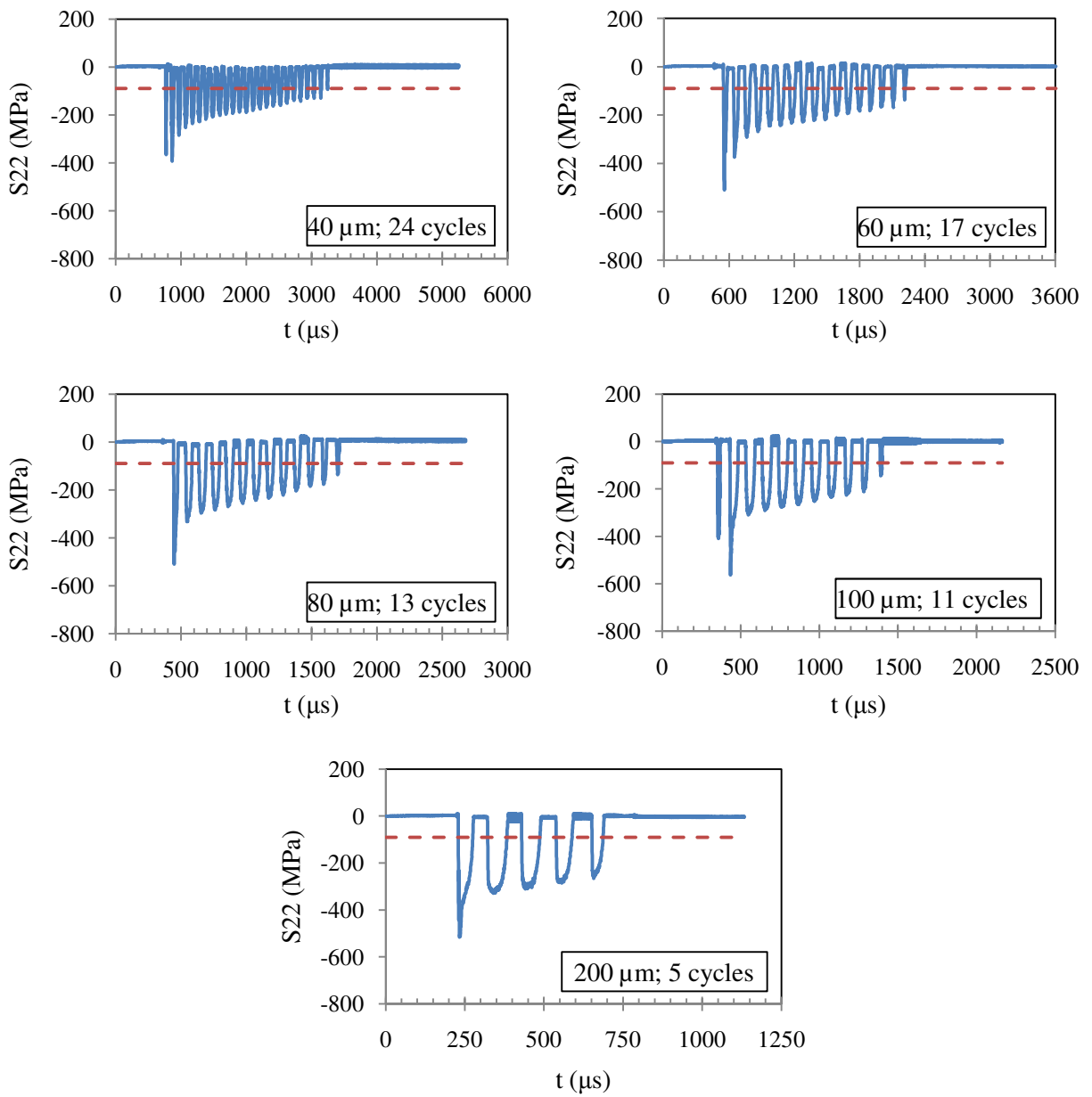


Fig. 9.11b Time history of contact stress at $X_1 = 2.4 \text{ mm}$ under different burnishing feeds ($P = 40 \text{ MPa}$; $V = 890 \text{ mm/min}$)

9.7.2. Effect of pressure and feed on surface roughness

Figure 9.12 shows the predicted and measured surface roughness values. X_1 and X_2 coordinates of the nodes in the burnished zone (figure 9.7) are predicted from simulations and then roughness parameter R_a is computed using following equation:

$$R_a = \frac{1}{L} \int_0^L |Z(X)| dX \quad (9.6)$$

The measured R_a does not show a significant change by increasing burnishing pressure in figure 9.12 c. A one-way ANOVA analysis was performed to validate this statistically. The calculated p -value (i.e. 0.541) was way above the 5% rejection criterion. Therefore, pressure being effect less on surface roughness is statistically valid. However, numerical predictions in figure 9.12 a show opposite and R_a increases considerably by increasing pressure.

On the other hand, measured R_a values in figure 9.12 d show an increasing trend with increasing burnishing feed. Feed being influential on surface roughness was validated statistically as well (p -value = 0.044). Numerical simulations predict the same ascending trend with increasing feed in figure 9.12 b, however, predictions are considerably greater than measurements in magnitude.

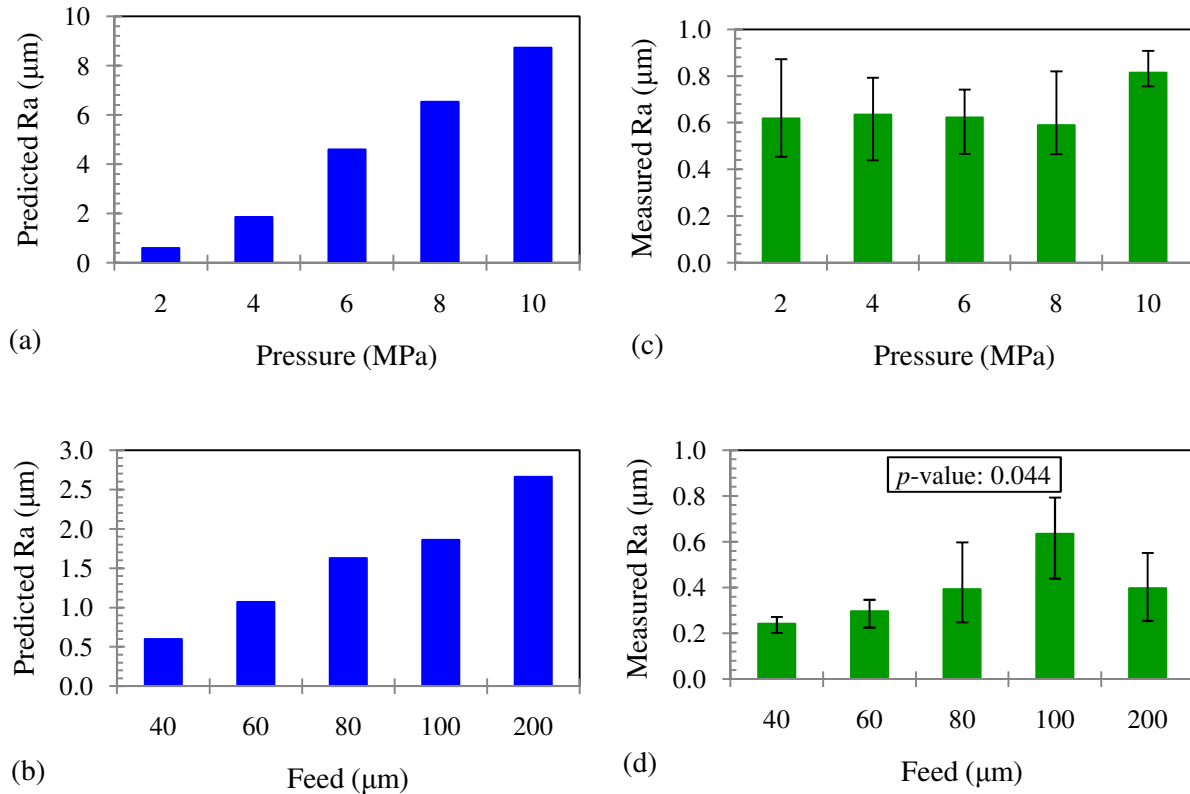


Fig. 9.12 Predicted and measured surface roughness under various combinations of burnishing pressure and feed

9.7.3. Effect of pressure and feed on residual stress profiles

Figure 9.13 illustrates how pre-existing surface roughness interacts with von Mises stress distribution and its evolution at first 100 μm of surface layer in first indentation cycle. The stress distribution is heavily non-uniform early in the indentation cycle ($t = 3.23 \mu\text{s}$). Red spots, representing highly stressed regions, exist right below the peaks of roughness profile. Peaks are first locations that burnishing ball comes into contact with workpiece and they act as stress concentrators. There are also blue spots, representing low stressed regions, at about 25 μm below valleys of the roughness profile. Valleys are last locations that burnishing ball comes into contact

with. This non-uniformity in stress distribution becomes less intense half-way through the cycle ($t = 40.4 \mu\text{s}$) since all points on the surface are in contact with the penetrating ball and therefore the load is transferred uniformly to the deforming material. However, at the end of the cycle ($t = 80.8 \mu\text{s}$), regions which were originally covered with blue spots are grown to pear-shaped regions with higher stress levels. Also, interestingly, regions which were originally covered with red spots are shrunk to almost $10 \mu\text{m}$ deep regions with lower levels of stress. These locally stressed surface regions are surrounded by uniformly stressed substrate. The stress variation at last stages of the cycle ($\sim 80 \text{ MPa}$) is not as large as what it was at early stages of the cycle ($\sim 240 \text{ MPa}$) which is due to establishment of full contact between ball and workpiece and consequently uniform transfer of load to all surface points.

In order to capture the possible effects of the roughness profile on residual stresses, six different paths were defined (as is shown in figure 9.14) to record residual stresses along them. Due to symmetry of the roughness profile and the presence of steady state deformation, this $25 \mu\text{m}$ wide region will be able to represent residual stresses of the whole burnished surface. Roughness profile is especially affecting in-burnish-direction component of the residual stress (S_{33}) particularly in first $70 \mu\text{m}$ below surface. However, this effect is expected to be somewhat underestimated due to ALE adaptive meshing and its effect on roughness profile during simulations. The average of these six stress profiles is used for each simulation case for the rest of this paper to compare predictions against each other and also against measurements.

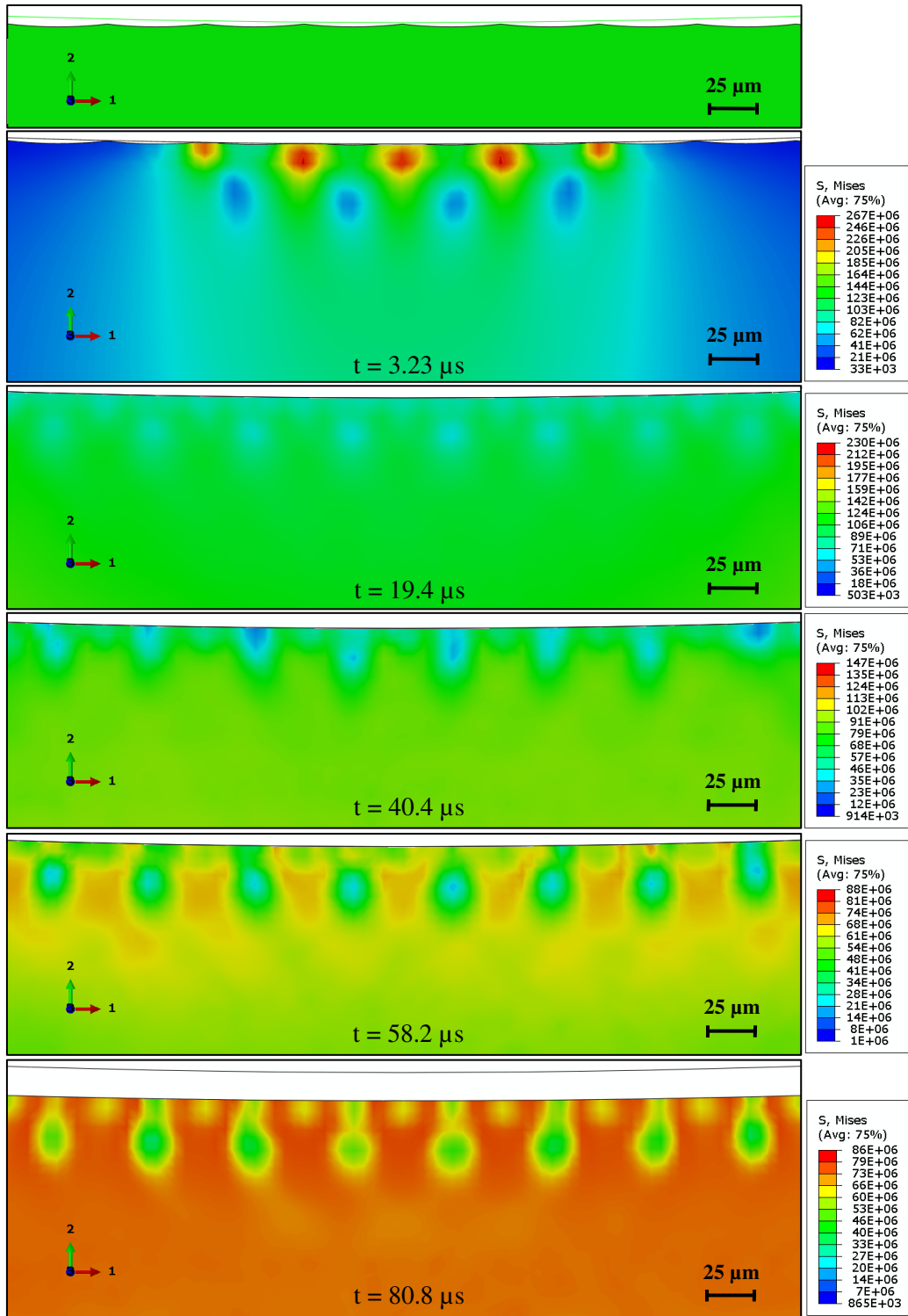


Fig. 9.13 Effect of pre-existing roughness on transient stresses in burnishing Mg-Ca0.8 ($P = 2 \text{ Mpa}$; $f = 100 \text{ μm}$; $V = 890 \text{ mm/min}$; first indentation cycle)

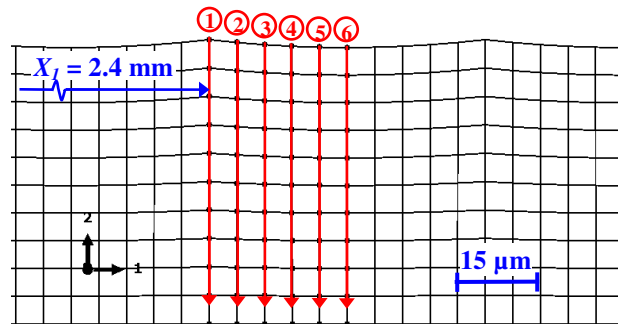
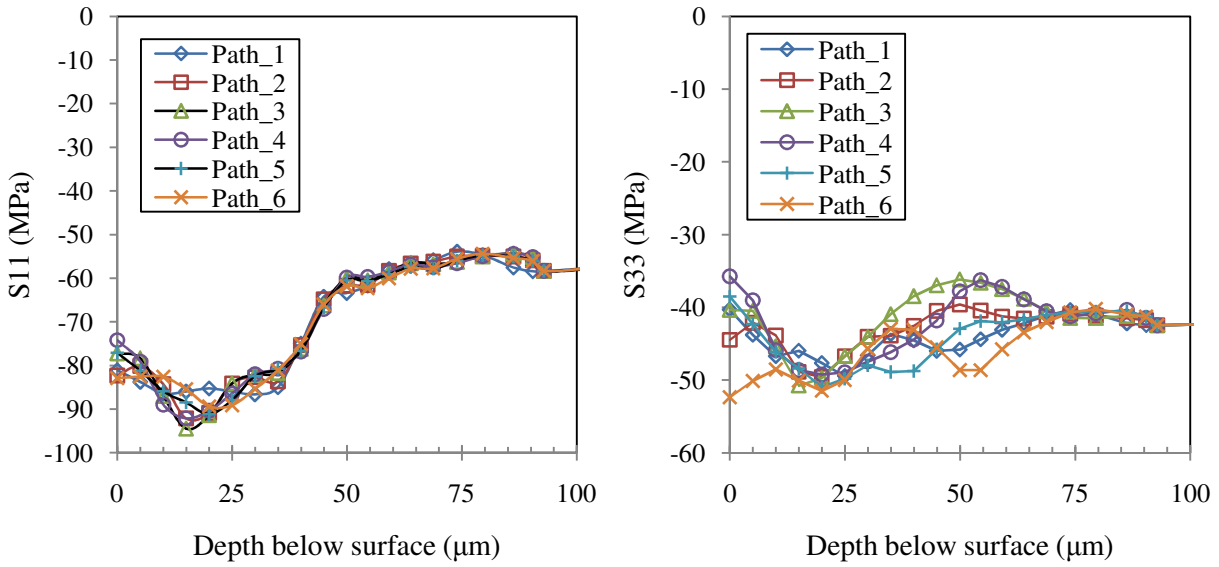


Fig. 9.14 Effect of pre-existing roughness on residual stresses ($P = 2 \text{ Mpa}$; $f = 100 \mu\text{m}$; $V = 890 \text{ mm/min}$)

Figure 9.15 shows predictions on how pressure and feed in burnishing affect residual stresses. These effects can be studied in two distinct regions: (i) right on the surface, and (ii) 3 mm thick layer below surface. S_{11} is in-feed-direction component of residual stress tensor and S_{33} is in-burnish-direction component. Right on surface, both components decrease with increasing pressure and they increase with increasing feed.

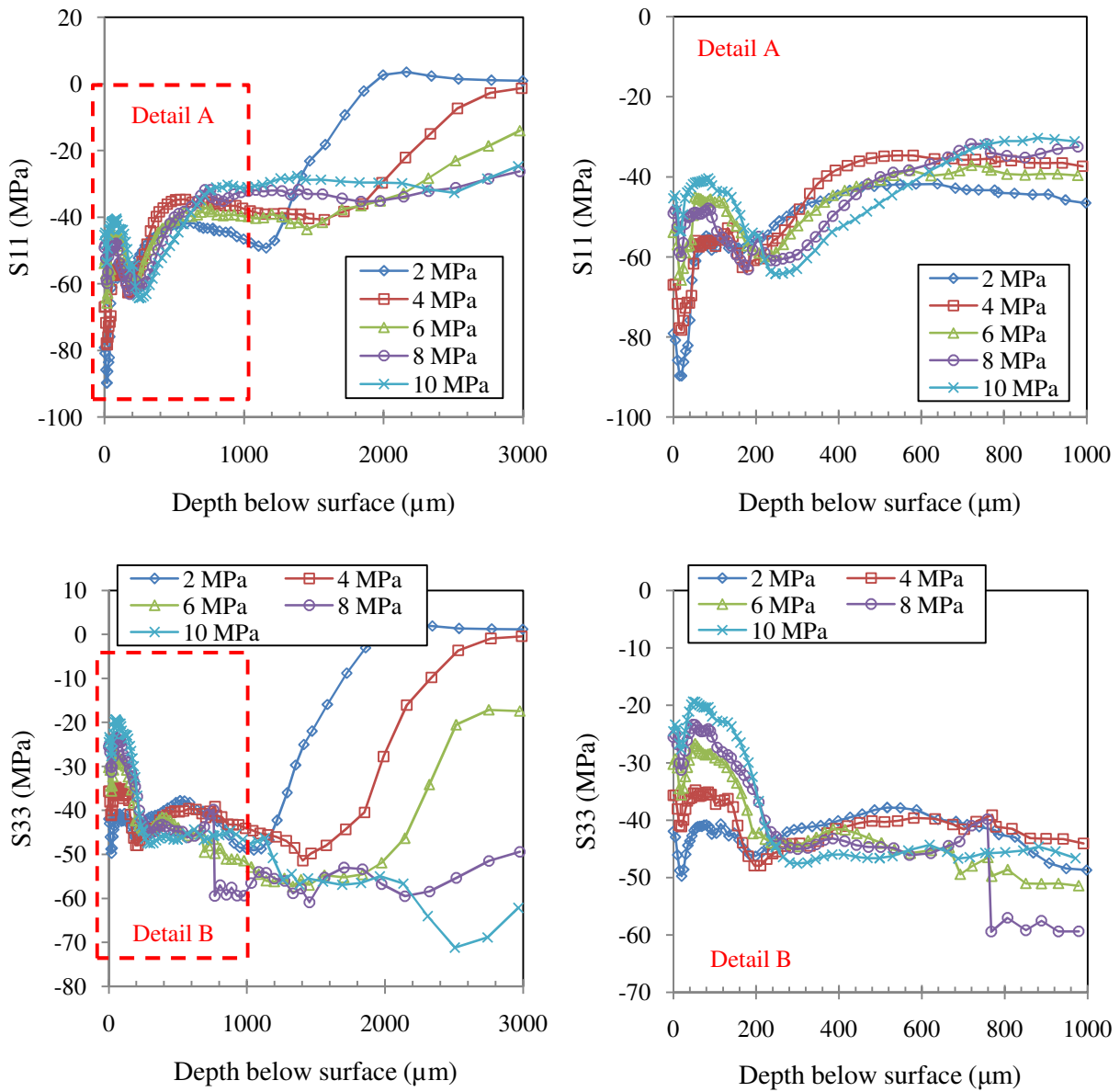


Fig. 9.15a Effect of burnishing pressure on residual stresses

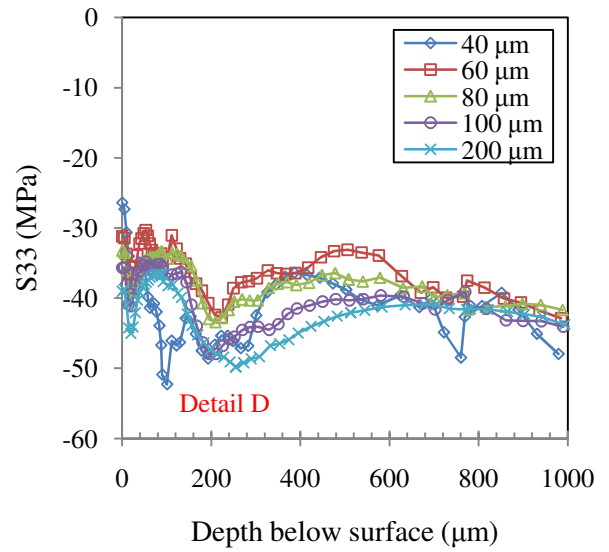
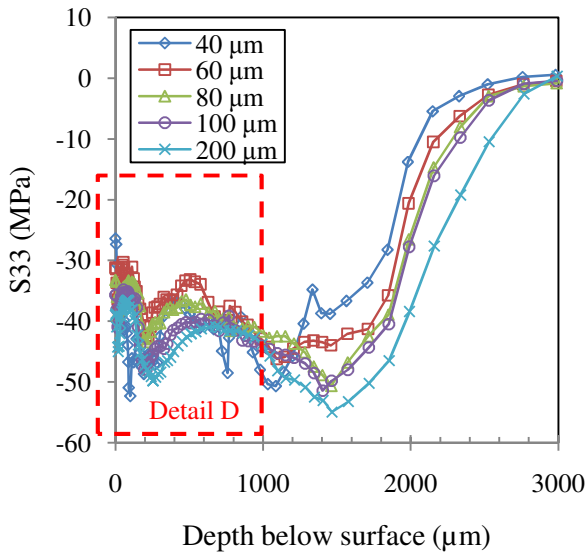
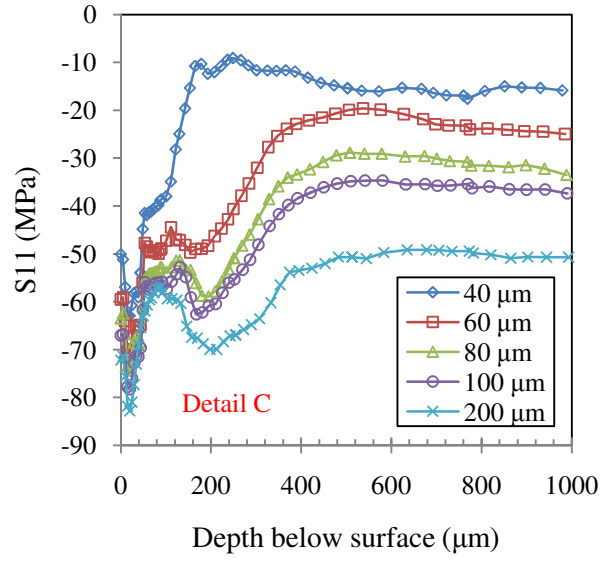
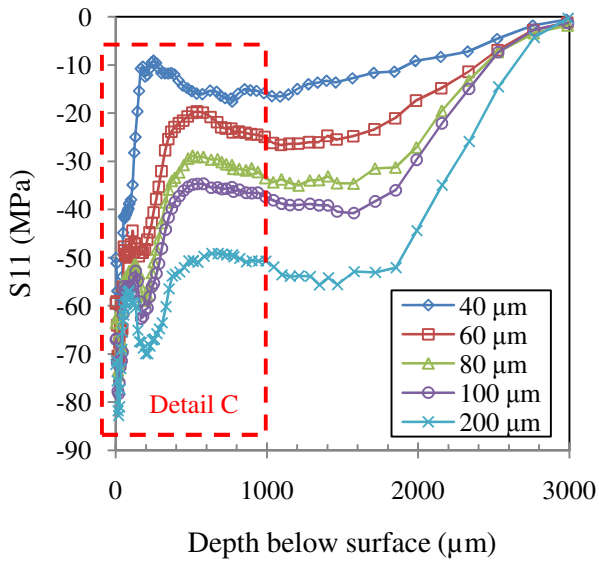


Fig. 9.15b Effect of burnishing feed on residual stresses

In-feed-direction component is affected by pressure differently at various depths below surface (figure 9.15a). In this context, subsurface layer can be divided roughly into four regions: (i) 0 - 200 μm : smaller pressure causes more compressive residual stress; (ii) 200 – 600 μm : larger pressure causes more compressive residual stress; (iii) 600 – 1200 μm : similar to region (i); and (iv) above 1200 μm : similar to region (ii). Magnitude of maximum compressive stress decreases from ~ -90 MPa down to ~ -65 MPa by increasing burnishing pressure while its location increases from 25 μm up to 260 μm , respectively. The effect of feed on *in-feed-direction* component is more uniform and increasing feed causes the subsurface stress profile to shift downwards resulting in more compressive stresses (figure 9.15b) . Aligned with this observation, maximum compressive stress stays at 25 μm depth while feed increases however its magnitude rises up to ~ -83 MPa from -63 MPa.

In-burnish-direction component shows different patterns under the influence of pressure at two distinct subsurface regions (figure 9.15a): (i) 0 – 200 μm : smaller pressure causes more compressive residual stress; (ii) above 200 μm : larger pressure causes more compressive residual stress. Magnitude of maximum compressive stress increases from ~ -50 MPa up to ~ -73 MPa by increasing burnishing pressure while its location also increases from 1100 μm up to 2500 μm , respectively. The effect of feed on *in-burnish-direction* component is more uniform and increasing feed causes the subsurface stress profile to shift slightly downwards and to the right. Accordingly, maximum compressive stress penetrates slightly deeper from 1000 μm down to 1400 μm with increasing feed and similarly its magnitude rises slightly from -50 MPa up to -55 MPa, respectively.

In summary, it is predicted that burnishing induces compressive residual stresses down to very deep layers, in the order of several millimeters. Larger burnishing pressure causes smaller

residual stresses on the surface and in first 200 μm below surface. Residual stresses penetrate deeper under larger burnishing pressures. Higher burnishing feed causes larger residual stresses on surface and in subsurface. Feed affects magnitude of residual stresses more than the depth they penetrate into.

Figure 9.16 shows a schematic of residual S_{11} and S_{33} stress profiles in first 1000 μm below the surface. Two distinct depth regions are recognizable on these profiles: (i) zero to X_o μm where S_{11} is more compressive than S_{33} ; and (ii) X_o to 1000 μm where S_{33} becomes more compressive than S_{11} . The two residual stress components are equal at X_o μm depth. The area enclosed between the two profiles in each region (i.e. A_i , $i=1, 2$) is an indication of the degree that one stress component is more compressive than the other. The general shape of the profiles remains unchanged by altering the pressure and feed values; however, X_o , A_1 , and A_2 change as are shown in figure 9.16 plots. X_o moves to deeper layers by increasing pressure and feed meaning the region that its S_{11} component is more compressive than S_{33} becomes deeper. However, the effect of feed on X_o is stronger than pressure. In 8 MPa ($X_o = 440$ μm) and 80 μm ($X_o = 320$ μm) cases, A_1 and A_2 become equal. In pressure effect cases, A_1 starts with being larger than A_2 and it stays that way through the whole pressure range while in feed effect cases, A_1 starts with being smaller than A_2 but with increasing feed and after $X_o = 320$ μm it becomes larger.

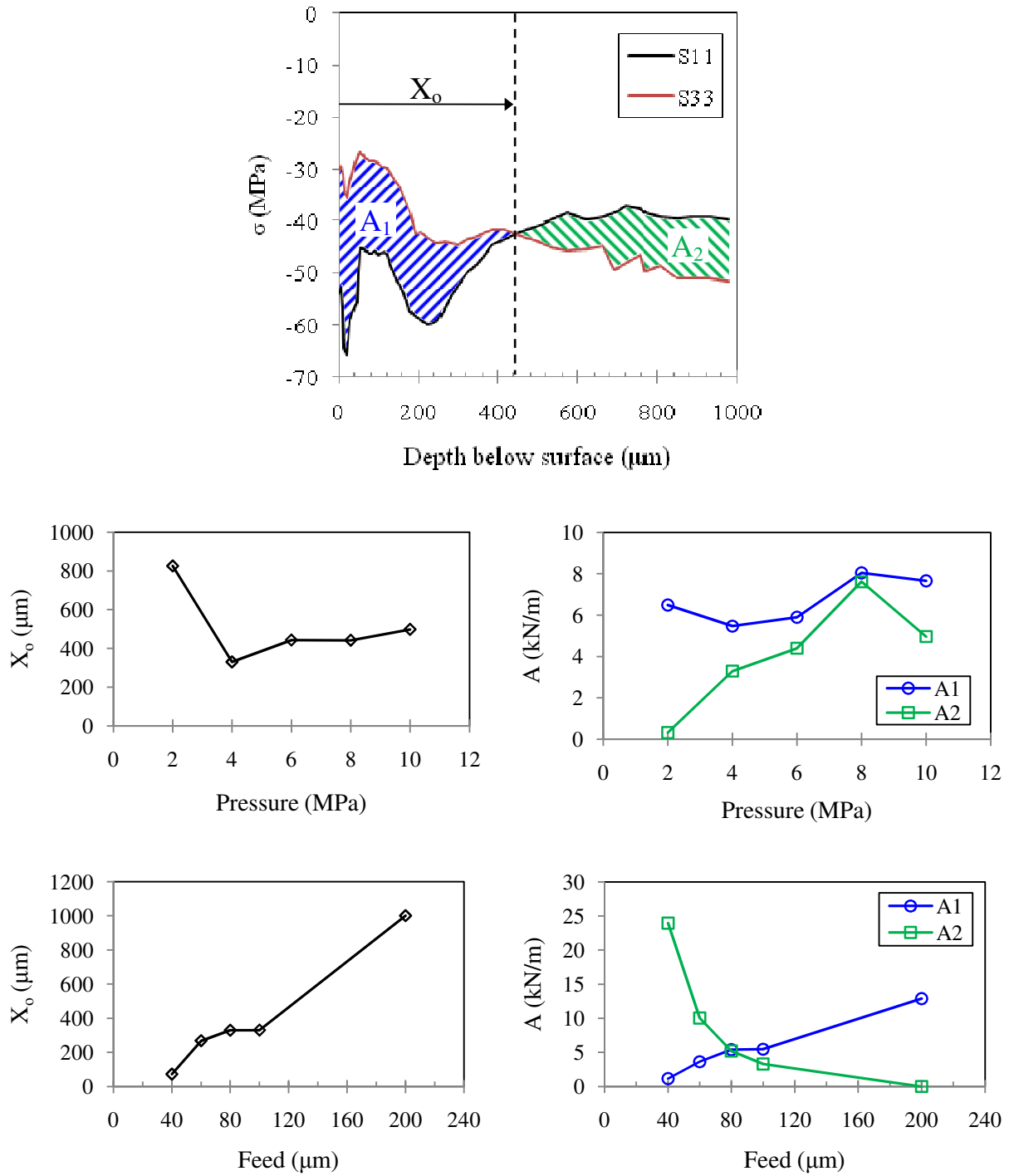
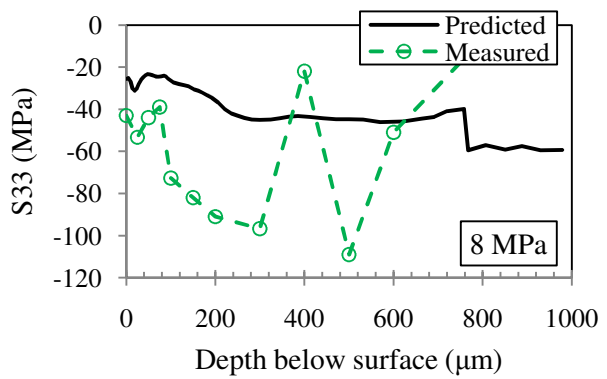
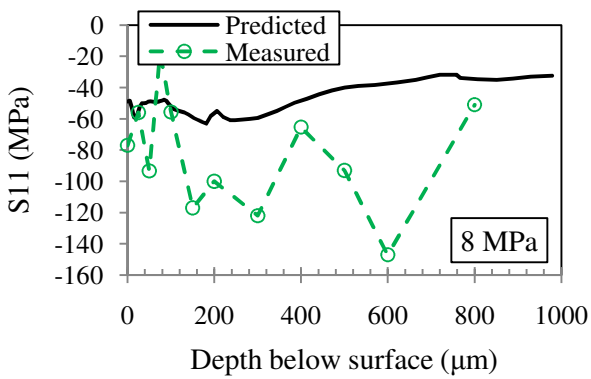
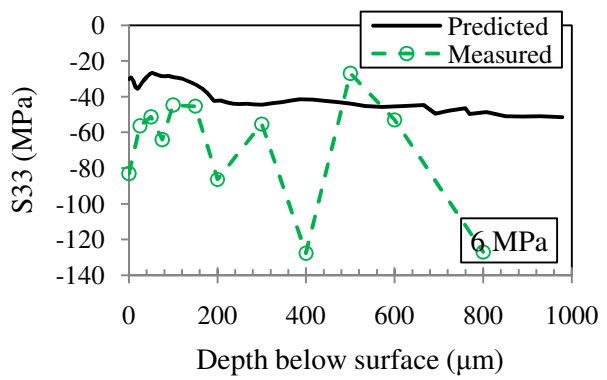
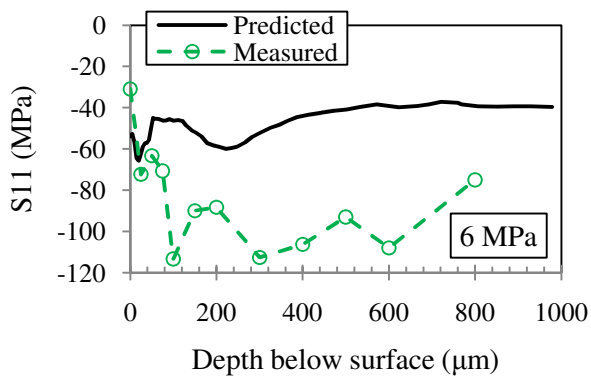
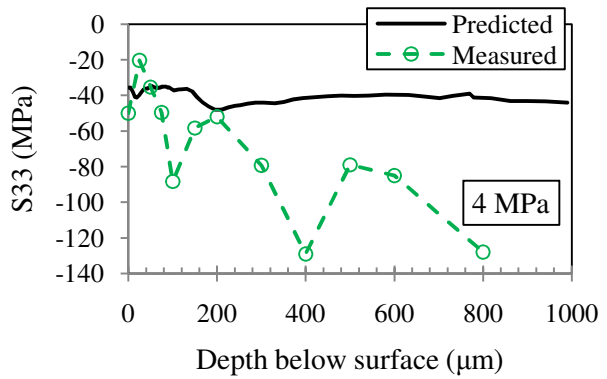
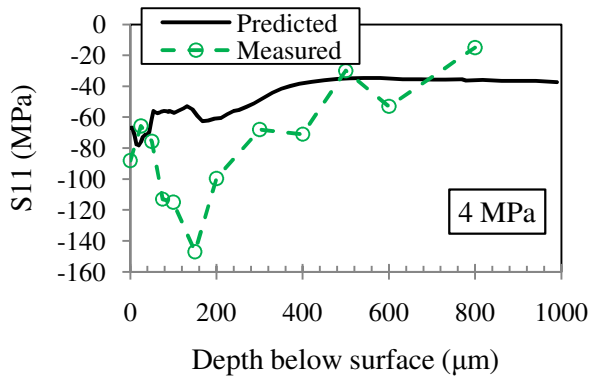
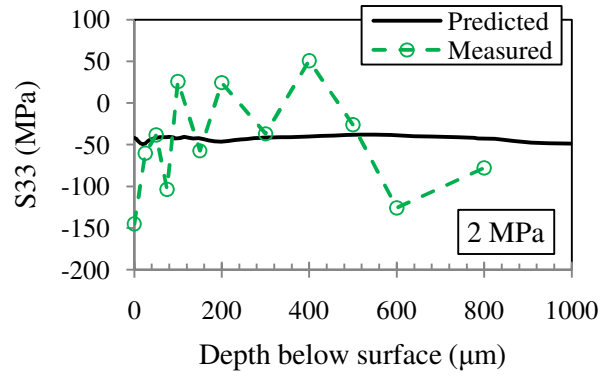
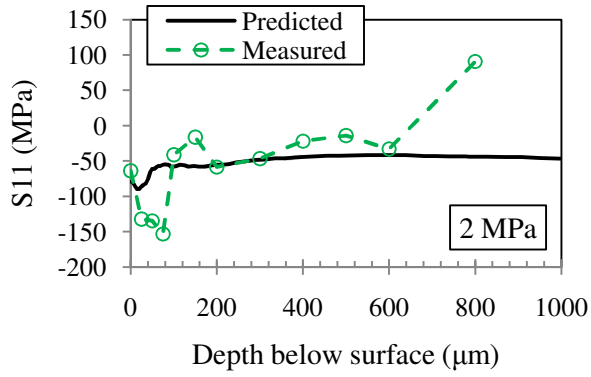


Fig. 9.16 Comparison between residual stresses in-feed and in-burnish directions

Residual stress predictions and measurements are compared in figure 9.17. Measurements are much larger than predictions. A possible reason might be the fact that the tool in 2D plane strain model is actually a cylinder rather than a sphere. Therefore, the applied load is expected to be less concentrated compared to spherical geometry and hence to induce smaller residual stresses. Predicted loads using cylindrical tool are compared to measured loads (dashed lines) in figure 9.18. Measured normal forces in Table 9.2 are divided by the corresponding contact area diameter to calculate an average load with appropriate unit (i.e. kN/m) comparable to predictions. It is seen that the measured load in spherical tool is larger than predicted load in cylindrical tool. The measured load is expected to be even larger than what is shown in figure 9.18 since a uniform load distribution was assumed in calculating measured load rather than the actual elliptical distribution in sphere-flat type contact. This assumption along with the fact that actual contact area in burnishing is smaller than numerically computed one in Table 9.2, cause an underestimation of the actual loading.

Underestimation of loading in numerical predictions is a possible reason for the observed discrepancy between measurements and predictions in figure 9.19 but it is not all. Optical images taken from the subsurface microstructure before and after burnishing (figure 9.19) show that extra large grains existed before burnishing are not refined through burnishing process against expectations. Therefore, the assumption of dealing with a polycrystalline material in the area exposed to x-ray radiations is not valid. This has caused non-uniform and poorly defined diffraction rings shown in figure 9.19 which are the basis for computing residual stresses. Therefore, some of the discrepancy is caused by the limitation of the measurement technique (maximum collimator size of 0.8 mm) and grain structure of the material.



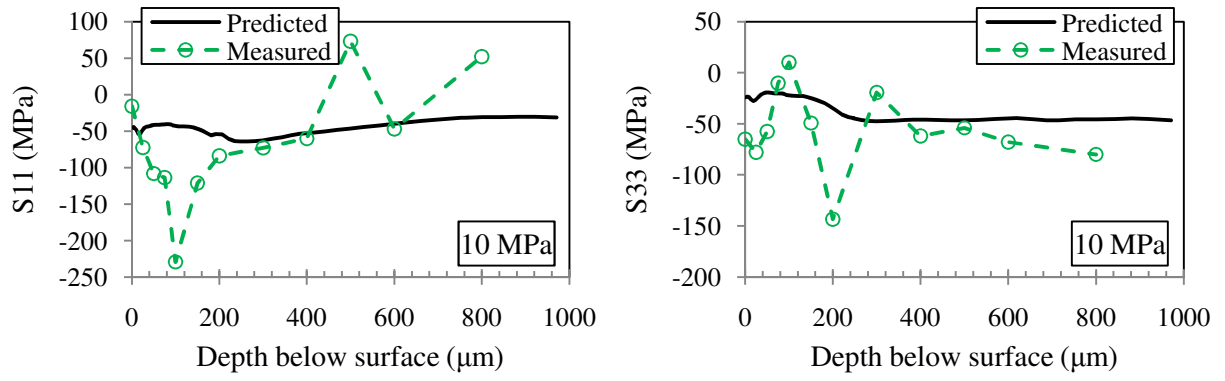
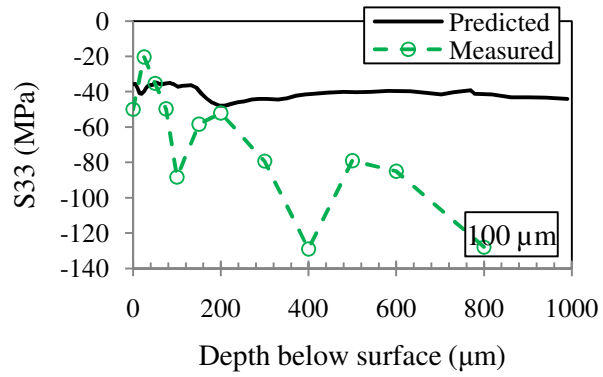
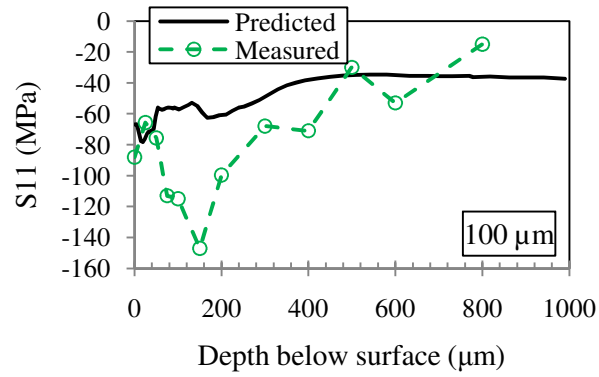
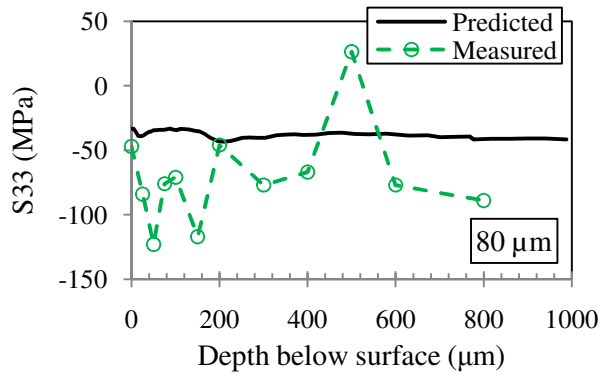
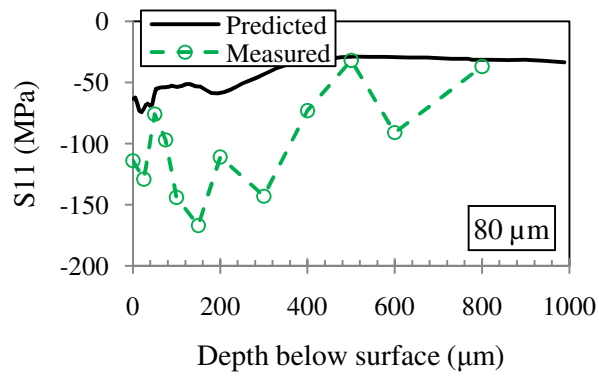
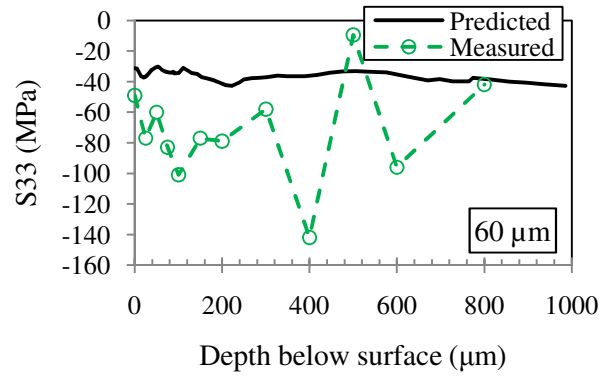
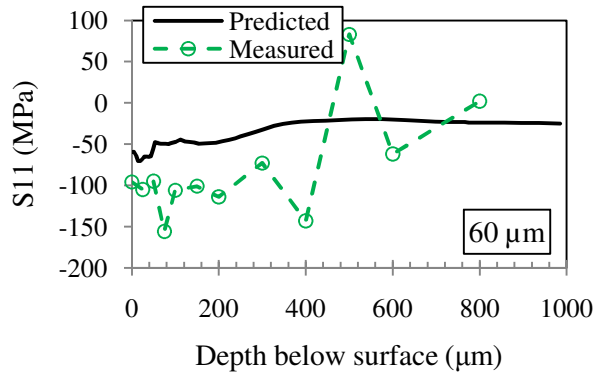
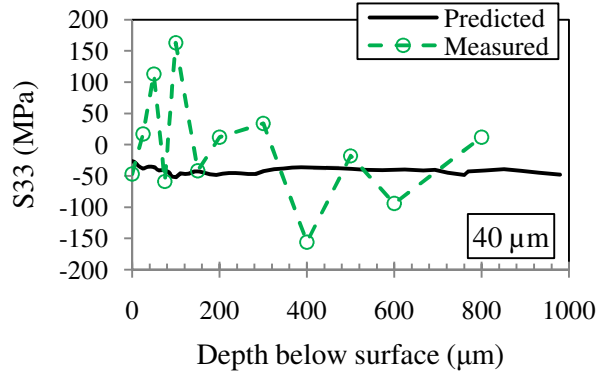
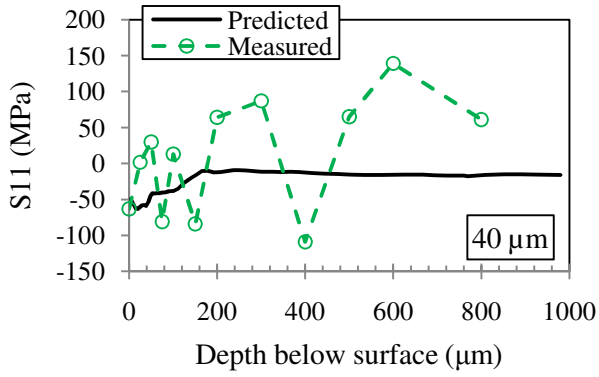


Fig. 9.17a Comparison between predicted and measured residual stresses (pressure effect)



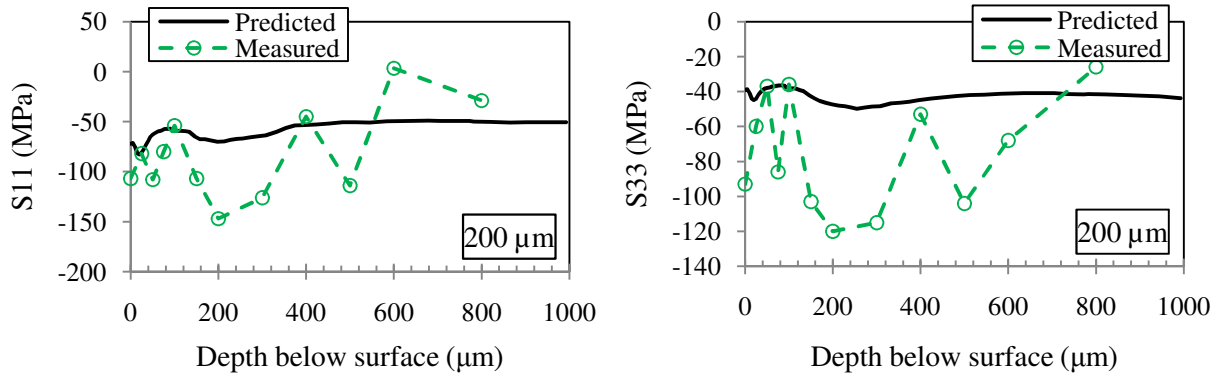


Fig. 9.17b Comparison between predicted and measured residual stresses (feed effect)

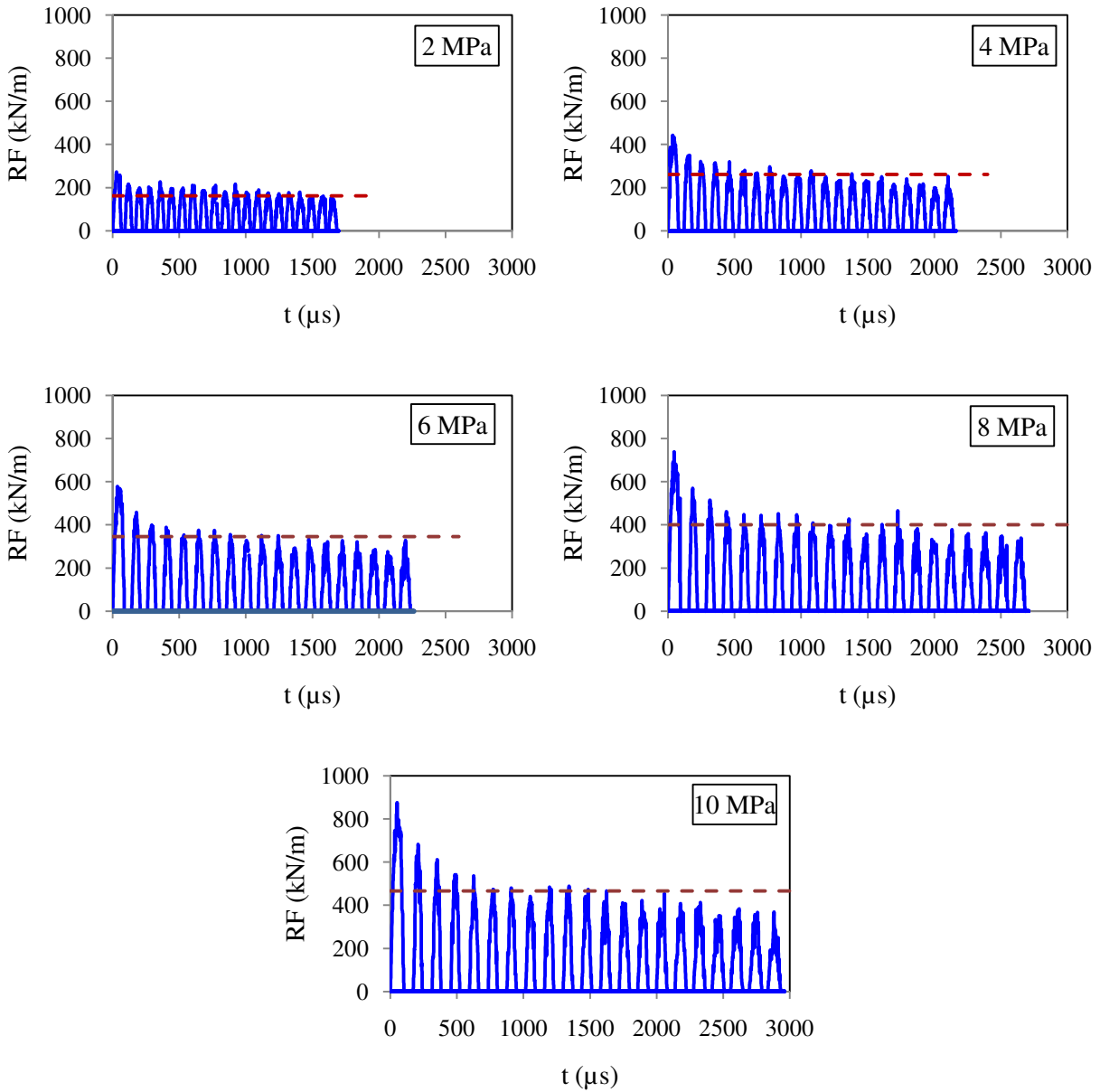


Fig. 9.18a Time histories of normal forces under different burnishing pressures ($f = 100 \mu\text{m}$; $V = 890 \text{ mm/min}$)

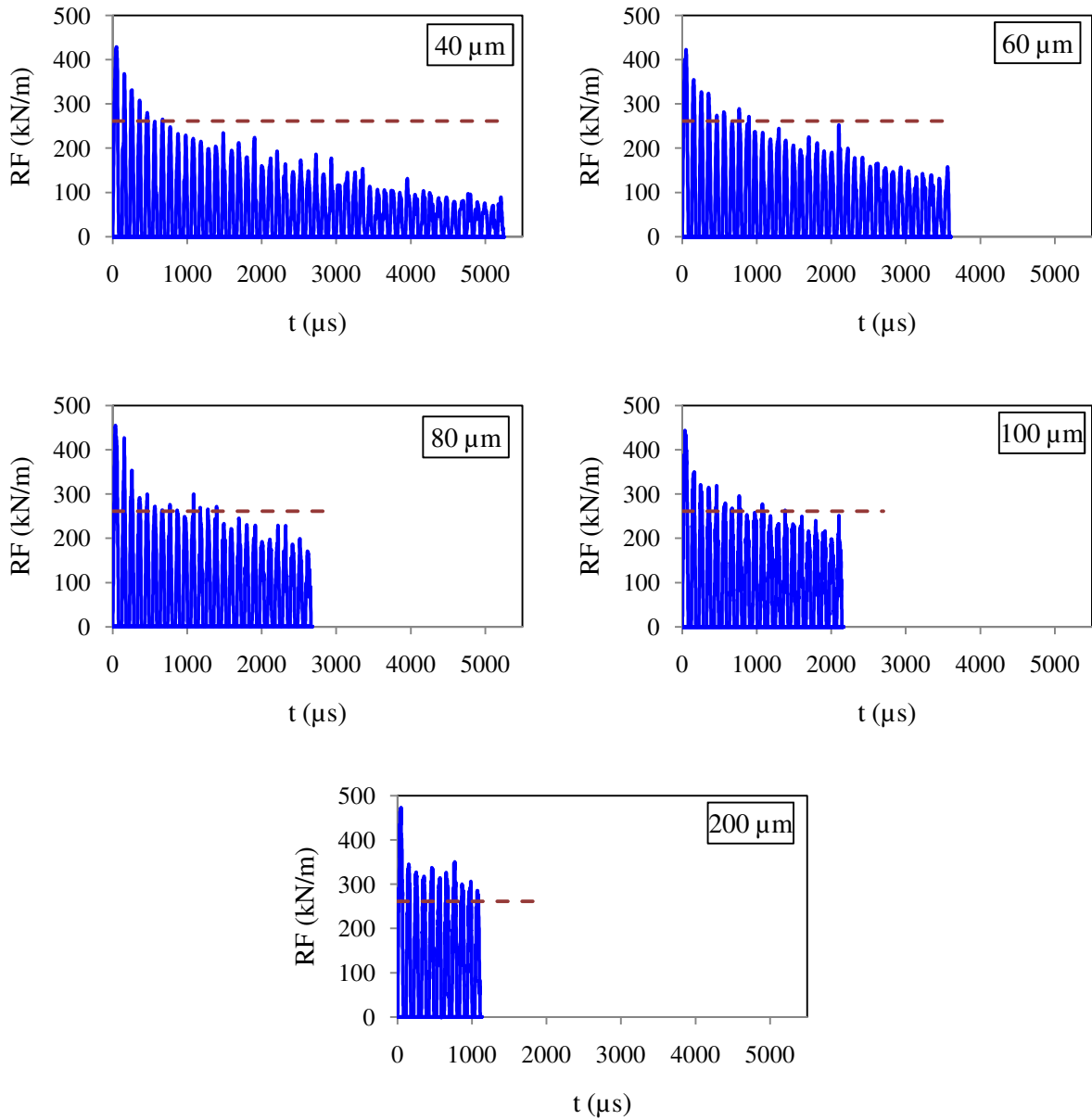


Fig. 9.18b Time histories of normal forces under different burnishing feeds
($P = 4$ MPa; $V = 890$ mm/min)

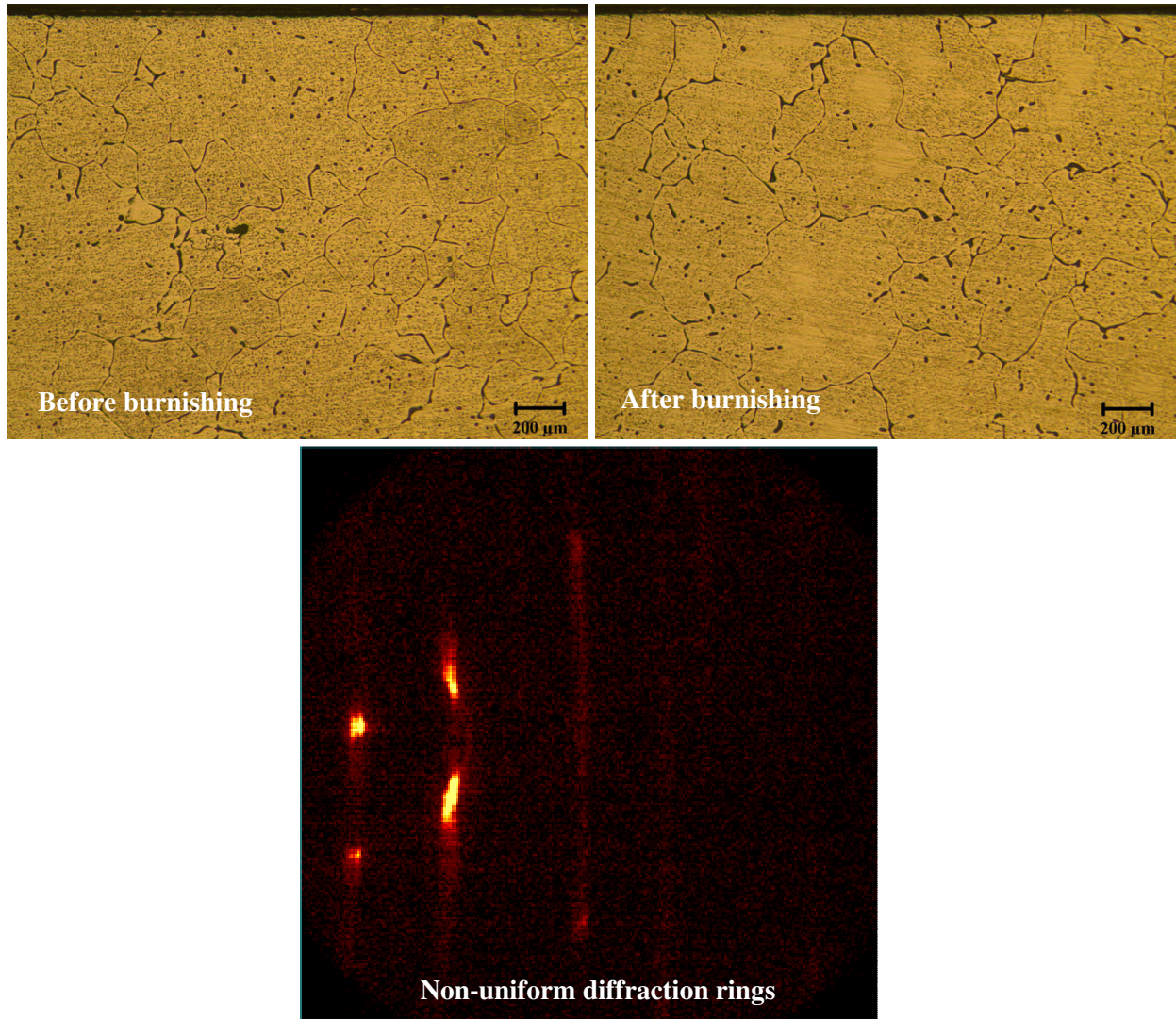


Fig. 9.19 Optical images of the subsurface microstructure before and after burnishing along with resulted diffraction rings

9.8. Conclusions

A semi-infinite, two-dimensional, plane strain model was developed to study hydrostatic burnishing mechanics and the way process parameters interact with surface integrity characteristics, especially residual stresses and surface roughness. Mechanical behavior of the

Mg-Ca_{0.8} biomaterial during burnishing was modeled using internal state variable (ISV) plasticity model. Followings are the conclusions of this study:

- The material removal rate in electro-polishing of Mg-Ca_{0.8} alloy using ASTM E1558 electrolyte and at 22 °C temperature is measured to be 0.389 μm/s
- Actual normal force is measured to be lower (23% on average) than theoretical value for Ecoroll HG13 tool. The discrepancy grows larger by increasing hydraulic pressure and is attributed to oil leakage and subsequent pressure loss at the tool's tip
- Number of burnishing cycles required to establish a steady state deformation depends on applied burnishing parameters. Higher pressures and smaller feeds require more cycles.
- Burnishing pressure is effect less on surface roughness based on measurement results. This is verified statistically by one-way ANOVA analysis. However, the 2D plane strain model predicts that surface roughness should increase by increasing the pressure
- Measured roughness parameter shows an increasing trend with increasing burnishing feed. Numerical simulations predict the same ascending trend; however, predictions are larger than measurements in magnitude
- The Mises stress evolves from a heavily non-uniform distribution to a more uniform one in each burnishing cycle. Roughness peaks and valleys are predicted to be the main reason for this non-uniformity. Later in each cycle, full contact between ball and workpiece is established and load is transferred in a more uniform fashion
- Roughness profile is predicted to affect residual stress distributions especially the in-burnish-direction component and particularly in first 70 μm below surface

- Surface residual stresses are predicted and measured to *decrease* with increasing burnishing pressure and to *increase* with increasing feed.
- In subsurface, it is predicted that burnishing induces compressive residual stresses down to very deep layers, in the order of several millimeters. Larger burnishing pressure causes smaller residual stresses in first 200 μm below surface. Residual stresses penetrate deeper under larger burnishing pressures. Higher burnishing feed causes larger residual stresses in subsurface.
- Measured residual stresses are much larger than predictions. Less concentration in applied load due to presence of cylindrical shaped tool rather than spherical one is a possible reason contributing to this discrepancy. The other factor is the presence of coarse grain structure in surface layer before and after burnishing which causes deviation from polycrystalline material assumption in X-Ray measurements.

References

1. P.S. Prevey, R.A. Ravindranath, M. Shepard, T. Gabb, Case studies of fatigue life improvement using low plasticity burnishing in gas turbine engine applications, *J. Eng. Gas Turbines and Power* 128 (2006) 865-872.
2. P.S. Prevey, J.T. Cammett, The influence of surface enhancement by low plasticity burnishing on the corrosion fatigue performance of AA7075-T6, *Int. J. Fatigue* 26 (2004) 975-982.
3. I. Nikitin, I. Altenberger, Comparison of the fatigue behavior and residual stress stability of laser-shock peened and deep rolled austenitic stainless steel AISI 304 in the temperature range 25-600 $^{\circ}\text{C}$, *Mater. Sci. Eng. A* 465 (2007) 176-182.
4. P. Juijerm, I. Altenberger, Effective boundary of deep-rolling treatment and its correlation with residual stress stability of Al-Mg-Mn and Al-Mg-Si-Cu alloys, *Scripta Materialia* 56 (2007) 745-748.

5. A. Schuh, C. Zeller, U. Holzwarth, W. Kachler, G. Wilcke, G. Zeiler, B. Eigenmann, J. Bigoney, Deep rolling of titanium rods for application in modular total hip arthroplasty, *J. Biomed. Mater. Res. B: App. Biomater.* 81B (2007) 330-335.
6. C.Y. Seemikeri, P.K. Brahmanekar, S.B. Mahagaonkar, Low plasticity burnishing: an innovative manufacturing method for biomedical applications, *J. Manuf. Sci. Eng.* 130 (2008) 021008/1-8.
7. J. Disegi, C. Sax, Effect of low plasticity burnishing on fatigue strength of spinal rods, in: J. Gilbert (Ed.), *Medical Device Materials V (Proc. Materials & Processes for Medical Devices Conf. 2009, Minneapolis, MN)*, ASM Int., Materials Park (2010) 220-226.
8. N.T. Kirkland, N. Birbilis, J. Walker, T. Woodfield, G.J. Dias, M.P. Staiger, In vitro dissolution of magnesium-calcium binary alloys: clarifying the unique role of calcium additions in bioresorbable magnesium implant alloys, *J. Biomed. Mater. Res. B* 95 (2010) 91-100.
9. T. Hassel, F.W. Bach, Production and properties of small tubes made from MgCa0.8 for application as stent in biomedical science, in: K.U. Kainer (Ed.), *Magnesium: Proc. 7th Int. Conf. Magnesium Alloys and Their Applications*, Wiley-VCH Verlag GmbH & Co. (2007) 432-437.
10. T. Hassel, F.W. Bach, C. Krause, Influence of alloy composition on the mechanical and electrochemical properties of binary mg-ca alloys and its corrosion behavior in solutions at different chloride concentrations, in: K.U. Kainer (Ed.), *Magnesium: Proc. 7th Int. Conf. Magnesium Alloys and Their Applications*, Wiley-VCH Verlag GmbH & Co. (2007) 789-795.
11. N. Von der Hoh, D. Bormann, A. Lucas, B. Denkena, C. Hackenbroich, A. Meyer-Lindenberg, Influence of different surface machining treatments of magnesium-based resorbable implants on the degradation behavior in rabbits, *Adv. Eng. Mater.* 11 (2009) B47-54.
12. B. Denkena, A. Lucas, Biocompatible magnesium alloys as absorbable implant materials – adjusted surface and subsurface properties by machining processes, *Ann. CIRP* 56 (2007) 113-116.
13. K. Skalski, A. Morawski, W. Przybylski, Analysis of contact elastic-plastic strains during the process of burnishing, *Int. J. Mech. Sci.* 37 (1995) 461-472.
14. A.J. Black, E.M. Kopalinsky, P.L.B. Oxley, Analysis and experimental investigation of a simplified burnishing process, *Int. J. Mech. Sci.* 39 (1997) 629-641.
15. W. Zhuang, B. Wickes, Multipass low plasticity burnishing induced residual stresses: three-dimensional elastic-plastic finite element modeling, *Proc. IMechE Part C: J. Mech. Eng. Sci.* 218 (2004) 663-668.

16. W. Beres, J. Li, P.C. Patnaik, Numerical simulation of the low plasticity burnishing process for fatigue property enhancement, ASME Conf. Proc. Turbo Expo: Power for Land, Sea, and Air 4 (2004) 809-818.
17. W. Bouzid, K. Saï, Finite element modeling of burnishing of AISI 1042 steel, Int. J. Adv. Manuf. Tech. 25 (2005) 460-465.
18. M. Korzynski, A model for smoothing slide ball-burnishing and an analysis of the parameter interaction, J. Mater. Process. Tech. 209 (2009) 625-633.
19. F. Klocke, V. Bäcker, H. Wegner, M. Zimmermann, Finite element analysis of the roller burnishing process for fatigue resistance increase of engine components, Proc. IMechE Part B: J. Eng. Manuf. 225 (2011) 2-11.
20. Y.C. Yen, P. Sartkulvanich, T. Altan, Finite element modeling of roller burnishing process, Ann. CIRP 54 (2005) 237-240.
21. P. Sartkulvanich, T. Altan, F. Jasso, C. Rodriguez, Finite element modeling of hard roller burnishing: an analysis on the effects of process parameters upon surface finish and residual stresses, J. Manuf. Sci. Eng. 129 (2007) 705-716.
22. K. Röttger, Walzen hartgedrehter oberflaechen, PhD dissertation, WZL, RWTH Aachen, Germany (2002).
23. D.J. Bammann, M.L. Chicsa, G.C. Johnson, Modeling large deformation and failure in manufacturing processes, Theor. App. Mech. (1996) 359-376.
24. M. Salahshoor, Y.B. Guo, Cutting mechanics in high speed dry machining of biomedical magnesium-calcium alloy using internal state variable plasticity model, Int. J. Mach. Tool. Manu. 51 (2011) 579-590.
25. J.F. Lathrop, BFIT – A program to analyze and fit the BCJ model parameters to experimental data, SANDIA Labs Report, SAND97-8218 (1996).
26. Y.B. Guo, W. Wen, M.F. Horstemeyer, An internal state variable plasticity based approach to determine loading history effects in manufacturing processes, Int. J. Mech. Sci. 47 (2005) 1423-1441.
27. I.C. Noyan, J.B. Cohen, Residual stress: measurement by diffraction and interpretation, Springer Verlag, NY (1987).
28. P.S. Prevey, X-ray diffraction residual stress techniques, ASM Metals Handbook 10 (1986) 380-392.

29. Y.B. Guo, M. Salahshoor, Process mechanics and surface integrity by high speed dry milling of biodegradable magnesium-calcium implant alloys, *CIRP Ann. Manuf. Tech.* 59 (2010) 151-154.
30. M. Salahshoor, Y.B. Guo, Contact mechanics in low plasticity burnishing of biomedical magnesium-calcium alloy, *Proc. STLE/ASME Int. Joint Tribology Conf.* (2010) 349-351.

CHAPTER 10

SURFACE INTEGRITY AND CORROSION PERFORMANCE OF MAGNESIUM-CALCIUM IMPLANTS PROCESSED BY SYNERGISTIC DRY CUTTING-HYDROSTATIC BURNISHING

Abstract

Biodegradable magnesium-calcium alloy is an attractive orthopaedic biomaterial compared to permanent metallic alloys. However, the critical issue is that magnesium-calcium alloy corrodes too fast in the human organism. Compared to dry cutting, the synergistic dry cutting-hydrostatic burnishing presented in this study can adjust corrosion rate by producing superior surface integrity including super surface finish, high compressive hook-shaped residual stress on the surface and in subsurface, reduced surface microhardness, and little change of grain size. The measured polarization curves, surface micrographs, microstructures, and element distributions of the corroded surfaces show a significant decrease of corrosion rate in simulated body fluid.

10.1. Introduction

Current commercial, permanent, metallic implants made of stainless steel, titanium, and cobalt-chromium alloys suffer two grand challenges: stress shielding and revision surgeries [1,2], which greatly reduce the life quality of the affected individuals and impose a heavy burden on the healthcare system. Mg-Ca alloys as biodegradable implant materials have the potential to

minimize stress shielding, avoid surgical interventions, and provide both biocompatibility and adequate strength [2-4]. However, the critical challenge of an Mg-Ca implant is that it has poor corrosion resistance in a saline media such as the environment of the human body. The control of the corrosion rate of Mg-Ca implants via adjusting surface integrity to match the healing rate of fractured bones is critical for the development of the next generation of biodegradable implants.

High speed dry machining/cutting (HSM) and hydrostatic/low plasticity burnishing (LPB) are surface treatment techniques which mechanically affect surface/subsurface layers. This selection utilizes different mechanics provided by material removal and forming processes. Each mechanic has distinct attributes in terms of magnitude and depth of influence on surface/subsurface layers. Penetration is at least ten times deeper in forming based treatment like hydrostatic burnishing as opposed to material removal technique and it can reach to several millimeters [5]. Synergistic dry cutting-hydrostatic burnishing combines these mechanics yielding a broad range of process parameters and physical, geometrical tool properties to explore, aimed at tailoring surface/subsurface properties of the workpiece for a specific bio-performance.

While high speed machining is a well-defined process, hydrostatic burnishing is a novel technique. It includes a spherical socket to support a smooth free-rolling ball that is pressed and rolled along the surface, deforming the workpiece surface/subsurface into a state of compression. This process is characterized by a unique combination of three physical effects: (I) producing deep and stable compressive residual stresses; (II) work hardening or increasing surface/subsurface microhardness; and (III) burnishing or decreasing surface roughness and micronotches. Hydrostatic burnishing can be performed in conventional machine shop

environments on CNC machine tools and in that sense it is affordable and compatible with manufacturing environment [5,6].

10.2. Synergistic dry cutting-hydrostatic burnishing of Mg-Ca_{0.8} alloy

Dry cutting of Mg alloys produces good surface quality by the combination of high cutting speeds and low feeds [7]. Lower feeds result in lower roughness, longer exposure to thermo-mechanical loads, higher chances for microstructural changes, and ultimately harder near surface layers. Faster cutting speeds produce higher temperature, more thermal softening on the shear plane, easier cut, and smoother surface. However, higher temperatures promote adhesion between cutting tool/work material and flank built-up (FBU) formation especially when a critical cutting speed is exceeded [8-10]. FBU leads to low surface finish. Therefore, thermal conductivity of the alloy and cutting material are key parameters in determining the magnitude of cutting speed and feed effects on surface integrity. Slower cutting speeds cause higher cutting forces and consequently larger compressive residual stresses in terms of magnitude and depth of penetration [2]. In general, the effect of dry cutting on subsurface residual stresses is minor with a shallow penetration depth to the extent that it would be hard to detect considering the inherent uncertainty of X-ray diffraction technique for residual stress measurement.

Hydrostatic burnishing of Mg alloys under higher rolling forces marginally improves the surface finish [2,7,11-13]. However, surface layers will become deteriorated when excessive forces are applied. Induced compressive residual stresses grow larger and the maximum shifts significantly towards deeper layers under higher rolling forces. As such, subsurface layers store more energy [2]. Residual stresses on surface become less compressive applying higher rolling

forces. Grains become compressed especially in maximum residual stress area and microstructure changes. Denkena et al. [2] did not detect significant microhardness change in Mg-Ca3.0 alloy while Bach et al. [7] observed increase in average microhardness of AZ31 under higher rolling forces.

Higher surface roughness has caused lower corrosion resistance in aggressive salt spray test of Mg alloys with automotive application [7] and in-vivo test of Mg-Ca0.8 alloy [4]. However, better surface finish did not show a significant influence on corrosion performance in turning Mg-Ca3.0 [2]. Burnishing seals surface micro-cracks and pores and avoids the corrosive medium to penetrate and attack subsurface. Hence, more uniform degradation is achieved in burnishing. Larger and deeper compressive residual stresses induce higher corrosion resistance in both dry cutting and hydrostatic burnishing [2,7].

Adjusting degradation kinetic of Mg-Ca0.8 alloy, as a new biodegradable implant material, using machining processes requires knowledge about the likely correlations between surface integrity and resulting corrosion behavior. The objectives of this study are to: (a) characterize surface integrity induced by synergistic dry cutting-hydrostatic burnishing; (b) investigate the effect of resulted surface integrity on corrosion kinetics in simulated body fluid (SBF) via potentiodynamic technique; (c) characterize morphology and elemental composition of the corroded surfaces using SEM and EDS, respectively.

10.3. Surface integrity by synergistic dry cutting-hydrostatic burnishing

Experimental setup and conditions: Non-commercial binary Mg-Ca0.8 alloy was prepared in a crucible using pure Mg of the ASTM grade 9980A and Mg-Ca30 master alloy [9].

Cylindrical samples of 38 mm diameter were synergistically machined utilizing the set-up shown in figure 10.1. A broad range of cutting speeds and rolling forces in Table 10.1 was used to investigate the effects of process parameters on surface integrity. Polycrystalline diamond (PCD) inserts were utilized in high speed face milling (figure 10.1a) to take advantage of low chemical affinity and friction between Mg and diamond in dry cutting process. High pressure hydraulic unit in figure 10.1c provides a pressurized hydro cushion for the silicon nitride ceramic ball (dia. 12.7 mm) at the tip of the burnishing tool in figure 10.1b. This avoids the contact between ball and spherical housing and guarantees free rolling along the sample surface. The power carrying fluid is anti-wear, dual purpose Aries 15 oil functioning as both coolant and lubricant.

Table 10.1 Synergistic dry cutting-hydrostatic burnishing conditions

High speed face milling	cutting speed (m/min): 2000; 2400; 2800 feed (mm/rev): 0.2; depth-of-cut (mm): 0.2
Hydrostatic burnishing	rolling force (N): 400; 600; 800 rolling speed (mm/min): 1000; feed (mm): 0.1

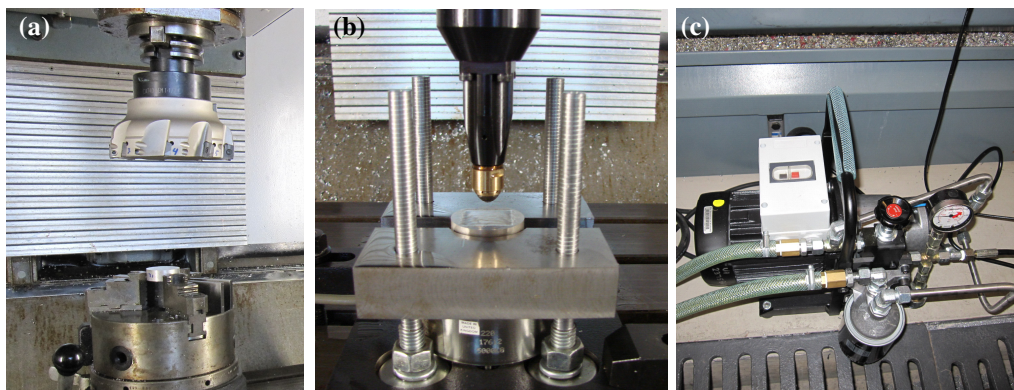


Fig. 10.1 Synergistic dry cutting-hydrostatic burnishing set up (a: high speed dry face milling; b: hydrostatic/low plasticity burnishing; c: high pressure hydraulic unit).

Surface finish: Figure 10.2 shows surface roughness obtained from dry cutting and hydrostatic burnishing operations. *Separately*, Cutting speed and rolling force have marginal effect on surface finish. This marginal effect manifests as slight decreasing trend with increasing each of parameters in figure 10.2. Higher cutting temperatures under faster cutting speeds cause material softening on shear plane, easier cuts, and smoother machined surface. Larger rolling forces act more effectively in closing surface cracks and pores. However, there is a limit on the positive effect of rolling force and beyond certain level, force acts as crack and cold weld producing source itself and so deteriorates the surface as discussed in section 8.4.1. *Comparatively*, burnished surface shows rougher than dry cut surface. This might be due to principal of volume conservation in plastic deformation which causes larger waviness on the surface by burnishing as opposed to milling which operates based on cutting rather than forming mechanism. More waviness in burnished surfaces is clearly visible in typical surface profiles shown in figure 10.2. Even though hammering action of the burnishing ball flattens the pre-existing cut marks and makes burnished surface look shinier than cut surface but yet increased waviness dominates in determining surface roughness.

Residual stress: Residual stresses were measured using 4-axis Bruker D8 machine. X-rays with $\lambda = 0.1542$ nm wavelength were generated applying 35 mA and 40 kV power to X-ray tube with copper source. $\{1\ 2\ 3\}$ crystallographic planes corresponding to $2\theta = 118.48^\circ$ were utilised to measure residual strains and then calculate residual stresses by $\sin^2\psi$ technique. Modulus of elasticity and Poisson's ratio for Mg-Ca0.8 alloy were 45 GPa and 0.33, respectively. Slower cutting speed in figure 10.3 produces more compressive residual stress on surface and shifts the maximum of generally hook-shaped stress profile to deeper layers in subsurface. Smaller rolling force causes larger compressive stress on the burnished surface.

However, deepest residual compression happens under largest rolling force. Neither cutting speed nor rolling force change the magnitude of the maximum compressive residual stress but its location in subsurface. *Comparatively*, in subsurface, high speed dry cutting induces -50 MPa stress at 100 μm depth while hydrostatic burnishing produces larger (-150 MPa) and deeper (600 μm) stress, i.e. three times in magnitude and six times in depth, respectively. In surface, hydrostatic burnishing makes larger compressive residual stresses as opposed to dry cutting.

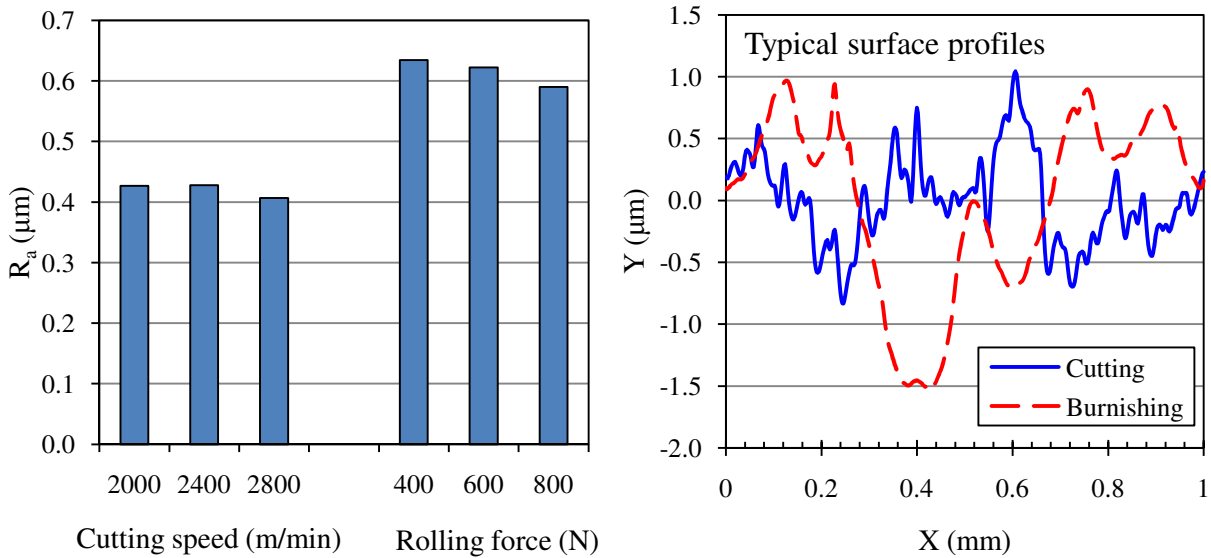


Fig. 10.2 Effects of process parameters on surface roughness.

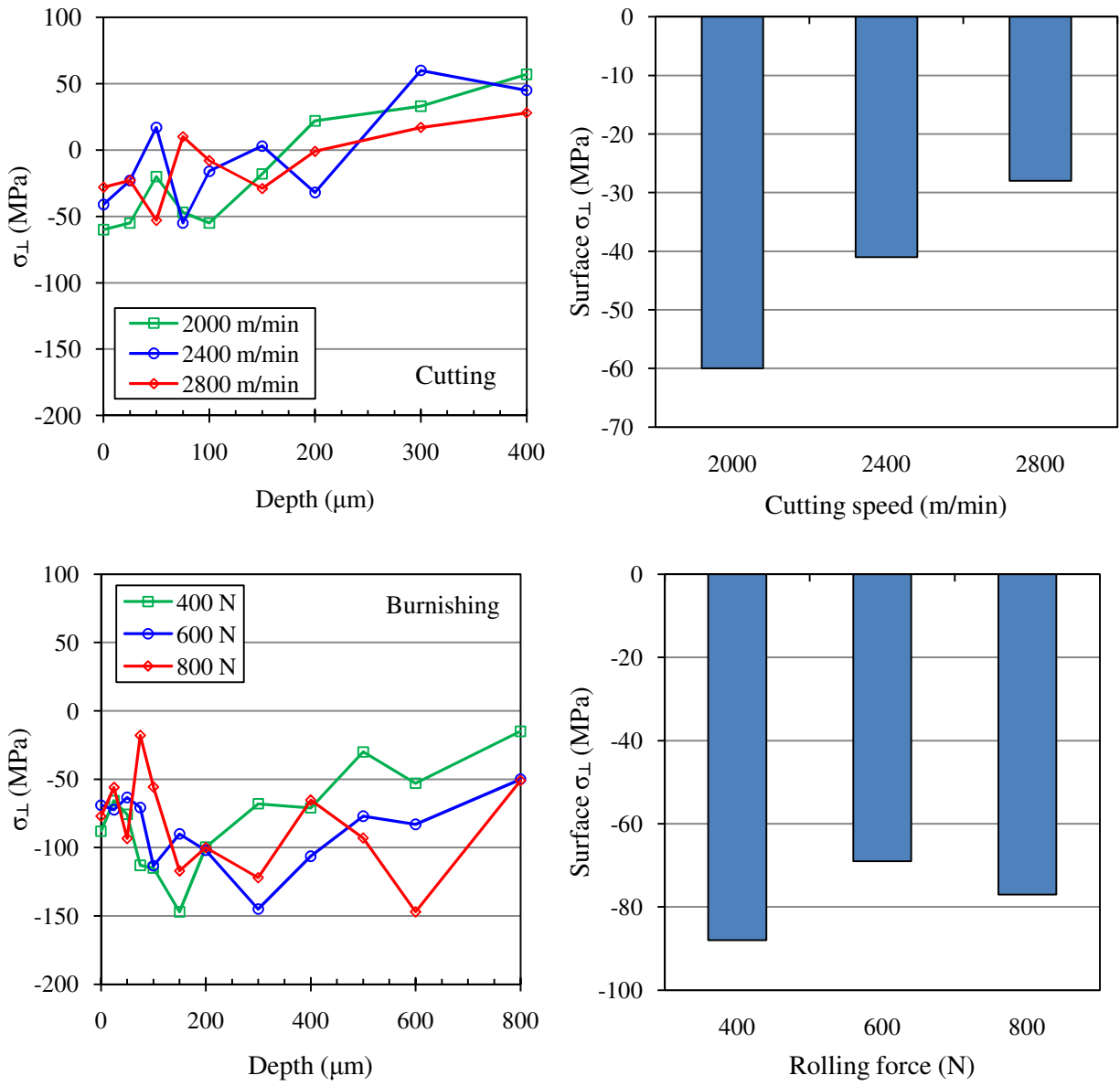


Fig. 10.3 Effects of process parameters on residual stresses

Microhardness: Figure 10.4 shows the extent of work hardening on surface and subsurface in dry cutting and burnishing. Faster cutting speed marginally increases the amount of microhardness on surface. Microhardness on surface shows a declining trend with increasing rolling force. However, subsurface is more work-hardened under larger rolling force. The maximum work-hardened depth in dry cutting is 50 μm and beyond that microhardness profile becomes stabilized. This depth is about 300 μm in burnishing process i.e. six times deeper than dry cutting. Deep layers of compressed material produced by shallow work-hardened layers is a unique attribute of burnishing process which can be seen in contrasting residual stress and microhardness profiles in figures 10.3 and 10.4. This fact is determinative in stability of induced residual stresses under service loadings [5,14]. Hence, it is expected that residual stresses produced by burnishing to be more stable under typical daily loadings on a bone implant and so to have longer lasting effect on corrosion performance.

Microstructure: Subsurface microstructure of dry cut and burnished samples are shown in figure 10.5. Very coarse grain structure with no grain refinement or texture is observable. Grain refinement and texture were expected to happen through 50 μm depth work-hardened material in dry cutting and through 300 μm depth work-hardened material in burnishing. High cutting temperatures, adiabatic nature of dry cutting, and sever plastic deformation due to shear action are the ingredients which could cause dynamic recrystallization (DR) and ultimately grain refinement. FE simulations [9] have shown that high surface cutting temperatures reduce to room temperature in a shallow depth of about 25 μm . However, DR is a diffusion controlled process and strongly depends on atomic migrations which are very slow in solid state and require a stable heat source to provide the necessary temperature. Primary and secondary shear zones around the cutting edge are moving heat sources which meet each surface point for a very short amount of

time. Therefore, the required time for DR is not provided. For the same reason, the observed coarse grains cannot be due to grain growth as well.

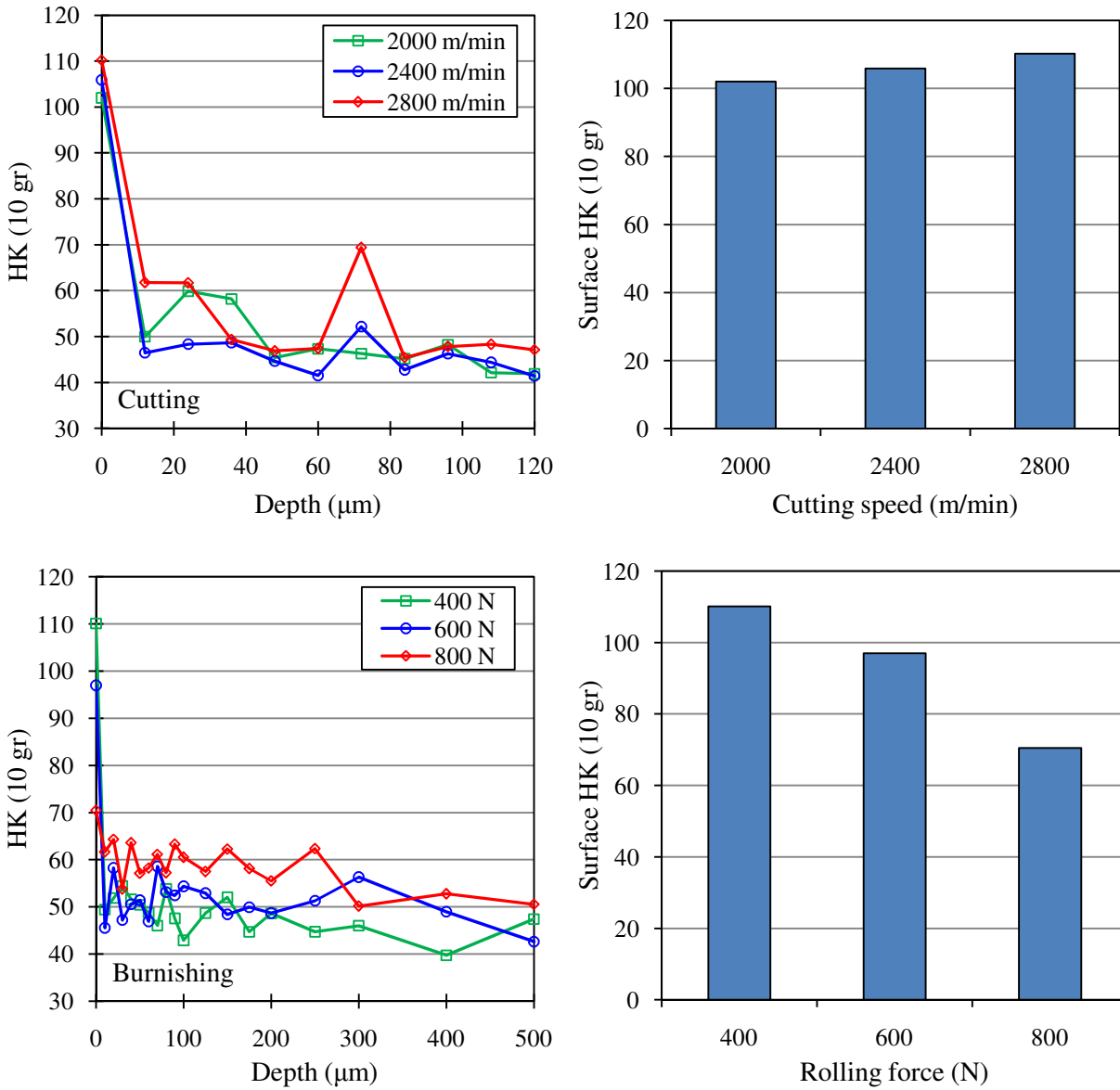


Fig. 10.4 Effects of process parameters on microhardness

Slow cooling after sand-casting seems to be the only reason for the observed coarse grain structure. Grain texture is more expected than refinement in burnishing since it is an isothermal process inherently due to presence of hydraulic oil which acts as a coolant. However, large grains clearly do not reflect the expected compression in figure 10.5.

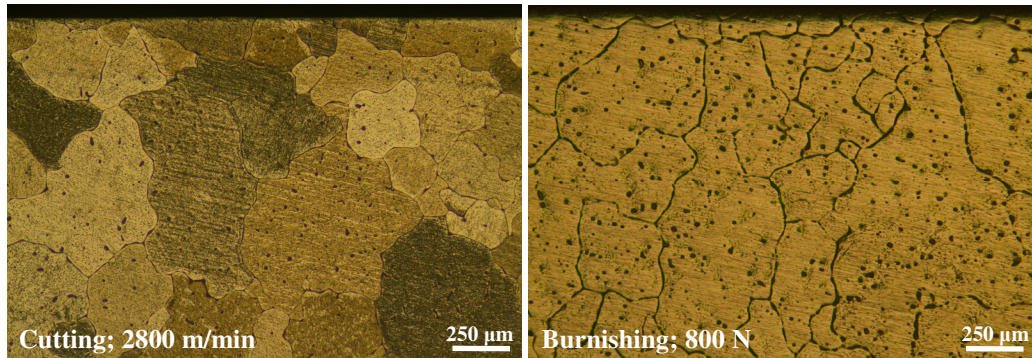


Fig. 10.5 Subsurface microstructures

10.4. Corrosion performance

Corrosion experiment setup: The corrosion performance of machined Mg-Ca0.8 samples was examined in simulated body fluid (SBF) with the composition listed in Table 10.2. Samples were ultrasonically cleaned with ethanol and then dried in a stream of air before test. The pH value of the SBF was adjusted to biological value of 7.4. The solution was stirred to keep the temperature and chemical concentration uniform all over the solution. The solution temperature was maintained at biological range of 37 ± 1 °C. To evaluate the corrosion performance potentiodynamic technique was used to measure electrochemical parameters E_{Corr} , and I_{Corr} , and ultimately to calculate corrosion rate $C.R.$ based on Faraday's law. The resulted polarization

curves are shown in figure 10.6. To avoid the effects of pH increase and accumulation of corrosion products on corrosion performance, large solution volume-to-surface area ratio was used and SBF solution was replaced for each new sample.

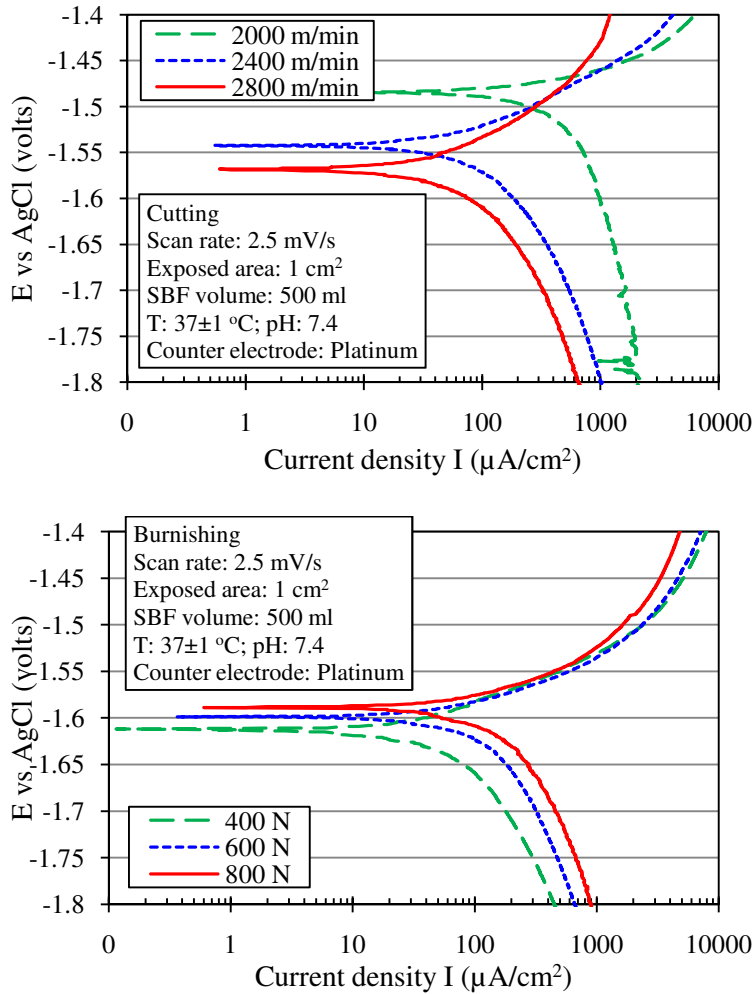


Fig. 10.6 Potentiodynamic polarization curves

Table 10.2 Composition of simulated body fluid (SBF)

Chemical component	Concentration (mg/l)	Chemical component	Concentration (mg/l)
NaCl	8000	MgSO ₄ •7H ₂ O	200
Glucose	1000	CaCl ₂ •2H ₂ O	186
KCl	400	Na ₂ HPO ₄ •7H ₂ O	90
NaHCO ₃	350	KH ₂ PO ₄	60

Electrochemical parameters indicating corrosion performance of the machined surfaces are shown in figure 10.7. Providing the possibility to investigate the effects of mechanical surface treatments on both electrochemical parameters, i.e. E_{Corr} and I_{Corr} , is an outstanding capability of potentiodynamic technique as compared to gravimetric and hydrogen evolution techniques. It is interestingly noticeable that when thermodynamic tendency or spontaneity of the corrosion reaction (E_{Corr}) decreases, corrosion kinetics (I_{Corr}) or corrosion rate (C.R.) becomes faster in both dry cutting and burnishing cases. Influencing degradation rate of a bone implant made out of Mg-Ca0.8 can be achieved either by postponing the corrosion initiation through having a nobler E_{Corr} or slowing corrosion kinetics through smaller I_{Corr} . However, it is acknowledged that potentiodynamic technique will be more reflective of the surface characteristics on corrosion performance rather than subsurface characteristics like residual stress, and microhardness due to short testing time (10 min in this case) as compared to long testing time in gravimetric and hydrogen evolution techniques (normally several days). Change in spontaneity is marginal especially in burnishing case as opposed to change in kinetics. Faster cutting speed produces a surface which corrosion reaction ($Mg + 2 H_2O \rightarrow Mg(OH)_2 + H_2$) has more spontaneity but slower kinetics on it. Similar trend happens for burnished surface under smaller rolling force.

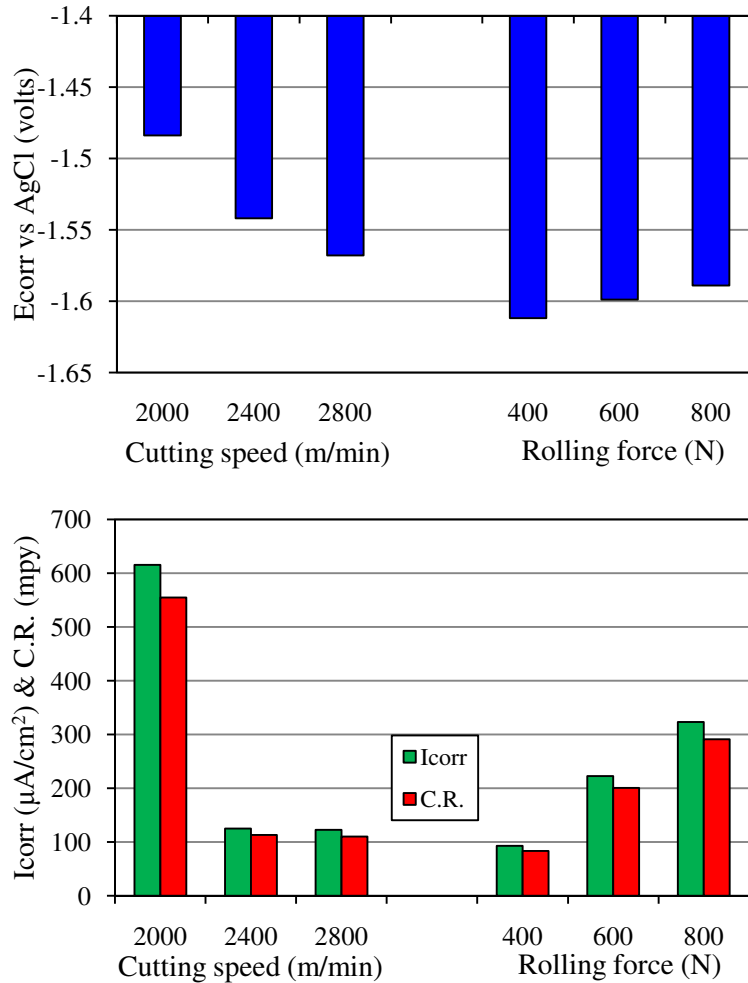


Fig. 10.7 Effects of process parameters on E_{Corr} , I_{Corr} , and C.R.

The surface of the samples after potentiodynamic tests were studied using energy dispersive spectroscopy (EDS) in figure 10.8 and scanning electron microscopy (SEM) in figure 10.9. It is clearly visible that due to corrosion, samples surface deplete from Mg but the amount of Ca increases on the surface as the result of corrosion products accumulation. This increase in the amount of Ca in addition to relatively large amounts of P and O could be due to formation of

hydroxyapatite (HA) with the formula $\text{Ca}_{10}(\text{PO}_4)_6(\text{OH})_2$. HA mineral is a naturally occurring form of calcium and has resemblance to the chemical and mineral components of teeth and bone. As a result of this similarity it stimulates bone cells to attack the implant surface and make proper bonding [4], which allows for fractured segments realign in correct anatomical position which is critical to recovery. Adherence of bone to implant is a sign of good biocompatibility. Energy dispersive spectrums of uncorroded dry cut and burnished surfaces show considerable amount of an unexpected element which might be Tc or Bi. Two possibilities are imaginable for the presence of these impurities: (I) been added to melt during casting process from an unknown source; (II) are adhered to machined surface from the cutting inserts during the preparation stage. However, the first possibility seems less likely to be the reason since none of Tc or Bi is observed in corroded surface spectrums. This speaks on the fact that whatever the reason might be, it has just affected the surface not the bulk material.

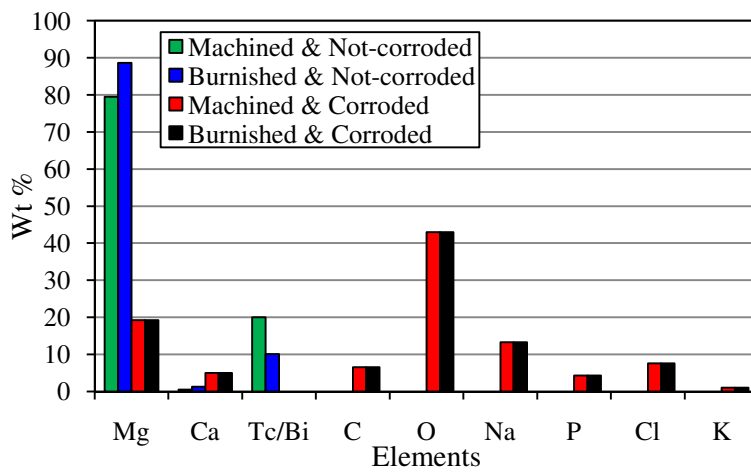
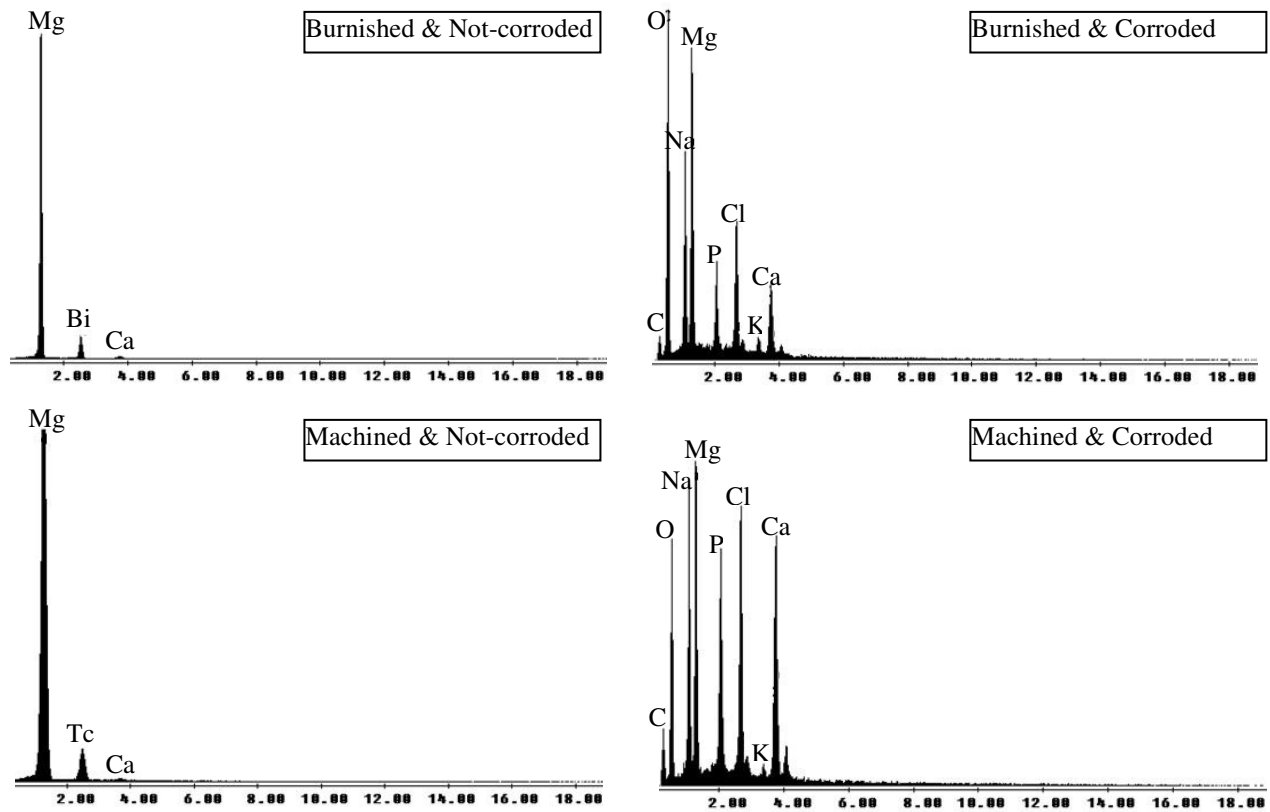


Fig. 10.8 Energy dispersive spectrum of corroded and uncorroded surfaces

SEM micrographs of dry cut surfaces in figure 10.9a, 10.9b, and 10.9c show more dispersion of corrosion products by increasing the cutting speed. This is in line with the observations made in figure 10.7 which imply faster corrosion kinetics under slower cutting speeds resulting in accumulation of more corrosion products and less dispersion. Increased rolling force in burnishing causes more corrosion products in figures 10.9d, 10.9e, and 10.9f relatively. The morphology of corroded surfaces processed by burnishing shows more uniform pattern than those processed by dry cut. This might be due to the fact that burnishing seals surface micro- cracks and pores and avoids the corrosive medium to penetrate and attack subsurface. Hence, more uniform degradation is achieved in burnishing. Localized corrosion and pitting is an undesired phenomenon which should be avoided in the case of bone implants since pits will act as stress concentrators causing reduction in mechanical strength and early failure of implants in load carrying applications.

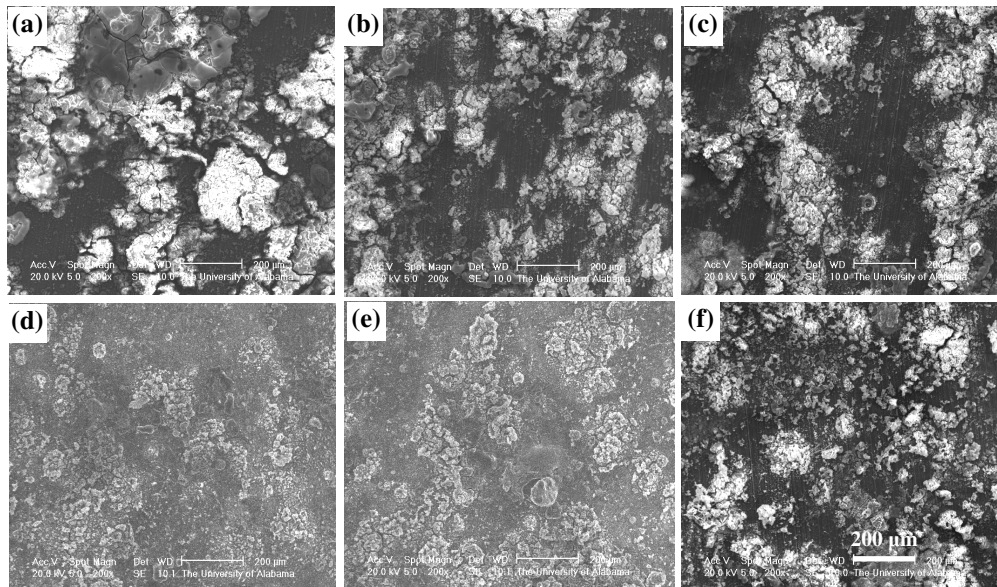


Fig. 10.9 Scanning electron micrographs of corroded surfaces (a: 2000 m/min; b: 2400 m/min; c: 2800 m/min; d: 400 N; e: 600 N; f: 800 N).

10.5. Conclusions

This study focuses on corrosion performance of surface integrity induced by synergistic dry cutting-hydrostatic burnishing process on Mg-Ca0.8 alloy. Key findings of this study are:

- Hydrostatic burnishing produces deep layers (~ 600 μm) of compressed material by work hardening shallow layers (~ 300 μm). Maximum compressive residual stress produced by burnishing is larger in magnitude (~ 150 MPa) and located deeper as opposed to dry cutting.
- Mechanical surface treatment affects both spontaneity and kinetics of Mg-Ca0.8 corrosion reaction. Potentiodynamic technique has unique capability in investigating these effects as opposed to gravimetric and hydrogen evolution techniques.
- Faster cutting speed produces a surface which corrosion reaction has more spontaneity but slower kinetics on it. Similar trend happens for burnished surface under smaller rolling force.
- Increased amounts of Ca, P, and O on corroded surfaces are an indication of hydroxyapatite formation which will stimulate bone adhesion to implant surface and will improve biocompatibility.
- Morphology of corrosion products on burnished surfaces shows more uniform pattern as compared to dry cut case.

References

1. F. Witte, N. Hort, C. Vogt, S. Cohen, K.U. Kainer, R. Willumeit, F. Feyerabend, Degradable biomaterials based on magnesium corrosion, *Current Opinion in Solid State and Materials Science* 12 (2008) 63 – 72.
2. B. Denkena, A. Lucas, Biocompatible magnesium alloys as absorbable implant materials – adjusted surface and subsurface properties by machining processes, *Ann. CIRP* 56/1 (2007) 113 – 116.
3. T. Hassel, F.W. Bach, C. Krause, Influence of alloy composition on the mechanical and electrochemical properties of binary Mg-Ca alloys and its corrosion behavior in solutions at different chloride concentrations, *Proc. 7th Int. Conf. Mg Alloys & Their App.* (2007) 789 – 795.
4. N. von Der Hoh, D. Bormann, A. Lucas, B. Denkena, C. Hackenbroich, A. Meyer-Lindenberg, Influence of different surface machining treatments of magnesium-based resorbable implants on the degradation behavior in rabbits, *Adv. Eng. Mater.* 11 (2009) B47 – 54.
5. P.S. Prevey, R.A. Ravindranath, M. Shepard, T. Gabb, Case studies of fatigue life improvement using low plasticity burnishing in gas turbine engine applications, *J. Eng. Gas Turbines & Power* 128 (2006) 865 – 872.
6. B. Denkena, R. Meyer, B. Breidenstein, Development of combined manufacturing technologies for high-strength structure components, *Adv. Mater. Res.* 22 (2007) 67 – 75.
7. F.W. Bach, B. Denkena, K. Weinert, P. Alpers, Influence of cutting and non-cutting processes on the corrosion behavior and the mechanical properties of magnesium alloys, *Proc. 7th Int. Conf. Mg Alloys & Their App.* (2007) 1076 – 1084.
8. N. Tomac, K. Tonnessen, Formation of flank build-up in cutting magnesium alloys, *Ann. CIRP* 40/1 (1991) 79 – 82.
9. Y.B. Guo, M. Salahshoor, Process mechanics and surface integrity by high-speed dry milling of biodegradable magnesium-calcium implant alloys, *CIRP Ann.-Manuf. Tech.* 59 (2010) 151 – 154.
10. H.K. Tönshoff, J. Winkler, The influence of tool coatings in machining of magnesium, *Surf. Coat. Tech.* 94-95 (1997) 610 – 616.
11. B. Denkena, J.C. Becker, C. Podolsky, A. Kuhlmann, Safe machining of magnesium parts by cutting and burnishing operations, *Proc. 7th Int. Conf. Mg Alloys & Their App.* (2004) 895 – 901.

12. T. Friemuth, J. Winkler, Machining of magnesium workpieces, *Adv. Eng. Mater.* 1/3-4 (1999) 183 – 186.
13. H.K. Tönshoff, T. Friemuth, J. Winkler, C. Podolsky, Improving the characteristics of magnesium workpieces by burnishing operations, *Mg Alloys & Their Applications* (2000) 406 – 411.
14. I. Nikitin, M. Besel, Residual stress relaxation of deep rolled austenitic steel, *Scripta Materialia* 58 (2008) 239 – 242.

CHAPTER 11

ADJUSTING DEGRADATION KINETICS OF A NOVEL BIODEGRADABLE MAGNESIUM-CALCIUM BIOMATERIAL BY HYBRID CUTTING-FORMING TREATMENT – LONG TERM TESTS

Abstract

Magnesium-calcium alloys are very promising biomaterials for orthopedic applications with biodegradability and suitable mechanical strength characteristics. However, their high corrosion rate in human body environment remains as a big challenge for their successful development as biomaterials. In this study, hybrid cutting-forming technique was utilized to adjust the degradation rate of the novel MgCa0.8 biomaterial. In-vitro immersion tests were performed in simulated body fluid to measure degradation kinetics of the processed implants. Morphology and elemental composition of the corroded surface layers were also studied. Hybrid cutting-forming technique showed very successful in adjusting the degradation rate. By using this technique, it would be possible to manufacture biodegradable MgCa0.8 implants with tailored degradation rate to meet the healing rate in various orthopedic applications.

11.1. Introduction

Biodegradable, metallic biomaterials have become very attractive recently particularly in orthopedic applications. Biodegradability alleviates the necessity for second surgeries to excise the implanted orthopedic devices in cases where implants are used for fixation rather than

replacement. This has tremendous economical impact on health care system. Currently, polymers are the only biomaterials with biodegradability characteristic. However, they suffer from lack of enough mechanical strength to be used in load carrying applications such as bone traumas in legs, arms, spine, etc. Currently available metallic biomaterials, e.g. titanium alloys, stainless steels, and cobalt-chromium alloys, have sufficient mechanical strength but they are not biodegradable and cause stress shielding and artificial osteoporosis. Magnesium-calcium (MgCa) alloys are metallic and biodegradable, and have minimal stress shielding effect due to closer proximity of their modulus of elasticity to that of bones. However, they have very low corrosion resistance in saline environments such as human body and fast degradation kinetics results in large of amount of hydrogen and hydroxide which interfere with metabolic reactions and delay the healing process. Successful development of MgCa alloys as novel biomaterials requires finding some alternatives to adjust the degradation rate in a manner that it matches healing rate of the bone trauma and absorption rate of the corrosion by products.

11.2. Mg and its alloys as biomaterials

There has been a great deal of effort recently to study the corrosion performance of Mg and its alloys in human body environment and to identify influential parameters. Hänzi et al [1] studied the degradation performance of the magnesium tip in a biodegradable rivet intended for tissue joining in endoscopic surgery. In-vitro degradation performance was assessed by immersion in simulated gastric fluid (SGF) and measurement of the relative diameter reduction. They investigated the effects of solution concentration (SGF and SBF), chemical composition of the alloy (WZ21 and ZQ30), temperature, and pH on degradation rate. Among all the parameters

pH showed the strongest effect on degradation rate. Xue et al [2] anodized pure Mg and AZ91D alloy and investigated the effects of anodized layer characteristics and process parameters on degradation rate in simulated body fluid (SBF). Polarization technique and immersion test were implemented to characterize the degradation rate. Corrosion tests were performed at room temperature and solution replacement was used to keep the pH relatively constant. They monitored the change in pH as a metric indicating the corrosion rate in immersion tests. They concluded, anodizing increased the corrosion resistance of both pure Mg and AZ91D samples.

Walter et al [3] compared the in-vitro degradation behavior of die-cast WE54 alloy to that of pure Mg and the widely researched sand-cast AZ91 alloy in SBF. WE54 exhibited a marginally higher in-vitro degradation resistance than that of pure magnesium but significantly lower resistance than that of AZ91. Walter et al related this observation to inferior passivating capacity of rare earth elements in WE54 compared to Al in AZ91. Hiromoto and Yamamoto [4] used pure magnesium to examine the effect of anodizing and autoclaving on degradation rate without the influence of alloying elements and microstructure. The degradation behavior of the surface modified specimens was investigated by an immersion test in a solution with composition similar to that of blood plasma. Every 24 h period, about 54.5% of the solution was replaced with a fresh one. The replacement was carried out to simulate the body fluid exchange of an adult human by the excretion of urine. Autoclaving after anodizing significantly decreased the degradation of the anodized specimens. Their results suggested that the occurrence of local corrosion depends on the porous morphology of surface film.

Kirkland et al [5] investigated the influence of increasing calcium (Ca) content in binary Mg-X Ca alloys along with the composition of the bio-fluid on in-vitro degradation rate. Different Ca content of 0.4, 0.8, 1.34, 5.0, 10.0, 16.2, and 28.0 wt% were considered. Three

different bio-fluids were used starting with regular SBF and progressing to more human serum-like fluids by adding amino acids and vitamins (the second bio-fluid) and finally proteins (the third bio-fluid) to SBF. It was observed that above solid solubility limit of ~ 1.34 wt% Ca, the corrosion rate increased with increasing Ca content and the corrosion potential became more negative. However, below the solubility limit, the corrosion rate stayed the same or even slightly decreased with increasing Ca additions. As the bio-fluid mimicked the human serum more closely, corrosion rate decreased between 10 to 290% and corrosion potential became more positive. Therefore, using more physiologically relevant test environments are necessary in in-vitro tests to effectively screen corrosion and biodegradation behavior of magnesium alloys. Their microelectrochemical test revealed that Mg_2Ca phase is more active than α -Mg and assumes the role of anode contradicting other intermetallics which are cathode in relation to Mg. Mg_2Ca has the identical crystal structure as Mg, however, twice the lattice parameter magnitudes. This reveals that Ca is a unique alloying addition to Mg in the context of biodegradable implants.

Ng et al [6] studied the corrosion behavior of pure Mg in Hank's solution at pH values ranging from 5.5 to 8.0 by means of hydrogen evolution measurement and electrochemical techniques. The pH value of the body fluid at the location of bone fracture changes during the course of recovery. The pH value of the test solution has tremendous effect on corrosion rate of Mg. The corrosion rate drops rapidly over two orders of magnitude from $800 \mu\text{m}/\text{day}$ ($150 \text{ ml}/\text{cm}^2/\text{day}$) at pH 5.5 to $6 \mu\text{m}/\text{day}$ ($1.0 \text{ ml}/\text{cm}^2/\text{day}$) at pH 7.4, and much more slowly to $3 \mu\text{m}/\text{day}$ at pH 8.0 due to corrosion products formed on the surface, thus retarding the corrosion process. Thomann et al [7] examined if the corrosion resistance of previously in-vivo tested MgCa0.8 alloy implants could be increased by applying a magnesium fluoride coating. The

analysis by weight before implantation, and 3 and 6 months after implantation showed a slight decrease in volume as compared to uncoated implants. Xin et al [8] investigated degradation behavior of AZ91 magnesium alloy in five different solutions using hydrogen evolution and electrochemical techniques. The concentration of buffering agents and the content of hydrocarbonates and hydrophosphates in test solutions have significant effect on degradation performance especially during the early stages of degradation. High contents of buffering agents cause more negative corrosion potentials higher initial degradation rates. Rapid reaction of OH⁻ with the large amount of buffers dramatically promotes transformation from Mg to Mg²⁺, constituting the main reason for the high degradation rates. Therefore, the proper selection of test solution with similar buffering capability and similar ingredients as biological fluids is imperative to the investigation of the degradation behavior of biomedical magnesium alloys. It has been verified that dissolved oxygen does not influence the evolution of hydrogen [9] and thus the experiments were carried out without deaeration.

Kannan and Singh [10] studied the degradation behavior of the die-cast AZ91 magnesium alloy using potentiodynamic polarization technique in SBF to understand the mechanistic aspect of in-vitro degradation of the alloy. In-vitro tests were carried out under various conditions: i) room temperature (20 ± 2 °C) and body temperature (36.5 ± 0.5 °C), ii) alkali-treated surface in 1M NaOH, and iii) plain-chloride solution with chloride concentration similar to that of SBF. Body temperature decreases the corrosion resistance of the alloy compared to room temperature. Alkali-treated surface shows more resistance to corrosion through formation of protective film. Chloride minimizes the corrosion resistance of the alloy with increase in immersion period. However, other constituents of SBF, i.e. phosphate, calcium, and carbonate, enhance the film forming tendency and hence corrosion resistance. Drynda et al [11] developed binary fluoride-

coated Mg-Ca alloys with improved degradation kinetics. The Ca content was 0.4, 0.6, 0.8, 1.2, and 2.0 wt%. Electrochemical properties of uncoated and coated alloys were characterized in 0.5, 0.9, 2.5, or 5.0% NaCl solutions at 37 °C. Degradation rates were investigated using hydrogen evolution technique. Calcium concentration of 0.8 wt% results in the minimum degradation rate compared to other Ca contents. MgF₂ coated Mg-Ca alloys showed slower rates (lower than 150 μA/cm²) and no further dependence on the Ca content. Moreover, no H₂ gas formation was detected within the first 8 to 40 hours in fluorinated alloys.

Kannan [12] investigated the effect of grain structure in die-cast and sand-cast AZ91 alloys on their in-vitro degradation behavior. Die-cast alloy has a fine grained microstructure as opposed to sand-cast alloy with coarse grained microstructure. Despite to significant difference in the microstructure, the overall degradation resistance of these alloys in SBF was similar. However, this is in contrast to the observations made in plain chloride-containing solution, where die-cast alloy showed higher degradation resistance than the sand-cast alloy. The improvement in the degradation resistance of die-cast alloy was attributed to the fine grain size, high aluminum content in the grains and the continuous network of stable grain boundary precipitates. Kannan suggests that the surprising observation made in SBF solution may be due to the higher temperature (36.5 ± 0.5 °C, body temperature) applied during the in-vitro tests as opposed to room temperature in plain chloride containing solutions. Although, grain structure did not have influence on degradation rate of the alloys, but post-degradation morphology analysis of the alloys suggested that the high volume fraction of secondary phase particles in the die-cast alloy may not be suitable for biodegradable implant applications, primarily due to the high stability of the secondary phase particles in physiological conditions. Note that this discussion may not be

applicable to Mg-Ca alloys since Ca and Al (in AZ91 alloy) produce totally different properties [5].

Zhou et al [13] explored ways of improving corrosion behavior of AZ91D magnesium alloy through heat treatment for degradable biocompatible application. Electrochemical and gravimetric (weight loss measurement) were used to study the short-term and long-term degradation behavior of the treated alloy in SBF at 37 °C, respectively. Heat treatment significantly affected microgalvanic corrosion behavior between cathodic β -Mg₁₇Al₁₂ phase and anodic α -Mg matrix. In T4 microstructure, dissolution of the β -phase decreased the cathode-to-anode area ratio, leading to accelerated corrosion of α -Mg matrix. Fine β -phase precipitates in T6 microstructure facilitated intergranular corrosion and pitting, but the rate of corrosion less than those of as-cast and T4 microstructures.

Ng et al [14] prepared an organic coating on pure Mg in an attempt to enhance the corrosion resistance. They used immersion tests to study the long-term corrosion behavior of the coated Mg for maximum of 30 days and in a case for 80 days. While anodic polarization tests provide information of corrosion behavior over a wide range of anodic potentials, they would damage the sample due to the high anodic potential reached. Thus they are not usually employed for long-term monitoring of corrosion behavior in immersion. The increase in corrosion resistance of coated Mg samples could reach as high as 4 orders of magnitude in the initial acidic period, and gradually drops to about 40 times in the long run. The improved resistance resulted from the barrier function of the thick, good quality organic coating. Degradation of coating could happen due to local rise of pH to about 9.0 (although the bulk pH is 7.4) and formation of corrosion products, e.g. Mg(OH)₂, leading to cracking and delamination.

Krause et al [15] investigated the initial mechanical strength and in-vivo degradation behavior of MgCa0.8, LAE442, and WE42 alloys along with the change in their mechanical properties due to degradation. MgCa0.8 showed an insufficient initial strength and a fast degradation. Although its ductility was constant during degradation and the degradation products were naturally occurring components of the organism, however, Krause et al believed its use as degradable osteosynthesis material for weight-bearing bones is limited. LAE442 degraded slower and its initial strength seemed sufficient for weight-bearing applications. However, rare earth alloying elements present in LAE442 produced products that their biocompatibility needs yet to be studied. They did not recommend WE43 as osteosynthesis material for fracture repair due to its heterogeneous and unpredictable degradation behavior.

Munro et al [16] explored the influence of surface modification by biomimetic calcium phosphate coating, biodegradable polymer coatings, and acid etching on the corrosion rate of the AZ31 alloy in SBF. Static immersion test was used to evaluate the in vitro degradation rate. The concentration of magnesium and calcium in the solution was quantified by flame atomic absorption. The results indicate that all of these surface modification treatments have a positive impact on the corrosion rate of the material and that in the early stages of implantation it is possible to tailor the corrosion rate through an appropriate choice of surface treatment.

Ymamoto and Hiromoto [17] performed 14 day long immersion tests of pure Mg in 4 kinds of physiological solutions simulating the body fluids to examine the effects of the chemical components of the body fluids on the degradation of Mg. The degradation rate of pure magnesium was strongly influenced by the kinds of the solution used. The average degradation rate in 0.125M NaCl solution for 8 – 14 days was about 100 times larger than that in amino acid and protein containing solution which is the closet solution to human blood plasma. Their results

suggest that protein adsorption and insoluble salt formation retarded magnesium degradation, whereas organic compounds such as amino acids encourage the dissolution of magnesium. Buffering the solution also influenced the degradation rate; buffering NaCl with HEPES increased the degradation rate but buffering with NaHCO₃ decreased it.

Zhang et al [18] applied Hydroxyapatite (HA) coating with two different thicknesses onto the surface of pure Mg substrates. HA is the main composition of natural bone. It has excellent bioactivity and osteoconductivity. The calcium and phosphate concentrations were measured using atomic absorption spectrometry and molybdenum blue method, respectively. HA coating substantially slowed down the corrosion of Mg, and the thicker the coating the more effective it was.

Mueller et al [19] evaluated the influence of the electrolyte composition on the corrosion behavior of Mg and two Mg-alloys (AZ31 and LAE442) in synthetic biological media. Electrochemical potentiodynamic polarization curves were recorded in NaCl and phosphate buffered solution (PBS) electrolytes with different chloride ion and albumin concentration. The results showed that Mg corrosion is localized in chloride- and albumin- containing buffer solutions. They also showed the chloride concentration and the presence of buffer and proteins strongly affect the electrochemical behavior of Mg and Mg-alloys.

Thomann et al [21] conducted in-vivo experiments to study effects of alloying Mg with calcium (in MgCa0.8), lithium, aluminum, and rare earth (in LAE442) elements on corrosion process. Extruded implants of these resorbable Mg alloys were implanted for a period of 12 month into the marrow cavity of both tibiae of New Zealand White rabbits. Beside an adequate primary stability and the ability to degrade without side effects, a good biocompatibility is required to use Mg alloys as materials for osteosynthesis. The reactions of the bone could be

used to evaluate the biocompatibility and there was a ring of bone covering the implant surface. This confirms the osteogenetic effect of this alloy. After 12 months the bone-implant-contact was clearly stronger in MgCa0.8 case. However, it degraded more than LAE442 but slow enough to avoid any gas bubble generation. Stability of the implants is of major concern at beginning of the implantation. Thomann et al reported a pitting corrosion of MgCa0.8 implants after three months into implantation which increased till 6 months. However, LAE442 showed a more uniform corrosion and in that sense had a superior degradation behavior to 0.8 wt%Ca-containing binary alloy. MgCa0.8 implants showed an average loss in the cross section of more than half of the initial area after 12 months. The decrease in volume of MgCa0.8 implants were 11%, 31%, and 51% after 3, 6, and 12 month implantation, respectively.

Von Der Höh et al [23] examined the in-vivo degradation behavior of Mg-based implants with 0.8wt% calcium and different surface conditions for 3 and 6 months, respectively. The employed MgCa0.8 implants were received turning, sand-blasting, and threading surface treatments. Their aim was to develop and manufacture metallic, nontoxic, and resorbable implants for osteosynthesis in weight bearing applications which will be gradually replaced by the surrounding tissue. Roughness depths were 3.65 μm for turned implants and 32.7 μm for sand-blasted implants. They used new bone formation and hydrogen gas evolution as metrics to study degradation behavior. Their study could confirm the general good clinical compatibility and osteoinductive potency of MgCa0.8 alloy leading to new bone formation. Increase in surface roughness led to a faster degradation rate. However, a univaribale analysis of variance with significance level of 0.05 showed that the influence of the surface roughness was statically not significant ($p = 0.257$). A faster decomposition of Mg implants leads to a greater release of gas. The sand-blasted cylinders decomposed the fastest. Furthermore, 53% of the radiographically

detectable gas generation appeared in sand-blasted implants. The turned cylinders which exhibited the least structural loss showed hardly any gas formation. The formed gas was resorbed in all cases except one without any clinical problems.

The corrosion mechanism is important, particularly with regard to the biomechanical properties of medical implant devices. Mg-alloys in general tend to pitting corrosion, especially close to chloride ions. In contrast, carbonate ions are able to suppress pitting corrosion totally. Calcium addition to Mg-based alloys enhances their general and pitting corrosion resistance significantly. Up to 0.8wt% Ca, Mg-Ca alloys showed a homogenous texture and a uniformly distributed corrosion. Higher percentages of calcium led to irregular and more widespread corrosion.

Von Der Höh et al found that MgCa0.8 shows obvious pitting corrosion for threaded cylinders but not for turned and sand-blasted implants. In addition, turned implants showed the best integration into the bone compared to sand-blasted and threaded cylinders. Therefore, it seems a smooth surface is particularly suitable when using resorbable implants made of Mg alloys as bone implants in osteosynthesis. This is against the fact that in case of conventional implants rougher surfaces lead to a greater bone-implant bonding. One probable reason for this is the quicker degradation associated with the rougher surface in the case of resorbable implants on a Mg basis.

Wang et al [23] demonstrated that the biodegradation rate of an AZ31 alloy can be significantly reduced by grain refinement produced by mechanical processing. They investigated three material states: (i) squeeze cast (SC), (ii) SC + hot rolled (HR), (iii) SC + HR + equal channel angular pressing (ECAP). SC material had a coarse-grained dendritic structure with average grain size of about 450 μm . Hot rolling changed the SC microstructure to a uniformly

fine microstructure with nearly equiaxed grains of about 15 μm size and no remaining of the dendritic structure. ECAP processing of the SC+HR material produced an even finer grain structure with average grain size of about 2.5 μm . The effect of grain structure on degradation behavior was studied using immersion in Hank's balanced salt solution up to 20 days and measurement of the weight loss after certain immersion times. Generally, the degradation process started off with a high degradation rate and slowed down with increasing immersion time. This retardation of the degradation was related to accumulation of the corrosion products (magnesium hydroxide, as well as phosphates and carbonates) and formation of a protective layer. Alloying elements like Al and Zn tend to have a stabilizing effect on the formed protective film in Mg alloys. Indeed, without these alloying elements, pure magnesium experiences a much faster biodegradation under similar testing conditions. Wang et al found the highest degradation rate for SC samples. The degradation rates of the HR and ECAP samples, which were significantly smaller than that for SC material, were rather similar. The prevalent mode of corrosion damage in SC sample was localized pitting. For HR and ECAP samples, pitting damage was significantly reduced and uniform corrosion became the main corrosion mode.

Kannan and Raman [24] examined the degradation behavior of calcium-containing Mg alloys using electrochemical technique in modified-simulated body fluid (m-SBF). AZ91Ca (1wt% Ca), AZ61Ca (0.4wt% Ca), and AZ91 (without Ca) were used in this study. The general and pitting corrosion resistance of calcium-containing Mg alloys in m-SBF was significantly improved as compared to the base alloy. The corrosion current was significantly lower in AZ91Ca alloy than that in AZ91 alloy. Furthermore, AZ91Ca alloy exhibited a five-fold increase in the surface film resistance than AZ91 alloy.

Denkena and Lucas [25] studied the possibility of adjusting degradation kinetics of biocompatible MgCa3.0 implants through adjusting surface and subsurface properties by machining processes. They focused on differences in subsurface properties while similar surface properties were achieved. Turning and deep rolling processes were used to change subsurface properties especially residual stresses. The process parameters were selected in a way to achieve comparable surface properties especially surface roughness. Significant differences occurred in subsurface residual stresses. Larger and deeper compressive residual stresses were achieved by deep rolling. The corrosion rates of the turned surfaces were approximately 100 times faster than the corrosion rates of the deep rolled surfaces. Within the range of surface qualities applied in their study, the better surface finish at low feed rate had no significant influence on the corrosion resistance. A homogeneous corrosion attack with moderate corrosion rates was observed in deep rolled surfaces. The corrosion resistance was improved until the modified layer of subsurface was dissolved and the unmodified bulk region was uncovered.

Xin et al [26] investigated the corrosion behavior of AZ91 alloy in SBF to determine its performance in a physiological environment. The degradation rate by immersion in SBF at 37 °C for 7 days was calculated from hydrogen evolution method. The hydrogen evolution rate in the first 2 h was very high and dropped significantly during the subsequent 4 h. It decreased more slowly after 6 h of immersion and stabilized from about 44 h. After immersion for a sufficiently long time, equilibrium between the formation and dissolution of the corrosion products was established leading to stable degradation rates. Both calcium and magnesium phosphates were present in the corroded products besides magnesium oxide. The phosphate content increased with immersion time and stabilized after about 4 days of immersion. Pitting corrosion was a common behavior of AZ91 soaked in SBF, but was self-limited due to accumulation and

stabilization of the corrosion products by OH⁻. The corrosion rates that were very high during early exposure decreased significantly afterward and stabilized from about 2 days.

Müller et al [27] studied the influence of the electrolyte composition on the corrosion behavior of pure Mg, AZ31, and LAE442 alloys using potentiodynamic techniques. Results showed localized attack in chloride containing media. Phosphate ions hinder the corrosion attack. Proteins like albumin also inhibit this process. The break down potential decreased when chloride concentration increased. The potential range of the passivation region was extended in the presence of albumin. The comparison between AZ31 and LAE442 alloys showed that LAE442 was more resistant to corrosion attack.

Witte et al [28] investigated the effects of the corrosive in-vitro and in-vivo environment on the corrosion rates of the gravity-casted Mg alloys AZ91D and LAE442. Immersion and electrochemical tests were used to study the in-vitro corrosion behavior. Immersion test was carried out at room temperature in 25 L seawater solution for 10 days and weight loss was measured. Electrochemical tests were performed in a borax-phosphate buffer (pH=7.0) at room temperature. The in-vivo corrosion tests were carried out by intramedullar implantation of sample rods of the magnesium alloys in guinea pig femura. They noticed that in-vivo corrosion rates were about four orders of magnitude smaller than those achieved from in-vitro tests. Moreover, LAE442 showed much faster corrosion in both in-vitro tests than AZ91D while this trend was vice versa in-vivo.

Witte et al [29] investigated the degradation mechanism at the bone-implant interface of different degrading magnesium alloys in bone and to determine their effect on the surrounding bone. Sample rods of aluminum-zinc containing Mg alloys AZ31 and AZ91 as well as two rare earth containing Mg alloys (WE43, LAE442) and a degradable polymer were implanted

intramedullary into the femora of guinea pigs. Results showed that alloying elements influence the in-vivo degradation of Mg alloys. Corrosion layer contained considerable amount of biological calcium phosphate and was in direct contact with the surrounding bone. The results further showed an increased bone mass around the Mg implants which lead to the conclusion that high magnesium ion concentration could cause bone cell activation. The degradation was less uniform in the Mg rods compared to biodegradable polymer. All degrading Mg implants exhibited visible subcutaneous gas bubbles. The gas bubbles appeared within one week after surgery and disappeared after 2-3 weeks. No adverse effects due to the gas bubbles were observed in the guinea pigs. The gas bubbles were punctured with a syringe, but no combustion of the out-flowing gas was observed.

In this study, a noncommercial binary alloy of Mg and Ca with 0.8wt% Ca content was made in-house. Hybrid cutting-forming technique was used to mechanically treat the implants surface. The effects of process parameters on degradation kinetics of the MgCa0.8 implants were investigated by immersion tests in simulated body fluid. Morphology and elemental composition of the corroded surfaces were studied using scanning electron microscopy (SEM) and energy dispersive spectroscopy (EDS). Subsurface microstructure of the corroded implants was also investigated.

11.3. Immersion tests

Cylindrical-shaped samples of MgCa0.8 (38 mm dia. × 12 mm th.) were face milled using polycrystalline diamond inserts without any coolant. A square-shaped area of 24 mm × 24 mm was burnished on each sample after face milling. All the samples were ultrasonically cleaned in ethanol and then dried in a stream of air. Unburnished surfaces of each sample were

covered to avoid them from coming into contact with simulated body fluid (SBF) in immersion tests. Table 10.2 shows the chemical composition of the applied SBF. Figure 11.1 demonstrates the set up used for immersion tests. The volume of the SBF in the corrosion cell was 2200 ml and its temperature was maintained at 37 ± 1 °C. The solution was also stirred to keep the temperature and chemical concentration uniform all over the cell. Two sets of immersion tests were performed to study the effect of burnishing feed and pressure on degradation kinetics of MgCa0.8. In pressure-effect set, there was one reference sample which was only face-milled in addition to three more samples processed under 2, 6, and 10 MPa burnishing pressure. Likewise, there were four samples in feed-effect set, a face-milled reference and three burnished samples under 60, 100, and 200 μm feed. Each test was run for 300 hours and every 12 hours, 500 ml of the solution was replaced with fresh SBF to account for the fluid exchange of an adult human by urination.

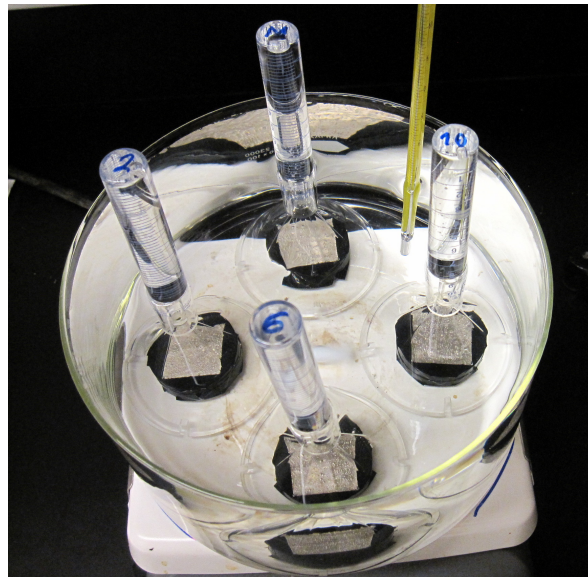


Fig. 11.1 Immersion test on processed samples using hybrid cutting-forming technique

11.4. Hydrogen evolution vs. time

Magnesium reacts very quickly with water, which is plentiful in human body fluid, and produces hydrogen gas and hydroxide according to following reaction:



Based on the stoichiometry in this reaction, oxidation or dissolution of 1 mole magnesium will produce 1 mole hydrogen. Therefore, collecting the evolved hydrogen gas and measuring its volume, *eudiometry*, in the course of time would be an indirect indication of magnesium degradation kinetics in simulated body fluid. *Gravimetry* is another way to study degradation behavior of magnesium in simulated body fluid in which the corroded layer is removed from the samples at certain time intervals and then they are weighed to calculate the amount of mass loss as an indication of degradation kinetics. In this technique a chemical solution, e.g. boiling 15% CrO_3 + 1% AgCrO_4 solution [13], is used to chemically clean the corroded samples from corrosion products and therefore there is always the minimal dissolution of base alloy. Eudiometry is easier to implement and more reliable than gravimetry to study long term degradation behavior of magnesium. In the next two sections, eudiometry of hydrogen is used to study the effects of pressure and feed in hybrid dry cutting-hydrostatic burnishing on in-vitro degradation kinetics of MgCa0.8.

11.4.1. Effect of burnishing pressure on degradation kinetics

Figure 11.2 shows the amount of evolved hydrogen collected during 300 hrs immersion tests on burnished samples processed under different burnishing pressures. It is clearly visible that there is significant improvement in corrosion resistance, particularly in first 100 hrs after implantation, by adding burnishing to the surface layers.

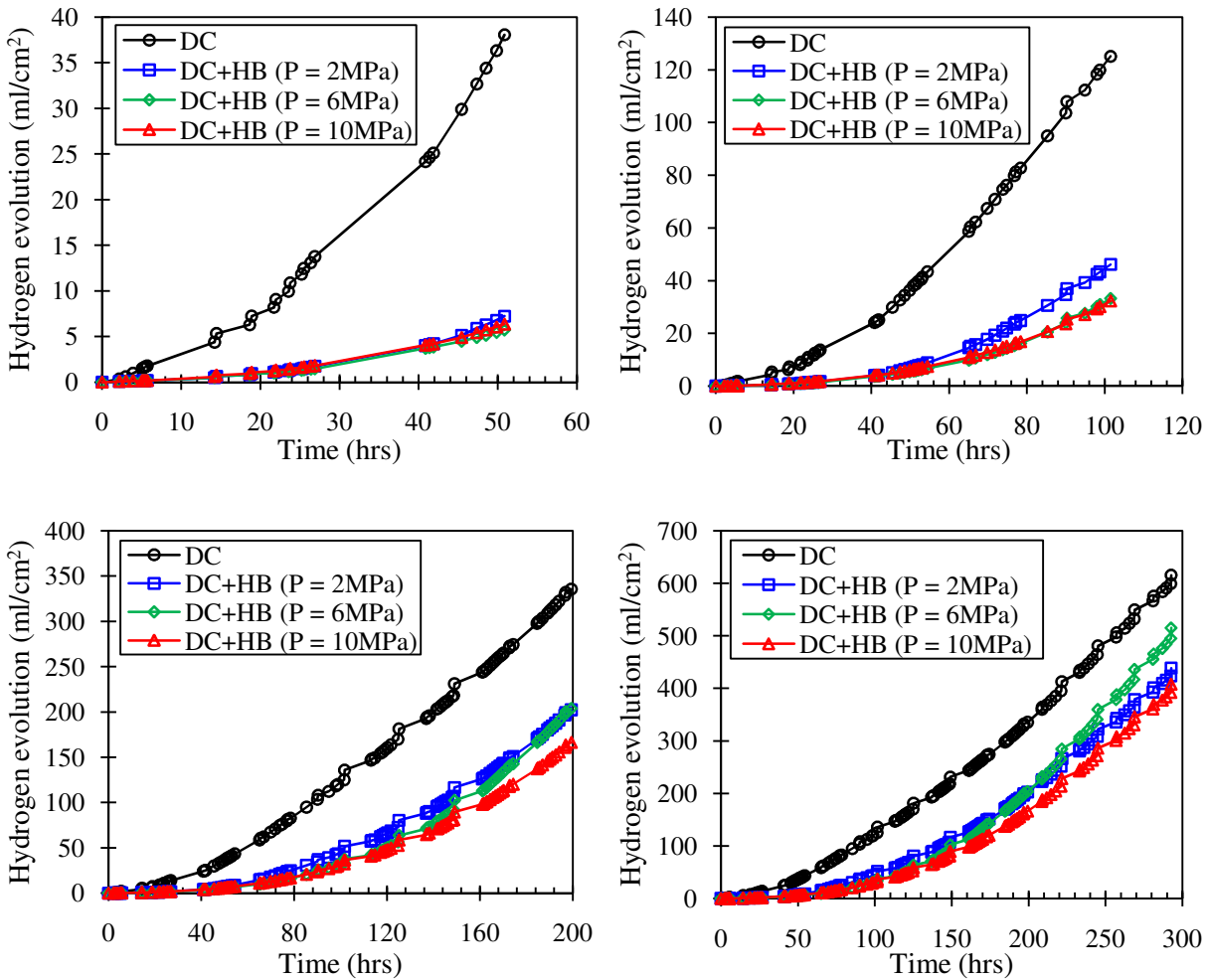


Fig. 11.2 Effect of pressure in hybrid dry cutting (DC)/hydrostatic burnishing (HB) on cumulative hydrogen evolution in 50, 100, 200, and 300 hrs immersion in SBF

The capability to adjust the degradation kinetics of MgCa0.8 biomaterial, particularly for several days after the surgery, is critical in the sense that absorption rate of the corrosion products could match the production rate in order to avoid accumulation of them in the operation site, disrupting the metabolic reactions, and ultimately delaying healing process. Undisturbed healing will provide bone cells with sufficient time to grow at fractured sites and hence the bone will gain increasingly higher strength for carrying daily life loads as the implant gets weaker due to corrosion.

Imposing surface layers of the implants to hybrid dry cutting-hydrostatic burnishing produces a spectrum of mechanical properties starting at the surface and decaying towards the bulk material at subsurface. Therefore, material layers with different mechanical and biodegradation properties would be unveiled as the corrosion progresses and at some point for all the samples, the bulk material with same mechanical and biodegradation properties would be attacked by corrosion reaction and that is when the slopes of the plots in figure 11.2 become identical. Higher burnishing pressures show more gain on corrosion resistance which is due to larger and deeper compressive residual stresses. It is worth mentioning that for this set of tests a plastic tape was used to cover unprocessed surfaces of implants. It was observed that corrosion had happened on those surfaces as well when the tape was removed at the end of the test. This might have been caused due to crevice corrosion. As the corrosion progresses on target areas of the implants, a narrow gap grows gradually between the surface and the tape which is a potential site for crevice corrosion and it spreads to the rest of the unprocessed surface from there as the time passes on. Therefore, some amount of the collected hydrogen in figure 11.2 is produced by unwanted surfaces; however, since all the samples were in same cell, under same condition, and covered identically the comparative study in figure 11.2 would still be valid. Crevice corrosion is

a probable reason that degradation curve corresponding to 6MPa pressure gets ahead of the 2MPa curve after 200 hrs immersion.

The solution temperature and pH were monitored, as are shown in figure 11.3, throughout the immersion test. The temperature was kept around physiological temperature of 37 °C, however, the pH was constantly above the physiological pH of 7.4 even though the solution volume to corroding surface area ratio was big and almost one quarter of the solution replaced every 12 hrs with fresh solution. The whole solution was replaced by fresh solution at 40th hour, seen as a sharp ditch in figure 11.3, to investigate whether there were other unforeseen factors affecting the pH or it was just the fast corrosion reaction producing large amount of hydroxide and rising pH. The pH read-out intervals were selected very short right after the solution replacement and it was noticed that the pH increased fairly quickly and stabilized around 9.65 for the rest of the test. It is expected for degradation to progress faster at physiological pH of 7.4. Higher pH values reflect the presence of larger amount of hydroxide in the solution which will in turn decrease the driving force of the reaction (1) to progress towards the right side and produce more corrosion products. This unconformity in the pH still does not affect the goal of this comparative study to investigate the effect of mechanical surface treatment by hybrid technique on degradation kinetics, since all the samples see same environmental conditions.

11.4.2. Effect of burnishing feed on degradation kinetics

Figure 11.4 shows degradation behavior of processed MgCa0.8 implants under different burnishing feeds in the simulated body fluid. Again it is clearly visible that hybrid technique has improved the corrosion resistance significantly particularly in the first 200 hrs. The slope of the

curves become more or less identical after 200 hrs immersion implying that mechanically affected zone (MAZ) is entirely corroded and the corrosion mechanism has started attacking the bulk material located under the MAZ. It is also observed that higher burnishing feed, which is synonymous with less overlap between consecutive burnishing passes, has the largest impact on corrosion resistance.

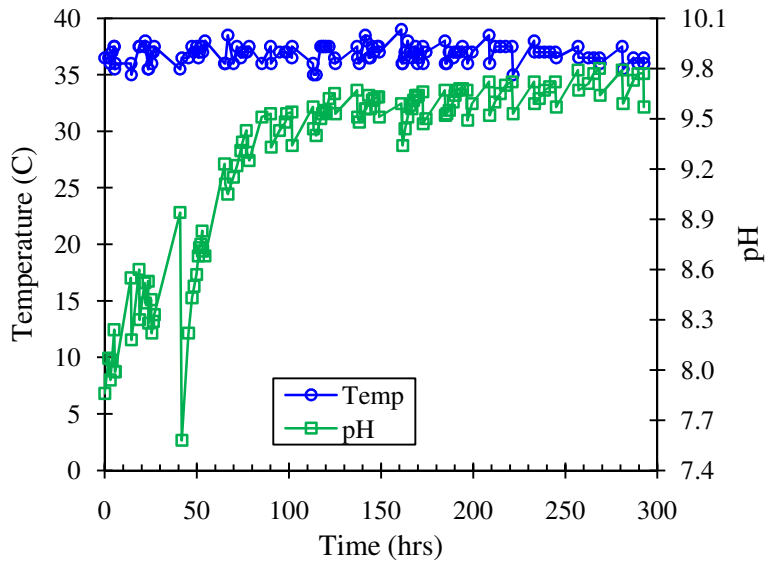


Fig. 11.3 Time history of solution temperature and pH in pressure-effect test

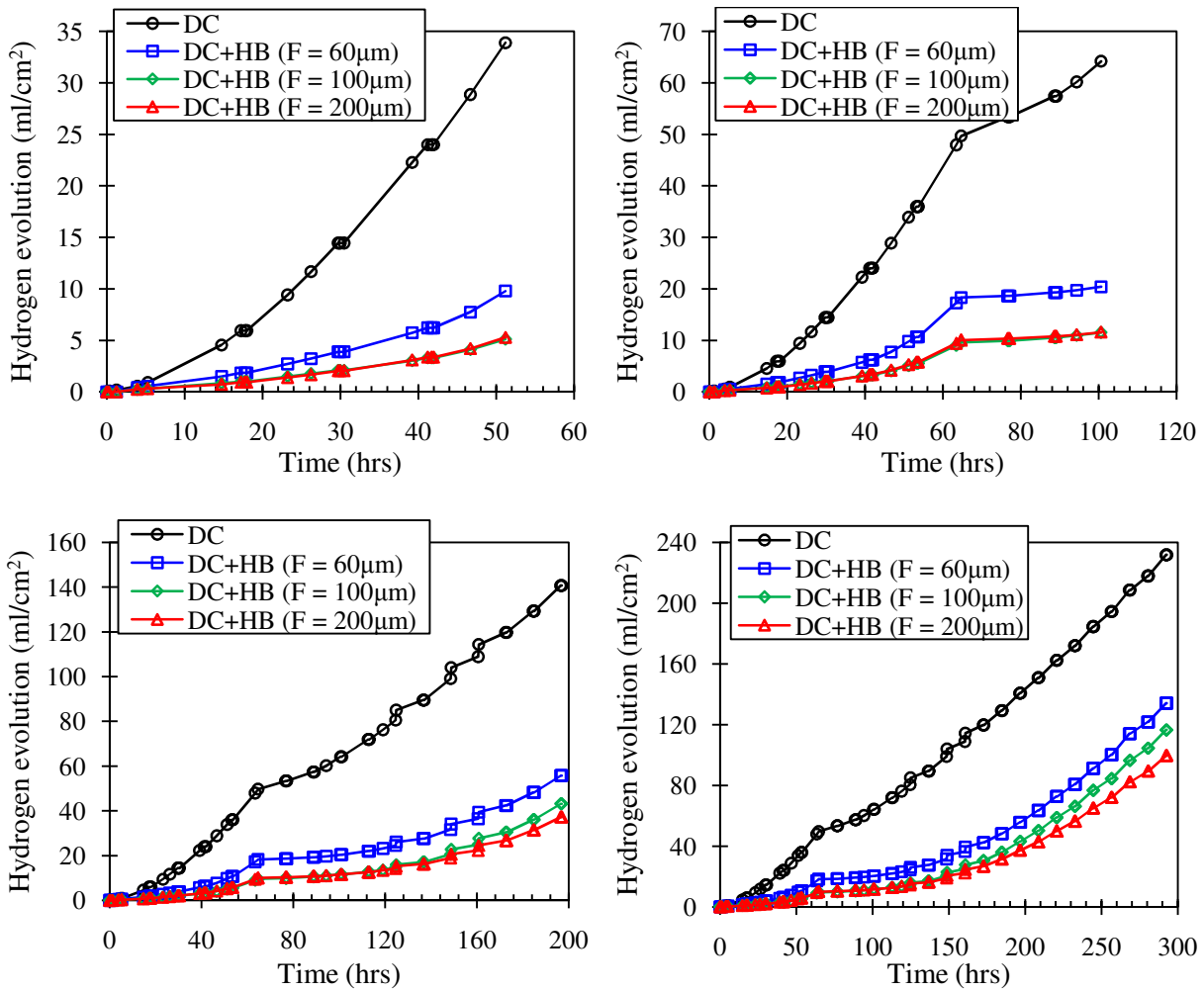


Fig. 11.4 Effect of feed in hybrid dry cutting (DC)/hydrostatic burnishing (HB) on cumulative hydrogen evolution in 50, 100, 200, and 300 hrs immersion in SBF

To avoid the occurrence of crevice corrosion in this set of samples, the unwanted surfaces of the implants were covered using nail polisher. However, after about 60 hrs immersion small particles of nail polish were spotted flowing around in the solution. That was an indication of potential break down in the protective layer in case the test was to run for longer periods. Therefore, the test was stopped and the samples were pulled out of the solution to try cold epoxy

mount as the last resort to protect the unwanted surfaces from crevice corrosion. The samples had to be sized smaller in order to fit the epoxy mount molds. That was done by grinding using SiO₂ abrasive papers and the final exposed area was 1.8 mm × 1.8 mm rather than original 2.4 mm × 2.4 mm. The little kink in degradation curves around 60 hr immersion is due to this change in the size of the exposed area. In order to plot the data collected before the cold epoxy mount and afterwards in the same diagram, the measured volume of the collected hydrogen was normalized by the exposed area.

The temperature and pH of the solution were monitored in this test as well (figure 11.5). The temperature was kept around the physiological value; however, the pH showed pretty much the same pattern as in pressure-effect case. The big pH drop in figure 11.5 around 60 hr immersion is caused by replacing the whole solution with fresh one after epoxy mounting of the samples.

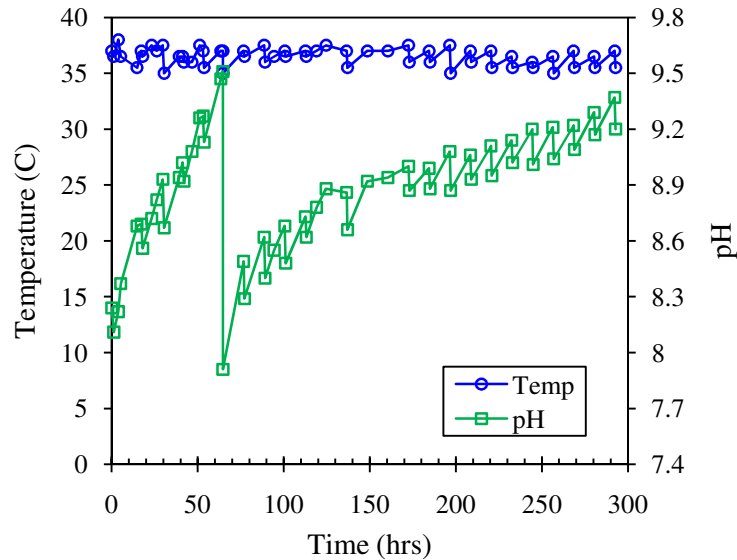


Fig. 11.5 Time history of solution temperature and pH in feed-effect test

11.5. Surface morphology and elemental composition

The surface morphology of the corroded implants after immersion tests is shown in the SEM images of figure 11.6. All samples show more or less same morphology characterized with heavily uneven pattern and strong indications of localized corrosion. Observation of similar morphology on all the samples was expected due to the fact that after nearly two weeks of immersion the mechanically affected zone (MAZ) would be dissolved entirely in the solution and underlying substrate would be exposed to corrosive medium. This substrate is the as-cast MgCa0.8 with same mechanical and biodegradation characteristics on all samples. Therefore, degradation will have pretty much the same dynamics on all the samples resulting in similar looking morphology as in figure 11.6.

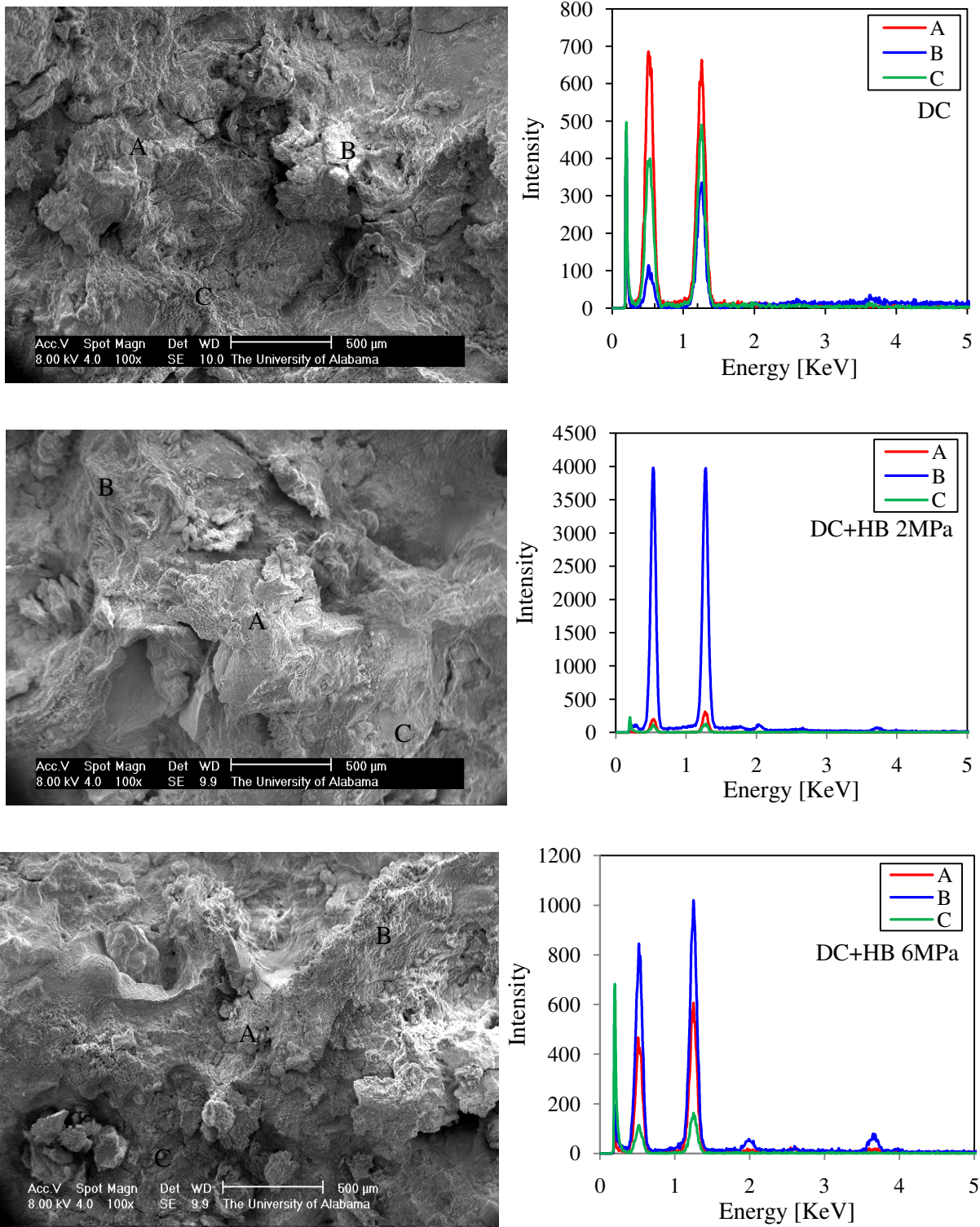


Fig. 11.6 Surface morphology and EDS spectrum of MgCa_{0.8} implants processed under different pressure and feed in hybrid dry cutting-hydrostatic burnishing

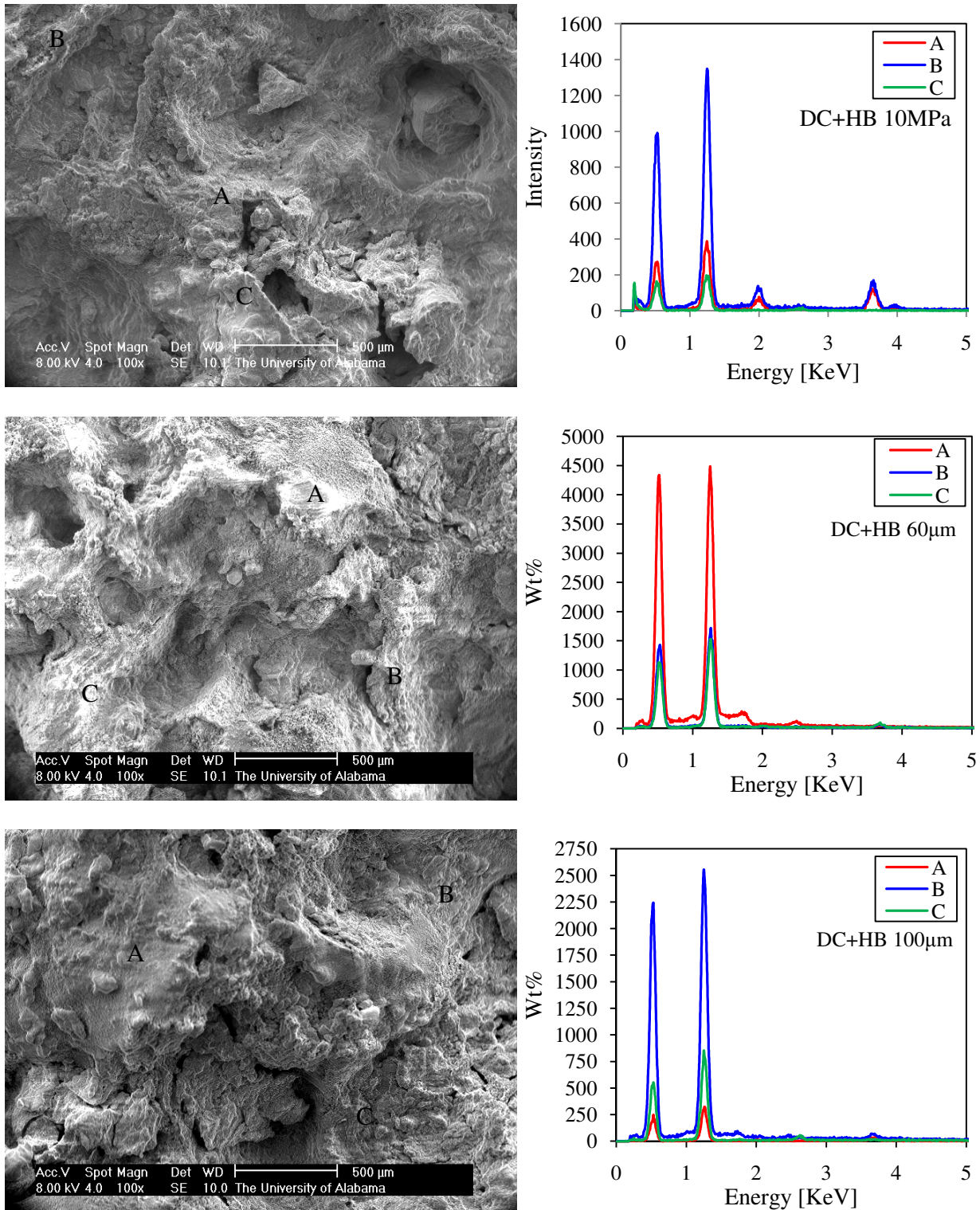


Fig. 11.6 *Contd.* Surface morphology and EDS spectrum of MgCa_{0.8} implants processed under different pressure and feed in hybrid dry cutting-hydrostatic burnishing

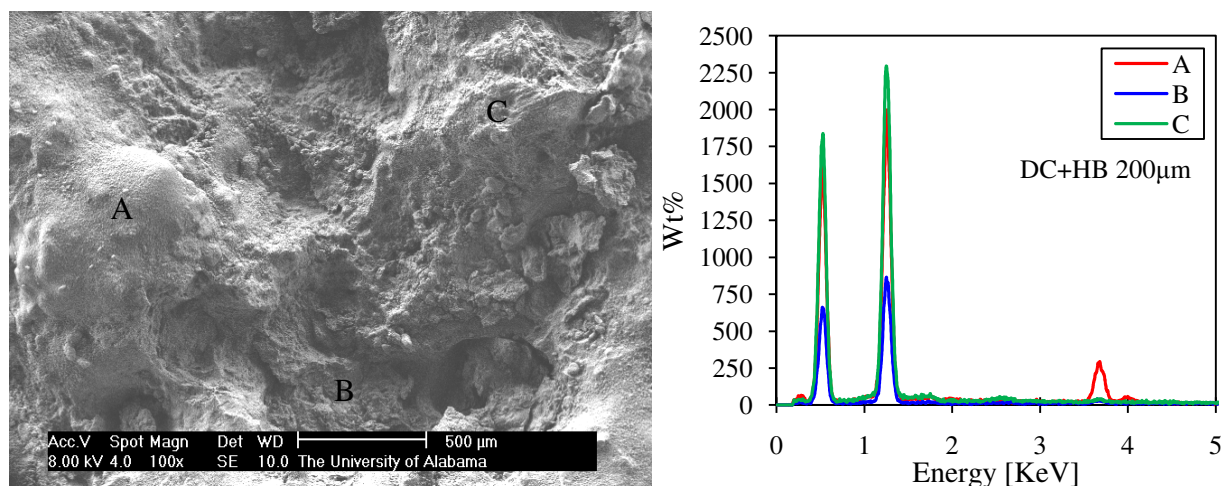


Fig. 11.6 *Contd.* Surface morphology and EDS spectrum of MgCa0.8 implants processed under different pressure and feed in hybrid dry cutting-hydrostatic burnishing

Energy dispersive spectroscopy (EDS) was also used to investigate the elemental composition of the corroded MgCa0.8 surfaces. Three spots on each sample were studied for this purpose and it was noticed that EDS spectrums show different intensities for same energy levels depending on the spot location. This nonhomogeneity in distribution of chemical elements on corroded surfaces strengthens the notion of localized corrosion. The constituting elements are identified and the average amount of each element is computed and shown in figure 11.7 for all the samples. Degradation depletes surface layer from Mg, more than 50%, while makes it richer in Ca content. It is also noticeable that more than 50% of the corroded surface layer is composed of oxygen. This could be due to diffusion of phosphate (PO_4^{3-}) and carbonate (CO_3^{2-}) ions from the solution into the surface or hydroxide (OH^-) formation on the surface. It is worth mentioning here that the surface of all samples was covered with a thick layer of powder-like, white-color substance which was removed mechanically to expose the surfaces shown in figure 11.6. There

is a very high chance for this substance to be magnesium hydroxide $Mg(OH)_2$ particularly due to high pH value of the solution in figures 11.3 and 11.5 which stabilizes the hydroxide. The other possibility is the formation of hydroxyapatite $Ca_{10}(PO_4)_6(OH)_2$ which is the naturally occurring form of calcium and has strong resemblance to the bone structure. This similarity is favored from medical side since it stimulates bone cells to attack the implant surface and make proper bonding which is vital for keeping bone fragments in their original anatomical alignment during recovery.

Characterizing the mentioned substance needs further investigation. Moreover, Si was detected on feed-effect samples as is shown in figure 11.7. This element was neither in the $MgCa_{0.8}$ alloy nor in the solution (Table 10.2). A possible source for this element is SiO_2 abrasive papers used in the grinding stage to resize the samples before cold epoxy mounting.

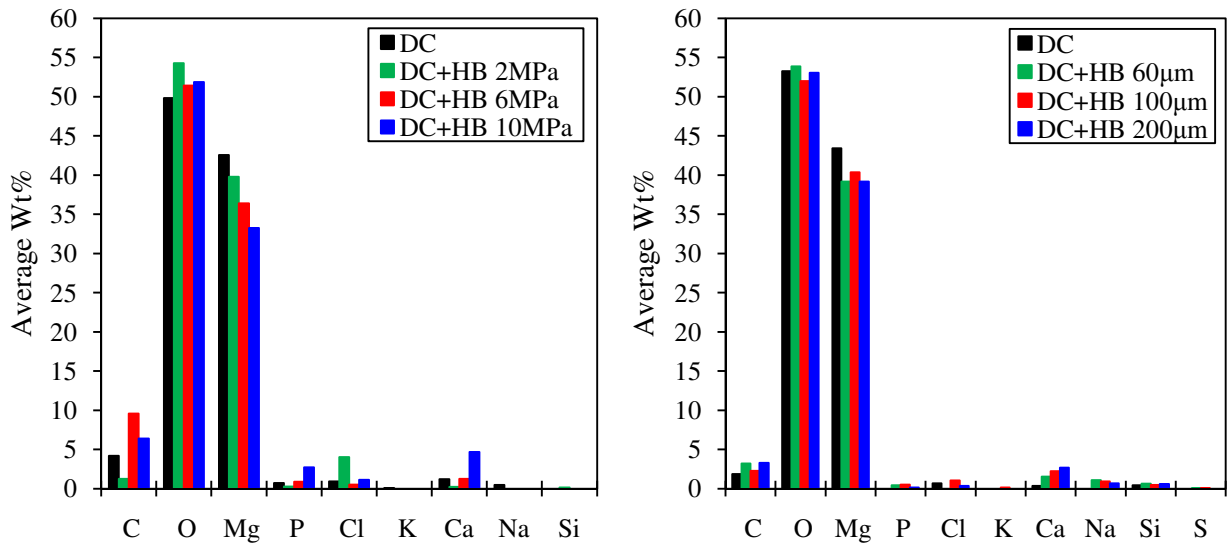
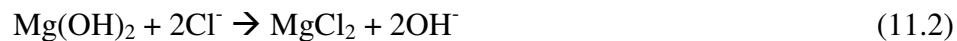


Fig. 11.7 Quantitative EDS and elemental composition of the corroded $MgCa_{0.8}$ surfaces

11.6. Subsurface micrographs

Figure 11.8 shows subsurface micrographs of all the samples after immersion tests. The localized nature of corrosion after two weeks immersion and irregular shaped pits are clearly visible in the optical pictures of the subsurface. The overall reaction (1) consumes H^+ and produces OH^- which causes the pH value to increase and favors the formation of $Mg(OH)_2$. Therefore, it seems the corrosion should stop at some point due to protective function of the formed hydroxide layer. However, in aqueous physiological solutions which contain chloride (Cl^-), hydroxide reacts and forms soluble magnesium chloride ($MgCl_2$) according to following reaction. This guarantees the degradation of the whole implant until it is completely degraded.



The other factor which acts against complete stabilization of the hydroxide layer is the body fluid flow in this study and in actual physiological case. The fluid flow caused by stirring action in the corrosion cell (figure 11.1) accelerates the mass diffusion around implants, prevents the precipitation of corrosion products to some extent, and results in acceleration of Mg^{2+} dissolution. The mechanism of the corrosion process is complex and is affected by metallurgical factors, alloying additions, and impurities. Mg_2Ca phase, formed on the grain boundaries, is more active than α -Mg [5] in the bulk of grains and it assumes the role of anode contradicting other intermetallics which are cathode in relation to Mg. Hence, the corrosion concentrates in the grain boundaries followed by undercutting and falling-out of grains. Evidences of such selective attack in grain boundaries are visible in the micrographs of figure 11.8. This might be a reason

for powder-like structure of the white substance mentioned in section 4. Evolution of the hydrogen gas might be another reason for that which fractures the formed films on the surface.

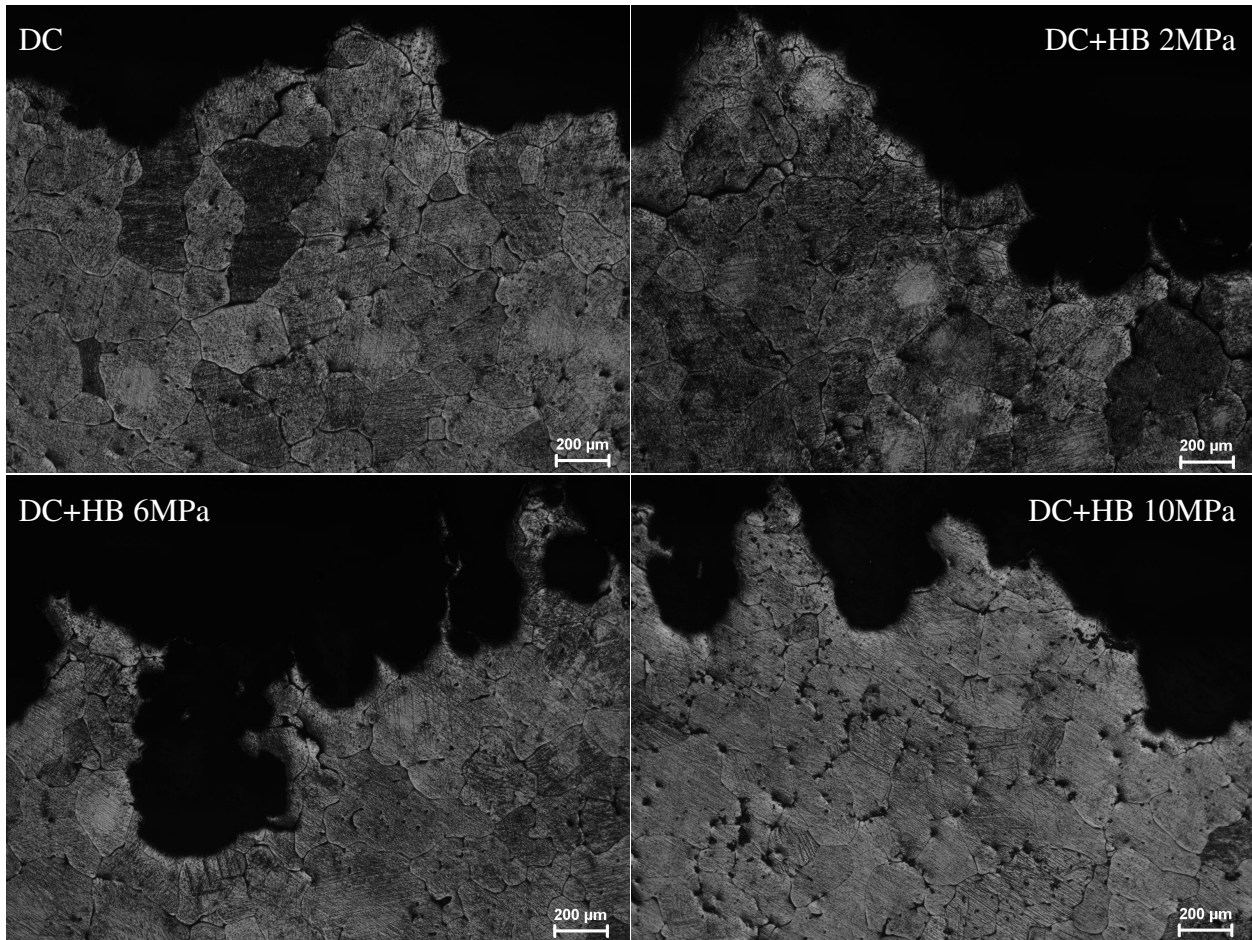


Fig. 11.8a Subsurface micrographs of the corroded MgCa_{0.8} surfaces processed under different burnishing pressures

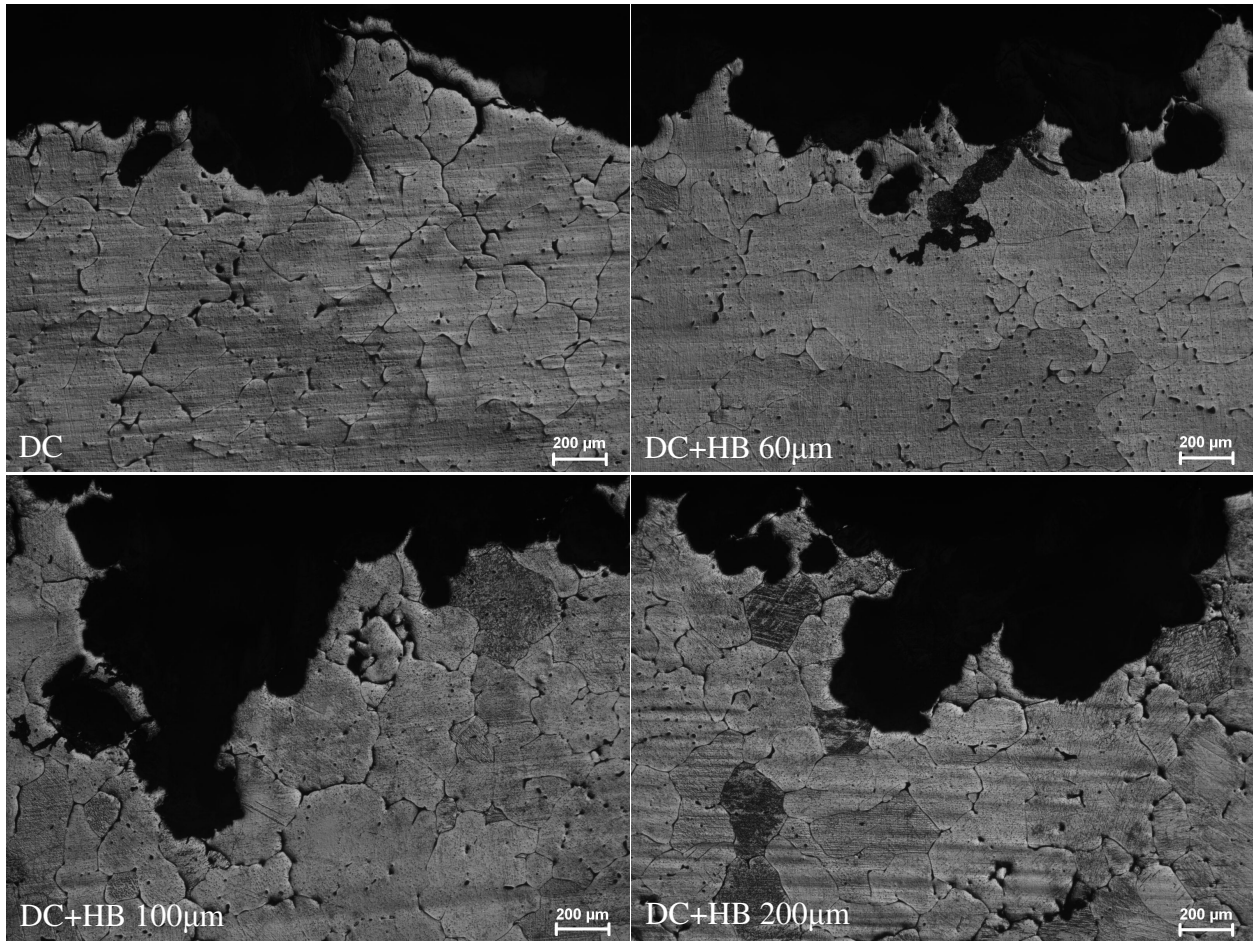


Fig. 11.8b Subsurface micrographs of the corroded MgCa0.8 surfaces processed under different burnishing feeds

11.7. Conclusions

A novel biomaterial which is a binary alloy of Mg and Ca were made in-house. The MgCa0.8 implants were processed using the hybrid dry cutting-hydrostatic burnishing and the effect of process parameters on long term degradation behavior of the implants were studied through immersion tests in simulated body fluid. Followings are the results of this study:

- Hybrid technique is successful in adjusting the bioperformance of biodegradable, metallic MgCa0.8 implants. The corrosion resistance of the implants could be improved significantly during the manufacturing stage applying the hybrid technique.
- Higher burnishing pressures and larger feeds result in higher corrosion resistance. This brings about the feasibility of adjusting the degradation profile of the implants to match the healing profile of the bone traumas in various applications simply by choosing the right processing parameters in manufacturing stage.
- Long term exposure to corrosive physiological medium will cause the mechanically affected zone (MAZ) to dissolve entirely and the corrosion will happen in more localized fashion afterwards. EDS analysis shows significant amount of oxygen in the composition of the corroded layers.

References

1. A.C. Hänzi, A. Metlar, M. Schinhammer, H. Aguib, T.C. Lüth, J.F. Löffler, P.J. Uggowitzer, 2011, Biodegradable wound-closing devices for gastrointestinal interventions: degradation performance of the magnesium tip, *Materials Science and Engineering C* 31 (2011) 1098 – 1103.
2. D. Xue, Y. Yun, M. Schulz, V. Shanov, Corrosion protection of biodegradable magnesium implants using anodization, *Materials Science and Engineering C* 31 (2011) 215 – 223.
3. R. Walter, M.B. Kannan, In-vitro degradation behavior of WE54 magnesium alloy in simulated body fluid, *Materials Letters* 65 (2011) 748 – 750.
4. S. Hiromoto, A. Yamamoto, Control of degradation rate of biodegradable magnesium by anodization and steam treatment, *Materials Science and Engineering C* 30 (2010) 1085 – 1093.

5. N.T. Kirkland, N. Birbilis, J. Walker, T. Woodfield, G.J. Dias, M.P. Staiger, In-vitro dissolution of magnesium-calcium binary alloys: clarifying the unique role of calcium additions in bioresorbable magnesium implant alloys, *J. Biomedical Materials Research B: Applied Biomaterials* 95 (2010) 91 – 100.
6. W.F. Ng, K.Y. Chiu, F.T. Cheng, Effect of pH on the in vitro corrosion rate of magnesium degradable implant material, *Materials Science and Engineering C* 30 (2010) 898 – 903.
7. M. Thomann, C. Krause, N. Angrisani, D. Bormann, T. Hassel, H. Windhagen, A. Meyer-Lindenberg, Influence of a magnesium-fluoride coating of magnesium-based implants (MgCa0.8) on degradation in a rabbit model, *J. of Biomedical Materials Research A* 93 (2010) 1609 – 1619.
8. Y. Xin, T. Hu, P.K. Chu, Influence of test solutions on in vitro studies of biomedical magnesium alloys, *J. of the Electrochemical Society* 157 (2010) 238 – 243.
9. G. Song, A. Atrens, Understanding magnesium corrosion, *Advanced Engineering Materials* 5 (2003) 837 – 858.
10. M.B. Kannan, R.K. Singh Raman, A mechanistic study of in vitro degradation of magnesium alloy using electrochemical techniques, *J. of Biomedical Materials Research A* 93 (2010) 1050 – 1055.
11. A. Drynda, T. Hassel, R. Hoehn, A. Perz, F.W. Bach, M. Peuster, Development and biocompatibility of a novel corrodible fluoride-coated magnesium-calcium alloy with improved degradation kinetics and adequate mechanical properties for cardiovascular applications, *J. of Biomedical Materials Research A* 93 (2010) 763 – 775.
12. M.B. Kannan, Influence of microstructure on the in-vitro degradation behavior of magnesium alloys, *Materials Letters* 64 (2010) 739 – 742.
13. W. Zhou, T. Shen, N.N. Aung, Effect of heat treatment on corrosion behavior of magnesium alloy AZ91D in simulated body fluid, *Corrosion Science* 52 (2010) 1035 – 1041.
14. W.F. Ng, M.H. Wong, F.T. Cheng, Stearic acid coating on magnesium for enhancing corrosion resistance in Hanks' solution, *Surface & Coating Technology* 204 (2010) 1823 – 1830.
15. A. Krause, N. von der Höh, D. Bormann, C. Krause, F.W. Bach, H. Windhagen, A. Meyer-Lindenberg, Degradation behavior and mechanical properties of magnesium implants in rabbit tibiae, *J. of Materials Science* 45 (2010) 624 – 632.
16. J.E. Gray-Munro, C. Seguin, M. Strong, Influence of surface modification on the in vitro corrosion rate of magnesium alloy AZ31, *J. of Biomedical Materials Research* 91 (2009) 221 – 230.

17. A. Yamamoto, S. Hiromoto, Effect of inorganic salts, amino acids and proteins on the degradation of pure magnesium in vitro, *Materials Science and Engineering C* 29 (2009) 1559 – 1568.
18. Y. Zhang, G. Zhang, M. Wei, Controlling the biodegradation rate of magnesium using biomimetic apatite coating, *J. of Biomedical Materials Research B: Applied Biomaterials* 89 (2009) 408 – 414.
19. G. Song, A. Atrens, D. Stjohn, J. Nairn, Y. Li, Electrochemical corrosion of pure magnesium in 1*N* NaCl, *Corrosion Science* 39 (1997) 855 – 875.
20. W.D. Müller, M.F.L. de Mele, M.L. Nascimento, M. Zeddies, Degradation of magnesium and its alloys: dependence on the composition of the synthetic biological media, *J. of Biomedical Materials Research A* 90 (2009) 487 – 495.
21. M. Thomann, C. Krause, D. Bormann, N. von der Höh, H. Windhagen, A. Meyer-Lindenberg, Comparison of the resorbable magnesium alloys LAE442 und MgCa0.8 concerning their mechanical properties, their progress of degradation and the bone-implant-contact after 12 months implantation duration in a rabbit model, *Materialwissenschaft und Werkstofftechnik* 40 (2009) 82 – 87.
22. N. Von Der Höh, D. Bormann, A. Lucas, B. Denkena, C. Hackenbroich, A. Meyer-Lindenberg, Influence of different machining treatments of magnesium-based resorbable implants on the degradation behavior in rabbits, *Advanced Engineering Materials* 11 (2009) B47 - B54.
23. H. Wang, Y. Estrin, Z. Zúberová, Bio-corrosion of a magnesium alloy with different processing histories, *Materials Letters* 62 (2008) 2476 – 2479.
24. M.B. Kannan, R.K. Raman, In vitro degradation and mechanical integrity of calcium-containing magnesium alloys in modified-simulated body fluid, *Biomaterials* 29 (2008) 2306 – 2314.
25. B. Denkena, A. Lucas, Biocompatible magnesium alloys as absorbable implant materials – adjusted surface and subsurface properties by machining processes, *Annals of CIRP* 56 (2007) 113 – 116.
26. Y. Xin, C. Liu, X. Zhang, G. Tang, X. Tian, P.K. Chu, Corrosion behavior of biomedical AZ91 magnesium alloy in simulated body fluid, *J. of Materials Research* 22 (2007) 2004 – 2011.
27. W.D. Müller, M.L. Nascimento, M. Zeddies, M. Córscico, L.M. Gassa, M.A. Fernandez, L. de Mele, Magnesium and its alloys as degradable biomaterials; corrosion studies using potentiodynamic and EIS electrochemical techniques, *Materials Research* 10 (2007) 5 – 10.

28. F. Witte, J. Fischer, J. Nellesen, H.A. Crostack, V. Kaese, A. Pisch, F. Beckmann, H. Windhagen, In vitro and in vivo corrosion measurements of magnesium alloys, *Biomaterials* 27 (2006) 1013 – 1018.
29. F. Witte, V. Kaese, H. Haferkamp, E. Switzer, A. Meyer-Lindenberg, C.J. Wirth, H. Windhagen, In vivo corrosion of four magnesium alloys and the associated bone response, *Biomaterials* 26 (2005) 3557 – 3563.

CHAPTER 12

SUMMARY AND FUTURE WORK

This research introduces a novel biodegradable metallic material suitable for orthopedic applications. This biomaterial which is a binary alloy of magnesium (Mg) and calcium (Ca) avoids further progress of artificial osteoporosis, alleviates pain and inflammatory discomfort, and eliminates the need for second surgeries. In this context, development of this biomaterial as next-generation, orthopedic material has significant socio-economical impact. Moreover, this research introduces a method to adjust degradation kinetics of the Mg-Ca implant so that its degradation rate matches absorption rate of the corrosion products and healing rate of the bone trauma in various physiological conditions. Followings are the key findings of this experimental/numerical investigation:

1. High speed dry cutting of Mg-Ca_{0.8} alloy is characterized with continuous chip formation, no spark or chip ignition even at finishing regimes, and limited, transient-nature flank built-up (FBU) formation. Materials adhesion, i.e. FBU, happens at cutting speeds above the critical speed even within short cutting time. No abrasion was observed on polycrystalline diamond cutting inserts.
2. Surface roughness of dry cut implants increased under larger feeds. The average surface roughness was measured to be 0.4 μm . No grain refinement was observed in near surface

zone after cutting. Work-hardened layer was very thin and subsurface microhardness profile stabilized after 12 μm depth. The measured residual stresses were highly compressive.

3. The developed numerical model simulating the chip formation in high speed dry cutting predicted continuous chip formation with no chip ignition consistent with experimental observations.
4. The developed numerical model to predict cutting-induced residual stresses made good first approximation of the measurements. The numerical analysis showed that work-hardening is more prominent than thermal softening in high speed dry cutting using diamond tools. Higher cutting speeds result in larger plowing, higher thrust forces, and deeper compressive residual stresses.
5. The numerical-experimental study of the mechanics in hydrostatic burnishing revealed that, due to pressure loss at the tip of the burnishing tool, actual rolling forces are 23% lower than theoretical values on average. It was also noticed that hydrostatic burnishing has isothermal nature and on average 8% elastic recovery of the deformed layer exists in this process.
6. Roughness had strong anisotropy on the burnished surfaces. The surfaces were rougher in perpendicular to burnish track. Higher burnishing pressure and feed caused higher anisotropy. The burnished surfaces were shinier and smoother than dry cut surfaces. Pressure had the strongest impact on pre-existing topography among all the burnishing parameters. No grain refinement was observed in near surface layers after burnishing. Higher work-hardening and microhardness was measured in subsurface layers of burnished implants compared to dry cut ones. Pressure has the strongest influence on microhardness among all the burnishing parameters. Surface residual stresses were compressive and anisotropic. Measured residual stresses in parallel to burnish track direction were noticeably smaller than

perpendicular direction. Hydrostatic burnishing produced deep layers (~ 600 μm) of compressed material by work-hardening shallow layers (~300 μm). Maximum compressive residual stress produced by burnishing was larger in magnitude (~ 150 MPa) and was located deeper compared to dry cutting.

7. The developed numerical model for hydrostatic burnishing revealed that number of burnishing cycles, required to establish a steady state deformation, would be larger under higher pressures and smaller feeds. Pre-existing roughness profile was predicted to affect residual stress distributions particularly in the first 70 μm below the surface. Surface residual stresses were predicted and measured to decrease with increasing burnishing pressure while to increase with increasing feed. However, subsurface residual stress predictions did not match with measurements very well.
8. Short-term electrochemical tests to study the effect of mechanical surface treatment on in-vitro degradation revealed that both spontaneity and kinetics of the corrosion reaction are affected by surface treatment. Potentiodynamic technique has the unique capability to decouple these effects as opposed to gravimetric and eudiometric tests. Faster cutting speed produced more spontaneity but slower kinetics. Similar trend was observed for burnishing under higher pressures and larger rolling loads. Morphology of the corroded surfaces revealed strong indications of uniform rather than localized corrosion.
9. Long-term eudiometric tests proved that hybrid dry cutting-hydrostatic burnishing is successful in adjusting the corrosion resistance of the Mg-Ca_{0.8} implants. Higher burnishing pressures and larger feeds resulted in more corrosion resistance. Study of the surface morphology after long-term corrosion tests revealed that severe pitting had happened. The

thickness of the mechanically affected zone is determinative of the time when corrosion switches from uniform pattern to more localized one.

Followings are the subjects for further investigation in future research work:

1. Study the effect of tool geometry on degradation using different ball diameters at the tip of the burnishing tool.
2. Refine the grain structure of Mg-Ca_{0.8} and study the effect of grain size on measured residual stresses and ultimately degradation.
3. Perform in-vivo tests to characterize bioperformance of the processed Mg-Ca_{0.8} implants more realistically.